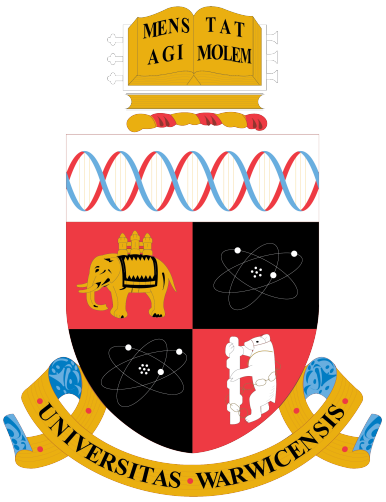

Structural and magnetic investigations of chiral magnets

by

Amelia Elisabeth Hall

Thesis

Submitted to the University of Warwick

for the degree of

Doctor of Philosophy

in Physics

Department of Physics

July 2022

THE UNIVERSITY OF WARWICK

Contents

List of Tables

List of Figures

Acknowledgments

There are many people that have aided me in a multitude of ways during my PhD. My first and most effusive thanks must go to my academic supervisor, Geetha Balakrishnan, for supporting me throughout and always driving me to produce the best possible work that I could. Her vast experience in the field of crystal growth and magnetism has been absolutely indispensable and this project would have been impossible without her.

In addition I would like to thank the Engineering and Physical Sciences Research Council for funding this project in the first place, as well as to all the members of the UK Skyrmion Project from Durham University, the University of Cambridge, the University of Southampton, the University of Oxford, and the University of Warwick. The atmosphere of this whole group has been incredibly welcoming and I am fortunate to be a small part of the research that has been conducted therein. I would also like to thank Pascal Manuel, Fabio Orlandi, and Dmitry Khalyavin for all their aid in learning both FullProf and JANA20202 and analysing the data taken at Wish at the ISIS Neutron and Muon Source.

I am also grateful for the entirety of the Superconductivity and Magnetism group for all their help in completing my project. I have learned a huge amount from my many discussions with Martin Lees who has been incredibly generous with his time and patient with my inquiries, and Oleg Petrenko's experience with neutron diffraction techniques and insightful questions have been very useful throughout my project. The amazing Tom Orton and Patrick Ruddy have been indispensable and without their technical expertise many of my experiments would not have taken place.

Aleš Štefančič taught me many things about the chemistry of materials and was endlessly patient with both my clumsiness and my many inquiries. I would like to thank him for all the things that he taught me and also express how pleased I am for the chance to work with him. In addition, I am incredibly grateful to Daniel Mayoh for his hard work and good humour, and for his support during this project.

I would like to thank my office mates Sam Holt, Sam Curley, Matt Pearce, and Lunci Xiang for all our office discussions and good times. Sam Holt especially has been a source of encouragement and an invaluable source of knowledge and humour. Additonally, Kathrin Gotze, Matthew Coak, Robb Williams, David Jonas, George Wood, Manisha Islam, and Shroya Vaidya are all lovely people and amazing physicists that I have had some great times and very interesting discussions with. Thanks to all of you for making my time spent in the Superconductivity and Magnetism group so enjoyable!

I would like to thank all of my friends who have been there for me throughout my PhD. Special thanks go to my friend Dominic Kennel for his tireless propping me up whenever I felt down, and my house mates Chloe Haynes, Katrina Bogus, and Alex Isaias for their endless support and for keeping me grounded during my PhD, as well as Marble the cat, a great muse whose demands to perch atop my laptop while I was working were ceaseless. A big thank you must also go to Matthew Clowe, for his encouragement and support - we got there in the end! Finally, I would like to thank my family for supporting me throughout. Georgia, Lilly, Serina and Adrian - without you all I wouldn't be here in the first place.

Declarations

This thesis has been constructed as a fundamental part of the degree of Doctor of Philosophy, has been submitted to the University of Warwick, and has not been used for any previous degree. In all cases, the work it contains has been completed by myself, except for that noted in the following declarations.

Polycrystalline samples of Mn_3IrSi and Mn_3RhGe were prepared at the National Cheng Kung university by Yu-Seng Chen and Lieh-Jeng Chang. S. York and myself were responsible for the energy dispersive x-ray measurements on the Mn_3XY materials. A metallographic slide of Mn_3RhGe was prepared and polished by David G. C. Jonas.

The electron diffraction images taken along the c axis of $M_{1/3}XS_2$ were taken by with the help of the Microscopy Group at the University of Warwick. The electron diffraction along the a^* axis for $Mn_{1/3}NbS_3$ and $Cr_{1/3}NbS_3$ and all Lorentz transmission electron microscopy measurements were taken with the aid of S. J. R. Holt from the University of Warwick and J. C. Loudon from the University of Cambridge, with the samples prepared for these measurements by A. C. Twitchett-Harrison using a focused ion beam. J. C. Loudon calculated the projected B-fields using the transport of intensity equation for $Cr_{1/3}NbS_2$ and $Mn_{1/3}NbS_2$. P. A. Midgley helped with the interpretation of some of the electron diffraction results and J. P. Tidey aided with the interpretation of the single crystal x-ray diffraction results for $Mn_{1/3}NbS_2$ and $Cr_{1/3}NbS_2$ and the reconstruction of the Ewald sphere for the former.

All neutron diffraction measurements were taken using WISH at the ISIS Neutron and Muon facility with the aid of P. Manuel, F. Orlandi, and D. D.

Khalyavin. The calculations involving Lifshitz invariants performed for $V_{1/3}NbS_2$ were done by D. D. Khalyavin, who also helped with the consideration of how the antiferromagnetic and ferromagnetic components of the magnetism coupled.

Work involved in this thesis was included in the following publications:

[1] Hall, A. E., Khalyavin, D. D., Manuel, P., Mayoh, D. A., Orlandi, F., Petrenko, O. A, Lees, M. R. and Balakrishnan, G. (2021) *Physical Review B*, **103** (17). 174431.

[2] Hall, A. E., Loudon, J. C., Midgley, P. A., Twitchett-Harrison, A. C., Holt, S. J. R., Mayoh, D. A., Tidey, J. P., Han, Y., Lees, M. R. and Balakrishnan, G. (2022) *Physical Review Materials*, **6** (2). 024407.

Work included in this thesis is also included in these papers that are in preparation for publication:

[1] Hall, A. E., Manuel, P., Khalyavin, D. D., Mayoh, D. A., Orlandi, F., Petrenko, O. A, Chang, L.-J., Chen, Y.-S., Lees, M. R. and Balakrishnan, G. (2022). *A powder neutron diffraction investigation of the magnetic structures of Mn_3IrSi and Mn_3RhGe.*

Some research that has not been included in this thesis but that I have been involved in during this project is published in:

[1] Holt, S. J. R., Štefančič, A., Ritter, C., Hall, A. E., Lees, M. R., and Balakrishnan, G. (2020) *Phys. Rev. Materials*, **4**. 114413.

[2] Hicken, T. J., Wilson, M. N., Franke, K. J. A., Huddart, B. M., Hawkhead, Z., Gomilšek, M., Clark, S. J., Pratt, F. L., Štefančič, A., Hall, A. E., Ciomaga Hatnean, M., Balakrishnan, G., and Lancaster, T. (2021) *Phys. Rev. B*, **103**. 024428.

[3] Mayoh, D. A., Bouaziz, J., Hall, A. E., Staunton, J. B., Lees, M. R., and Balakrishnan, G. (2022) *Phys. Rev. Research*, **4**. 013134.

[4] Hicken, T. J., Hawkhead, Z., Wilson, M. N., Huddart, B. M., Hall, A. E., Balakrishnan, G., Wang, C., Pratt, F. L., Clark, S. J., and Lancaster, T. (2022) *Phys. Rev. B*, **105**. L060407.

Finally, work included in this thesis was presented at these meetings:

- *Intercalated Transition Metal Dichalcogenides: Chiral Soliton Lattice*, British-German WE-Heraeus-Seminar, Bad Honnef, Germany, December 2019 - **Poster**
- *Intercalated Transition Metal Dichalcogenides: Chiral Soliton Lattice*, Frontiers in Condensed Matter Physics, Bristol, UK, January 2020 - **Talk**
- *Magnetic Properties of Intercalated Transition Metal Dichalogenides:* $V_{1/3}NbS_2$ *and* $Cr_{1/3}NbS_2$, Magnetism and Magnetic Materials, Online, October 2020 - **Poster**
- *A comparative study of the magnetic behaviour of intercalated transition metal dichalcogenides* $Cr_{1/3}NbS_2$ *and* $Mn_{1/3}NbS_2$, CRIM 2021: Magnetic Skyrmions, Online, September 2021
- *A neutron diffraction study of the magnetic structure of the intercalated transition metal dichalcogenide* $V_{1/3}NbS_2$, Condensed Matter and Quantum Materials, Online, June 2021- **Talk**
- *The Magnetic Behaviour of Intercalated TMDCs*, ISIS International Women's Day Symposium, Didcot, UK, March 2022 - **Talk**
- *The magnetic structure of* $V_{1/3}NbS_2$, UK Neutron and Muon Science and User Meeting, Coventry, UK, October 2022 - **Talk**.

Abstract

Investigations of the magnetic structures and phase diagrams of chiral magnetic materials has led to the discovery of topological magnetic phenomena such as skyrmions and the chiral soliton lattice, which are of interest for spintronics device applications. In this thesis, the structural and magnetic properties of several chiral magnetic materials are explored, focusing on the intercalated transition metal dichalcogenides and the frustrated antiferromagnetic Mn_3XY (X =Rh,Ir, Y =Si,Ge) families of materials.

Firstly, the magnetic structure of $V_{1/3}NbS_2$ is studied and found to display behaviour consistent with a canted antiferromagnet. Two propagation vectors are required to index all the magnetic Bragg peaks present in powder neutron diffraction data; the $\mathbf{k_0}$ = (0,0,0) propagation vector is associated with an in-plane A-type antiferromagnetic ordering, while the $\mathbf{k_{1/3}}$ = (0,0,1/3) magnetic propagation vector can be associated with an up-down-down configuration of moments along the c axis. A ferromagnetic component too small to be resolved in these measurements is expected from magnetisation data.

This thesis goes on to describe a detailed structural and magnetic investigation to compare single crystals of $Mn_{1/3}NbS_2$, $Cr_{1/3}NbS_2$, and $Cr_{1/3}TaS_2$. Lorentz transmission electron microscopy measurements show the presence of helimagnetic ordering in $Cr_{1/3}NbS_2$ below $T_C = 111$ K, while there is no evidence that $Mn_{1/3}NbS_2$ exhibits helimagnetic ordering below $T_C = 45$ K. An analogue is drawn between the magnetic phase diagrams of $Cr_{1/3}NbS_2$, $Cr_{1/3}TaS_2$, and $Mn_{1/3}NbS_2$, constructed from *ac* susceptibility measurements.

Finally, this thesis describes an investigation into Mn_3IrSi, Mn_3RhGe, and Mn_3RhSi. A single crystal of Mn_3RhSi has been successfully grown and its magnetic properties investigated with *dc* susceptibility measurements to show a magnetic transition at 228 K. Powder neutron diffraction investigations into polycrystalline Mn_3IrSi and Mn_3RhGe reveal a three-dimensional frustrated antiferromagnetic ground state for both materials, while Mn_3RhGe exhibits an incommensurate helical magnetic phase at 200 K.

Abbreviations

ac alternating current

dc direct current

CSL chiral soliton lattice

CSL-1 Highly helical chiral soliton lattice phase

CSL-2 Highly field polarised chiral soliton lattice phase

CVT chemical vapour transport

PND powder neutron diffraction

XRD x-ray diffraction

SQuID superconducting quantum interference device

MPMS magnetic property measurement system

QDPPMS Quantum Design physical property measurement system

ACMS alternating current measurement system

VSM vibrating sample magnetometer

TMDC transition metal dichalcogenide

EDX energy-dispersive x-ray analysis

SEM scanning electron microscope

TEM transmission electron microscope

LTEM Lorentz transmission electron microscopy

FIB focused ion beam

CCD charge coupled device

ZFC zero-field cooling

FCC field-cooled cooling

DMI Dzyaloshinskii-Moriya interaction

RKKY Ruderman-Kittel-Kasuya-Yosida

GEV general electrical varnish

FFM forced ferromagnetic

PM paramagnetic

TIE transport of intensity equation

x(y) values given in parenthesis following a number represent the associated error

Chapter 1

Introduction

This thesis contains an investigation into several materials that display, or have the potential to display, exotic magnetic phenomena. Recent advancements in the sensitivity of instruments and the capability to effectively measure subtle magnetic effects has led to a surge of interest in topological magnetic phenomena and the advancement of spintronics as a field of study. This has increased interest in the discovery of new materials that display interesting and novel magnetic textures.

Magnetic materials have been used for centuries, with Fe_3O_4, also known as magnetite and lodestone, and its ability to attract iron documented as long as 2500 years ago [1], and eventually inspiring the creation of compasses. In 1820, the discovery of the relation between magnetism and electric current led to the ability to produce more powerful magnetic fields than those created from Fe_3O_4, and the study of magnetism and magnetic properties progressed in leaps and bounds, eventually leading to successes such as the creation of magnetic storage hard drives.

A material can be considered magnetic if its magnetic moments are ordered in some fashion. There are many types of magnetism, from paramagnetism, where magnetic moments align with an applied field; to ferromagnetism, where magnetic moments preferentially orientate in the same direction; to antiferromagnetism, where nearest neighbour magnetic moments preferentially align themselves opposite to one another; and more. The ground state magnetism of a material will be its lowest energy state, and what this lowest energy state is will vary depending on the parameters of the material.

Magnetic ordering can also be chiral; that is, magnetic moments can order in such a way that the holistic magnetic structure of the magnetic moments cannot be superimposed onto its mirror image. There are multiple types of chiral magnetic orderings, such as chiral helimagnetism, where the magnetic moments curl around in a

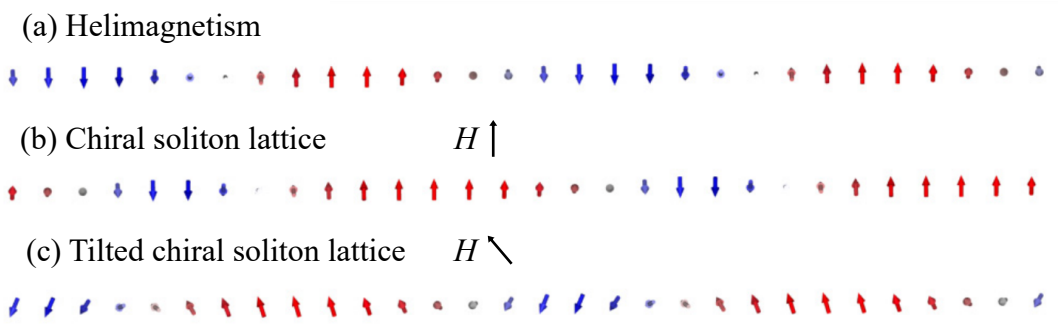

Figure 1.1: Visualisation of (a) chiral helimagnetism, (b) a chiral soliton lattice (CSL), and (c) a tilted chiral soliton lattice in $Cr_{1/3}NbS_2$, with the helical axis stretching along the c axis of the material, taken from [5]. The period of the chiral soliton lattice is increased relative to the period of the helical state. The chiral soliton lattice and the tilted chiral soliton lattice are stabilised on the application of an external field, the direction of which is marked in the figure for each phenomenon respectively.

helical winding. Chiral helimagnetism arises in these materials from the competition between symmetric ferromagnetic exchange interactions which align neighbouring moments in the same direction and the Dzyaloshinskii-Moriya exchange interaction that can arise in non-centrosymmetric materials that aligns neighbouring moments antiparallel with each other. The magnetic spins can then form a spiral, conical, or a helical structure [2] in response to this competition. In addition to helical windings, where the magnetic moments rotate in a plane perpendicular to the helical axis, there additionally exists cycloidal, where the magnetic moments rotate in a plane aligned with the cycloidal axis, and conical windings, where the magnetic moments rotate in a three-dimensional manner, too.

Topological phenomena that can be stabilised with the application of a magnetic field, such as the chiral soliton lattice (CSL), are common in chiral magnetic materials. The CSL takes the form of an array of ferromagnetic domains separated by 360^o domain walls that can occur in strongly anisotropic chiral magnets upon application of a magnetic field applied perpendicular to the helical axis[3]. Fig. 1.1 illustrates helimagnetism as it evolves into a CSL with increasing magnetic field as well as a tilted chiral soliton lattice, which can instead be stabilised in materials such as $Cr_{1/3}NbS_2$ by applying a magnetic field at some angle inbetween perpendicular or parallel to the c axis of the material [4].

Another example of a novel magnetic texture stabilised by magnetic fields are magnetic skyrmions, which were originally proposed by Tony Skyrme to explain the

stability of hadrons [6]. The first experimental evidence for skyrmions was found in the chiral non-centrosymmetric B20 materials, such as MnSi [7]. Since their discovery, there has been a push to find whether skyrmions can present in other kinds of materials. Skyrmions are novel magnetic vortices which are topologically protected and robust, and thus of interest for potential future device applications [8]. The discovery of skyrmions in thin films [9, 10, 11, 12, 13] as well as bulk chiral magnetic materials has led to a renewed interest in 2D materials due to the ease of using these 2D materials to make heterostructures [14, 15, 16, 17].

There are different mechanisms for the formation of skyrmions, one of which is their formation upon the application of a magnetic field to a chiral helimagnetic material. One example of a skyrmionic family of materials are Co-Zn-Mn alloys, which form skyrmions due to the DMI mechanism, and can in fact form skyrmions up to room temperature [18]. This set of alloys adopt the same structure as $\beta-$manganese. Magnetic investigations into $\beta-$manganese reveal it to be a Pauli paramagnet that is strongly enhanced to the point of almost ferrimagnetism [19], with NMR and polarised neutron scattering measurements revealing strong spin correlations in $\beta-$Mn despite it being paramagnetic down to 1.4 K [20]. This complexity and the high transition temperature of the Co-Zn-Mn alloys makes the $\beta-$manganese structure type interesting for further research.

The following sections of the introduction go on to describe the two families of materials investigated as part of this thesis.

1.1 Intercalated transition metal dichalcogenides

The transition metal dichalcogenides (TMDCs) are a family of materials that have attracted considerable interest over the years due to the properties they exhibit such as superconductivity [28, 29, 30], charge density waves [31, 32], and even defect-induced magnetism in Mo-based TMDCs [33, 34]. The subset of this family that adopts the hexagonal 2H-$X\mathrm{S}_2$ polytype, where X is a transition metal, crystallises in structures formed of layers bound together by the weak van der Waals force, allowing thin layers (monolayers, bilayers, etc.) to be isolated via mechanical exfoliation [35]. These layers have been found to exhibit different and sometimes more exotic properties that differ from that of the bulk crystal behavior and have been used to successfully synthesize different heterostructures [36].

In this family of materials, magnetic atoms can be intercalated between the layers and, at the critical concentration of $M_{1/3}\mathrm{XS}_2$, where M is a $3d$ transition metal; X = Nb, Ta; and Y = S, Se; the compounds transform from the hexagonal

Table 1.1: Magnetic ordering and transition temperatures of several intercalated transiton metal dichalcogenides. Materials that form in the non-centrosymmetric hexagonal $P6_322$ space group of stoichiometry $M_{1/3}XY_2$ and tha form in the centrosymmetric hexagonal $P6_3/mmc$ space group of stoichiometry $M_{1/4}XY_2$, where M is a transition metal, X = Nb, Ta and Y = S, Se, are tabulated.

$M_{1/3}XY_2$				
Formula	T_O (K)	Magnetic ordering	Reference	Additional Information
$Mn_{1/3}NbS_2$	45	Chiral helimagnetic or ferromagnetic	[21, 22, 23]	Neutron results suggest an incommensurate magnetic order such as chiral helimagnetic but are not definitive.
$Mn_{1/3}TaS_2$	70	Ferromagnetic	[21]	
$V_{1/3}NbS_2$	50	Canted antiferromagnet	[24]	
$V_{1/3}TaS_2$	32	Canted antiferromagnet	[24]	
$Ti_{1/3}NbS_2$	N/A	Paramagnetic	[25]	
$Cr_{1/3}NbS_2$	111-127	Chiral helimagnetic	[3, 21]	
$Cr_{1/3}TaS_2$	150	Chiral helimagnetic	[26]	
$Fe_{1/3}NbS_2$	42	Antiferromagnetic	[21]	
$Fe_{1/3}TaS_2$	40	Ferromagnetic	[21]	Very large fields required to saturate the magnet, easy axis lies along c-axis - possible signs of canted antiferromagnetism
$Co_{1/3}NbS_2$	26	Antiferromagnetic	[21]	
$Co_{1/3}TaS_2$	30	Antiferromagnetic	[21]	
$Ni_{1/3}NbS_2$	90	Antiferromagnetic	[21]	
$Ni_{1/3}TaS_2$	120	Antiferromagnetic	[21]	
$M_{1/4}XY_2$				
$Mn_{1/4}NbS_2$	105	Ferromagnetic	[27]	
$Mn_{1/4}TaS_2$	80	Ferromagnetic	[21]	
$Fe_{1/4}NbSe_2$	155	Antiferromagnetic	[21]	

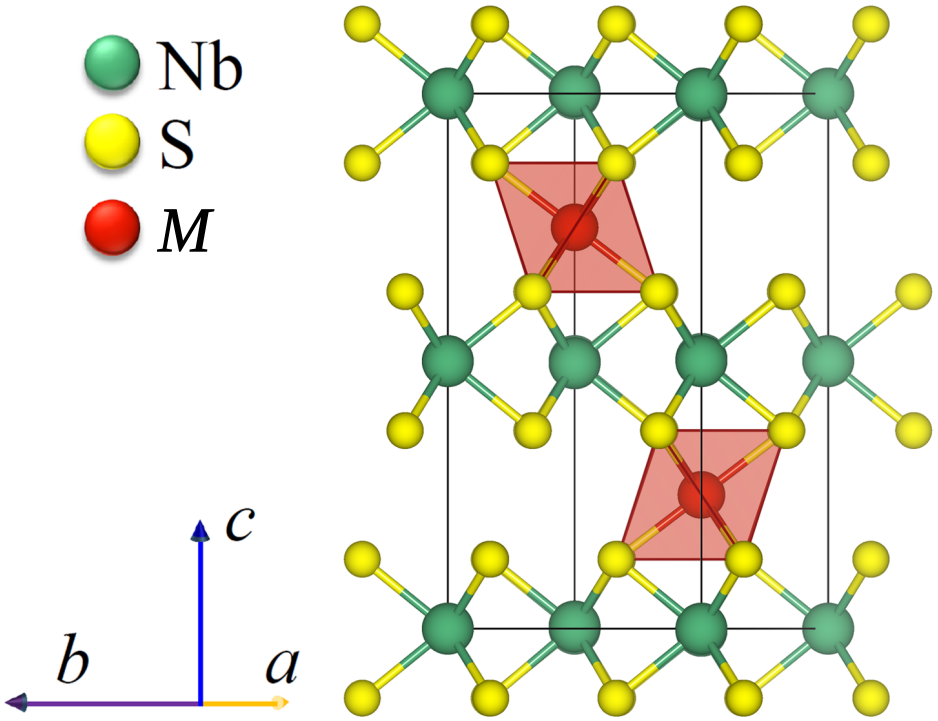

Figure 1.2: Structure of $M_{1/3}NbS_2$ which crystallises in the hexagonal, chiral, non-centrosymmetric $P6_322$ space group, viewed along the a^* direction. The intercalate, M, is shown in dark (red) between layers of S and Nb. The octahedra around the M atoms are shown.

centrosymmetric space group $P6_3/mmc$ to the hexagonal non-centrosymmetric chiral space group $P6_322$. The intercalated atoms occupy octahedral $2c$ or $2d$ Wyckoff positions [37] and form a superlattice of a kind determined by the stoichiometry of the material, with the $M_{1/3}XS_2$ family hosting a $\sqrt{3} \times \sqrt{3}$ superstructure. These materials tend to display radically different behaviour to the pristine TMDCs. The crystal structure showing the arrangement of the atoms intercalated in NbS_2, typical of most members of this family of TMDCs, is shown in Fig. 1.2.

In the 2H polytype, the magnetic exchange interactions between the intercalant atoms could be due to the superexchange interactions across the S atoms, the antisymmetric Dzyaloshinskii-Moriya interaction (DMI) due to the non-centrosymmetric structure of the material, or the Ruderman–Kittel–Kasuya–Yosida mechanism through the conduction electrons. The differing strengths of these interactions give rise to the observation of a variety of magnetic phases in the family. This can vary from antiferromagnetism to chiral helimagnetism depending on the nature of the transition metals present in the material [21, 38, 39], see Table 1.1.

Many of these intercalated transition metal dichalocogenides display com-

plex electronic and magnetic behaviours. As an example, $Fe_{1/3}NbS_2$ exhibits antiferromagnetic behavior at temperatures below 42 K [40, 41], with the intercalated Fe atoms forming a triangular array. Optical measurements of $Fe_{1/3}NbS_2$ suggest that it contains a nematic phase that breaks rotational symmetry, with an in-plane nematic director existing in addition to the out-of-plane magnetization [42]. This in-plane component of the magnetic ordering can be rotated using current pulses, which is particularly interesting for spintronics applications [41]. Meanwhile, $Co_{1/3}NbS_2$ is found to be a canted antiferromagnet at temperatures below 26 K, with a small ferromagnetic component of 0.0013 μ_B per Co atom [43]. Addtionally, $Co_{1/3}NbS_2$ displays a large anomalous hall effect that cannot be explained by this ferromagnetic component alone, and is instead attributed to either the effect of this intrinsic moment on the band structure or some complex magnetic texture. Finally, $V_{1/3}NbS_2$ was originally reported as a ferromagnet [21], but has recently been found to display behaviour more consistent with a canted antiferromagnet [24].

Of particular interest for exotic magnetic textures are the $Cr_{1/3}NbS_2$, $Cr_{1/3}TaS_2$, and the $Mn_{1/3}NbS_2$ compounds, which have been reported to display chiral helimagnetic behavior [44, 45, 26]. Of the intercalated TMDCs, to date only $Cr_{1/3}NbS_2$ and $Cr_{1/3}TaS_2$ have been proven to host a CSL [3, 46, 26]. It has been suggested that this CSL, rather than skyrmions, is formed due to a combination of chiral helimagnetism and a strong magnetic anisotropy.

The wide variation in the behaviors of the intercalated TMDCs, depending on the intercalate, has led to great interest in this family. The discovery of which materials might display a chiral soliton lattice, and why some materials might not, requires further investigation, which is carried out in this thesis.

1.2 The Mn_3XY family

Manganese has long been an interesting material presence in many different compounds, due to how often it induces non-collinear magnetism [19, 49]. The less common $\beta-$type Mn allotropy, meanwhile, has been of especial interest for its own peculiar properties. The NMR and NQR measurements on $\beta-$Mn even raise the possibility that it might be an itinerant antiferromagnet with a Nèel temperature of 0 K [50]. This Mn type has a complex structure that crystallizes in the cubic $P4_132$ space group with a unit cell containing 20 atoms [51], with the Mn atoms occupying two different sites, the 8*c* and 12*d* Wyckoff positions, and the atoms filling the latter sites forming a sublattice of corner-sharing triangles, which has been theorised to be a source of geometrical frustration in $\beta-$Mn.

Table 1.2: Magnetic ordering and transition temperatures of several members of the Mn_3XY family.

Formula	T_N (K)	Magnetic ordering	Reference	Additional Information
Mn_3IrSi	225(10)	Frustrated antiferromagnet	[47]	
Mn_3IrGe	225(10)	Frustrated antiferromagnet	[47]	
Mn_3CoSi	100	Possible competition between frustrated antiferromagnetism and ferrimagnetism	[48]	Neutron results were different from the other Mn_3XY materials. Simulations suggest that both the non-collinear antiferromagnetic structure as well as a ferrimagnetic structure can be stabilised, and their competition may explain the difficulty in establishing the exact magnetic structure.
Mn_3CoGe	145	Frustrated antiferromagnet	[48]	Calculations suggest that a small moment is possible on the Co atom, though it is too small (approximately 0.3 μ_B) to be seen in the neutron data.
$Mn_3IrSi_{0.9}Ge_{0.1}$	225(10)	Frustrated antiferromagnet	[47]	
$Mn_3IrSi_{0.7}Ge_{0.3}$	225(10)	Frustrated antiferromagnet	[47]	
$Mn_3IrSi_{0.5}Ge_{0.5}$	225(10)	Frustrated antiferromagnet	[47]	
$Mn_3IrSi_{0.25}Ge_{0.75}$	225(10)	Frustrated antiferromagnet	[47]	
$Mn_3Ir_{0.8}Co_{0.2}Si$	160	Frustrated antiferromagnet	[48]	
$Mn_3Ir_{0.6}Co_{0.4}Si$	130	Frustrated antiferromagnet	[48]	
$Mn_3Ir_{0.4}Co_{0.6}Si$	85	Frustrated antiferromagnet	[48]	
$Mn_3Ir_{0.2}Co_{0.8}Si$	70	Short range corrlations	[48]	
$Mn_3CoSi_{0.5}Ge_{0.5}$	125	Frustrated antiferromagnet	[48]	

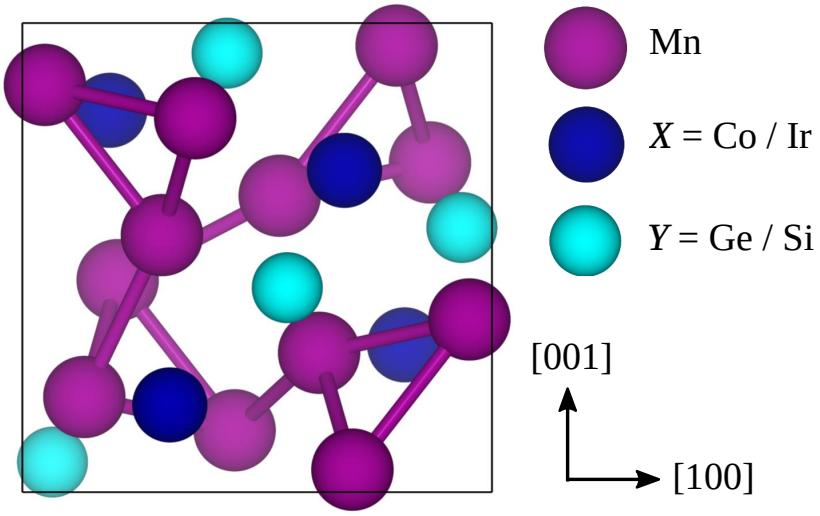

Figure 1.3: The nuclear structure for the Mn_3XY family. The corner-sharing triangles formed by the Mn atoms are shown.

The Mn_3XY family of materials, where X = Co, Ir and Y = Si, Ge, are a group of materials that adopt an ordered form of the $\beta-$Mn structure. This structure crystallises in the $P2_13$ space group, with the Mn occupying the sublattice postions where antiferromagnetically ordered moments experience geometric frustration [52, 48]. This structure can be seen in Fig. 1.3. Despite the similarities in the structures of the Co-Zn-Mn alloys and this family of materials, they display very different magnetic behaviours. Mn_3CoGe, Mn_3IrSi, and Mn_3IrGe materials have been investigated with powder neutron diffraction measurements and have been found to share very similar frustrated antiferromagnetic orderings [52, 48, 53, 47] with 120° between these magnetic moments, which are associated with the Mn atoms. It is clear, then, that any skyrmions present in these ternary materials must arise from mechanisms different to those in the Co-Zn-Mn alloys, such as the frustrated skyrmions found in Gd_2PdSi_3 [54] and $Gd_3Ru_4Al_{12}$ [55]. This makes them interesting candidates for skyrmions - especially as Mn is well-known for its presence causing non-collinear magnetic ordering [56], though it should be noted that non-collinear states are possible for any element or compound with correctly tuned band filling and exchange splitting, so Mn is not in fact unique in this [57].

The magnetic structure of Mn_3CoSi has also been investigated with neutron powder diffraction, and was found to be different to the other members of this family and harder to identify. Noncollinear linear-muffin-tin orbital calculations

showed that for Mn_3CoSi a ferrimagnetic ordering could be stabilised in addition to the non-collinear antiferromagnetic phase otherwise common to this family. These two magnetic structures competing may have led to the difficulty in identifying the magnetic structure of Mn_3CoSi in the literature study [48], which critically showed the presence of broad magnetic shoulders to several Bragg peaks at temperatures below 70 K. In addition, similar calculations for Mn_3CoGe indicated the presence of a small (0.3 μ_B) magnetic moment present on the Co atom, though this moment was in fact too small to be measured with the neutron diffraction [48].

A study on a series of solid solutions of the form $Mn_3Ir_{1-y}Co_ySi$ found that doping Ir with Co had an effect on the magnetic structure. The common non-collinear antiferromagnetic ground state was found for compositions with $y = 0.2$ as well as pure Mn_3IrSi, while incommensurate short-range magnetic orderings were found for $y = 0.8 - 1.0$. Meanwhile, further studies into the series of solid solutions of the form $Mn_3Ir(Si_{1-x}Ge_x)$ found a linear variation of the unit cell with silicon content, but no change in the magnetic ordering of the frustrated antiferromagnetic materials or the $T_N = 225(10)$ K magnetic transition temperature [47]. Doping Mn_3CoSi with Ge in the form $Mn_3Co(Si_{1-x}Ge_x)$ for $x = 0.5$ resulted in the non-collinear antiferromagnetic ground state shared by Mn_3CoGe, Mn_3IrGe, and Mn_3IrSi.

There is interest in synthesising Mn_3RhY materials to investigate how this might effect the magnetism displayed. This thesis reports on synthesis Mn_3RhSi and Mn_3RhGe, and compares the magnetism of Mn_3RhGe and Mn_3IrSi as investigated with powder neutron diffraction.

1.3 Overview

The thesis will focus on the structural and magnetic investigation into several members of the intercalated transition metal dichalcogenide and Mn_3XY families.

1.3.1 Chapter 2: Theory

The theoretical considerations for this project are detailed in Chapter 2, which focuses on the mechanisms of magnetism, especially the formation of exotic chiral textures and geometric frustration. The theoretical underpinning of electron, x-ray, and neutron diffraction techniques, which were central to this project, are also discussed at length.

1.3.2 Chapter 3: Experimental details

This thesis goes on to describe the techniques used in this project in Chapter 3. Here, the methods used to synthesise polycrystalline and single crystal samples of different materials are explained, as are the techniques used to make a detailed investigation into the materials studied.

1.3.3 Chapter 4: Neutron diffraction study of $V_{1/3}NbS_2$

Chapter 4 is the start of the chapters detailing the results. This chapter focuses on the magnetic and structural investigation of $V_{1/3}NbS_2$ using *dc* and *ac* susceptibility measurements and powder and single crystal neutron diffraction studies to explore its ground state magnetic structure. Single crystal x-ray diffraction measurements were also performed to characterise the structure of this material.

1.3.4 Chapter 5: A comparative study of the magnetic properties of $Mn_{1/3}NbS_2$, $Cr_{1/3}NbS_2$

The results continue in Chapter 5, which compares three materials that have been reported to display chiral helimagnetic ground states. Lorentz transmission electron microscopy (LTEM) and *dc* and *ac* susceptibility measurements display a significant difference between the magnetic behaviours of $Mn_{1/3}NbS_2$ and $Cr_{1/3}NbS_2$ and may explain why the former does not seem to display a chiral soliton lattice like $Cr_{1/3}NbS_2$ and $Cr_{1/3}TaS_2$. Electron and single crystal x-ray diffraction measurements also reveal extra sublattice reflections in $Mn_{1/3}NbS_2$ indicative of extreme twinning effects.

1.3.5 Chapter 6: Neutron diffraction studies of Mn_3IrSi and Mn_3RhGe

In the final results chapter, the magnetism of Mn_3IrSi and Mn_3RhGe is compared using powder neutron diffraction measurements. The *dc* susceptibility measurements were found to be dominated by small amounts of magnetic impurities in these materials, so heat capacity measurements were used to determine transition temperatures for these materials. Additionally, a large single crystal of Mn_3RhSi is successfully synthesised, and characterisation measurements are performed on its polycrystalline counterpart.

1.3.6 Chapter 7: Conclusions and further work

Finally, this thesis concludes with Chapter 7. Here, the results are summarised and compared, and points that require further investigation are elucidated.

Chapter 2

Theory

2.1 Diffraction

Diffraction refers to the tendency of certain waves or particles to spread out and self-interfere when propagating through an aperture of similar size to the wavelength of the propagating wave or particle. Electrons, neutrons, and electromagnetic waves such as x-rays are all capable of diffraction and are of use in multiple techniques that give detailed information about the nuclear and magnetic structure of a material.

In this section, useful crystallographic terms that are helpful when considering nuclear and magnetic structures are first reviewed, after which the theory underpinning x-ray, electron, and neutron diffraction techniques are considered.

2.1.1 Crystals

Crystal lattice and reciprocal space

Crystals form many different types of structure. Crystal structures can be described by one of 230 space groups, which can be further separated into 32 different crystallographic point groups. A set of mathematical tools are needed to understand the nuclear structure of different crystals and the crystal field that magnetic atoms exist in.

A crystal can be defined as a lattice of mathematical points upon which a basis of groups of atoms can be placed. Crystals are therefore fundamentally periodic structures, which can be defined by

$$r' = r + u_1 a_1 + u_2 a_2 + u_3 a_3, \tag{2.1}$$

i.e. one set of points r can be transformed into a new set of points r' by the

addition of the product of some integers u_i and some translation vectors a_i. For a three dimensional lattice, there are three possible translation vectors; one for each direction [58].

From this, we can see that the smallest possible repeatable unit that can be used to describe the lattice, the unit cell, must have a primitive volume:

$$V_p = a_1 \cdot a_2 \times a_3. \tag{2.2}$$

Lattice vectors can then be defined in reciprocal space, which is very useful for Fourier analysis.

$$\mathbf{G} = \mathrm{h}\mathbf{b_1} + \mathrm{k}\mathbf{b_2} + \mathrm{l}\mathbf{b_3}, \tag{2.3}$$

where the integers (hkl) are known as the Miller indices, b_i are the three reciprocal lattice vectors, and $\mathbf{G}$ is the set of these vectors. The interplanar spacing is dependent on this set of vectors, which, in the physics convention, can be written as:

$$d_{hkl} = \frac{2\pi}{|\mathbf{G}|} \tag{2.4}$$

and the reciprocal lattice vectors can be defined separately as:

$$b_1 = 2\pi \frac{a_2 \times a_3}{a_1 \cdot a_2 \times a_3}, \tag{2.5}$$

$$b_2 = 2\pi \frac{a_3 \times a_1}{a_1 \cdot a_2 \times a_3}, \tag{2.6}$$

and

$$b_3 = 2\pi \frac{a_1 \times a_2}{a_1 \cdot a_2 \times a_3}. \tag{2.7}$$

Crystalline anisotropy

The crystal environment that magnetic ions are situated within can often affect the magnetism displayed due to the effect of spin-orbit coupling. Here, uniaxial anisotropy will be discussed, which describes a strong preference for the system to magnetise along one particular direction.

For the uniaxial case, the magnetocrystalline anisotropy energy density, W, can be written:

$$W = K_1 \sin^2\theta + K_2 \sin^4\theta ... \tag{2.8}$$

where K is the anisotropy constant, and θ is the angle between the magnetisation direction and the easiest axis to magnetise. The sign of K indicates whether the easy axis lies along the principal axis or in the plane perpendicular to the principal axis. The $\sin^2\theta$ term shows that the anisotropy is independent with respect to rotations around the principal axis and is only reliant on θ [59].

2.1.2 X-ray diffraction

Due to the periodicity inherent to crystals, incident x-rays interact with the electrons orbiting the atoms of the basis and are diffracted, due to the interplanar spacing being of the same magnitude as the wavelength of the x-ray. This is very useful for extracting information about the nuclear and magnetic structure of different crystalline materials.

For elastic scattering, Bragg's law [60, 58, 61] describes the constructive interference of x-rays that occurs when the path difference is an integral number, n, of wavelengths, λ, apart. It can be written as:

$$2d_{hkl} \sin\theta = n\lambda, \tag{2.9}$$

where d_{hkl} is the interplanar spacing and θ is the incident angle of the x-rays with respect to the plane it is reflecting from. This reflection is specular, i.e. the incident angle is equivalent to the angle of the 'reflected' x-ray with respect to the plane. In actuality, x-rays that are incident upon electrons cause them to oscillate and emit another coherent x-ray. The intensity of the scattered ray from an individual atom with spherical electron density can be written as:

$$I = I_0 \left(\frac{\mu_0}{4\pi}\right)^2 \left(\frac{e^4}{m_e^2 r^2}\right) \sin^2\alpha, \tag{2.10}$$

where I_0 is the intensity of the incident x-ray beam, e is the charge of the electron, and α is the angle between the direction the beam is scattered in and the direction of the acceleration of the electron.

The difference between the phase factors of two x-ray beams scattered from elements a distance $\mathbf{r}$ apart can be written as $e^{i(\mathbf{k}-\mathbf{k}')\cdot\mathbf{r}}$, where $\mathbf{k}$ and $\mathbf{k}'$ are the wavevectors of the incident and outgoing x-rays, respectively, and the difference between them, $\mathbf{\Delta k}$, is indicative of the momentum transfer. This relation can be used to define a scattering amplitude, F, such that

$$F_{\mathrm{x-ray}} = \int n(\mathbf{r})\mathbf{e}^{\mathbf{i\Delta k\cdot r}}\ \mathrm{d}\mathbf{V}, \tag{2.11}$$

where the electron number density $n(\mathbf{r})$ can be written as

$$n(\mathbf{r}) = \sum_{\mathbf{G}} \mathbf{n_G}\mathbf{e}^{\mathbf{iG\cdot r}}. \tag{2.12}$$

This scattering amplitude is therefore only of significant magnitude under the special condition

$$\Delta k = \mathbf{G}, \tag{2.13}$$

and it can therefore be seen that special directions are required for measurable scattering cross-sections.

Another geometrical representation of diffraction theory can be achieved by taking the dot product of Δk and $\mathbf{G}$ with the lattice vectors, resulting in the Laue equations:

$$a_1 \cdot \Delta k = 2\pi\nu_1, \tag{2.14}$$

$$a_2 \cdot \Delta k = 2\pi\nu_2, \tag{2.15}$$

and

$$a_3 \cdot \Delta k = 2\pi\nu_3. \tag{2.16}$$

where ν_i are integers. Δk must satisfy all of these equations at once, i.e. it must lie in a common intersection of three cones, each cone about a_1, a_2, and a_3, respectively. The Ewald construction visualises the requirements for this condition by drawing a sphere of radius $k = \frac{2\pi}{\lambda}$ about the origin of $\mathbf{k}$. A diffracted beam, directed along $\mathbf{k}'$, is formed at any point where this sphere intersects with a lattice point. The Ewald sphere construction is useful for the visualisation of crystal structures in reciprocal space.

To describe the efficiency of the scattering of the incident x-ray from an atom in a given direction, the atomic scattering factor, also known as the atomic form factor, is used . It is essentially a ratio of the amplitude of the wave scattered by an atom to the amplitude of the wave as scattered by a single electron. It is given by the equation:

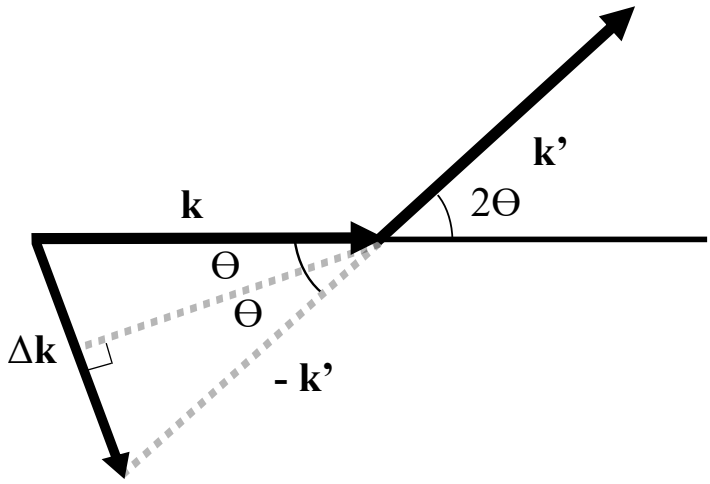

Figure 2.1: A vector diagram for elastic scattering through an angle of 2θ. Using this diagram, Δk can be related to θ, and it can also be related to wavelength λ using $\mathbf{k} = \frac{\mathbf{2\pi}}{\lambda}$.

$$f_j = \int n_j(\rho)\mathbf{e}^{-\mathbf{iG}\cdot\rho}\mathrm{d}\mathbf{V} = \frac{\sin \mathbf{Gr}}{\mathbf{Gr}}, \tag{2.17}$$

where $\rho = \mathbf{r} - \mathbf{r_j}$. This can be written in sinusoidal form due to the following relation for elastic scattering:

$$\Delta k = \frac{4\pi \sin\theta}{\lambda}, \tag{2.18}$$

where θ is half the angle between each value of k and the scattering plane [See Fig.2.1]. The scattered wave can then be expressed in the form:

$$Ae^{i\phi} = fe^{2\pi i(\mathbf{G}\cdot\mathbf{r})}, \tag{2.19}$$

where A is some constant.

To extend this view to all atoms of the unit cell, the structure factor can be used. Analogously to the atomic form factor, the structure factor is a ratio of the amplitude of the wave scattered by all the atoms of the unit cell to the amplitude of the wave scattered by a single electron. It can be written as:

$$S_{\mathbf{G}} = \sum_j f_j e^{-i\mathbf{G}\cdot\mathbf{r_j}}. \tag{2.20}$$

Finally, the measurable quantity extracted from diffraction experiments is the differential cross-section. This is defined as a ratio of $\mathrm{R}(2\theta, \phi)$ the number of

x-rays deflected by $(2\theta,\ \phi)$ per unit solid angle Ω to the number of incident particles per unit area of beam Φ per number of scattering units of interest N. This can be expressed as follows:

$$\frac{\mathrm{d}\sigma}{\mathrm{d}\Omega} = \frac{R\left(2\theta, \phi\right)}{N\Phi\Delta\Omega}. \tag{2.21}$$

where

$$R\left(2\theta, \phi\right) \propto |S_G|^2. \tag{2.22}$$

2.1.3 Electron diffraction

Electron diffraction [62] can be considered in a similar manner to x-ray diffraction. Electrons are tiny ($\mathrm{m_e} = 9.1 \times 10^{-31}$ kg), negatively charged particles that are incredibly important to the field of magnetism. They can be represented by the wave function:

$$\Psi = \Psi_0 e^{i\phi}, \tag{2.23}$$

where Ψ_0 is the amplitude of the wave and ϕ is its phase. The change in phase of an electron can be expressed as a function of path difference Δx as follows:

$$\Delta\phi = \frac{2\pi}{\lambda}\Delta x, \tag{2.24}$$

where λ is the electron wavelength.

A useful tool for describing electron scattering behaviour is the Rutherford scattering cross-section, which describes differential scattering from the nucleus, and can be modified to include screening and relativistic effects like so:

$$\sigma_{\mathrm{R}} = \frac{Z^2\lambda_{\mathrm{R}}^4}{64\pi^4 a_0^2}\frac{\mathrm{d}\Omega}{[\sin^2\left(\frac{\theta}{2}\right) + \frac{\theta_0^2}{4}]^2}, \tag{2.25}$$

where Z is the atomic number, λ_{R} is the relativistically-corrected electron wavelength, θ is the angle the electron is scattered through, θ_0 is the screening parameter given by:

$$\theta_0 = \frac{0.117Z^{\frac{1}{3}}}{E_0^{\frac{1}{2}}}, \tag{2.26}$$

where E_0 is the energy of the electrons in keV, and a_0, the Bohr radius, can be defined as:

$$a_0 = \frac{h^2 \epsilon_0}{\pi m_e e^2}, \tag{2.27}$$

where ϵ_0 is the dielectric constant.

We can define a scattering amplitude for electrons using the Mott-Bethe formula, such that:

$$F = \frac{\left(1 + \frac{E_0}{m_e c^2}\right)}{8\pi^2 a_0} \left(\frac{\lambda}{\sin\frac{\theta}{2}}\right)^2 (Z - F_{\mathrm{x-ray}})\,. \tag{2.28}$$

where $F_{\mathrm{x-ray}}$ is the scattering amplitude factor for x-rays. The structure factor can be calculated for electrons in the same manner one would use for x-rays.

2.1.4 Neutron diffraction

Neutron diffraction is now considered [61]. The neutron case is slightly different, due to the fact that neutrons are neutrally-charged particles with an intrinsic magnetic spin $\mu_s = -1.913\mu_N$ where the nuclear magneton is defined as $\mu_N = \frac{e\hbar}{2m_n}$ and the mass of a neutron is $m_n = 1.67 \times 10^{-27}$. Neutrons are spin-half particles that can adopt a spin-up or spin-down configuration - the orientation of these spins is unpolarised in most cases, though at very low temperatures the spin-up case is slightly energetically favourable.

This leads to neutrons interacting with the nucleus in a manner akin to as if it was a point source, which itself leads to a form factor that is invariant with respect to wavelength and angle. This can be written as:

$$f_{\mathrm{neutron}}(\lambda, \theta) = -b, \tag{2.29}$$

where b is the scattering length and the minus sign is due to convention. There are a few cases where this does not quite hold true, especially where absorption is likely to play a large role compared to scattering in the diffraction experiment. These b values are isotope specific, depend on the spin-up or spin-down state of the atom the neutron interacts with, and do not scale simply with Z.

Due to the magnetic spin of the neutrons, the magnetic form factor of neutron diffraction can also be considered. In this case, the magnetic interaction arises from unpaired electrons in the outer shells of atoms and thus is ion-specific and subject to a form factor. Neutrons only interact with magnetisation perpendicular to the momentum transfer Δk:

$$M_{\perp} = M - (M \cdot \hat{\Delta k})\hat{\Delta k}, \tag{2.30}$$

where $\hat{\Delta k}$ is a unit vector in the direction of the momentum transfer, M is the magnetisation, and $M_{\perp}$ is the component of the magnetisation perpendicular to Δk. The scattering cross-section for neutrons can be defined as:

$$\sigma_{\text{neutron}}(\lambda) = 2\pi \int_{2\theta=0}^{\pi} |f(\lambda, \theta)|^2 \ \sin 2\theta \ \mathrm{d}\theta, \tag{2.31}$$

which, in the nuclear case for b values independent of λ and θ, reduces to:

$$\sigma_{\text{neutron, nuclear}} = 4\pi |b|^2. \tag{2.32}$$

As with the x-ray and electron case, the differential scattering cross section is proportional to the square of the structure factor.

2.2 Magnetism on the atomic level

In this section, the atomic origins of magnetism are considered. Magnetism can arise from the spin angular momentum of electrons, which are spin-half fermions, i.e. have a spin quantum number $s = \frac{1}{2}$. Magnetism is therefore fundamentally quantum mechanical in nature and has to be treated as such. However, when considering the magnetic moment, an analogue can be drawn to the classical consideration of a current loop:

$$\mathrm{d}\mu = I \ \mathrm{d}\mathbf{S}, \tag{2.33}$$

where $\mathrm{d}\mu$ is the magnetic moment, and I is the current around some infinitesimal loop of area $|\mathrm{d}\mathbf{S}|$. This can also be seen to be the magnetic equivalent to an electric dipole, i.e. two charges of opposite sign separated by some small distance, where for the magnetic dipole this distance is in the same direction as $\mathrm{d}\mathbf{S}$ [63].

From this consideration, we can calculate a value for the magnitude of this atomic magnetic moment, resulting in the Bohr magneton, μ_{B}, which is a useful unit for describing the size of magnetic moments in general. Knowing that the angular momentum of the electron must be equal to $\hbar$ in its ground state, we can state:

$$\mu_{\mathrm{B}} = \frac{e\hbar}{2m_{\mathrm{e}}}, \tag{2.34}$$

where e is the charge of the electron, m_{e} is the mass of an electron, and $\hbar = \frac{h}{2\pi}$,

where h is Planck's constant.

On a larger length scale it is useful to define the magnetisation $\mathbf{M}$ of a magnetic material as the magnetic moment per unit volume. On this length scale we can write:

$$\mathbf{B} = \mu_\mathbf{0} \left(\mathbf{H} + \mathbf{M} \right), \tag{2.35}$$

where $\mathbf{B}$ is the magnetic flux density, $\mathbf{H}$ is the magnetic field, and μ_0 is the permeability of free space [1, 63]. We can additionally define a magnetic susceptibility, χ, which for the case of a material with a magnetisation that scales linearly with applied magnetic field is simply:

$$\chi = \frac{\mathbf{M}}{\mathbf{H}}. \tag{2.36}$$

For a more accurate picture of magnetism on the atomic level, a quantum mechanical view of such a system must be returned to. The quantum mechanical state of an electron is represented by four quantum numbers: the principal quantum number n is a discrete variable that describes how tightly bound the electron is to the nucleus; the azimuthal quantum number l that describes the orbital angular momentum of the electron, with a maximum value of $n-1$ due to the Pauli exclusion principle and a minimum value of zero; the magnetic quantum number m_l, which defines the number of orbitals available for each electron shell and can thus be defined solely between $+l$ and $-l$; and finally the spin magnetic quantum number m_s, which describes the intrinsic spin angular momentum of the electron. It is also worth reiterating that the spin quantum number $s = \frac{1}{2}$, for all electrons, and thus m_s must be $\pm\frac{1}{2}$.

Angular momentum associated with the magnetic moment of an atom can arise from the intrinsic electron spin and the orbital movement of the electron. The total spin angular momentum is defined as:

$$\mathbf{S} = \sum_\mathbf{i} \mathbf{s_i} \tag{2.37}$$

and the total orbital angular momentum as

$$\mathbf{L} = \sum_\mathbf{i} \mathbf{l_i}, \tag{2.38}$$

which finally allows a total angular momentum, $\mathbf{J}$, to be calculated from the sum of these components:

$$\mathbf{J} = \mathbf{L} + \mathbf{S}. \tag{2.39}$$

It is clear that the sum over filled electron shells for l_i and s_i is zero, and thus only partially filled shells contribute to the total angular momentum.

This allows the magnetic moment, $\hat{\mu}$, to be defined in terms of total angular momentum $\mathbf{J}$:

$$\hat{\mu} = g_{\mathrm{j}}\mu_{\mathrm{B}}\hat{\mathbf{J}}, \tag{2.40}$$

where the Landé g-factor, g_{j} can be defined as:

$$g_{\mathrm{j}} = \frac{3}{2} + \frac{S(S+1) - L(L+1)}{2J(J+1)}. \tag{2.41}$$

Hund's rules can then be used to describe how the the angular momentum affects the energy of the system. They are as follows:

1. The electronic wavefunction with the maximum $\mathbf{S}$ value will have the minimum Coulomb energy, due to the Pauli exclusion principle, which prevents quantum states from being doubly occupied. This results in aligned spins being forced into the next available orbital, reducing the Coulomb interactions that closer electrons would otherwise experience.

2. After Hund's first rule is considered, $\mathbf{L}$ should then be maximised. This reduces the Coulomb energy as electrons moving in the same orbital direction are less likely to be forced into close contact.

3. Finally, in order to minimise the energy from the spin-orbit coupling, $\mathbf{J} = |\mathbf{L} - \mathbf{S}|$ if the electron shell is less than half full and $\mathbf{J} = |\mathbf{L} + \mathbf{S}|$ in any other case. This rule is often disobeyed when the spin-orbit energies are minimal compared to other energy terms, such as, for example, those due to the crystal field.

The next section extends our view of magnetism from a purely atomic standpoint by considering the role of exchange interactions in mediating long-range magnetic ordering.

2.3 Exchange interactions

Exchange interactions can be thought of as electrostatic interactions arising as a consequence of the energy lost by bringing two like charges close together and saved by keeping those charges far apart. As the Pauli exclusion principle prevents a single quantum state being doubly occupied, this Coulomb interaction that favours aligned spins competes with the fact that it requires energy to fill a higher electron orbital

which favours anti-aligned spins, and this results in what is called an exchange interaction [63].

A wavefunction can be defined to describe the interaction between two electrons at positions $\mathbf{r_1}$ and $\mathbf{r_2}$ respectively, which must be overall antisymmetric due to the fact that electrons are fermions. This allows either an antisymmetric singlet state χ_{S} ($S = 0$) that is spatially symmetric (i.e. the spin states of the two electrons are aligned), or a symmetric triplet state χ_{T} ($S = 1$) that is spatially antisymmetric (i.e. the spin states of the two electrons are anti-aligned). This can be written as:

$$\Psi_S = \frac{1}{\sqrt{2}}[\psi_a(\mathbf{r_1})\psi_{\mathbf{b}}(\mathbf{r_2}) + \psi_{\mathbf{a}}(\mathbf{r}_)\psi_{\mathbf{b}}(\mathbf{r_1})]\chi_{\mathbf{S}} \tag{2.42}$$

for the singlet state, and

$$\Psi_T = \frac{1}{\sqrt{2}}[\psi_a(\mathbf{r_1})\psi_{\mathbf{b}}(\mathbf{r_2}) + \psi_{\mathbf{a}}(\mathbf{r_2})\psi_{\mathbf{b}}(\mathbf{r_1})]\chi_{\mathbf{T}} \tag{2.43}$$

for the triplet state. These states each have an associated energy, which can be written as:

$$E_S = \int \Psi_S^* \hat{\mathcal{H}} \Psi_S \ \mathrm{d}\mathbf{r_1}\mathrm{d}\mathbf{r_2} \tag{2.44}$$

where $\mathrm{E_S}$ is the energy of the singlet state and

$$E_T = \int \Psi_T^* \hat{\mathcal{H}} \Psi_T \ \mathrm{d}\mathbf{r_1}\mathrm{d}\mathbf{r_2} \tag{2.45}$$

where $\mathrm{E_T}$ is the energy of the singlet state, for normalised χ_{S} and χ_{T}. An exchange constant J can be defined as the difference between these two energies such that:

$$J_{\mathrm{ex}} = \frac{E_S - E_T}{2} = \int \psi_a^*(\mathbf{r_1})\psi_{\mathbf{b}}^*(\mathbf{r_2})\hat{\mathcal{H}}\psi_{\mathbf{a}}(\mathbf{r_2})\psi_{\mathbf{b}}(\mathbf{r_1}) \ \mathrm{d}\mathbf{r_1}\mathrm{d}\mathbf{r_2}. \tag{2.46}$$

This allows for the spin-dependent term of the effective Hamiltonian to be written as:

$$\hat{\mathcal{H}} = -\sum_{ij} J_{\mathrm{ex},ij} \ \mathbf{S_i} \cdot \mathbf{S_j}, \tag{2.47}$$

assuming that this interaction applies between all neighbouring atoms. The sign of J_{ex} indicates the spin state is stabilised, with $J_{\mathrm{ex}} > 0$ implying that $\mathrm{E}_S > \mathrm{E}_T$ and thus the spins are symmetric, and likewise $J_{\mathrm{ex}} < 0$ indicating that $\mathrm{E}_S < \mathrm{E}_T$ and thus the stabilised state is for anti-aligned spins.

There are many types of exchange interaction; some of the most relevant

exchange interactions for this project are described in the following sections.

2.3.1 Direct exchange

Direct exchange occurs between nearest neighbour atoms and thus does not require any mediating force. It is, however, rarely the force driving magnetic ordering due to the fact that it is fairly rare for sufficient direct overlap of magnetic orbitals [63].

2.3.2 Indirect exchange

Indirect exchange occurs between non-neighbouring magnetic atoms and requires an intermediary. Here we will consider two types of indirect exchange: superexchange and the Ruderman-Kittel-Kasuya-Yosida (RKKY) interaction.

Superexchange

Superexchange is mediated by non-magnetic ions situated between magnetic ions. The electron orbitals of these atoms will overlap, and the preferred way the electron spins will align (or anti-align) will depend on how this overlap presents and how filled the electron bands are. The simplest cases of this behaviour are described by the Goodenough-Kanamori rules [64, 65, 66]. The original examples show that for cations experiencing an octahedral crystal field, if the angle that the non-magnetic ion makes with the magnetic ions is 90°, the spins it will be more energy-efficient for the spins to align, whereas if this angle is instead 180° they will anti-align [66]. This is due to how this angle between ions affects the overlap of electron orbitals - the Goodenough-Kanamori rules show that a large overlap between partly occupied orbitals of magnetic ions will result in a strong preference for the electron spins to anti-align due to the Pauli exclusion principle, whereas if the overlap is instead between a partially occupied and an unoccupied orbital, then the spins will be weakly influenced to align due to the Coulomb interaction [67].

Ruderman-Kittel-Kasuya-Yosida interaction

In metals, a different form of indirect exchange is known as the RKKY interaction [68, 69, 70, 71]. Metals contain delocalised conduction electrons. The spin of a localised magnetic moment can polarise these electrons, which can then couple to another localised magnetic moment situated a distance r away. For large r values, the exchange constant for this interaction can be written:

$$J_{\mathrm{ex,RKKY}}(r) \propto \frac{\cos(2k_{\mathrm{F}}r)}{r^3}, \tag{2.48}$$

where k_{F} is the radius of a spherical Fermi surface [63]. This equation shows that the exchange constant varies sinusoidally with distance.

Double exchange

Double exchange is another example of an exchange interaction, in this case between ions with different oxidation states. An electron from an atom with a higher oxidation state can hop to a vacant site in a neighbouring atom with a lower oxidation state, in order to reduce kinetic energy. As Hund's first rule states that the state with the highest S is the lowest energy, it is energetically favourable for these spins to be aligned with each other. This is somewhat similar to ferromagnetic superexchange for an extended system [63].

2.3.3 Dzyaloshinskii-Moriya interaction

Another example of an exchange interaction is the antisymmetric Dzyaloshinskii-Moriya interaction (DMI). The DMI is described by:

$$\mathcal{H}_{\mathrm{DM}} = \sum_{ij} \mathbf{D}_{ij}[\mathbf{S}_i \times \mathbf{S}_j] \tag{2.49}$$

where $\mathcal{H}_{DM}$ is the Hamiltonian for the DMI, D is the Dzyaloshinskii-Moriya constant, and $\mathbf{S_i}$ and $\mathbf{S_j}$ are neighbouring spins [72, 73, 74]. In order for the DMI to have a significant effect within a material, $\mathbf{D}$ must be non-zero, which is possible for crystal systems that lack an inversion centre of symmetry.

Moriya describes several rules that fall out mathematically from the DMI [73], namely that for two ions each situated at i and j, respectively, with a centre point C halfway along a line connecting them:

1. When a centre of inversion is situated at C, then $\mathbf{D} = \mathbf{0}$.
2. When a mirror plane perpendicular to ij passes through C, then $\mathbf{D} \perp ij$.
3. When there is a mirror plane including i and j, then $\mathbf{D} \perp$ mirror plane.
4. When a two-fold rotation axis perpendicular to ij passes through C, then $\mathbf{D} \perp$ two-fold axis.
5. When there is an n-fold ($n > 2$) axis along ij, then $\mathbf{D} \parallel ij$.

From these rules it can be determined that while the scalar magnitude of D is determined by the strength of the spin-orbit coupling, its direction is determined by the bond symmetry of the crystal structure.

In the continuum limit, Lifshitz invariants [75] can be used to describe the DMI, which take the form:

Table 2.1: A list of Lifshitz invariants for several different relevant crystallographic point groups [76], with the vorticity ω and helicity γ for each noted as well.

Point group	$w_{\mathrm{DM}} = D\mathcal{L}(\mathbf{m})$	ω	γ
C_{nv}	$D(\mathcal{L}_{xz}^{(x)} + \mathcal{L}_{yz}^{(y)})$	1	0
T	$D(\mathcal{L}_{yx}^{(z)} + \mathcal{L}_{xz}^{(y)} + \mathcal{L}_{zy}^{(x)})$	1	$\pm\frac{\pi}{2}$
O	$D(\mathcal{L}_{yx}^{(z)} + \mathcal{L}_{xz}^{(y)} + \mathcal{L}_{zy}^{(x)})$	1	$\pm\frac{\pi}{2}$
D_n	$D(\mathcal{L}_{xz}^{(y)} - \mathcal{L}_{yz}^{(x)}) + D'(\mathcal{L}_{xy}^{(z)})$	1	$\pm\frac{\pi}{2}$
C_n	$D(\mathcal{L}_{xz}^{(x)} + \mathcal{L}_{yz}^{(y)}) + D'(\mathcal{L}_{xz}^{(y)} - \mathcal{L}_{yz}^{(x)})$	1	-arctan($\frac{D'}{D}$)
S_4	$D(\mathcal{L}_{xz}^{(x)} - \mathcal{L}_{yz}^{(y)}) + D'(\mathcal{L}_{xz}^{(y)} + \mathcal{L}_{yz}^{(x)})$	1	arctan($\frac{-D'}{D}$)
D_{2d}	$\mathcal{L}_{xz}^{(y)} + \mathcal{L}_{yz}^{(x)}$	-1	$\pm\frac{\pi}{2}$

$$\mathcal{L}_{ij}^{(k)} = m_i \partial_k m_j - m_j \partial_k m_i, \tag{2.50}$$

where k is the cartesian direction along which the magnetic vector propagates, and ij are the cartesian coordinates along which the spins rotate, m is the magnetic unit vector along i and j, at times partially differentiated with respect to k [76, 77]. These Lifshitz invariants represent the contribution of the DMI to the free energy of the system. It is by minimising the free energy of all the components of a magnetic system that the solution to the magnetic ground state for a magnetic material can be arrived at, so calculating these Lifshitz invariants for different magnetic systems is highly useful.

The directions used for $\mathcal{L}_{ij}^{(k)}$, $\mathcal{L}(\mathbf{m})$, are dependent on the crystal structure of the magnetic material which is being considered, specifically the point group. The chiral energy density, $w_{\mathrm{DM}} = D\mathcal{L}(\mathbf{m})$ for each point group is tabulated in Table 2.1.

2.3.4 Zeeman energy

The Zeeman effect describes the interaction of intrinsic magnetic moments with an external magnetic field. The application of an external magnetic field is necessary to stabilise different spin structures such as skyrmions, the chiral soliton lattice, and more. The Hamiltonian term associated with the tendency of the magnetic moments to align with an externally applied field can be written as:

$$\hat{\mathcal{H}_{\mathrm{Ze}}} = -\mu \cdot \mathbf{B}, \tag{2.51}$$

where $\mathbf{B} = \mu_{\mathbf{0}}\mathbf{H}$ is the local induced field and μ is the local magnetic moment.

The next section will cover the different types of long-range magnetic orderings that arise from these exchange interactions.

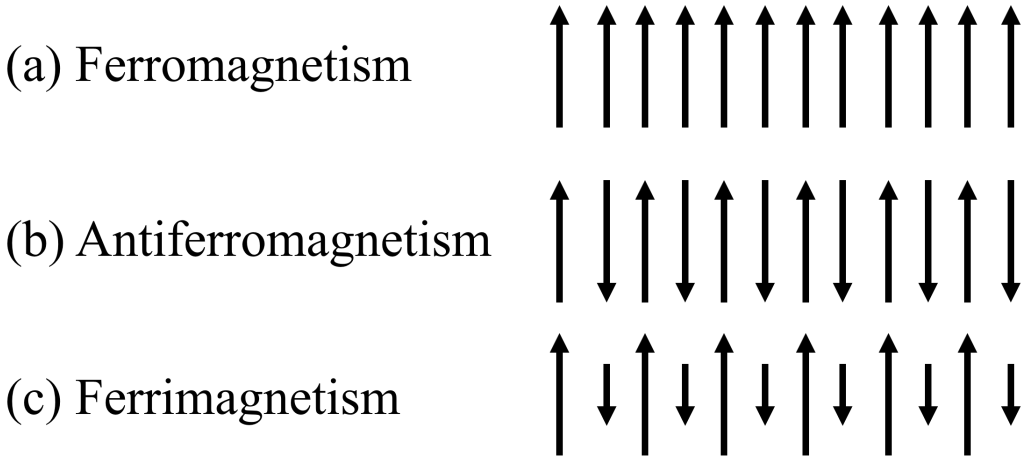

Figure 2.2: An example of (a) ferromagnetism, where neighbouring spins align, (b) antiferromagnetism, where each spin aligns antiparallel to its neighbour, and (c) ferrimagnetism, where each spin aligns antiparallel to its neighbour, but the neighbouring spins are of differing magnitudes. This is simply a one-dimensional example of possible antiferromagnetic and ferrimagnetic orderings; multiple different configurations are possible when more dimensions are considered.

2.4 Long range magnetic ordering

It is now possible to begin to consider long-range magnetic orderings. For this, we must then consider the environment our magnetic moments exist in.

2.4.1 Ferromagnetism

A ferromagnetic material exhibits spontaneous magnetisation even in the absence of an externally applied magnetic field. In a ferromagnet, the exchange constant is positive, resulting in the ground state energy being minimised when neighbouring spins align. An example of ferromagnetism can be seen in Fig. 2.2(a).

Ferromagnets are magnetic until the thermal energy is larger than the magnetic energy, which occurs at a threshold transition temperature called the Curie temperature, T_{C}. Assuming that the direct exchange interaction applies, this can be calculated as:

$$T_{\mathrm{C}} = \frac{2J_{\mathrm{ex}}J(J+1)}{3k_{\mathrm{B}}} \tag{2.52}$$

where J_{ex} is the exchange constant, J is the total angular momentum, and k_{B} is Boltzmann's constant. At temperatures above T_{C}, the material can be considered to be paramagnetic, i.e. incapable of spontaneous order but susceptible to aligning

with an externally applied field.

A useful tool for modelling the behaviour of a magnet in a paramagnetic state is the Curie-Weiss law [1], which can be written as follows:

$$\chi = \frac{C}{T - \theta}, \tag{2.53}$$

where T is the temperature, θ is the Weiss temperature, which should be positive and similar to T_{C} (see equation 2.52) for a ferromagnet, negative for an antiferromagnet and similar to T_{N} (see equation 2.56), and 0 for a paramagnet. This arises from the expansion of the Brillouin function [63]. C is the Curie constant, which can be calculated as

$$C = \frac{N\mu_0\mu_{\mathrm{B}}^2}{3k_{\mathrm{B}}}\mu_{\mathrm{eff}}^2, \tag{2.54}$$

where N is Avogadro's constant, and the effective moment is

$$\mu_{\mathrm{eff}} = g_j\sqrt{J(J+1)}, \tag{2.55}$$

which can be calculated for magnetic atoms and compared to experimental data.

It is worth noting, that a net magnetic moment of zero can be measured for a bulk ferromagnetic material in zero field due to the tendency of ferromagnets to break into domains of opposing magnetism. These domains form to minimise magnetostatic energy - a ferromagnetic material consisting of a single domain exerts a large external magnetic field, whereas a material with multiple domains instead exerts a far smaller magnetic field, requiring less energy.

2.4.2 Antiferromagnetism

Another case to be considered is for when $J_{\mathrm{ex}} < 0$, and the lowest energy ground state is found for spins that align antiparallel to their neighbours, see Fig. 2.2(b). Materials displaying this sort of long-range order are known as antiferromagnets. In this case, the temperature at which the material transitions from antiferromagnetic to paramagnetic is known as the Néel temperature, T_{N}, and can be calculated by:

$$T_{\mathrm{N}} = \frac{g_j\mu_{\mathrm{B}}(J+1)|\lambda|M_{\mathrm{s}}}{3k_{\mathrm{B}}}, \tag{2.56}$$

where M_{s} is the saturation magnetisation, J is the total angular momentum, and $|\lambda|$ is the modulus of the molecular field constant, which can be defined as:

$$\lambda = \frac{2J_{\text{ex}}}{ng^2\mu_{\text{B}}^2}. \tag{2.57}$$

In order to extract T_{N} from magnetic susceptibility data, taking the derivative of χT with respect to temperature gives a close approximation [78].

One way of considering antiferromagnetism is two superimposed magnetic lattices, each with its own spins aligned, but arranged such that the directions of the spins of each lattice oppose each other. Due to the multiple ways the magnetic structure can be arranged such that there are an equal number of opposing spins, there are many possible types of antiferromagnetic ordering.

2.4.3 Ferrimagnetism

In the case of a ferrimagnet, the magnetic structure can again be considered as two superimposed magnetic sublattices of spins, with each sublattice antiparallel to the other. However, in this case, the magnitude of each lattice of spins is different, such that a net magnetic moment is still present despite the antiferromagnetic ordering, see Fig. 2.2(c).. A different molecular field is often needed for each sublattice to induce ferrimagnetism and these different molecular fields can lead to complicated temperature dependencies.

2.4.4 Spin glasses

A spin glass state refers to a highly disordered type of ordering, where random distributions of dilute magnetic orderings are present within the material, and different spin structures are 'frozen' at some transition temperature from a high-temperature disordered state to a low-temperature disordered state. One of the hallmarks of a spin glass is frequency-dependence of the temperature at which magnetic features in frequency-dependent χ can be seen [79, 80, 81].

2.4.5 Chiral magnetism

Chirality refers to an inability to superimpose an object onto its mirror image - a famous example of a chiral object is the human hand. Magnetic ordering can be chiral, usually due to competing exchange interactions. The chirality of an object can be described with helicity, which is positive or 'right-handed' if the spin moves in the same direction that it points, or negative or 'left-handed' if the spin moves oppositely to the direction it points. Here, several examples of possible ground state chiral magnetic orderings are described.

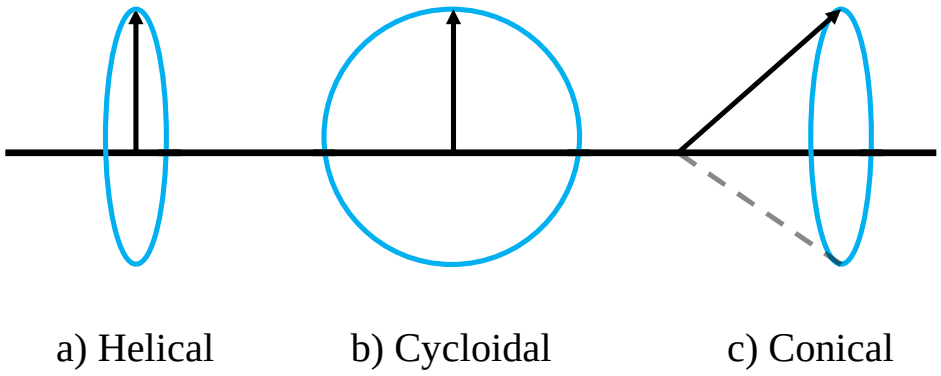

Figure 2.3: An illustration of the differences between (a) helimagnetism, (b) cycloidal magnetism, and (c) conical magnetism. The spiral plane around which the magnetic spin rotates throughout the unit cell is indicated by the blue circle.

One example of a chiral magnetic phenomenon is a domain wall. The regions between magnetic domains in a ferromagnet contain magnetic moments that slowly vary from the direction of one magnetic domain to that of the other. This can either be done by rotating the magnetic moments in the plane of the 'wall', to form a Néel domain wall, or by rotating the magnetic moments perpendicular to the plane of the wall, to form a Bloch domain wall. The crystal structure, i.e. the type of Lifshitz invariants present in the material, determines which type of wall is formed. These magnetic domain walls can propagate along the direction of an applied magnetic field.

Chiral magnetic long-range orderings include helimagnetic ordering, which arises from the competition between the symmetric ferromagnetic exchange interaction and the antisymmetric DMI. The first of these prefers to align spins parallel to each other, while the latter favours a turn angle of 90°. For a material in which the atoms lie in successive layers of basal planes, such as dysprosium, the exchange interaction can be described as:

$$E = -2NS^2 \left(J_{ex,1}\cos\,\theta + J_{ex,2}\cos\,2\theta\right), \tag{2.58}$$

where N is the number of atoms in each plane, $J_{ex,1}$ is the nearest neighbour exchange constant, $J_{ex,2}$ is the next-nearest neighbour exchange constant, and θ is the in-plane angle of the spins. This can be minimised by setting $\frac{\partial E}{\partial \theta} = 0$, i.e.

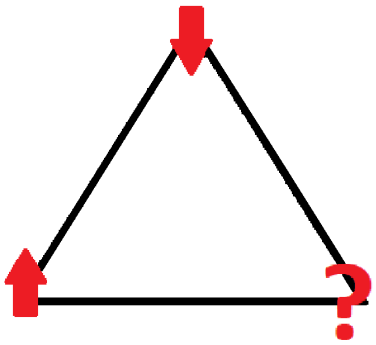

Figure 2.4: An illustration of triangular geometrical frustration. By placing two antiferromagnetically aligned spins at two corners of a triangular lattice, the third spin becomes frustrated, as it cannot align antiparallel to both spins.

$$0 = (J_{ex,1} + J_{ex,2}\cos\,\theta)\sin\,\theta. \tag{2.59}$$

Clearly, either $\sin\theta = 0$ (the ferromagnetic or antiferromagnetic state), or

$$\cos\,\theta = -\frac{J_{\mathrm{ex},1}}{4J_{ex,2}}, \tag{2.60}$$

which is the chiral helimagnetic state. The helical pitch, $L\,(0)$, can be calculated [3, 4] using:

$$L\,(0) \approx 2\pi a\frac{J}{D}, \tag{2.61}$$

where J is the Heisenberg interaction, D is the Dzyaloshinskii-Moriya constant, and a is a lattice parameter.

Cycloidal magnetism is very similar to helical magnetism, however; where in helimagnetism the spiral plane is perpendicular to the propagation vector, in cycloidal magnetism the spiral plane lies in the direction in which the magnetism propagates. In conical magnetism, meanwhile, is three-dimensional, with the spins rotating around in a conical shape.

2.4.6 Frustrated magnetism

Geometrical frustrated magnetism arises from the positioning of atoms within a crystal structure. In a triangular array, two spins are easily able to order antiferromagnetically. However, this would make the energy of the third spin ordering as spin-up equal to the energy of it ordering spin-down. This spin is therefore referred

to as frustrated. A simple schematic of this phenomenon is shown in Fig. 2.4. As every spin in the triangle experiences this frustration, the ground state of the system becomes sixfold degenerate.

Particularly relevant to this project is the antiferromagnetic trillium lattice [82], where sets of atoms are arranged in corner-sharing triangles [See Fig. 1.3]. It is important to note that there are two solutions to the spin ground state for lattices such as these, the hard spin constraint:

$$|s_i|^2 = 1, \tag{2.62}$$

and the soft spin constraint, which allows the magnetism to vary spatially throughout the model:

$$|s_i^\alpha|^2 + |s_i^\beta|^2 + |s_i^\gamma|^2 + |s_i^\delta|^2 = 4, \tag{2.63}$$

where $\alpha, \gamma, \gamma, \delta$ all refer to different positions in the unit cell. The soft spin constraint is not unusual in itinerant magnetic systems [83], and the type of constraint used for calculating the magnetic structure of materials with this magnetic system strongly affects the magnetic order that results. With a Heisenberg calculation utilising the hard spin constraint, a magnetic ground state with 120° angles between spins was calculated, whereas with a mean field approximation using the soft spin constraint, instead a highly degenerate partially-ordered ground state was realised.

2.5 Topological magnetic spin structures

Applying an external magnetic field to a chiral system can have a number of interesting effects on its magnetic behaviour. In select materials, these effects include the stabilisation of exotic spin structures such as the chiral soliton lattice [3, 46, 84],as well as skyrmions [8, 7, 85].

2.5.1 The chiral soliton lattice

The chiral soliton lattice (CSL) can be described as regions of moments which are ferromagnetically aligned with the external field and separated by 360° domain walls [See Fig. 2.5]. As the applied field is increased, the extent of these ferromagnetic regions, and thus the period of the CSL, are increased, until eventually the moments are aligned in a field polarized state.

A winding number, w, appropriate for one-dimensional solitons can be applied to the CSL. This is defined as:

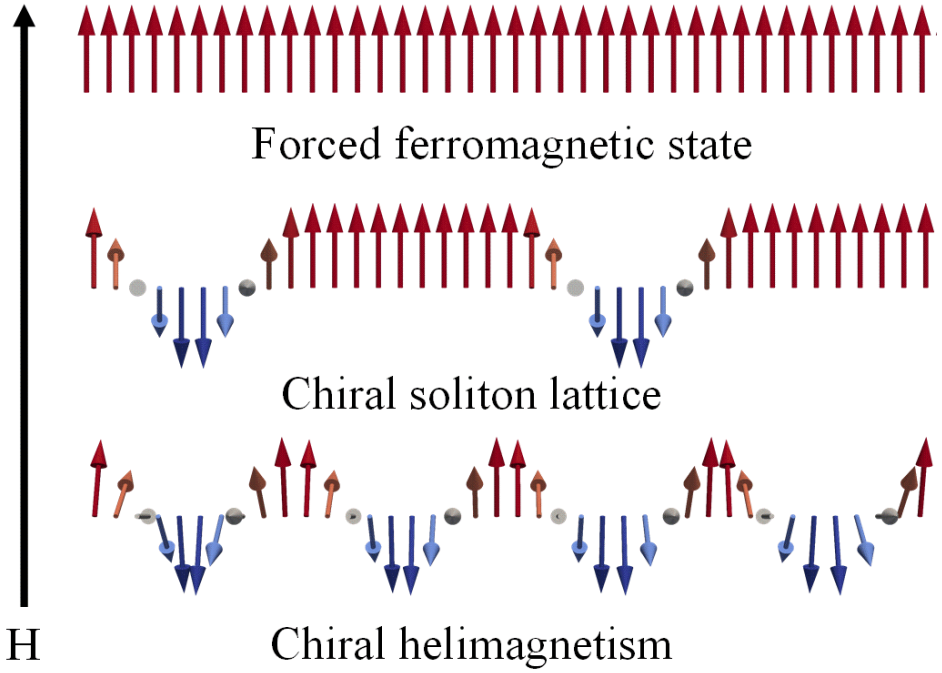

Figure 2.5: Visualisation of chiral helimagnetism, a chiral soliton lattice (CSL), and a forced ferromagnetic state. The arrows show the magnetic moments of each atom. As the magnetic field (H) increases, the part of each helix that is aligned with the field expands in size, increasing the period of the CSL, until finally the moments are arranged in a forced ferromagnetic state.

$$w = \frac{1}{2\pi} \int_{-\infty}^{\infty} \partial_x \phi \, \mathrm{d}x, \tag{2.64}$$

where ϕ is the azimuthal spin angle and x is the direction along the chain. As w is always an integer, the number of times that solitons wrap around a sphere is equal to a topological invariant - meaning that the solitons are topologically protected. The CSL is therefore robust to deformation [3, 86] from factors such as thermal fluctuations or material defects, and therefore of considerable interest for spintronic applications [87].

Known CSL hosts include $Cr_{1/3}NbS_2$ [3, 86] and $Cr_{1/3}TaS_2$ [26], members of the hexagonal layered transition metal dichalcogenides (TMDCs) intercalated with $3d$ transition metals that occupy octahedral $2c$ or $2d$ Wyckoff positions [37] between

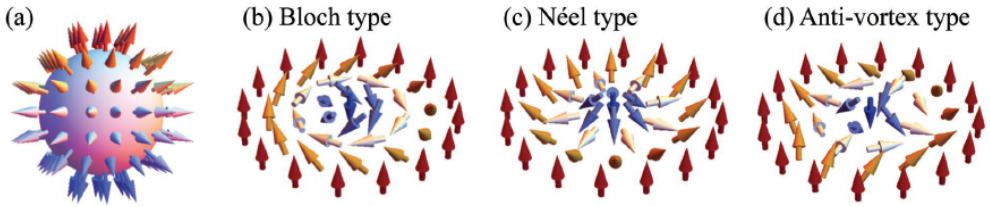

Figure 2.6: An example of a) a 3D hedgehog skyrmion, b) a 2D Bloch skyrmion, c) a 2D Néel skyrmion, and d) a 2D anti-vortex skyrmion, taken from [88].

the trigonal prismatic layers [See Fig. 1.2].

2.5.2 Skyrmions

Skyrmions are swirling magnetic vortices that can be characterised by a topological charge known as the skyrmion number, $\mathbf{\Phi}$:

$$\mathbf{\Phi} = \frac{1}{4\pi} \int \mathbf{n} \cdot \left(\frac{\partial \mathbf{n}}{\partial x} \times \frac{\partial \mathbf{n}}{\partial y} \right) \mathrm{d}^2\mathbf{r}, \tag{2.65}$$

where $\mathbf{n} = \dfrac{\mathbf{m}}{|\mathbf{m}|}$ is a unit vector parallel to the magnetic moment $\mathbf{m}$ [88]. As with the CSL, this winding number must be an integer, and skyrmions are topologically protected. This stability is part of what makes skyrmions so attractive for use in memory storage devices. Fig. 2.6 illustrates different types of skyrmions. The 2D Bloch skyrmion corresponds to a projection of the 3D hedgehog skyrmion; the edge of the skyrmion is parallel to the field direction but a gradual change in spin orientation exists that results in the centre of the skyrmion being antiparallel to the field direction. The size of the skyrmion is therefore related to the ratio of the ferromagnetic exchange interaction and the DMI - usually under 100 nm [8]. In an alternate case, a Néel skyrmion rotates in the radial plane rather than perpendicular to the radial plane like the Bloch skyrmion [89]. Finally, while both Bloch and Néel skyrmion have a topological charge of $+1$, it is also possible to stabilise an anti-vortex skyrmion. or anti-skyrmion as it is sometimes known, which has a topological charge of -1. An example of the different types of skyrmion can be seen in Fig. 2.6.

Skyrmions can form in helimagnetic materials due to the DMI. The skyrmion phase, previously known as an A-phase, was in fact originally discovered in the noncentrosymmetric B20 material MnSi [7]. This led to the study of a great many B20 materials with the same space group: $P2_13$. This includes: MnGe, FeGe, and Cu_2OSeO_3. The latter is of particular interest due to its multiferroic insulating

properties, which may lead to a capability of manipulating skyrmions formed in this material with an electric field [90]. Of the skyrmions that are formed due to an interplay of the DMI and the ferromagnetic exchange interaction under an applied field, another particularly interesting family of materials are the Co-Zn-Mn alloys. These alloys form in the $P4_132$ space group, and have displayed skyrmions at high temperatures, up to and including room temperature [18].

However, the DMI is not the only mechanism by which skyrmions can form - in thin films, for example, the competition between the easy-axis anisotropy and the magnetic dipole-dipole reaction can, upon application of a magnetic field, form large (3-100 μm) magnetic bubbles that have been considered a kind of skyrmion. Other methods considered as potential ways of forming skyrmions include four-site ring [9] and frustrated exchange interactions [91, 54, 55].The latter of these is especially relevant to this project and warrants deeper consideration.

A phase diagram was initially simulated for triangular-lattice antiferromagnets, using a Monte-Carlo simulation and mean-field calculations, and this revealed the presence of several multiple-q states, where q is the wavevector. A triple-q state was found to have the spin structure of a skyrmion lattice, suggesting that frustrated magnets are capable of hosting skyrmions [91]. Another point of interest is that the mechanism of skyrmion formation in this case does not include the DMI and enables the presence of both skyrmions and anti-skyrmions in a new Z-phase [91]. Skyrmions have since been observed in the centrosymmetric frustrated triangular-lattice magnet Gd_2PdSi_3 [54], detected through transport measurements, and in $Gd_3Ru_4Al_{12}$ [55], which materialises a breathing Kagomé network, where they have been directly observed using Lorentz transmission electron microscopy.

Chapter 3

Experimental Details

3.1 Sample synthesis

3.1.1 Solid state synthesis

The following samples were prepared in an inert atmosphere within a glovebox, with S prepared previously by evacuating overnight to remove excess moisture. Mn pieces were also prepared prior to being placed in the glovebox to remove any oxide that had formed on their surfaces by placing the pieces in a beaker containing a ratio of isopropyl alchohol and nitric acid of 1 ml to 1 pipette droplet, respectively. This beaker was then placed into a water bath and agitated to encourage the removal of the oxide. Once the dull oxide was removed from the shiny surface of the manganese pieces, they were transported to the glovebox and ground into a powder using a mortar and pestle immediately prior to being placed inside the quartz ampoule to minimise the chance of oxidation.

The vapour pressure of S is high, so to prevent any fracturing of the quartz ampoules under the increasing pressure as the temperature rose, all materials were heated to 450 °C to ensure they were above the boiling temperature of sulfur, to allow S to react with the other constituent materials. After the sulfur was no longer visible in the quartz ampoules, the materials were then heated to temperatures high enough to form the desired end material. The heating cycles used can be seen in Fig. 3.1. Before the final solid state synthesis reaction, it was necessary to press $Cr_{1/3}TaS_2$ into a pellet to prevent the powder from caking to the sides of the quartz ampoule, which would cause the ampoule to fracture due to undue pressure upon heating. In order to press a pellet, a small amount of $Cr_{1/3}TaS_2$ powder was placed between two metal dies in a die body. It was then placed under several tonnes of pressure for five minutes using a pellet press.

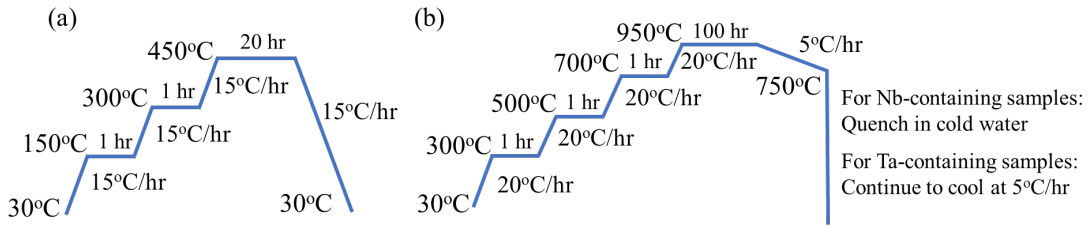

Figure 3.1: The (a) first and (b) final heating cycles for $M_{\frac{1}{3}}XS_2$ and $M_{\frac{1}{4}}XS_2$, to react the sulphur present in the sample and to form the final product, respectively.

Removing the Nb-containing samples from the furnaces after the completion of the synthesis involved quenching them in cold water from high heat in order to force the material into the desired hexagonal 2H polytpe. This family of materials can be stabilised in many different polytypes, and when cooling the sample slowly, a different polytype is produced. On the other hand, for $Cr_{1/3}TaS_2$, the sample needed to be cooled slowly to achieve the 2H polytype, and quenching the sample would instead result in the trigonal 1T polytype instead [92].

3.1.2 Arc melting

Arc melting was used for the synthesis of polycrystalline alloys such as the Mn_3XY family, where X = Rh, Ir and Y = Ge, Si. Polycrystalline Mn_3RhSi was prepared in-house, with Rh powder, and Mn and Si pieces. Mn_3IrSi and Mn_3RhGe were prepared in the same manner by collaborators at the National Cheng Kung University, Taiwan.

A stoichiometrically correct ratio of the starting elements Mn (99.5%, metals basis, Alfa Aesar), Rh (99.5%, metals basis, Alfa Aesar), and Si (99.9999%, NewMet) were placed in a copper crucible that was then evacuated and flushed through with argon several times, until a pressure of 0.1 mbar was reached. The argon line was then left open to create an over-pressure of argon and electrodes connected to a power source were used to strike an arc against a metal notch in the crucible [See Fig. 3.2]. A water cooling system was employed to prevent the equipment from over heating.

The arc was used to heat a titanium ingot to remove any oxygen still present in the system. The presence of an excessive amount of oxygen would cause the ingot to tarnish, indicating a problem with the vacuum. Otherwise, another arc was struck and slowly transferred to the sample to melt it. The arc furnace used for sample synthesis is shown in Fig. 3.2.

Figure 3.2: The crucible of the arc furnace. The arc is struck against the metal notch, as otherwise the large power output from the electrode causes it to fuse to the crucible. Inset: the electrode for the arc furnace.

3.1.3 Chemical vapour transport

To form single crystals of the intercalated transition metal dichalcogenides using the previously synthesised polycrystalline powder samples as seeds, chemical vapour transport (CVT) across a closed system was used. This method used a three-zone tube furnace to create a temperature gradient - a transport agent, I_2, acted as a catalyst to volatilise the sample, which then diffused along the temperature gradient. Once it reached an area with a sufficiently different temperature, I_2 separated from the transported sample, which nucleated and crystallised. The I_2 then travelled back through the system to reach the sample and the process was repeated. Due to this, only small amounts of transport agent were needed. For all chemical vapour transport growths involved with this project, 250 mg of I_2(99.99%, Alfa Aesar) was used for 2.5 g of sample. A schematic of chemical vapour transport is shown in

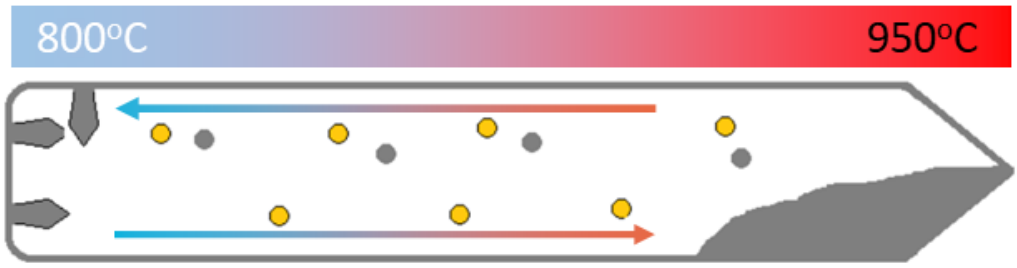

Figure 3.3: A schematic of chemical vapour transport. The iodine (yellow circle) reacts with the sample (grey circle) to form an iodine-sample complex. This complex is then transported down the temperature gradient and deposits the sample, which crystallises.

Fig. 3.3.

Both the size of the temperature gradient and the type and amount of transport agent used impacted the crystal growth significantly. For example, too large a temperature gradient can prevent the desired dissolution of the sample-iodine compound at the 'cold' end of the gradient. Due to the difference between the NbS_2 and TaS_2 systems, a slightly different heating cycle was needed to grow $Cr_{1/3}TaS_2$ than was used for the rest of the materials. For the Nb-containing systems, the 'hot' zone of the furnace was set to 950°C and the 'cold' zone of the furnace was set to 800°C. For $Cr_{1/3}TaS_2$, however, a temperature gradient of 950°C to 880°C was used instead. All samples were held at these temperatures for approximately 500 hours before being cooled at 50°C/hr to room temperature. Table 3.1 contains information on the single crystal growth procedures used for several members of the intercalated transition metal dichalcogenide family.

3.1.4 Modified Bridgman growth

The Bridgman technique is a useful tool for crystal growth and refers to a crystal growth method where a quartz ampoule containing molten material is slowly lowered through a tube furnace with a large negative temperature gradient at its bottom. Encountering the temperature gradient causes the molten sample to crystallise [93]. To grow single crystal samples for the Mn_3XY family, a modfied version of the Bridgman technique was used.

This modified Bridgman technique made use of a box furnace. Samples of polycrystalline Mn_3XY were placed inside an alumina crucible with a conical tip. This crucible was then double-sealed inside two quartz ampoules, which were evacuated and then flushed with 1/3 atm of argon gas. This gas was used in an attempt to equalise the pressure these tubes undergo at the high temperatures

Table 3.1: Growth conditions for the transiton metal dichalcogenides.

Formula	T_1 (°C)	T_2 (°C)	Crystal quality	Extra information
$Mn_{1/4}NbS_2$	800	950	Several mm long and thick crystals.	Grown using $Mn_{1/3}NbS_2$ as a seed if no excess Mn was added during crystal growth.
$Mn_{1/3}NbS_2$	800	950	Several mm long and thick crystals.	Grown using $Mn_{1/3}NbS_2$ as a seed with 2% excess Mn added.
$V_{1/3}NbS_2$	800	950	Several mm long and thick crystals.	
$Ti_{1/3}NbS_2$	800	950	Sub mm long, very thin crystals.	Growth conditions at this temperature gradient seem sub-optimal.
$Cr_{1/3}NbS_2$	800	950	Several mm long and very thin crystals.	
$Cr_{1/3}TaS_2$	880	950	Sub mm to a couple of mm long and very thin crystals.	
$Cr_{1/4}TaS_2$	800	950	Several mm long crystals, thicker than $Cr_{1/3}NbS_2$ crystals.	
$Mn_{1/4}TaS_2$	800	950	Several mm long and thick crystals.	Grown using $Mn_{1/3}TaS_2$ powder as a seed. Tried using 0 and 2% excess Mn with $\approx Mn_{1/4}TaS_2$ as a result both times.
$V_{1/4}TaS_2$	800	950	Several mm long and thick crystals.	Grown using $V_{1/3}TaS_2$ powder as a seed.

needed to melt the polycrystalline material within. The samples were heated past their melting points and held at this temperature for three days to ensure they were fully melted, and then slowly cooled to room temperature at a rate of 3°C/hr. On reaching the conical tip of the alumina crucible, the material crystallised into a boule.

3.2 Energy dispersive x-ray analysis

Energy dispersive x-ray analysis (EDX) was performed using a scanning electron microscope (SEM). Samples were prepared by affixing them to carbon tabs on sample holders and evacuating the sample chamber. An electron beam was used to bombard the sample, exciting electrons within the material to higher energy states. These electrons then decayed from the high energy states and emitted x-rays with energies dependent on the element they were emitted from. The number of x-rays produced were then counted and the intensity of the x-ray peaks relative to their neighbours were used to determine the percentage of each constituent part of the material. The penetration distance of the electron beam with respect to the sample depends on the incident energy, which was consistently set to 20 kV for all samples measured.

3.3 Heat capacity

Heat capacity measurements were performed in a Quantum Design Physical Property Measurement System (PPMS) using the 2τ thermal relaxation method at temperatures from 1.8 to 300 K in zero applied field. Apiezon N grease was used to ensure good thermal contact between the sample and the sample stage, which was housed in a puck.

The 2τ thermal relaxation method measures the heat capacity of a material using two time constants, τ_1 the relaxation time between the sample platform and the puck, and τ_2 the relaxation time between the sample and the sample platform. The heater is turned off and the sample system is allowed to relax, which takes the form:

$$T_p(t) = T_0 + Ae^{\frac{-t}{\tau 1}} + Be^{\frac{-t}{\tau 2}}, \tag{3.1}$$

where T_p is the platform temperature at time t, T_0 is the initial temperature, and A and B are constants. The relaxation method was originally optimised for low

temperature measurements [94, 95], before being extended to room temperature [96, 97, 98, 99, 100]. Here,

$$\tau_m = C_m/K_m, \tag{3.2}$$

where $C_1 = C_s + C_p$ is the sum of the heat capacities of the sample and the platform for τ_1, $C_2 = C_p + C_h$ is the sum of the heat capacities of the platform and the heat sink for τ_2, K_1 is the thermal conductivity between the sample and the platform, and K_2 the same parameter for the platform and the heat sin.

Model values for these two τ can be calculated and compared to the measured data, producing a value for heat capacity. A simpler model assuming perfect thermal coupling between the sample and sample stage and thus using only one value of τ is also calculated and compared to the data, allowing the best model of the two to be selected by the PPMS software. Baseline measurements for the puck were performed to identify any features in the data that were associated with the puck itself.

The Debye-Einstein model was used to calculate the lattice contribution to the heat capacity in order to subtract it; allowing for the calculation of the entropy associated with the magnetic ordering. This phonon contribution can be estimated using

$$C_{\mathrm{D-E}}(T) = \gamma T + n\delta C_{\mathrm{D}}\left(\frac{T}{\Theta_{\mathrm{D}}}\right) + n(1-\delta)C_{\mathrm{E}}\left(\frac{T}{T_{\mathrm{E}}}\right), \tag{3.3}$$

where γ is the electronic contribution to the heat capacity, n is the number of atoms per formula unit of the materials, δ is the fractional contribution of C_{D}, Θ_{D} is the Debye temperature, T_{E} is the Einstein temperature, C_{D} is the Debye contribution to the heat capacity:

$$C_{\mathrm{D}}\left(\frac{T}{\Theta_{\mathrm{D}}}\right) = \int \frac{\Theta_{\mathrm{D}}^4 e^{\frac{\Theta_{\mathrm{D}}}{T}}}{T^4(e^{\frac{\Theta_{\mathrm{D}}}{T}}-1)^2}, \tag{3.4}$$

and C_{E} is the Einstein contribution to the heat capacity:

$$C_{\mathrm{E}}\left(\frac{T}{T_{\mathrm{E}}}\right) = \int \frac{\Theta_{\mathrm{E}}^2 e^{\frac{\Theta_{\mathrm{E}}}{T}}}{T^2(e^{\frac{\Theta_{\mathrm{E}}}{T}}-1)^2}. \tag{3.5}$$

It is worth noting that at low temperatures the magnetic contribution to the heat capacity from antiferromagnetic spin waves can be approximated as:

$$C_{\mathrm{mag}}(T) = cn\left(\frac{k_{\mathrm{B}}T}{2|J_{\mathrm{ex}}|S}\right)^3, \tag{3.6}$$

where c is a constant that has been calculated for several different lattices [101], $\mathrm{J_{ex}}$ is the exchange constant, and S is the spin angular momentum. This clearly has a T^3 dependence, which can be expected to appear roughly linear at very low temperatures. As the phonon contribution to the heat capacity also has a T^3 dependence, it can be very difficult to easily separate the magnetic and lattice contributions to the heat capacity for antiferromagnetic materials.

At low temperatures, the heat capacity can be approximately modelled to $C(T)/T = \gamma + \beta T^2$, where $\beta = \frac{12}{5}\frac{nR\pi^4}{\Theta_{\mathrm{D}}^3}$, and where R is the molar gas constant. As this is expected to be linear for materials with an antiferromagnetic ordering, it can be used to estimate values for γ and β. The Dulong-Petit value, $3nR$, can also be calculated to indicate how close the sample was to reaching the saturation value for the heat capacity at room temperature.

3.4 Diffraction techniques

The periodic structure of crystals means that they can act as a diffraction grating for electrons, x-rays, and neutrons. These diffraction techniques are incredibly useful for probing the structural and, for neutrons especially, magnetic properties of different crystalline materials.

3.4.1 Electron diffraction

Two transmission electron microscopes (TEMs) were used to investigate the structures of different single crystals. To distinguish centrosymmetric from non-centrosymmetric structures, measurements were made along the [001] direction of the crystals of $\mathrm{Mn_{1/3}NbS_2}$, $\mathrm{Cr_{1/3}NbS_2}$, $\mathrm{V_{1/3}NbS_2}$, and $\mathrm{Cr_{1/3}TaS_2}$. Samples were prepared by using a scalpel to graze the surface at the edge of a crystal of each material. The scrapings were then deposited upon a lacey carbon TEM grid in order to fill the grid with tiny crystallites. Images and selected area electron diffraction patterns were recorded using a JEOL2100 transmission electron microscope, operated at 200 kV with a Gatan OneView digital camera. The electron wavelength, λ_{e}, can be related to the voltage, V, of the TEM [62] using:

$$\lambda_{\mathrm{e}} = \frac{h}{[2\mathrm{m_e}eV(1+\frac{eV}{2m_ec^2})]^{\frac{1}{2}}}, \tag{3.7}$$

where h is Planck's constant, m_e is the mass of the electron, e is the charge of an electron, c is the speed of light.

To examine the in-plane structural features of $Mn_{1/3}NbS_2$ and $Cr_{1/3}NbS_2$, the samples were instead prepared using an FEI NanoLab-600 Helios Dual-Beam focused ion beam (FIB) microscope equipped with an Omniprobe-200 micromanipulator. Single crystals of these materials were mounted inside the FIB on their (001) face and samples of approximate size 20×5 μm^2 and 1 μm thickness were cut normal to this face using gallium ion milling. They were then lifted out with the micromanipulator and platinum deposition was used to attach the samples to Omniprobe grids. Further gallium ion milling was used to thin the samples to approximately 100 nm so that they were electron-transparent. These samples were then measured using an FEI Titan^3 80-300 transmission electron microscope operated at an acceleration voltage of 300 kV and equipped with a high-brightness XFEG field-emission electron gun. Images were recorded on a 2048 $\times$ 2048 pixel CCD using either a Gatan Ultrascan 1000 camera or a Gatan 865 Tridiem camera which allows images to be energy-filtered. A 2 T field was applied to the samples to force them into a magnetically saturated state before diffraction images were taken.

TEMs utilise an electron gun and a series of electromagnetic lenses to focus an electron beam on the atomically thin sample. An example schematic of a JEOL JEM2100 TEM is shown in Fig. 3.4.

3.4.2 X-ray diffraction

X-ray diffraction has already been discussed at length in Section 2.4. Here the details of the experimental equipment used for this project are discussed.

Powder x-ray diffraction

In a polycrystalline material such as a powder, every set of lattice planes are capable of diffracting as the different crystallites within the powder orient randomly along different faces with respect to the beam [60, 58].

The diffractometer used for this project was the Panalytical X'Pert Pro MPD, which has a beam radius of 240 mm and a Cu K-α x-ray source ($\lambda = 1.5406$ Å). A monochromator ensured only the K-α_1 wavelengths were emitted. The detector was moved around 2θ for each scan, which were usually made to span values 10 - 90^o. Peaks form in the diffraction profile at different (hkl) values which can be predicted from knowledge of the sample, i.e. the peak at the lowest 2θ value is from the plane with the greatest allowed spacing. This can be used to check the phase purity of a

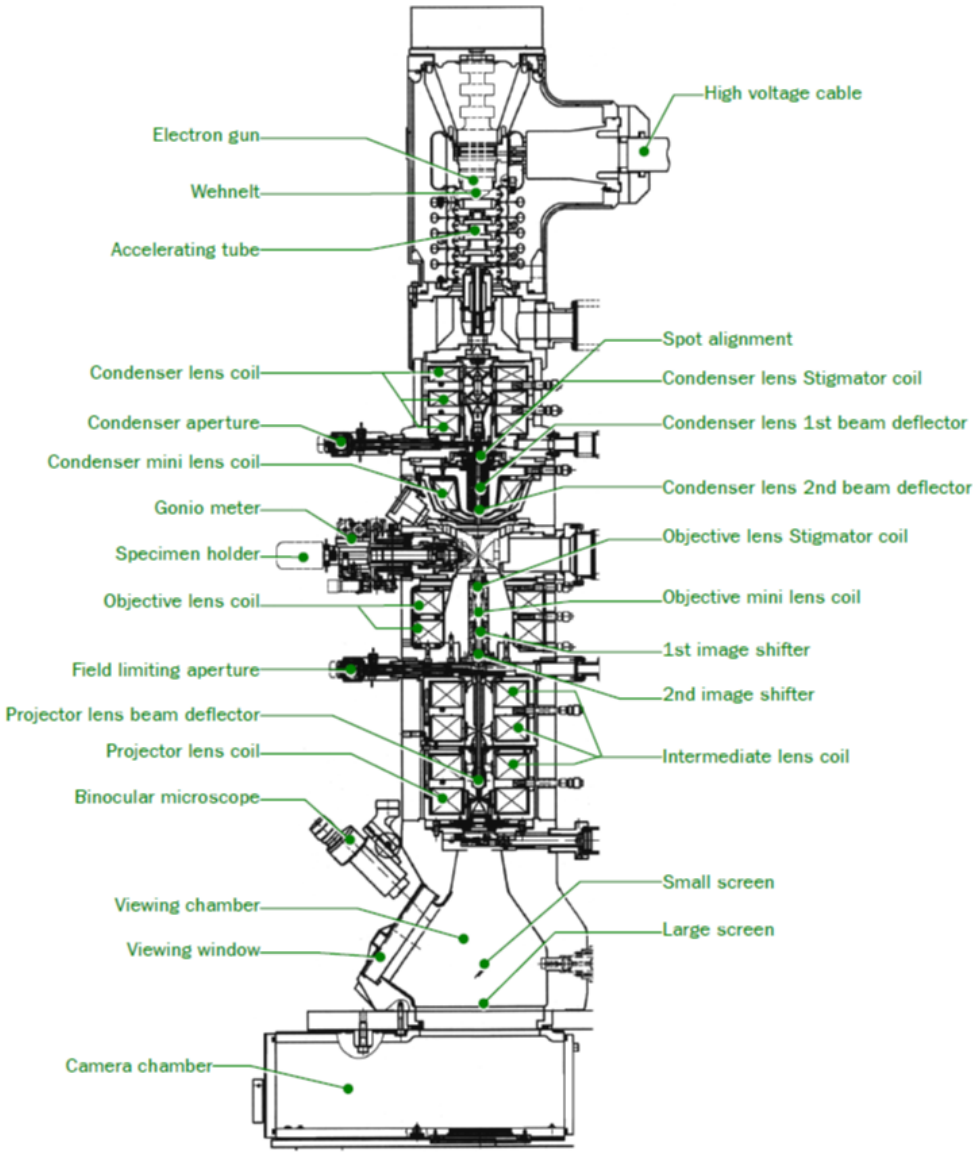

Figure 3.4: A schematic cross-section of a JEOL JEM2100 transmission electron microscope. Taken from [102].

material. Data was analysed using the Rietveld refinement method implemented in the Topas academic v6.0 sofware [103].

The Rietveld refinement method uses the least squares regression method to minimise the difference between the calculated fit (y_{calc}) and observed data (y_{obs}) [104, 105, 106]. The best possible fit to the data is calculated as

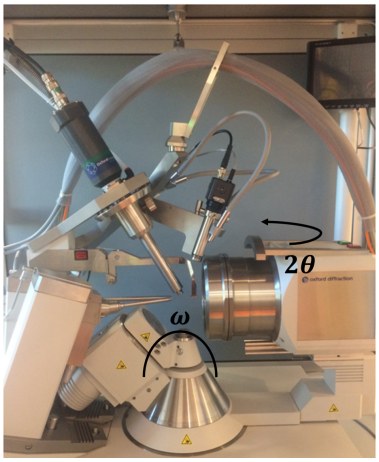

Figure 3.5: An image of an Oxford Diffraction Gemini single crystal diffractometer with the directions ω and 2θ marked.

$$R_{\text{exp}} = \sqrt{\frac{N-P}{\sum_{i=1}^{N} w_i (y_{obs,i})^2}}, \tag{3.8}$$

where N is the number of data points, P is the number of parameters, $w_i = \frac{1}{\sigma^2(y_{obs,i})}$ is the weighting, and σ^2 is the variance of the intensity. This value can be compared to R_{wp} the weighted difference between the observed data and calculated fit:

$$R_{\text{wp}} = \sqrt{\frac{\sum_{i=1}^{N} (y_{obs,i} - y_{calc,i})^2}{\sum_{i=1}^{N} w_i (y_{obs,i})^2}}, \tag{3.9}$$

in order to estimate the goodness of fit χ:

$$\chi = \frac{R_{wp}}{R_{exp}}. \tag{3.10}$$

Single crystal x-ray diffraction

The single crystal x-ray diffraction method used in this project was a transmission technique. Samples were rotated through an angle ω while the detector was moved through angle 2θ in order to build up a three-dimensional image with the diffraction from the sample. An image of the single crystal diffractometer is displayed in Fig. 3.5

Single crystal x-ray diffraction data of $Cr_{1/3}NbS_2$ and $V_{1/3}NbS_2$ were collected for a crystal of dimensions $0.13 \times 0.12 \times 0.02\,\text{mm}^3$ and $0.07 \times 0.03 \times 0.03\,\text{mm}^3$, respectively, using an Oxford Diffraction Gemini diffractometer, employing graphite monochromated Mo K-α radiation ($\lambda = 0.71073$ Å) generated by a fine-focus sealed

tube Enhance x-ray source and detected by a Ruby CCD detector.

Single crystal diffraction data of $Mn_{1/3}NbS_2$ and $Cr_{1/3}TaS_2$ were collected for a crystal of dimensions $0.21 \times 0.14 \times 0.08$ mm^3 and $0.10 \times 0.07 \times 0.013$ mm^3, respectively, using a Rigaku Oxford Diffraction Synergy diffractometer, employing mirror monochromated Mo K-α radiation ($\lambda = 0.71073$ Å) generated by a micro-focus sealed tube PhotonJet x-ray source and detected at a HyPix hybrid photon counting detector.

In all cases, the temperature was controlled using an Oxford Cryosystems Cryostream [107] at 295 and 300 K, respectively, with data collection, indexing, reduction and absorption correction mediated using CrysAlisPRO [108]. For the Cr system, absorption was accounted for by use of an empirical, spherical harmonics approach as implemented in SCALE3 ABSPACK while for the Mn system, a Gaussian integration over a multifaceted crystal model was employed.

Structural solutions were obtained using SHELXT [109] and further refined by full-matrix least squares, using SHELXL [110], both operating through Olex^2 [111].

Laue x-ray diffraction

A backscattering x-ray Photonic-Science Laue camera system was used to assess the quality and orientation of the single crystals. The Laue backscattering method of x-ray diffraction satisfies Bragg's law by fixing the angle of incidence and varying the wavelength of the incident light. The x-ray beam is passed through a hole in the CCD (charge-coupled device) and is incident on the single crystal sample. Some of this beam is then backscattered by the sample onto the CCD, resulting in diffraction spots projected in an imaginary cone from the illuminated area [60, 58]. Due to this, Laue diffraction is useful for crystal orientation, as different symmetries will result in different patterns from different crystallographic orientations. The expected Laue pattern of a material with a known space group and lattice parameters can be simulated and compared to experimental results for different crystallographic orientations in order to find the desired orientation. If multiple orientations are required then the sample can be cut to suit. Fig. 3.6 displays the experimental set-up used throughout this project.

3.4.3 Neutron diffraction

Powder and single crystal neutron diffraction measurements were performed using the WISH instrument at the ISIS neutron source [112] [See Fig. 3.7]. The theory of neutron scattering has been discussed previously in Section 2.5, so in this section

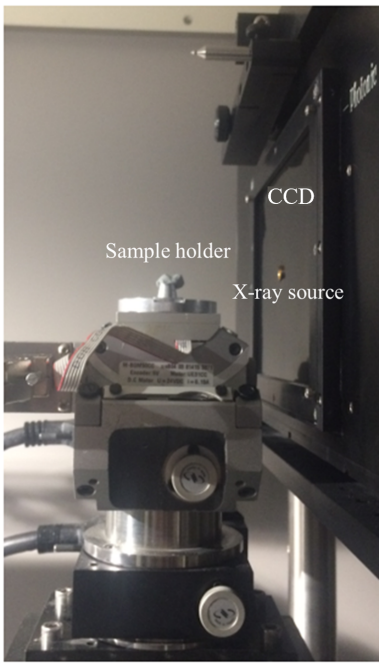

Figure 3.6: An image of the Laue diffractometer.

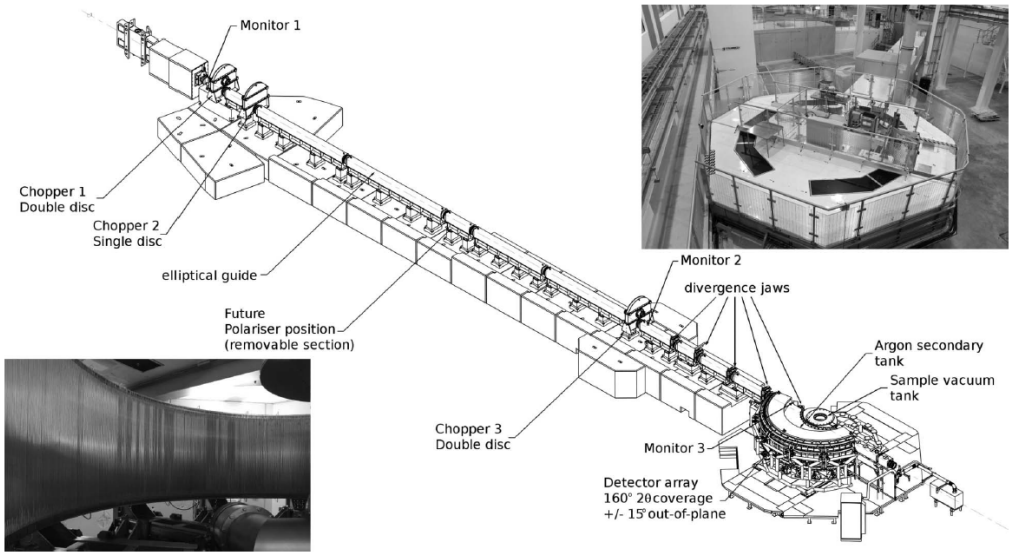

Figure 3.7: A schematic of the Wish diffractometer, taken from [112], inbetween a picture of the instrument (left) and the array of ^{3}He detectors inside the experimental blockhouse (right). An elliptical neutron beam is transported by a ballistic supermirror guide that starts 1.7 m from the source and ends 0.5 m from the sample-point.

the experimental setup used for this project will be elaborated on.

The WISH instrument uses a spallation source that emits neutrons in pulses using a proton accelerator. This allows for time-of-flight neutron scattering measurements. WISH has a long repetition time and is thus better suited to slower-moving long-wavelength neutrons to better probe short-d magnetic features. A fixed bank of 5 multi-angle detectors cover a broad 2θ range. The wavelengths of the large bandwidth wavelengths of neutrons can be determined using a basic kinematic equation:

$$\lambda = h\left(t + t_0\right)/m_n\left(L + L_0\right), \tag{3.11}$$

where t is the time of flight it takes a neutron to travel a distance L from the moderator to the target, t_0 and L_0 are offset values for each experimental set-up that must be calibrated, m_n is the mass of the neutron, and h is Planck's constant [61].

Powder neutron diffraction

The powder neutron diffraction data were taken at zero field for a range of temperatures between 1.5 and 300 K for multiple samples. The powder polycrystalline materials were mounted inside vanadium canisters due to the low coherent scattering length of vanadium for neutrons, rendering it almost invisible to the neutrons.

Useful R-factors can be extracted from this data as well in the same way as for powder x-ray diffraction. We can additionally define the Bragg R-factor as:

$$R_{\text{Bragg}} = \frac{\sum |I_{\text{obs}} - I_{\text{calc}}|}{\sum |I_{\text{obs}}|}, \tag{3.12}$$

where I_{obs} is the observed intensity and I_{calc} is the calculated intensity. Note that this R-factor can also be used for x-ray diffraction, and that a version for the magnetic refinement can be defined in the same way, and is called R_{Mag} to distinguish it from the R-factor used for nuclear structure.

Single crystal neutron diffraction

The single crystal $V_{1/3}NbS_2$ was attached to an aluminium holder using aluminium tape and the alignment was checked in-situ and found to be accurate to within 1-2°. The single crystal neutron diffraction data were collected in both the $(hk0)$ and $(h0l)$ scattering planes at 1.5 K for a range of magnetic fields between 0 and 8 T. For the measurements in the $(hk0)$ scattering plane, the magnetic field was applied parallel to the c axis, while in the $(h0l)$ scattering plane, the magnetic field was applied along the [110] direction. A further temperature scan was performed in the

($h0l$) scattering plane, from 1.5 to 52 K in zero field. The large number of position sensitive detectors within WISH provide good resolution, and also allowed for data to be taken several degrees outside of both of these scattering planes, i.e. the (hk$\pm\frac{1}{3}$) peaks were accessible. The single crystal neutron diffraction data were treated using the single crystal interface of MantidPlot [113] and the powder neutron diffraction data were analysed with the FullProf software suite [114] and JANA2020 [115].

3.5 Magnetisation

3.5.1 *dc* susceptibility

A Quantum Design Magnetic Property Measurement System (MPMS) was used to measure the magnetisation between 1.8 and 300 K in applied magnetic fields up to 7 T. This Superconducting Quantum Interference Device (SQuID) uses the concept of inductance - a magnetic sample is moved some vertical distance through a pickup coil in the presence of a magnetic field. The moving sample cuts flux lines and induces a current in the coil proportional to the magnetisation of the sample. This current itself induces a flux in the input coil, which is coupled to the SQuID. This consists of two Josephson junctions connected in parallel in a superconducting loop [116]. A basic schematic of this SQUID setup can be seen in Fig. 3.8. It is worth noting that the coil has three 'sections' - it is wound one way in the top and bottom sections, and it is wound in the opposite direction in the middle section.

Any changes to the magnetic flux across the system will result in changes to the phases of the wavefunctions at these Josephson junctions, and therefore the current running through them. The signal output by the SQUID is small and therefore needs amplification, but remains very sensitive to changes in magnetic flux.

The polycrystalline samples were prepared in gel capsules while the single crystal samples were attached to teak sample holders with general electrical varnish (GEV). The capsules or holders were then mounted inside low-magnetic-background plastic straws at the midpoint to ensure the background deduction was symmetric. $V_{1/3}NbS_2$ was mounted directly onto the straw using GEV due to the background from the sample holder posing issues with the measurements due to the very small signal these crystals produced. Holes were poked throughout the straws to prevent the trapping of oxygen around the sample.

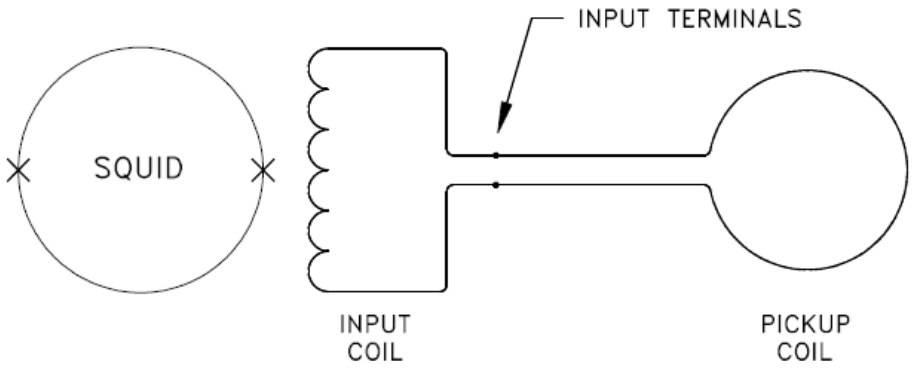

Figure 3.8: A schematic of SQuID pickup coils. Taken from [117].

3.5.2 Magnetisation as a function of field

Field-dependent magnetisation measurements up to 10 T were performed using an Oxford Instruments vibrating sample magnetometer (VSM). The magnetic field was applied parallel and perpendicular to the c axis. The samples were aligned along the different crystallographic directions to within 1-2° using superglue and PTFE tape to attach them to the sample stick.

Like the SQuID, the VSM uses inductance to perform its measurements. The sample is attached to a sample stick and a constant magnetic field is applied. The stick is then set to vibrate, causing the magnetised sample to create an alternating magnetic field that induces an electric field in the pickup coils of the VSM. The current produced is proportional to the magnetisation of the sample. The applied field was then varied in order to record the hysteresis loop that the sample produces.

3.5.3 *ac* susceptibility

A Quantum Design Physical Property Measurement System (QDPPMS) with an alternating current measurement system (ACMS) attachment was used for the *ac* susceptibility measurements on single crystal samples, which were orientated so that the magnetic field was applied perpendicular to the c axis. In *ac* susceptibility measurements, a small alternating field is applied to the sample. This causes the moment of the sample to vary with time without any need for moving the sample. If the force applied to the magnetisation is linear, it acts as a driven, damped, simple harmonic oscillator. While the applied frequency is small, the results are most like what would be measured for *dc* susceptibility, with

$$M_{\mathrm{AC}} = \chi H_{\mathrm{AC}} \sin(\omega t), \tag{3.13}$$

where M_{AC} is the moment induced by H_{AC} the alternating magnetic field, t is the time, and ω is the angular frequency.

At higher frequencies, dynamic effects prevent the *ac* susceptibility from following the curve that *dc* susceptibility measurements would follow. The *ac* susceptibility can lag behind the driving field, causing the need to separate χ into two components: the real in-phase component χ' and the imaginary out-of-phase component χ". These can be written as:

$$\chi' = \chi \cos(\phi), \tag{3.14}$$

$$\chi'' = \chi \sin(\phi), \tag{3.15}$$

where ϕ is the phase shift of the susceptibility relative to the driving signal and

$$\chi = \sqrt{\chi'^{\,2} + \chi''^{\,2}}. \tag{3.16}$$

For this reason, the imaginary χ" is indicative of dissipative processes in the material.

3.6 Lorentz transmission electron microscopy

Lorentz transmission electron microscopy uses the Lorentz force to image magnetic features in samples. In normal electron microscopy, an electron beam is focused onto a sample. The magnetism present in the sample will deflect the electrons in a direction dependent on the direction the magnetism orders in, due to the Lorentz force. Therefore, if a certain amount of defocus is applied to the microscope instead, alternating bright and dark features will be visible due to the magnetism present in the sample. A schematic view of this concept is displayed in Fig. 3.9 for a material with magnetic domains that alternate in orientation.

For the Lorentz transmission electron microscopy measurement, samples were prepared using a focussed ion beam (FIB), as discussed in Section 3.4.1., using the same FEI Titan^3 80-300 transmission electron microscope operated at an acceleration voltage of 300 kV and equipped with a high-brightness XFEG field-emission electron gun. However, instead of the 2 T field applied in normal operation, images of the magnetic structure were acquired either in Lorentz mode where the image

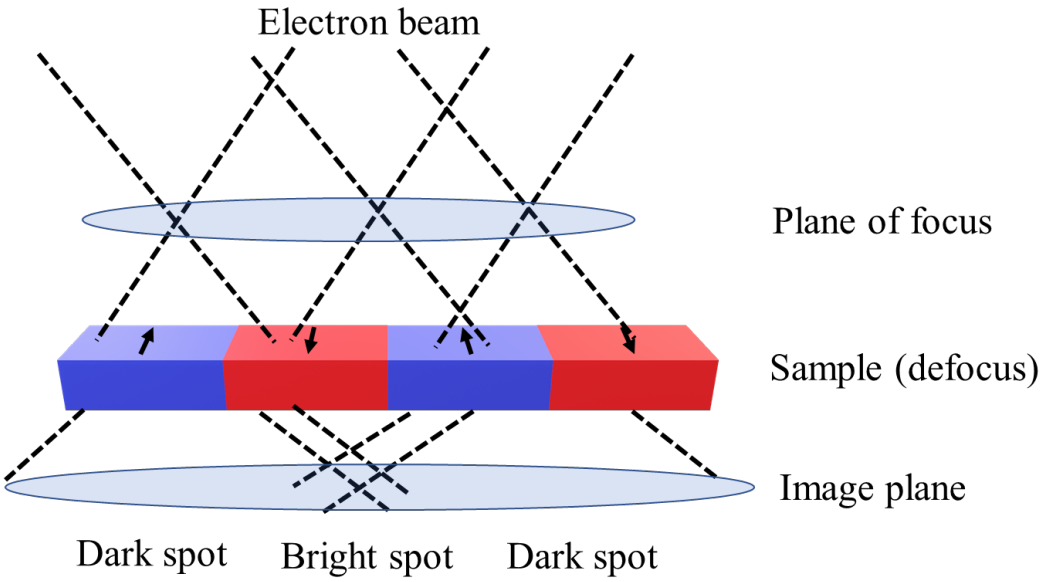

Figure 3.9: An example of Lorentz transmission microscopy. A sample with magnetism alternately pointing into the page (blue) and out of the page (red) is placed at a point outside of the focused plane of the TEM. At this point it deflects the incoming electron beam in different directions depending on the direction of the magnetism, causing dark and bright spots in the image plane.

is formed using the Lorentz lens or in low-magnification mode where the image is formed using the diffraction lens. Neither of these lenses applies a significant field to the sample and when an applied field was required, the objective lens was weakly excited to apply a field parallel to the electron beam. The applied magnetic field corresponding to a given objective lens current had been calibrated to within 1 mT using an FEI Hall probe holder.

The transport of intensity (TIE) equation was used to estimate the projected B-field within the sample. The TIE is a partial differential equation that relates the varial axial intensity of the optical field to its phase [118]. The TIE can in general be written as:

$$-k\frac{\partial I\left(x,y,z\right)}{\partial z}=\nabla\cdot\left[I\left(x,y,z\right)\nabla\phi\left(x,y\right)\right], \tag{3.17}$$

where $k=\frac{2\pi}{\lambda}$ is the wave number, $I\left(x,y,z\right)$ is intensity distribution at the x-y plane located at propagation distance z, and ∇ is gradient operator over the x-y plane, and ϕ is the phase shift of the material. Solving the TIE for ϕ requires the comparison images with a large amount of positive and negative defocus with a

Gaussian defocused image to estimate $\frac{\partial I(x,y,z)}{\partial z}$ [119]. Knowing the phase shift allows the estimation of the B field within the material as they are proportional:

$$\phi(x) = \frac{etx}{\hbar} B_y, \tag{3.18}$$

where e is the charge of the electron, t is the thickness of the sample, x is the in-plane direction perpendicular to the optical axis, and B_y is the magnetic flux density along the direction perpendicular to both x and the optical axis. By applying a gradient to the reconstructed phase, the in-plane B field can then be retrieved:

$$\nabla\phi(x,y) = \frac{et}{\hbar}(B \times \hat{n_z}), \tag{3.19}$$

where $\hat{n_z}$ is a unit vector along the optical axis.

The specimen thickness was measured by taking in-focus images of an area both with and without energy filtering. By dividing the unfiltered image by the filtered image and taking the natural logarithm, the thickness as a multiple of the inelastic mean free path of the electrons can be extracted in order to create a 't-over-lambda' map [62]. In order to calibrate the inelastic mean free path, the absolute specimen thickness was measured at 15 positions using the two-beam convergent-beam electron diffraction technique described in ref. [62], resulting in a map of the absolute thickness across the whole specimen to within 10 nm accuracy.

The amount of defocus applied is critical and heavily affects what is visible during the measurement. Agar Scientific's S106 calibration specimen, which consists of 463 nm spaced lines on an amorphous film, allowed for the calibration of the defocus and the magnification by using the same lens settings as the calibration specimen. Taking a Fourier transform of these images results in dark rings from the contrast transfer function of the lens, the radii of which can be measured and used to estimate the defocus.

All Lorentz transmission electroscopy experiments were performed at the University of Cambridge with collaborators James Loudon and Alison Twitchett-Harrison.

Chapter 4

Neutron diffraction study of $V_{1/3}NbS_2$

4.1 Introduction

While many members of the intercalated transition metal dichalcogenide family have been well-investigated, there remain several of the intercalated TMDCs that merit further study. One such example is $V_{1/3}NbS_2$, a material that was originally reported as a paramagnet [25] but was later reported to order ferromagnetically at temperatures below 50 K [21], with an additional transition observed as the temperature decreased below 20 K and the field was directed perpendicular to the c axis. It has since been predicted that $V_{1/3}NbS_2$ could host a chiral soliton lattice using calculations that consider the effect of spin-orbit coupling [120].

Interestingly, the paramagnetic Weiss temperature for $V_{1/3}NbS_2$ was reported to be negative, which is unexpected for a ferromagnetic material, and therefore attributed to a large contribution from crystal field effects [21]. However, a more recent study on the magnetism of $V_{1/3}NbS_2$ and its sister compound $V_{1/3}TaS_2$ using neutron diffraction and *dc* susceptibility measurements, reported that both of these materials are canted antiferromagnets, as expected for materials with negative Weiss temperatures [24]. This study also found evidence for a $\mathbf{k} = (0, 0, 0)$ magnetic propagation vector, and described the magnetic structure of the material as an A-type antiferromagnet with some canting present along the c axis described by the coupling of two irreducible representations.

In this chapter a detailed investigation into the magnetism of $V_{1/3}NbS_2$ is presented, using well-characterized single crystals and polycrystalline material. Techniques such as powder and single crystal neutron and x-ray diffraction, as well

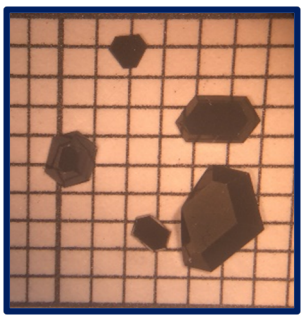

Figure 4.1: Single crystals of $V_{1/3}NbS_2$ on mm paper.

as heat capacity and *ac* magnetisation measurements, have been used to probe the magnetic structure of $V_{1/3}NbS_2$. It is shown that $V_{1/3}NbS_2$ becomes antiferromagnetic below 50 K. Two magnetic propagation vectors were extracted from the powder neutron diffraction data: $\mathbf{k_0} = (0, 0, 0)$ and $\mathbf{k_1} = (0, 0, \frac{1}{3})$. The $\mathbf{k_0}$ propagation vector represents an in-plane component of the magnetism, with antiferromagnetically-coupled ferromagnetic layers of vanadium atoms. The $\mathbf{k_1}$ propagation vector represents a canting out of the plane. In addition, evidence is provided for diffuse magnetic scattering in this material.

4.2 Sample preparation

Polycrystalline and single crystal samples of $V_{1/3}NbS_2$ were prepared using the processes detailed in Section 3.1, i.e. with a solid state reaction within a box furnace, and with chemical vapour transport (CVT) using the polycrystalline powder as a seed and iodine as a transport agent. 5 g of polycrystalline powder was synthesised, and 2.5 g was used during the CVT crystal growth process. Some of the crystals synthesised in this process are displayed on mm paper in Fig. 4.1. The size of the crystals varied from sub-mm in length and thickness, to approximately $4.0 \times 2.5 \times 1.0$ mm^3.

4.3 X-ray diffraction

4.3.1 Laue x-ray diffraction

A Laue pattern from the single crystal used for the following experiments, [Fig. 4.2], indicates that the crystal is of high quality. The *c* axis of the material was found to point out-of-plane, as expected, which made it simple to orient the samples for all further measurements.

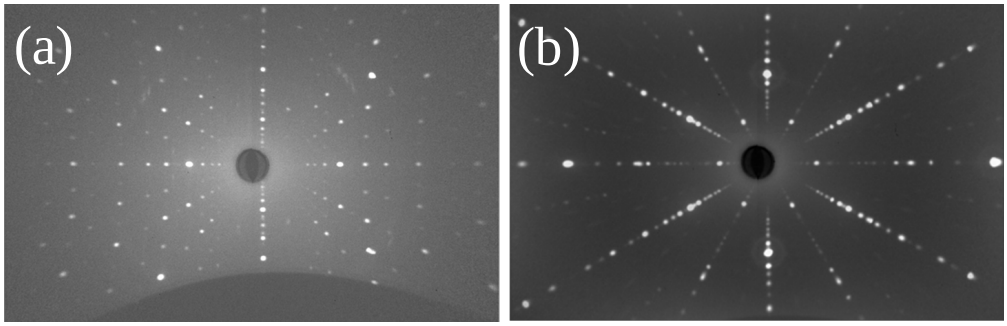

Figure 4.2: Laue back reflection pattern along the (a) [100] and (b) [001] orientations of an aligned $V_{1/3}NbS_2$ crystal.

Several spots in Fig. 4.2 were not well defined due to stacking faults present in the crystal measured, such as for example the twisting of crystal layers relative to each other. Due to the weak van der Waals bonding between the layers in this family of materials, and in fact many van der Waals materials, this particular stacking fault is common.

4.3.2 Single crystal x-ray diffraction

Single crystal x-ray diffraction data taken at room temperature for $V_{1/3}NbS_2$ has been used to create the model shown in Fig. 4.3. The parameters of this model are displayed in Table 4.1, which shows excellent agreement between the calculated and observed structure factors when modelled in the non-centrosymmetric space group $P6_322$, while refinement in the centrosymmetric space group $P6_3/mmc$ provides a significantly worse fit and a far more complex structure. The Flack parameter of the model is poor, indicating the presence of twinning in the material. Due to this, an inversion twin law is employed in the refinement for completeness for which the twin component scale factor refines to within error of zero [3(6)], where the value given in parenthesis is the associated error. A proportion of disorder over the main 2c Wyckoff site of the V atom (occupancy 0.413(12)) and the Wyckoff 2*b* (0.284(16)) and 2*d* positions (0.264(16)) was observed. Due to the relatively high amount of disorder present in the system, as well as the ambiguous twin scale factor present in this model, electron diffraction was used as a complementary method to confirm that the material had crystallised in the non-centrosymmetric $P6_322$ space group.

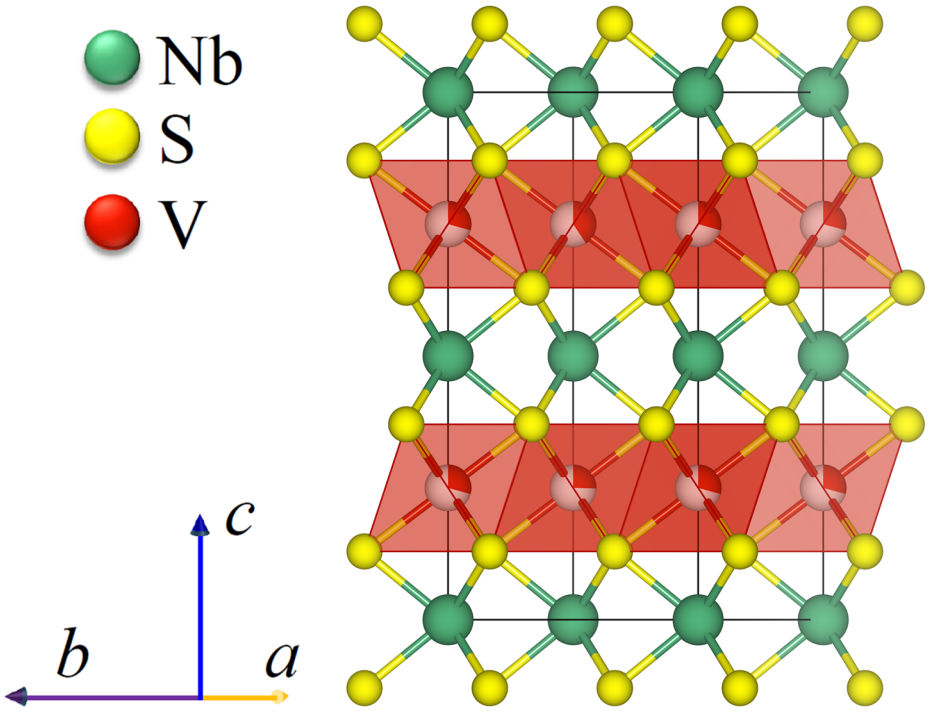

Figure 4.3: Nuclear structure of $V_{1/3}NbS_2$ constructed from single crystal x-ray diffraction measurements. The occupancy of the V atoms are shown as the percentage of each atom coloured in red. The octahedral sites that the V atoms occupy are displayed.

Table 4.1: Atomic positions and occupancies for $V_{1/3}NbS_2$ refined using single crystal x-ray diffraction.

	$a = 5.7693(3)$ Å	$c = 12.1794(7)$ Å	$R_1 = 4.91\%$	$wR_2 = 10.32\%$	BASF[3(6)]
Atom	Wyckoff	x	y	z	Occ.
V1	$2c$	$\frac{1}{3}$	$\frac{2}{3}$	$\frac{1}{4}$	0.413(12)
Nb1	$2a$	0	0	0.00000	1.000
Nb2	$4f$	$\frac{1}{3}$	$\frac{2}{3}$	0.50031(11)	1.000
S1	$12i$	0.03345(7)	0.0007(5)	0.12953(11)	1.000
V2	$2b$	0	0	$\frac{1}{4}$	0.284(16)
V3	$2d$	$\frac{2}{3}$	$\frac{1}{3}$	$\frac{1}{4}$	0.264(16)

4.4 Electron diffraction

Electron diffraction was used as well as x-ray diffraction to investigate the structural properties of $V_{1/3}NbS_2$. Electron diffraction was performed along the [001] direction of this material and the samples were prepared as discussed in Section 3.4.1, i.e. by depositing scrapings of single crystals onto lacey TEM carbon grids. A JEOL2100 transmission electron microscope with a Gatan OneView digital camera was operated at 200 kV to take the images.

Fig.4.4c displays the electron diffraction pattern measured. This pattern was compared against simulations of $V_{1/3}NbS_2$ in the $P6_322$ space group and simulations of the centrosymmetric material $V_{1/4}NbS_2$, which crystallises in the centrosymmetric $P6_3/mmc$ space group. These two space groups display key pattern differences in certain directions. Along the [001] direction, a significant difference in the relative intensities of key spots is a good indication of the space group that the material has crystallised in [see Fig. 4.4b].

4.5 *dc* susceptibility and magnetisation

The *dc* magnetic susceptibility, $\chi_{\mathrm{dc}}(T)$, of single-crystal $V_{1/3}NbS_2$ was measured in a field of 3.3 mT applied parallel and then perpendicular to the c axis, [Fig. 4.5]. The Curie-Weiss law is used to fit the zero-field cooled (ZFC) data in the paramagnetic state to give effective moments 2.90(2) μ_{B}/f.u. and 3.03(2) μ_{B}/f.u. for the field parallel and perpendicular to c, respectively. These values are in agreement with values calculated in previous work [21] and are both close to the expected spin-only value for V^{3+} of 2.83 μ_{B}/f.u..

A magnetic transition was observed at 50 K, with a sharp increase in the field-cooled cooling (FCC) susceptibility especially at this temperature. The ZFC and FCC curves are in fact significantly different from each other for both field directions, with a highly suppressed susceptibility in the magnetically ordered state in the ZFC regime when compared to the FCC regime, which increases at the transition temperature to form a peak. When $H \perp c$, an additional upturn in $\chi_{\mathrm{dc}}(T)$ is observed at $T < 10$ K. A larger signal is observed for $H \parallel c$ than for $H \perp c$, but the moment measured is still far smaller than would be expected for a ferromagnetic material.

The *ac* magnetisation M as a function of magnetic field H is shown in Fig. 4.6. Hysteresis is present for all temperatures for both field directions. This hysteresis is small when the field is applied perpendicular to c [Fig. 4.6(b) inset]. However, when

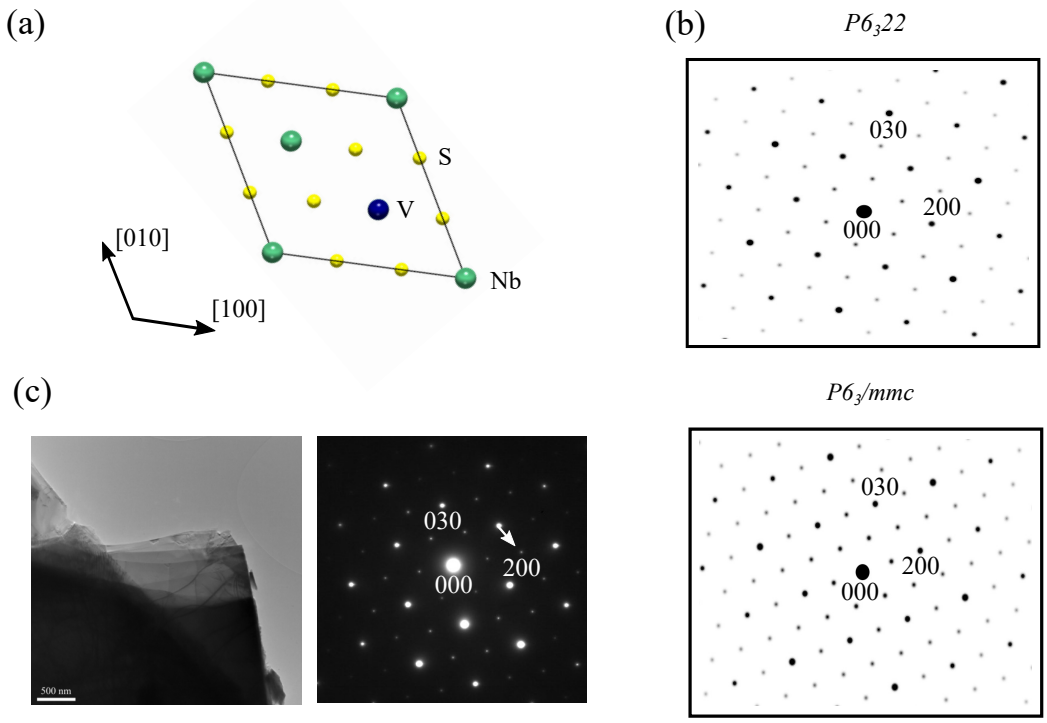

Figure 4.4: (a) $V_{1/3}NbS_2$ structure viewed along the [001] direction. (b) Simulations of the expected electron diffractions for $V_{1/3}NbS_2$ in the non-centrosymmetric $P6_322$ and centrosymmetric $P6_3/mmc$ space groups. The relative brightness between certain key spots (e.g. the (030) and (200) spots) are very different between the two space groups. (c) Experimental electron diffraction pattern and image of a prepared single crystal of synthesised $V_{1/3}NbS_2$ single crystal. The experimental pattern matches excellently with the simulation for the $P6_322$ space group.

the magnetic field is applied parallel to c, the hysteresis is far larger, with a coercive field of up to 1 T. Step-like features are observed in this magnetic hysteresis loop at low-fields when the magnetic field is applied at any intermediate angle between exactly perpendicular and parallel to the c axis, even for very small angles.

The *dc* magnetisation of $V_{1/3}NbS_2$ does not saturate in fields of up to 100 T regardless of the crystal orientation. As can be seen in Fig. 4.6, a maximum *dc* magnetisation of $\approx 0.2\ \mu_B$/f.u. is reached by 10 T, which is significantly lower than the expected moment for V^{3+}. This large difference between the observed and expected moment, despite the full effective moment obtained from the Curie-Weiss fits in the paramagnetic state [Fig. 4.5], strongly indicates a long range magnetically ordered structure that is largely antiferromagnetic, with near-perfect cancellation of the moments between the magnetic sublattices, and that the introduction of a

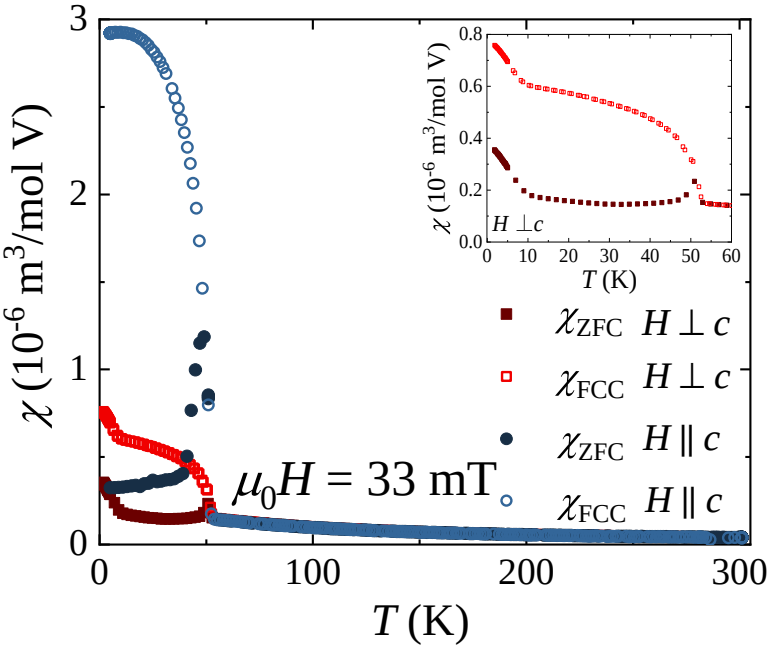

Figure 4.5: Temperature dependence of the *dc* magnetic susceptibility $\chi_{\mathrm{dc}}(T)$ for $V_{1/3}NbS_2$ collected in zero-field cooled (ZFC) and field-cooled cooling (FCC) modes in an applied field of $H = 3.3$ mT for $H \parallel c$ and $H \perp c$. The inset shows the magnetic susceptibility for $H \perp c$ between 1.8 and 50 K, with a magnetic transition visible at 50 K.

magnetic field does not significantly modify this structure. The sharp increase in the FCC $\chi_{\mathrm{dc}}(T)$ at 50 K in Fig. 4.5 indicates that there must be some ferromagnetic component to the magnetic ordering, such as a canting of the magnetic moments.

4.6 *ac* susceptibility

The *ac* susceptibility of $V_{1/3}NbS_2$ as a function of temperature was measured at several different applied *dc* magnetic fields oriented both perpendicular and parallel to the *c* axis of $V_{1/3}NbS_2$ [see Fig. 4.7]. For $H \parallel c$, a large χ' component is present at low temperatures < 10 K. This corresponds well with the feature seen in χ_{dc}. This feature is suppressed with field and is entirely absent when $H = 100$ mT. By comparing the two datasets in Fig. 4.7(a), it can also be seen that a further gradient change occurs in the 0 mT dataset at 30 K, after which point the 100 mT and 0 mT data sit neatly on top of each other, except for during the transition to the paramagnetic state at temperatures around 50 K. At these temperatures, a sharp peak is visible in χ' for 0 applied *dc* field, which is significantly suppressed with an

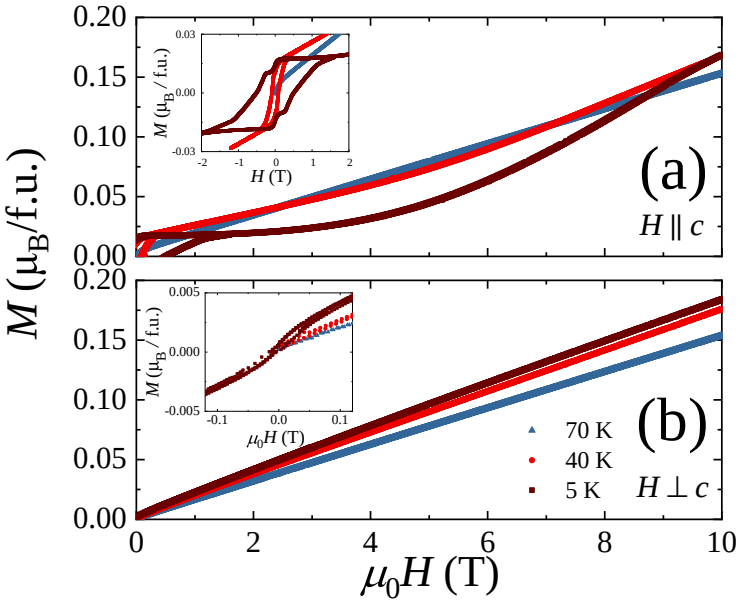

Figure 4.6: Field dependence of the *dc* magnetisation M per formula unit of VNb_3S_6 for various temperatures. The field was applied (a) parallel and (b) perpendicular to the c axis. The insets show the low field hysteresis for both field directions.

applied *dc* field of 100 mT. In χ", there is no evidence of the features seen in χ' at low temperatures, however the peak at the transition can again be seen for 0 mT applied *dc* field, and is again suppressed when 100 mT is applied.

For *dc* fields applied perpendicular to the c axis, something slightly different can be seen. Instead of a large χ' component at low temperatures, there is a small decrease in χ' at temperatures less than 10 K. Between 10 and 50 K, for all *dc* applied fields, χ' increases, and then decreases slightly between 50 K and 70 K. A peak is again visible at the transition temperature for 0 mT, that is suppressed with increasing fields. As the *dc* field applied to the material is increased, the χ' follows the same curve, but at a slightly increased background level. In χ", no features were visible except a peak at the transition temperature at 0 applied *dc* magnetic field.

4.7 Heat capacity

The heat capacity as a function of temperature for $V_{1/3}NbS_2$ is shown in Fig. 4.8. The magnetic transition at 50 K is clearly visible as an anomaly in the data. A value for the electronic contribution to the heat capacity γ as well as the Debye temperature Θ_D can be extracted from the low temperature heat capacity data [Fig. 4.8 inset] using $C(T)/T = \gamma + \beta T^2$, as mentioned in Sec. 3.3. In this case

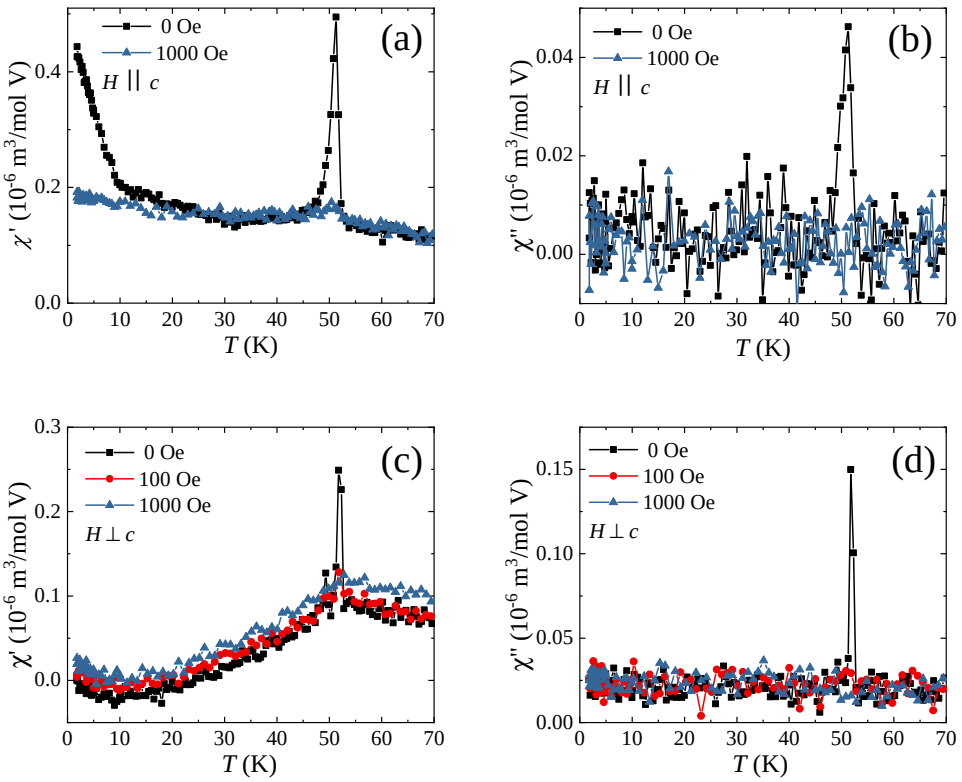

Figure 4.7: Temperature dependence of the *ac* magnetic susceptibility χ_{ac} for $V_{1/3}NbS_2$ collected with applied fields $H \parallel c$ and $H \perp c$ for both real χ' [(a) and (c), respectively] and imaginary χ" [(b) and (d), respectively].

n = 10 is the number of atoms per formula unit of VNb_3S_6.

This gives $\gamma = 7.5(2)$ mJ/mol K^2, a value that is reasonable for a metallic material [38]. As disorder prevalent in intercalated TMDCs has been shown to increase γ in other layered materials [121, 122], this may also have contributed to γ. The Debye temperature obtained from the same fit, $\Theta_D = 382(2)$ K, is consistent with the heat capacity at 300 K falling below the Dulong-Petit value $3nR$. A magnetic contribution to the heat capacity would result in a higher value for Θ_D, which is also consistent with the higher temperature data. Assuming 3D antiferromagnetic spin waves, this magnetic contribution would be proportional to T^3, making it difficult to distinguish from phonons. The linear dependence of $C(T)/T$ vs T^2 is, however, compatible with antiferromagnetic ordering.

The entropy associated with the magnetic ordering can be calculated by integrating over $\Delta C/T$, where $\Delta C(T) = C(T) - C_{D-E}(T)$. However, to ensure

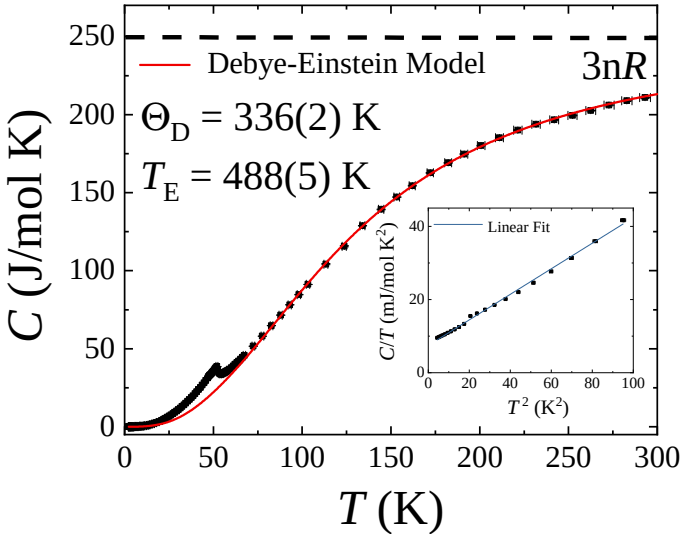

Figure 4.8: Heat capacity C of $V_{1/3}NbS_2$ as a function of temperature T from 1.8 to 300 K. The line is a fit using the Debye-Einstein model. The inset shows the linear behavior of C/T as a function of T^2 at low temperatures giving γ = 7.5(2) mJ/mol K^2 and Θ_D = 382(2) K.

that only the magnetic entropy is considered, the lattice contribution to the heat capacity must first be removed. This phonon contribution can be estimated using a Debye-Einstein model, see Eq. 6.1. The heat capacity data as fitted using Eq. 6.1 is shown in Fig. 4.8.

To limit the number of free parameters in this fit, the fractional contribution δ was constrained to 0.4. This was done as, of the n = 10 atoms present, the one V and three Nb atoms are far heavier in comparison to the six lighter sulfur atoms. The Debye contribution C_D is well suited to modelling the heavier atoms, while the Einstein contribution C_E works well for modelling the lighter sulfur atoms. In addition, γ was fixed to the value obtained from the low temperature data. Finally, to ensure that no aspect of the magnetic contribution to the entropy was removed in the estimation of the phonon contribution to the heat capacity, the Debye-Einstein model was restricted to data between 80 and 300 K, and then extrapolated to lower temperatures. This was done as evidence of short-range magnetic correlations in the magnetisation data were present until around 70 K.

Considerations such as these were useful in confining the flexible Debye-Einstein model to what is physically reasonable. The best fit to the data was obtained with a Debye temperature Θ_D = 336(2) K and an Einstein temperature

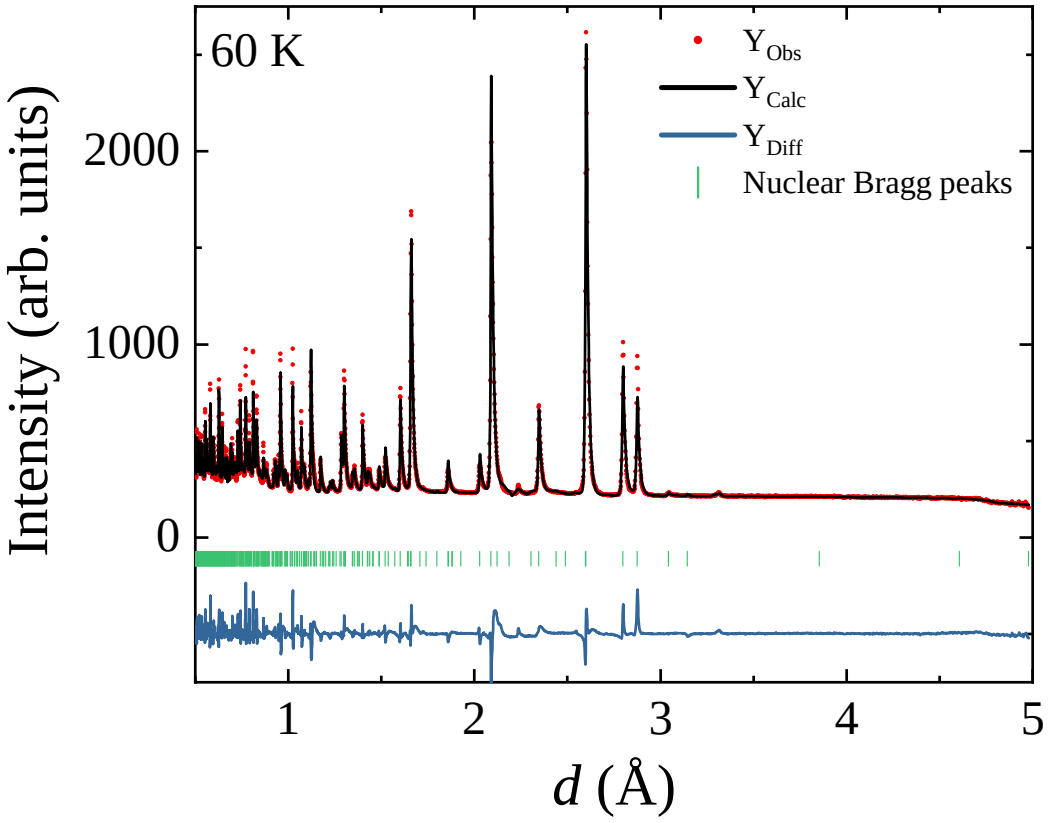

Figure 4.9: Powder neutron diffraction profile of $V_{1/3}NbS_2$ at 60 K with a calculated fit to the data.

$T_E = 488(5)$ K. These values fall either side of the $\Theta_D = 382(2)$ K obtained from the low temperature fit, as expected. The calculated entropy $\Delta S = 9(1)$ J/mol K is within error of the expected result of $\Delta S = R \ln 3$ from the $S = 1$ spin-only moment of V^{3+}. This data gives strong evidence for long-range magnetic ordering in $V_{1/3}NbS_2$ with magnetic correlations above the ordering temperature.

4.8 Powder neutron diffraction

A fit was performed at 60 K to determine the nuclear structure of $V_{1/3}NbS_2$, with a Bragg R-factor of $R_{Bragg} = 7.978$ %. $V_{1/3}NbS_2$ was found to form in the $P6_322$ space group with lattice parameters of $a = 5.7521(2)$ Å and $c = 12.1778(7)$ Å. The refined atomic positions are tabulated in Table 4.2 at both 60 and 5 K. The temperature term for the V atom was taken from powder x-ray diffraction and left invariant due to the fact that almost all neutrons scatter incoherently from

Table 4.2: Atomic coordinates for $V_{1/3}NbS_2$ extracted from the powder neutron diffraction refinement at 60 K and 5 K in the hexagonal space group $P6_322$. The reliability factors for each nuclear phase are $R_{\text{Bragg}} = 7.978\%$ and $R_{\text{Bragg}} = 6.1\%$, respectively. The magnetic reliability factors for the phase at 5 K are found to be $R_{\text{Mag}} = 19.2\%$ and 30.9% for the magnetic phases associated with the $\mathbf{k_0}$ and $\mathbf{k_1}$ propagation vectors, respectively.

60 K					
	$a = 5.7521(2)$ Å		$c = 12.1778(7)$ Å		
Atom	x	y	z	Occ.	B_{iso} (Å^2)
V1	$\frac{1}{3}$	$\frac{2}{3}$	$\frac{1}{4}$	1	0.3
Nb1	0	0	0	1	0.2(7)
Nb2	$\frac{1}{3}$	$\frac{2}{3}$	1.0046(9)	1	0.1(2)
S1	0.334(12)	0.012(4)	0.1271(3)	1	-0.10(15)
5 K					
	$a = 5.7519(2)$ Å		$c = 12.1768(5)$ Å		
Atom	x	y	z	Occ.	B_{iso} (Å^2)
V1	$\frac{1}{3}$	$\frac{2}{3}$	$\frac{1}{4}$	1	0.3
Nb1	0	0	0	1	0.4(4)
Nb2	$\frac{1}{3}$	$\frac{2}{3}$	1.0046(5)	1	0.6(2)
S1	0.333(5)	0.001(3)	0.1273(2)	1	0.08(7)

vanadium. For the same reason, the disorder over the vanadium sites was found to have little effect on the refinement, and so was not included in the fit. The thermal displacement parameter, B_{iso}, calculated from the fit was negative. This is not a physically possible result, though it should be noted that the negative displacement was very small and within error of a positive value.

Powder neutron diffraction measurements taken for temperatures between 5 and 52 K are displayed in Fig. 4.10(a). The data range shown is restricted to between 3 and 5.5 Å to better show the evolution of two of several of the magnetic Bragg peaks. Magnetic Bragg peaks become visible at temperatures around ≈ 47 K, near the ordering temperature. As the temperature decreases to 41 K, the Bragg peaks increase in intensity, culminating in a significant increase at temperatures between 37.5 and 41 K. Any further changes to the size or shape of the magnetic Bragg peaks below 20 K is marginal.

The data taken at 5 K using the WISH banks with an average 2θ value of 54° are shown in Fig. 4.10(b) along with the calculated fit in the models for nuclear and magnetic structures, which are refined in the fit as separate phases and discussed below. The refined atomic positions and their thermal displacement parameters are tabulated in Table 4.2. The data are consistent with the presence

Table 4.3: Atomic components of the basis functions localised on the 2c Wyckoff position of the $P6_322$ paramagnetic space group and transformed by the irreducible representations associated with $\mathbf{k_0} = (0,0,0)$ ($m\Gamma_2$ and $m\Gamma_5$) and $\mathbf{k_1} = (0,0,\frac{1}{3})$ ($m\Delta_1$ and $m\Delta_2$) propagation vectors.

Irrep	$V_1(\frac{1}{3},\frac{2}{3},\frac{1}{4})$	$V_2(\frac{2}{3},\frac{1}{3},\frac{3}{4})$
$m\Gamma_5$		
η_1	$(\frac{1}{3},\frac{2}{\sqrt{3}},0)$	$(-\frac{1}{2},-\frac{2}{\sqrt{3}},0)$
η_2	$(1,0,0)$	$(-1,0,0)$
$m\Gamma_2$		
δ	$(0,0,1)$	$(0,0,1)$
$m\Delta_1$		
ρ_1	$(0,0,\frac{1}{2})+i(0,0,-\frac{\sqrt{3}}{2})$	$(0,0,1)+i(0,0,0)$
ρ_2	$(0,0,\frac{\sqrt{3}}{2})+i(0,0,\frac{1}{2})$	$(0,0,0)+i(0,0,1)$
$m\Delta_2$		
ξ_1	$(0,0,\frac{\sqrt{3}}{2})+i(0,0,\frac{1}{2})$	$(0,0,0)+i(0,0,-1)$
ξ_2	$(0,0,-\frac{1}{2})+i(0,0,\frac{\sqrt{3}}{2})$	$(0,0,1)+i(0,0,0)$

of the $\mathbf{k_0} = (0,0,0)$ propagation vector, in agreement with a previous study [24] that reported $\mathbf{k_0}$ magnetic reflections for the magnetic structure of both $V_{1/3}NbS_2$ and $V_{1/3}TaS_2$. This magnetic propagation vector describes an exact repeat of the magnetic structure for every repeat of the nuclear unit cell. However, there is another set of reflections which cannot be accounted for using just this propagation vector. Indexing of these reflections, $(10\frac{5}{3})$ at 4.11 $\mathring{A}$ and $(01\frac{1}{3})$ at 4.95 $\mathring{A}$, requires a second propagation vector $\mathbf{k_1} = (0,0,\frac{1}{3})$. With the current data, it is not possible to unambiguously confirm whether these two propagation vectors belong to the same or different phases. However, the fact that both the $\mathbf{k_0}$ and $\mathbf{k_1}$ reflections appear at the same temperature [Fig. 4.10(a)], within the accuracy of the measurements, indirectly suggests that they originate from the same magnetic phase.

The $\mathbf{k_0}$ magnetic intensities can be fitted with a model consisting of ferromagnetic layers, antiferromagnetically coupled and stacked along the c axis [Fig. 4.11(a)] [24], in an example of A-type antiferromagnetism. This was deduced from the quantitative refinement of the neutron data, which found, via symmetry analysis, this magnetic structure the best fit out of the four possible irreducible representations. The refined moment extracted from this data and associated with this model is 0.90(5) μ_B, with the spins confined in the ab plane. The presence of a canting in the magnetic structure of the material due to a small ferromagnetic component along the c axis is consistent with the previously discussed dc magnetisation data [Figures 4.5 and 4.6], and has been suggested in previous literature [24]. However, the

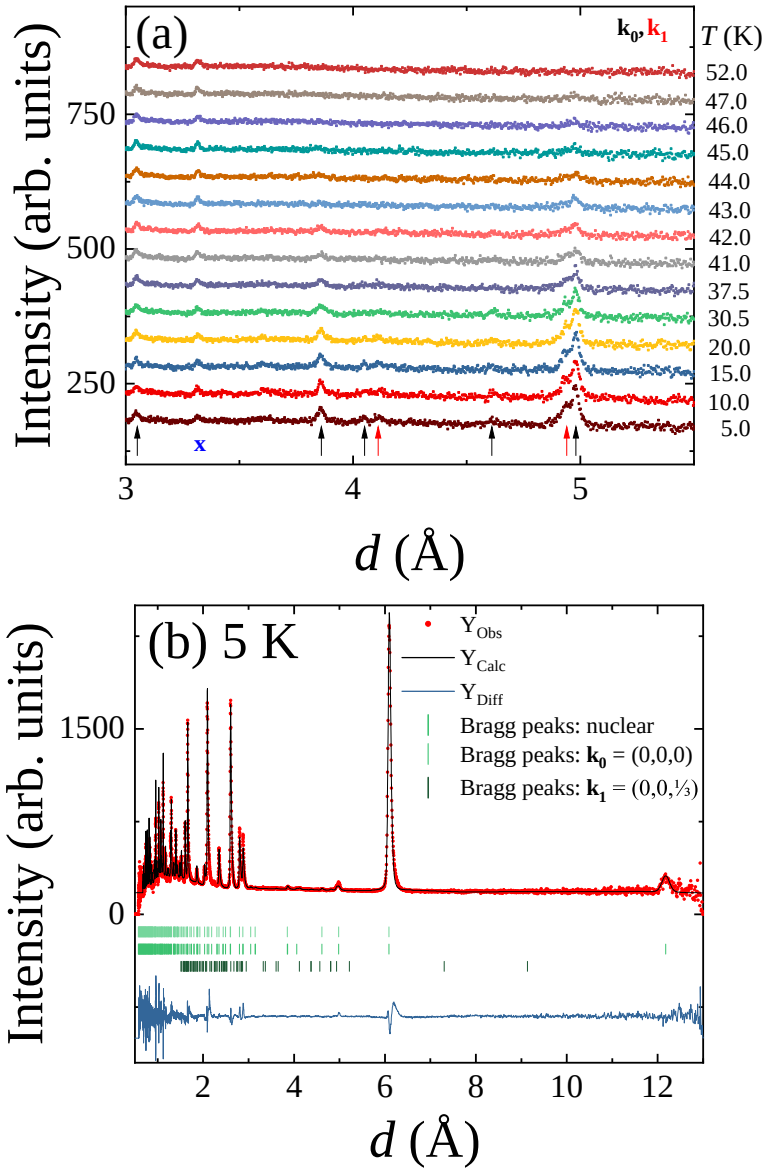

Figure 4.10: (a) Evolution of the powder neutron diffraction profiles with temperatures for $V_{1/3}NbS_2$ between 5 and 52 K. For clarity, each profile is offset by 50 units. The k_0 and k_1 magnetic peaks are marked with black and red arrows, respectively. A small impurity peak is marked with a blue x. (b) Powder diffraction profile at 5 K with a calculated fit using a hexagonal structure in space group $P6_322$ and magnetic components with propagation vectors $\mathbf{k_0} = (0, 0, 0)$ and $\mathbf{k_1} = (0, 0, \frac{1}{3})$. The Bragg positions for each phase are shown below the pattern.

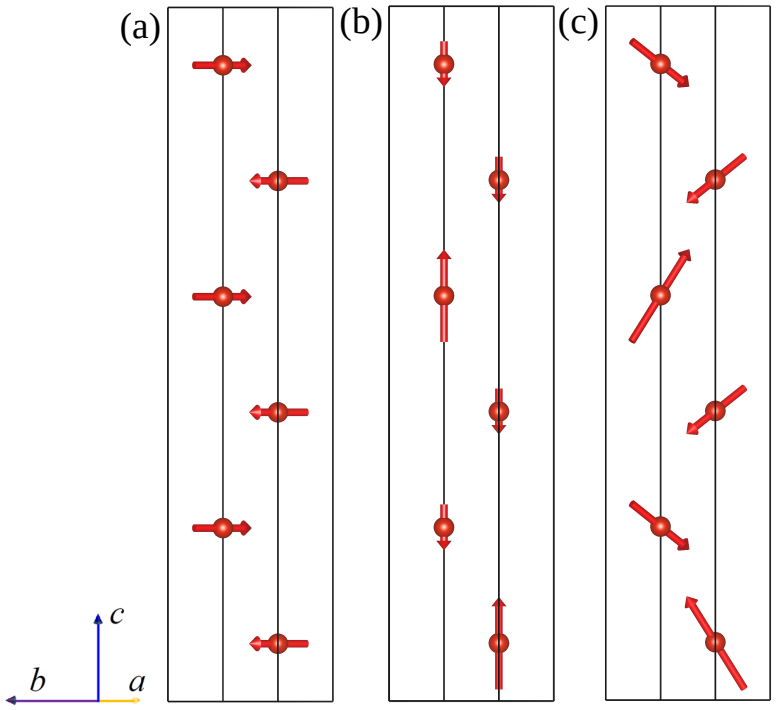

Figure 4.11: Magnetic moments on the vanadium atoms in a unit cell of $V_{1/3}NbS_2$ viewed along the a^* direction. (a) In-plane moments associated the $\mathbf{k_0} = (0, 0, 0)$ propagation vector, (b) the out-of-plane up-down-down moments associated with the $\mathbf{k_1} = (0, 0, \frac{1}{3})$ propagation vector and (c) the superposition of these two components.

origin of the coupling between the ferromagnetic and antiferromagnetic components requires particular consideration.

Typically, weak ferromagnets have their ferromagnetic and antiferromagnetic order parameters coupled via the bilinear free-energy invariant [72]. In the case of $V_{1/3}NbS_2$ however, the in-plane antiferromagnetic component is transformed by the two-dimensional irreducible representation $\mathrm{m}\Gamma_5(\eta_1, \eta_2)$ of the $P6_322$ space group while the out-of-plane ferromagnetic component is transformed by the $\mathrm{m}\Gamma_2(\delta)$ representation (Table 4.3) [123, 124]. This means that the two components are instead coupled via a linear-cubic term, $3\delta\eta_1^2\eta_2$-$\delta\eta_2^3$ [123]. This coupling is sensitive to the in-plane direction of the antiferromagnetic component, being allowed and maximal for the high symmetry order parameter direction $(0, \eta_2)$ corresponding to the magnetic space group $C2'2'2_1$ and the V spins parallel to the a axis, and vanishing for the $(\eta_1, 0)$ order parameter, corresponding to the magnetic space group $C222_1$ [124] and the case when the V spins are perpendicular to the a axis. Thus, based on the *dc* magnetisation data [Figures 4.5 and 4.6] and the symmetry arguments, one

can conclude that the $\mathbf{k_0}$ antiferromagnetic component in $V_{1/3}NbS_2$ is likely to be along the a axis. A similar coupling between in-plane antiferromagnetic and out-of-plane ferromagnetic components through the linear-cubic free-energy term has been recently discussed for the trigonal ruthenates Sr_3ARuO_6, with A =(Li, Na) [125]. It has been concluded that the microscopic interaction behind this coupling is the magneto-elastically induced antisymmetric Dzyaloshinskii–Moriya exchange. The magneto-elastic coupling is anisotropic and it depends on the in-plane direction of the spins. This breaks the degeneracy between the different in-plane antiferromagnetic configurations choosing a particular direction, which activates the additional antisymmetric energy term.

For the $\mathbf{k_1}$ component, the crucial observation is the absence of $(0, 0, l) \pm \mathbf{k_1}$ magnetic satellites, which strongly indicates that this spin component is along the c axis. The symmetry analysis based on representation theory [124], reveals two two-dimensional irreducible representations associated with $\mathbf{k_1}$ and transforming the out-of-plane spin component, $\mathrm{m}\Delta_1(\rho_1, \rho_2)$ and $\mathrm{m}\Delta_2(\xi_1, \xi_2)$ (Table 4.3). Both describe longitudinal spin density waves whose global magnetic phase is controlled by the order parameter direction (admixing coefficients ρ_1/ρ_2 and ξ_1/ξ_2). The difference between the $m\Delta_1$ and $m\Delta_2$ is the relative magnetic phase between the spin density waves localized on the two V sites. In the former case the difference is $\frac{\pi}{3}$ and in the latter case it is $\frac{2\pi}{3}$.

The quantitative refinement of the neutron diffraction data indicates that the $\mathrm{m}\Delta_2$ representation provides a better fitting quality [Fig. 4.10(b)]. It is well known that neutron diffraction is not sensitive to the global magnetic phase and therefore the order parameter direction cannot be experimentally determined in the $m\Delta_2$ representation space. The magnetic symmetry, however, depends on the global phase and this fact can provide additional information through various coupling phenomena controlled by the symmetry. In particular, a coupling of macroscopic ferromagnetic component along the c axis is possible when the order parameter takes the $(0, \xi_2)$ direction in the representation space. The relevant coupling term is similar to the one discussed above, $3\delta\xi_1^2\xi_2$-$\delta\xi_2^3$. The corresponding magnetic structure is up-down-down type with the $P6_32'2'$ magnetic space group [Fig. 4.11(b)]. The two moment values were refined as 1.21(12) μ_B (up) and 0.61(6) μ_B (down). The up and down spin components are not constrained by the symmetry to compensate one other, resulting in a net ferrimagnetic moment, which is, however, too small to be refined from the neutron diffraction data. Thus, the experimentally observed weak ferromagnetism [Figures 4.5 and 4.6] can also be explained by the small ferrimagnetic moment associated with the $\mathbf{k_1}$ component. It is possible that coupling between

the in-plane $\mathbf{k_0}$ and out-of-plane $\mathbf{k_1}$ magnetic order parameters takes place via the common ferromagnetic component shared by these order parameters in the scenario where both $\mathbf{k_0}$ and $\mathbf{k_1}$ belong to the same magnetic phase. In the latter case, the resultant magnetic space group which accounts for the presence of both propagation vectors [Fig. 4.11(c)] is $C2'2'2_1$ with the lattice vectors and origin related to the parent $P6_322$ paramagnetic space group as $(0,1,0)$, (-2,-1, 0), $(0,0,3)$ and $(0,0,0)$, respectively [124]. In this case, each moment is canted significantly out of plane, with the "down" vectors experiencing a cant of 34° out of plane and the "up" vectors being canted 55° degrees out of plane in the opposite direction.

Finally, let it be noted that the antisymmetrised square of both $\mathrm{m}\Gamma_5$ and $\mathrm{m}\Delta_2$ irreducible representations contain the vector representation. This implies that Lifshitz invariants [75] promoting inhomogeneous long-period modulated states are allowed in the free-energy decomposition. In particular, these types of invariants are responsible for the formation of magnetic helical state [126] and the field-induced chiral soliton lattice in $Cr_{1/3}NbS_2$ [127] as well as in some other systems with non-centrosymmetric crystal structures, such as MnSi [7], $Ca_3Ru_2O_7$ [128] and $BiFeO_3$ [129]. It is not clear why the commensurate ground state in $V_{1/3}NbS_2$ is robust against the chiral interactions behind the Lifshitz terms. A possible explanation is that the magneto-elastic coupling and associated anisotropic interactions discussed above are stronger and dominate in this compound.

4.9 Single crystal neutron diffraction

Extracting the magnetic structure from powder neutron diffraction measurements alone can be challenging. Single crystal neutron diffraction measurements were performed to confirm the suitability of the possible magnetic structures obtained from powder neutron diffraction.

The (010) peak was initially examined in the configuration for the $(hk0)$ scattering plane, in which case the magnetic field is applied parallel to the c axis. An example of the zero-field intensity maps at 1.5 and 300 K is given in Fig. 4.12(a). For clarity, in Fig. 4.12(b), a cut taken along $[01l]$ with 0.1 width in h is presented. The large out-of-plane coverage of the WISH detectors allowed data to be taken several degrees outside of this scattering plane along l. Peaks exist at $(01\frac{1}{3})$ and $(01\text{-}\frac{1}{3})$ that can be associated with the $\mathbf{k_1}$ magnetic propagation vector. Diffuse scattering is clearly visible between the (010) peak and the $(01\pm\frac{1}{3})$ peaks flanking it, and this scattering appears to be magnetic in nature, as it disappears above the transition temperature 50 K (see 300 K data inset). In Fig. 4.12(b) the line plot

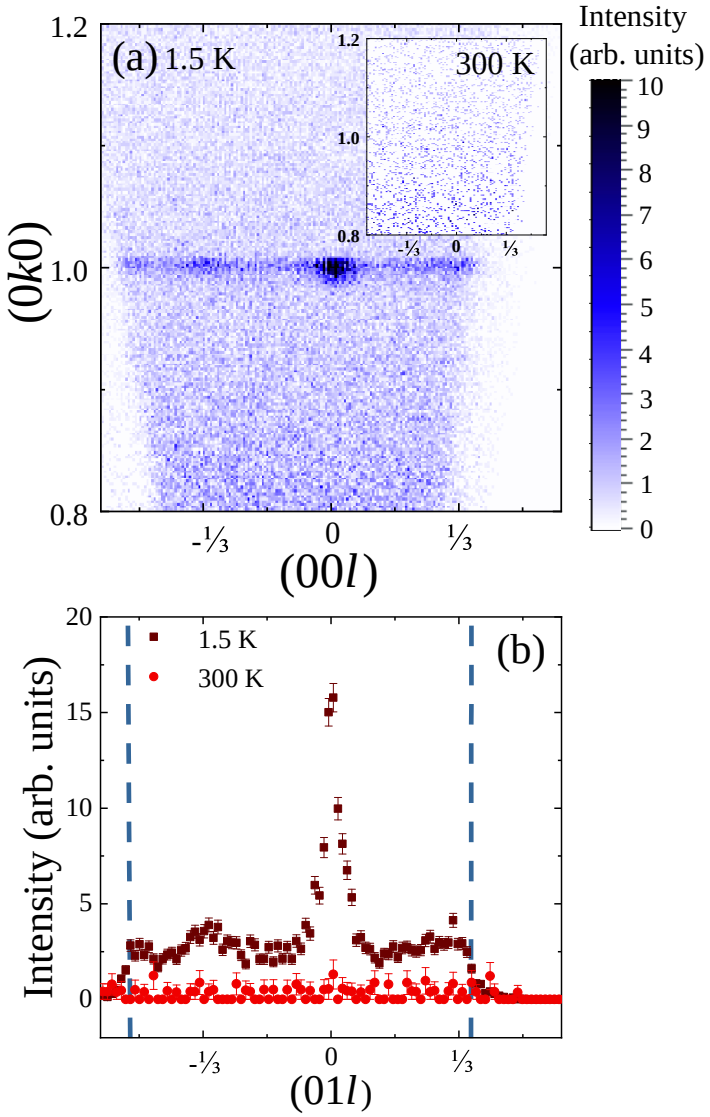

Figure 4.12: (a) Area detector image depicting the (010) and (01$\pm\frac{1}{3}$) Bragg peaks and the diffuse scattering between them, with $H \parallel c$. (b) Cut taken from the area detector image along [01l] at 1.5 and 300 K to compare the intensities of the peaks with the intensity of the diffuse scattering. The limits of the detector are shown as dashed blue lines.

of the (010) and (01$\pm\frac{1}{3}$) peaks shows more clearly that the latter two peaks exist above the diffuse scattering. This diffuse scattering implies the presence of a level of disorder to the magnetic structure, and appears between peaks that correspond to the $\mathbf{k_0}$ and $\mathbf{k_1}$ propagation vectors.

Figure 4.13 shows the integrated intensities of the peaks of interest for sev-

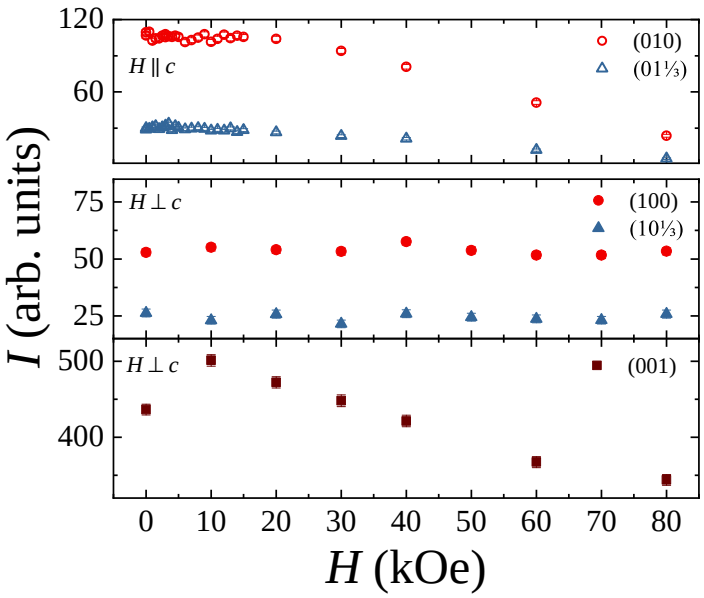

Figure 4.13: Integrated intensity of several different structural and magnetic peaks and their dependence on applied magnetic field. (Top) Field dependence of the integrated intensities of the (010) and $(01\frac{1}{3})$ peaks with the field directed $H \parallel c$. (Middle) Integrated intensities of the (100) and $(10\frac{1}{3})$ and (bottom) (001) peaks in the $(h0l)$ scattering plane with the field directed along [110].

eral different applied field strengths. The (001) peak was examined, and shows an increase in intensity upon the application of a magnetic field up to 1 T in strength, before steadily decreasing between 1 and 8 T in a manner consistent with antiferromagnetism. The magnetism of this peak can be associated with the magnetic propagation vector $\mathbf{k_0}$ and does not show the same behavior as the (100) and associated peaks.

The (100) peak in the $(h0l)$ scattering plane shows similar behavior to the (010) peak in the $(hk0)$ scattering plane at zero field, i.e. diffuse scattering exists that is no longer present above the magnetic transition temperature. A magnetic field scan, however, reveals that the (100) and (010) peaks evolve differently under the influence of an external magnetic field. The (010) and $(01\pm\frac{1}{3})$ peaks, under a magnetic field applied parallel to the c axis, begin to decrease in intensity as the magnetic field increases between 2 and 8 T. The (100) and $(10\pm\frac{1}{3})$ peaks, however, do not change significantly in intensity for an applied field along the [110] direction between 0 and 8 T. This must be related to the direction of the applied field as these two peaks are equivalent for a hexagonal system.

Figure 4.14 displays the temperature dependence of the integrated intensities

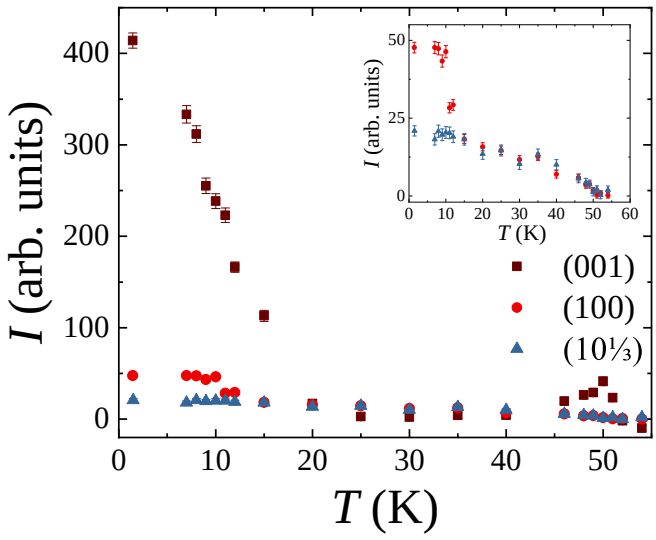

Figure 4.14: Integrated intensity of several different structural and magnetic peaks and their dependence on temperature. The integrated intensities of the (100) and $(10\frac{1}{3})$ and (001) peaks between 1.5 and 54 K are plotted on the same axes. The inset depicts the region of interest for the (100) and $(10\frac{1}{3})$ peaks.

of certain Bragg peaks in the $(h0l)$ scattering plane. While the $(10\pm\frac{1}{3})$ peaks show a steady decrease in intensity as the temperature increases, the (100) and (001) peaks show a sharper decrease in intensity between 10 and 20 K, which coincides with the additional transition visible in the *dc* susceptibility data in Fig. 4.5 and the *ac* susceptibility data in Fig. 4.7. It is worth noting that the (100) and $(10\frac{1}{3})$ peaks sit on a background of diffuse scattering that was not present around the (001) peak.

The (001) peak intensity at temperatures below 20 K is far greater than the corresponding intensities of the (100) and $(10\frac{1}{3})$ peaks. It then drops to approximately zero between 20 and 50 K, which is considerably lower than the corresponding (100) and $(10\frac{1}{3})$ peak intensities, before briefly increasing in intensity at the ordering temperature. The behavior of the (001) peak is remarkably reminiscent of the behavior seen in the *ac* and *dc* susceptibility data for H applied perpendicular to the c-axis in Figs. 4.5 and 4.7. This implies highly anisotropic behaviour and that the magnetic moment is suppressed at these temperatures for certain field directions.

4.10 Summary

In summary, the magnetic structure of $V_{1/3}NbS_2$ has been investigated using *dc* susceptibility, heat capacity, and powder and single crystal neutron diffraction measurements. $V_{1/3}NbS_2$ is found to undergo a magnetic transition at $T_N = 50$ K, with magnetic field scans revealing that the moment does not saturate at magnetic fields up to 10 T. Heat capacity measurements were also used to further characterise the evolution of $V_{1/3}NbS_2$ with temperature.

The powder neutron diffraction data reveals the presence of two magnetic propagation vectors, $\mathbf{k_0} = (0, 0, 0)$ and $\mathbf{k_1} = (0, 0, \frac{1}{3})$, which correspond to magnetic structures with antiferromagnetic stacking of vanadium layers with a refined moment of 0.90(5) μ_B and a canting along the c axis in an up-down-down configuration with refined moments of 1.21(12) and 0.61(6) μ_B, respectively. This explains the lack of saturation that is observed in the *dc* magnetisation even in magnetic fields of 10 T, as well as the sharp increase of the *dc* susceptibility at 50 K in the FCC measurements. The presence of the $\mathbf{k_1}$ propagation vector opens the possibility of the expected ferromagnetic canting along the c axis originating from this propagation vector rather than from the $\mathbf{k_0}$ propagation vector as proposed earlier [24]. Both $\mathbf{k_0}$ and $\mathbf{k_1}$ magnetic components are capable of coupling with an out-of-plane ferromagnetic moment consistent with magnetisation data.

Analysis of the single crystal neutron diffraction data reveals diffuse magnetic scattering between the (010) and (01$\pm\frac{1}{3}$) Bragg peaks, indicating a level of disorder in the magnetic structure of $V_{1/3}NbS_2$. Additionally, the magnetic structure seems to be highly anisotropic, with the integrated intensity of the Bragg peaks dependent on the direction of the applied magnetic field - remaining constant in intensity between 0 and 8 T for H in the ab-plane, or decreasing in intensity with increasing field for H parallel to the c axis.

The study here, adopting a multi-technique approach, has shown that the material $V_{1/3}NbS_2$ has a complex magnetic structure that is very different to the magnetism previously observed in other members of this family such as $Mn_{1/3}NbS_2$, and the CSL observed in $Cr_{1/3}NbS_2$. Due to the nature of the canted antiferromagnetic ordering in this material, it seems unlikely that a CSL phase can be induced. In showing the existence of a secondary, mostly diffuse, component to the magnetic structure associated with the $\mathbf{k_1}$ propagation vector, greater detail has been uncovered about the magnetic structure of this material.

Chapter 5

A comparative study of the magnetic properties of $Mn_{1/3}NbS_2$, $Cr_{1/3}NbS_2$, and $Cr_{1/3}TaS_2$

5.1 Introduction

In select chiral helimagnetic materials, applying an external magnetic field perpendicular to the helical axis stabilizes spin structures such as skyrmions [8] or a chiral soliton lattice (CSL) [3, 46], as discussed in Section 2.5. One known CSL host is $Cr_{1/3}NbS_2$, a member of a family of hexagonal layered transition metal dichalcogenides (TMDs) intercalated with $3d$ transition metals that occupy octahedral $2c$ or $2d$ Wyckoff positions [37] between the trigonal prismatic layers. The layers are bonded by weak van der Waals forces, allowing for easy 'twisting' of layers relative to each other, causing the common stacking faults that are observed in these materials.

$Cr_{1/3}NbS_2$ is a well-studied material that displays a helical magnetic ground state below its magnetic ordering temperature $T_C = 127 - 130$ K [127, 130, 131, 4]. Disorder effects in this material have been shown to suppress the magnetic transition temperature to values as low as $T_C = 88$ K [132]. It has a 48 nm helical pitch in zero field, which increases as the helix continuously transforms into the CSL on application of an external field perpendicular to the c axis. The CSL and other novel magnetic textures [3, 133, 18, 134, 135, 136] can be imaged using Lorentz transmission electron microscopy (LTEM).

The phase diagram of $Cr_{1/3}NbS_2$ under an external magnetic field applied

parallel to the *ab* plane indicates the presence of five magnetic states: paramagnetism at temperatures above the transition temperature, chiral helimagnetism as the magnetic ground state, a highly-helical CSL phase (CSL–1), a highly-ferromagnetic CSL phase (CSL–2), and at high enough magnetic field a region of field polarised forced ferromagnetism aligned with the external magnetic field [130]. Additionally, if instead the external magnetic field is applied parallel to the *c* axis of the material, a chiral conical magnetic phase is produced, while at most oblique fields directed at the material there is a tilted CSL phase produced [137, 5]. Some form of CSL phase is, therefore, stabilized for a large number of external field magnitudes and directions, which is an exciting prospect for device applications.

Recently, $Cr_{1/3}TaS_2$ has been shown to form a CSL phase, showing that $Cr_{1/3}NbS_2$ is not unique among the intercalated TMDCs in exhibiting this phenomenon [26, 138]. Additionally, $Mn_{1/3}NbS_2$ has been reported as being chiral helimagnetic [139] with an ordering temperature of $T_C = 45$ K and a more recent study using neutron diffraction suggests that it was possible that $Mn_{1/3}NbS_2$ was either a ferromagnet with a small domain size of 250 nm along the *c* axis or a helimagnet with a modulation size far larger than the one found in $Cr_{1/3}NbS_2$ [22].

A combination of powder neutron diffraction and heat capacity measurements have been used to suggest a change in the magnetic ordering in the material below 20 K. A magnetic field – temperature phase diagram constructed from hysteresis in magnetization measurements suggests that $Mn_{1/3}NbS_2$ might be helimagnetic at temperatures under 20 K [23]. Recent Lorentz transmission electroscopy (LTEM) measurements of $Mn_{1/3}NbS_2$ [23] were used to support this conclusion. The 3D Heisenberg model has been applied to $Mn_{1/3}NbS_2$ and the magnetic moments were found to be short-range and isotropic, allowing for coupling both within the *ab* plane and to the *c* axis [140].

In this chapter, a detailed investigation of the magnetic properties of the single crystals of $Cr_{1/3}NbS_2$, $Cr_{1/3}TaS_2$, and $Mn_{1/3}NbS_2$ is presented, using *ac* and *dc* susceptibility, as well as LTEM measurements, to probe any differences between the magnetic structures of these materials. These magnetic measurements show $Cr_{1/3}NbS_2$ and $Cr_{1/3}TaS_2$ display chiral helimagnetism below its magnetic ordering temperature (T_C) of 111 K and 120 K respectively, while there is no evidence that $Mn_{1/3}NbS_2$ exhibits helimagnetic ordering below its transition temperature $T_C = 45$ K. Establishing the correct structural space group in these crystals can often prove difficult with just single crystal x-ray diffraction techniques. Here, it is shown how it is possible to unambiguously distinguish between the centrosymmetric and non-centrosymmetric structures in a detailed structural investigation of

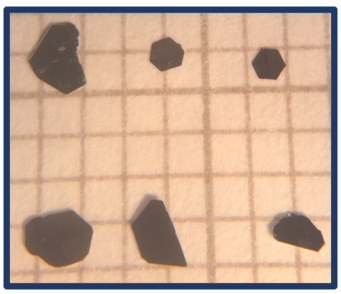

Figure 5.1: Single crystals of $Cr_{1/3}NbS_2$ on mm paper.

these materials using electron and single crystal x-ray diffraction measurements, which also indicate how substitutional disorder and stacking faults can manifest in $Cr_{1/3}NbS_2$, $Cr_{1/3}TaS_2$ and $Mn_{1/3}NbS_2$, and give rise to additional superlattice reflections in diffraction patterns acquired from $Mn_{1/3}NbS_2$.

5.2 $Cr_{1/3}NbS_2$

5.2.1 Sample preparation

Polycrystalline and single crystal samples of $Cr_{1/3}NbS_2$ were prepared using the processes detailed in Section 3.1, i.e. with a solid state reaction within a box furnace quenched in cold water from 950 °C, and with chemical vapour transport (CVT) using the polycrystalline powder as a seed and iodine as a transport agent, respectively. 5 g of polycrystalline powder was synthesised, and 2.5 g was used during the CVT crystal growth process. Some of the crystals synthesised in this process are displayed on mm paper in Fig. 5.1. The size of the crystals varied from sub-mm in length and thickness, to approximately $2.0 \times 1.5 \times 0.2$ mm^3.

5.2.2 X-ray diffraction

Several different x-ray diffraction techniques were used to probe the structure of synthesised $Cr_{1/3}NbS_2$ polycrystalline and single crystal material.

Laue diffraction

A Laue diffraction pattern was obtained along the c axis of a $Cr_{1/3}NbS_2$ crystal [see Fig. 5.2]. A high number of diffraction spots are found to be ill-defined, indicating a high level of stacking faults, i.e. rotation of layers in the material relative to each other, present in the crystals measured.

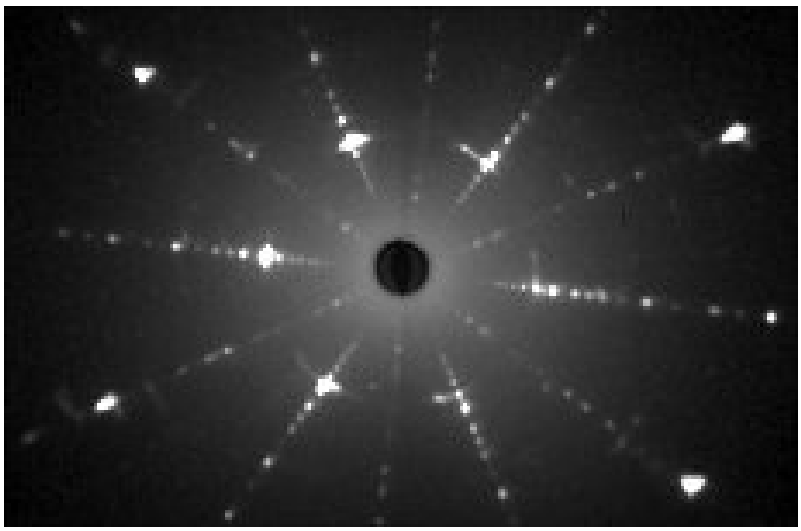

Figure 5.2: Laue backscattered reflection pattern along the [001] orientation of a $Cr_{1/3}NbS_2$ crystal.

Single crystal x-ray diffraction

To distinguish the non-centroymmetric $M_{1/3}NbS_2$ materials, in the space group $P6_322$, from the centrosymmetric $M_{1/4}NbS_2$ materials in the space group $P6_3/mmc$, structural investigation techniques such as single crystal x-ray diffraction are necessary.

A representation of the model derived from single crystal x-ray diffraction data taken at room temperature for $Cr_{1/3}NbS_2$ is shown in Fig. 5.3. This material was well-modelled in the non-centrosymmetric space group, with excellent agreement between the calculated and observed structure factors. Comparatively, modelling the structure in the centrosymmetric space group $P6_3/mmc$ provides a significantly worse fit and a less simple structural model. The Flack parameter was found to be ambiguous and so an inversion twin law is employed in the refinement for completeness for which the twin component scale factor refines to effectively zero [0.1(6)], though with a very high associated error. A small proportion of disorder was found over the main Cr site (occupancy 0.952(2)) and site "i" (occupancy 0.048(2)). The values for extracted from the single crystal x-ray diffraction measurements are displayed in Table 5.1.

5.2.3 Electron diffraction

Figure 5.4 shows bright-field images and electron diffraction patterns acquired from $Cr_{1/3}NbS_2$ at room temperature and viewed along the [100] direction. Figure 5.4(a)

Table 5.1: Atomic positions and occupancies for $Cr_{1/3}NbS_2$

$Cr_{1/3}NbS_2$ ($P6_322$)

$a = 5.7396(2)$ Å $\quad c = 12.1325(3)$ Å $\quad R_1 = 2.58\%$ $\quad wR_2 = 5.48\%$ $\quad$ Flack $= 0.1(6)$

Atom	Wyckoff	x	y	z	Occ.
Cr1	$2c$	$\frac{1}{3}$	$\frac{2}{3}$	$\frac{1}{4}$	0.952(2)
Nb1	$2a$	0	0	0	1.00
Nb2	$4f$	$\frac{1}{3}$	$\frac{2}{3}$	0.99735(2)	1.00
S1	$12i$	0.33246(7)	-0.00030(8)	0.13058(3)	1.00
Cr2	$2b$	0	0	$\frac{1}{4}$	0.048(2)

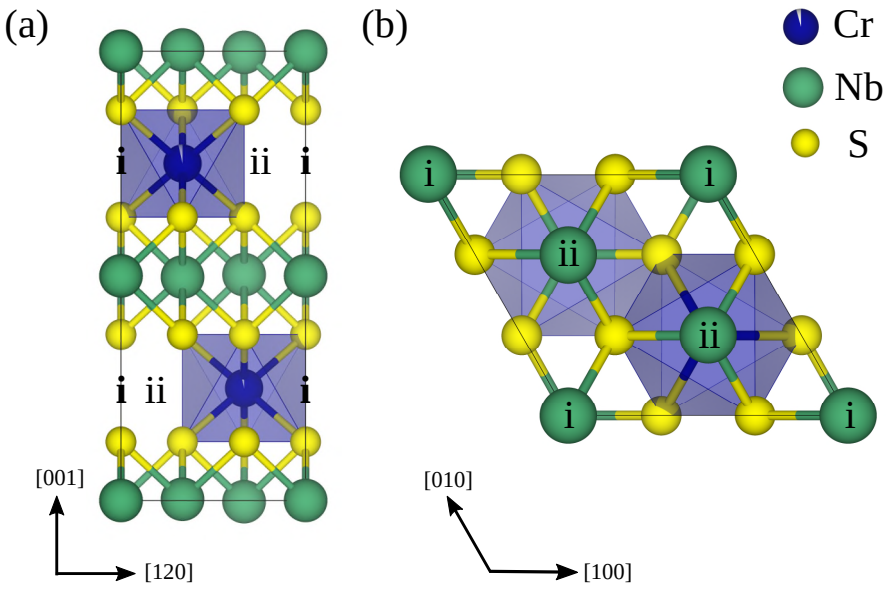

Figure 5.3: Crystal structure of $Cr_{1/3}NbS_2$ viewed along (a) the a axis and (b) the c axis, with S atoms shown in yellow, Nb atoms shown in green, and Cr atoms shown in blue. The occupancy of the intercalated sites is reflected by the proportion of the site shown in blue. The octahedral sites of the 2c Wyckoff position are shown by blue polyhedra. The projection of the 2b and 2d sites as seen from each direction are indicated using i and ii, respectively.

shows the arrangement of atoms expected in this orientation and Fig. 5.4(b) shows a simulated kinematic diffraction pattern. The experimental diffraction patterns were taken from regions 670 nm in diameter. The pattern for $Cr_{1/3}NbS_2$ shown in Fig. 5.4(c) is consistent with the simulation. Bragg reflections at (00l) are kinematically forbidden when l is odd but these appear in the experimental pattern because electrons are scattered multiple times as they pass through the specimen.

5.2.4 *dc* susceptibility and magnetisation

The *dc* magnetization of $Cr_{1/3}NbS_2$ was measured at temperatures between 5 and 300 K with a field of 0.01 T applied either parallel or perpendicular to the c axis, (see Fig. 5.5). In the paramagnetic state, the data were isotropic and could be fitted using the Curie-Weiss law. For *dc* field $H \perp c$ the Weiss temperature of +109(2) K for $Cr_{1/3}NbS_2$ indicated that the interactions between the magnetic ions are ferromagnetic. In the ordered state, the large difference between the magnitude of the susceptibility when the field is applied parallel or perpendicular to the c axis

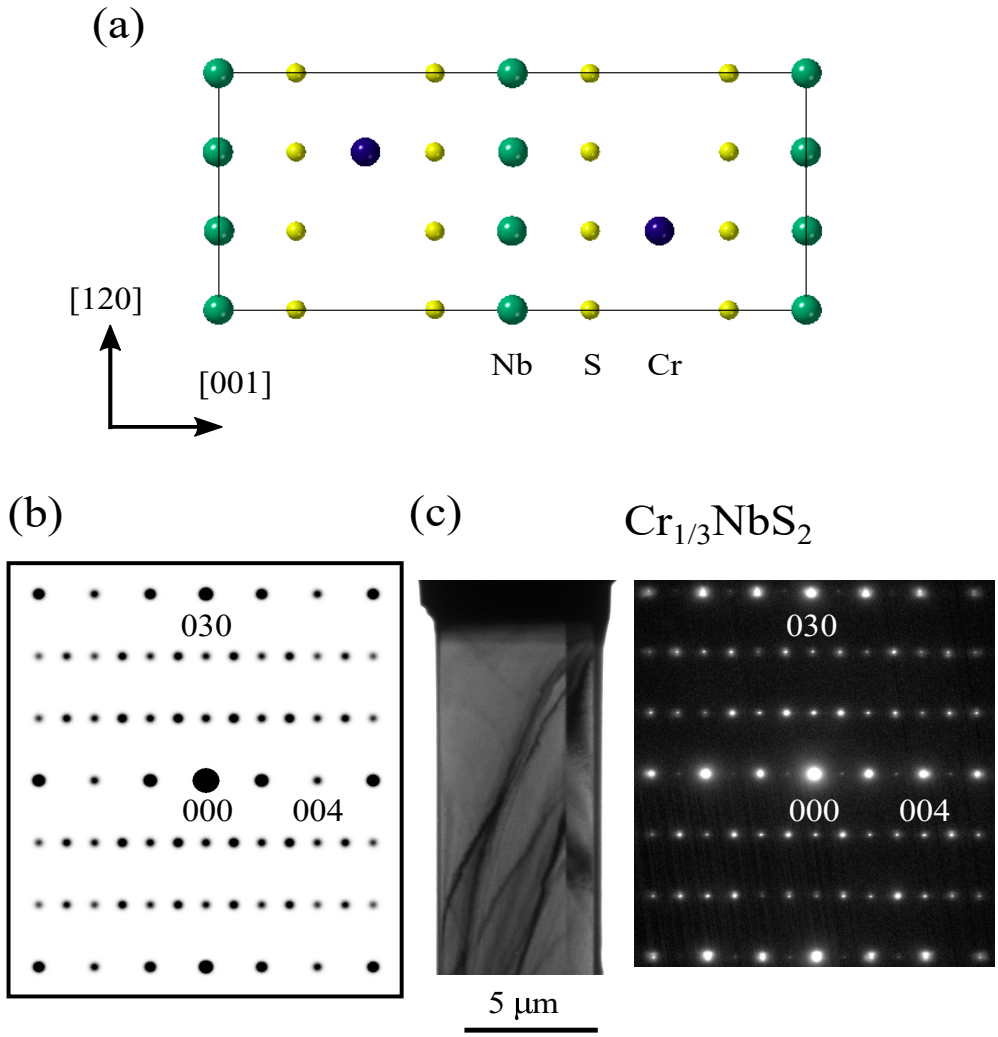

Figure 5.4: (a) The unit cell of $Cr_{1/3}NbS_2$ viewed along [100] direction. (b) A simulation of the corresponding electron diffraction pattern. (c) Bright-field images and electron diffraction patterns from $Cr_{1/3}NbS_2$. The $Cr_{1/3}NbS_2$ pattern matches well with the simulation.

shows that the ordered moments strongly prefer to lie in the *ab* plane and that this material is highly anisotropic.

For $Cr_{1/3}NbS_2$, the effective magnetic moment, calculated from the Curie-Weiss law, $\mu_{\text{eff}} = 3.94(13)\ \mu_B/\text{Cr}$ for $H \perp c$ is within error of the quenched spin-only Cr^{3+} ($3.87\ \mu_B/Cr^{3+}$). An earlier report states that the Cr ions can adopt different valence states in this material [141], with the majority of the ions being Cr^{3+} but with regions in the material where the helical order is broken and the ions instead adopt the Cr^{4+} ($2.83\ \mu_B/Cr^{4+}$) valence.

Figure 5.5 shows that the single crystals of $Cr_{1/3}NbS_2$ order magnetically at

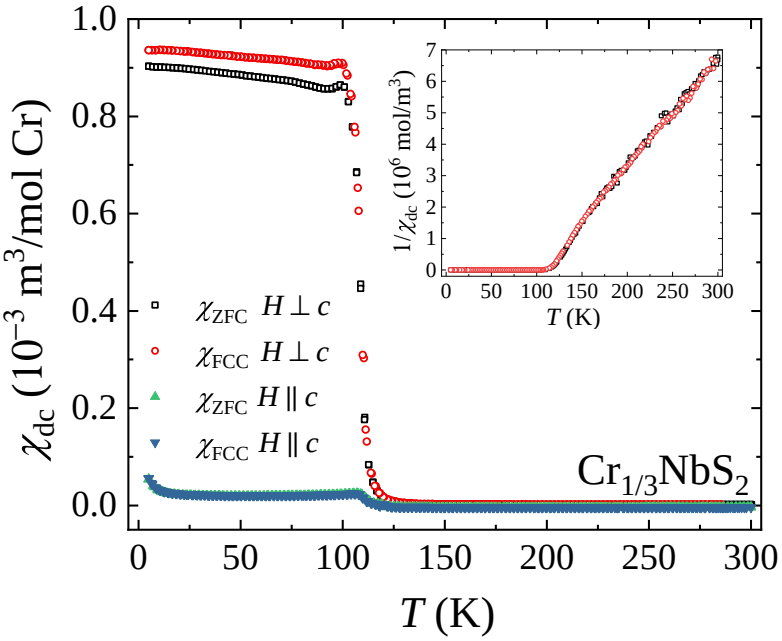

Figure 5.5: Temperature dependence of the *dc* susceptibility $\chi_{dc}(T)$, collected in zero-field-cooled (ZFC) warming and field-cooled cooling (FCC) modes, for $Cr_{1/3}NbS_2$ in an applied field of 10 mT. It is clear from the large difference between the susceptibility for each field direction that this is a highly anisotropic material, with the *ab* plane as the easy plane. An inset shows the inverse ZFC and FCC susceptibility with $H \perp c$, measured in an applied field of 33 mT to increase the signal in the paramagnetic state.

111 K, which is lower than the reported 130 K transition temperature, which can be attributed to a degree of substitutional disorder [132]. This disordered state is a possible interpretation of the single crystal diffraction data taken for $Cr_{1/3}NbS_2$. Additionally, a peak in $\chi(T)$ appears close to the transition temperature, and has been previously modeled with the chiral XY model and attributed to a commensurate-incommensurate magnetic transition [142, 143, 139].

Figure 5.6(a) displays the *dc* magnetisation versus applied field measurements for $Cr_{1/3}NbS_2$ at several temperatures. It is immediately clear that the magnetisation of the $Cr_{1/3}NbS_2$ sample studied here saturates at lower magnetic fields than those reported in Ref. [127]. This is consistent with the *ac* susceptibility measurements displayed in the next section. The first derivative of the magnetization with respect to field at 60 and 90 K [Fig. 5.6(b)] can be compared with Fig. 5.7(b), with features in dM/dH marking the various phase boundaries appearing at fields that are in good agreement with the values extracted from the *ac* susceptibility data.

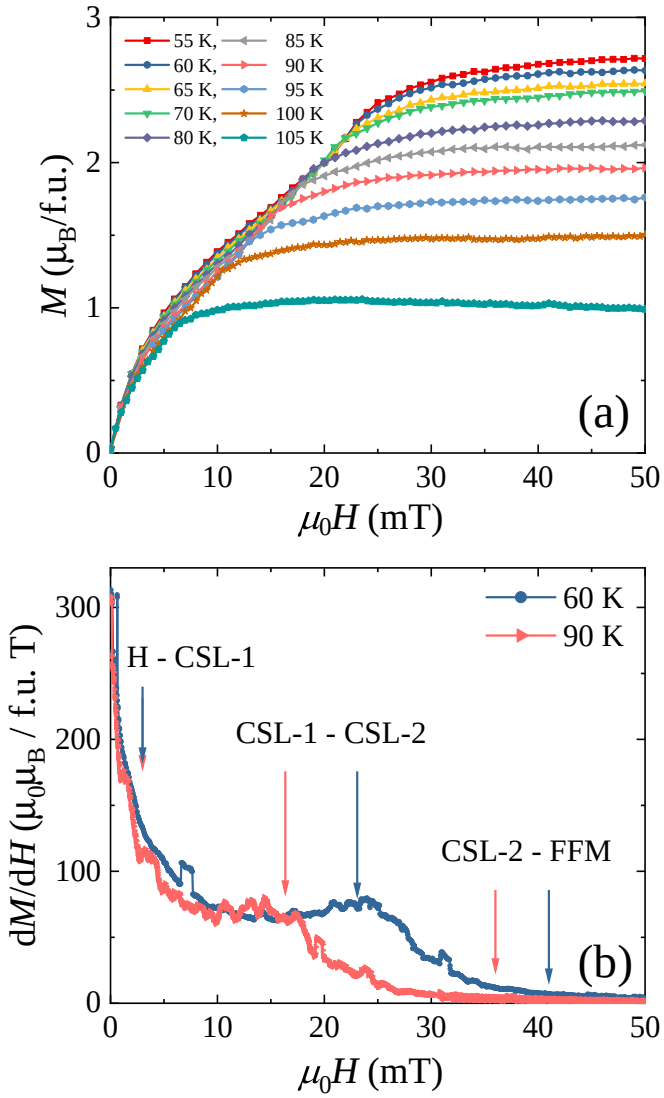

Figure 5.6: (a) Magnetization M as a function of magnetic field H directed perpendicular to the c axis for different temperatures and (b) dM/dH versus magnetic field at 60 and 90 K, for $Cr_{1/3}NbS_2$. The magnetic phase boundaries are marked with either blue (60 K) or red (90 K) arrows.

5.2.5 *ac* susceptibility

Figure 5.7 shows the in-phase component of the *ac* susceptibility χ' and its first derivative with respect to the *dc* magnetic field $d\chi'/dH$, as a function of magnetic field H for $Cr_{1/3}NbS_2$ at 60 and 90 K. Here, an *ac* field of 113 Hz with an amplitude of 0.3 mT was applied perpendicular to the c axis of the crystal. For $Cr_{1/3}NbS_2$, a

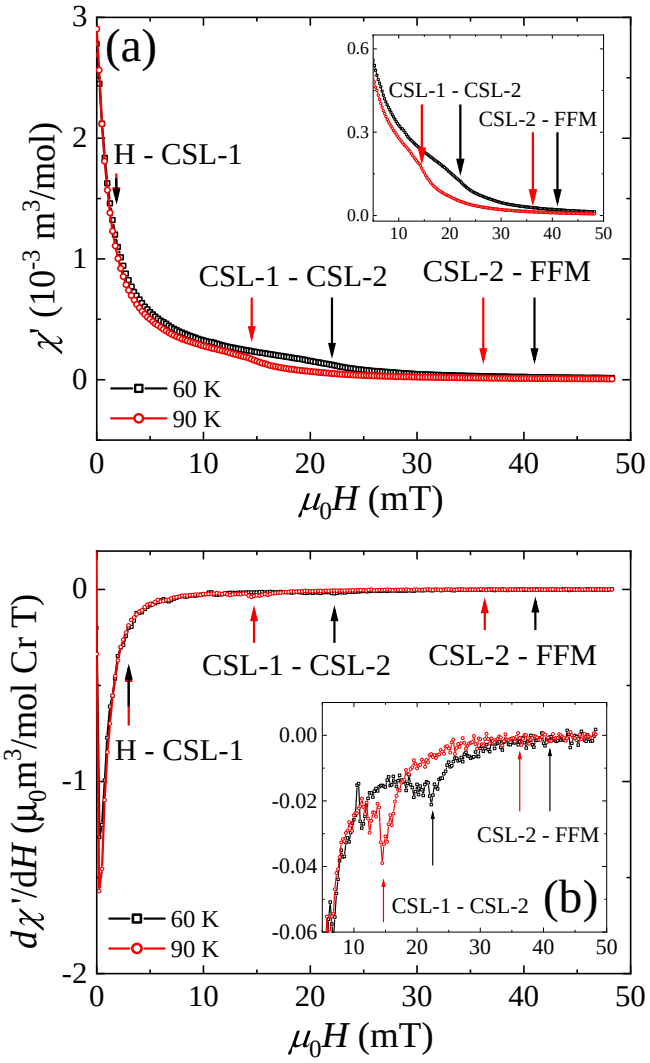

Figure 5.7: (a) In-phase component of the *ac* susceptibility χ' as a function of *dc* field H directed perpendicular to the c axis and (b) $d\chi'/dH$ versus *dc* field H at 60 and 90 K for $Cr_{1/3}NbS_2$. Insets show the same data between 5 and 50 K. The features used to define magnetic phase boundaries are marked by the arrows. All the measurements were performed in an *ac* field of 0.3 mT at a frequency of 113 Hz.

dramatic fall in $\chi'(H)$ with increasing H marks the boundary between the helimagnetic ground state and the chiral soliton lattice (CSL) phase, while a drop in $\chi'(H)$ (evident as a shallow minimum in $d\chi'/dH$) is present at the crossover from the helicity-rich CSL-1 phase to the more ferromagnetic CSL-2 phase [See Figs. 5.7(a) and 5.7(b)]. This drop is more obvious at 90 K, but is still present at 60 K. The

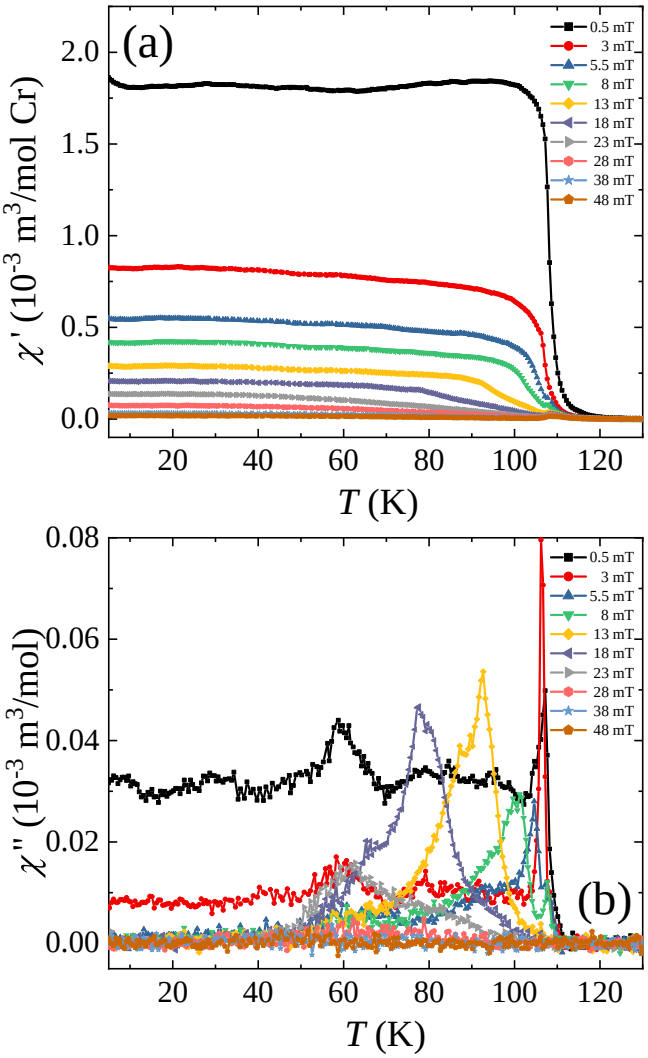

Figure 5.8: Temperature dependence of the *ac* susceptibility $\chi(T)$ in different *dc* magnetic fields applied perpendicular to the *c* axis of single crystals of $Cr_{1/3}NbS_2$. (a) In-phase component of the *ac* susceptibility $\chi'(T)$ and (b) out-of-phase component of the *ac* susceptibility $\chi''(T)$ for $Cr_{1/3}NbS_2$. All the measurements were performed using an *ac* field of 0.3 mT at 113 Hz.

transition from the CSL-2 to the field polarized, or forced ferromagnetic (FFM) state is harder to locate, and the boundary was chosen at the point where the susceptibility ceases to change significantly with field ($d\chi'/dH = 0$). This is due to the fact that the material is saturated at the point when it enters into this state, and so an obvious anomaly in the data is not expected to mark this transition.

Fig. 5.8 shows *ac* susceptibility versus temperature scans in different *dc* fields for $Cr_{1/3}NbS_2$. The transition from the paramagnetic to an ordered state is marked by an increase in $\chi'(T)$ that occurs at an almost fixed temperature with increasing *dc* magnetic field. This increase in $\chi'(T)$ evolves into a peak, that is clearest in the $Cr_{1/3}NbS_2$ sample at 13 mT, followed by a shoulder that shifts to lower temperatures as the applied *dc* magnetic field is increased.

In low *dc* magnetic fields, in the helimagnetic phase of $Cr_{1/3}NbS_2$, a large signal in $\chi''(T)$ is visible at all temperatures. This low-temperature component subsides when the CSL-1 and CSL-2 states are entered leaving a peak in $\chi''(T)$ which shifts to lower temperatures with increasing *dc* field as the CSL-1 and CSL-2 phase boundaries are crossed and disappears in fields above 23 mT. The features in $\chi''(T)$ match well with the temperature at which the shoulder is visible in $\chi'(T)$.

The magnetic field - temperature phase diagrams for $Cr_{1/3}NbS_2$, constructed using *ac* susceptibility versus field measurements at fixed temperatures, similar to those shown in Fig. 5.7, are displayed in Fig. 5.9. The temperatures of the transitions from a paramagnetic to a magnetically ordered state are in good agreement with those obtained from *dc* susceptibility. The transitions present in the ordered state for $Cr_{1/3}NbS_2$ occur at significantly lower magnetic fields than previously reported [130]. This highlights the sensitivity of the magnetic response of these materials to disorder [132].

Five different magnetic phases can be seen in the $Cr_{1/3}NbS_2$ material [Figs. 5.9(a) and 5.9(b)], which correspond well to the helimagnetic (H), CSL-1, CSL-2, forced ferromagnetic (FFM), and paramagnetic (PM) phases established in previous literature [130]. The helical phase coincides with a maximum in χ' at zero field. χ' initially falls rapidly under the application of a *dc* magnetic field. Clear changes in χ' and/or $d\chi'/dH$ delineate the other phase boundaries. There is also a significant increase in the imaginary susceptibility at low fields, at all temperatures up to the onset of magnetic order at 111 K. This is further evidence for the chiral helimagnetic state in $Cr_{1/3}NbS_2$. χ'' also shows a large pocket of intensity that begins just below the ordering temperature in low *dc* magnetic fields and extends in an arc up to 25 mT at 60 K. This feature is reduced in intensity at higher frequencies. There are several possible reasons for this feature. For example, the creation and destruction of novel phenomena such as the CSL. Alternatively, this signal could be explained by effects such as domain wall motion and pinning by defects, which are especially prevalent in layered materials like these.

The changes in $\chi(T)$ with frequency for $Cr_{1/3}NbS_2$ are investigated in Fig. 5.10. The data were collected in a *dc* field of 13 mT in order to cut through the maximum

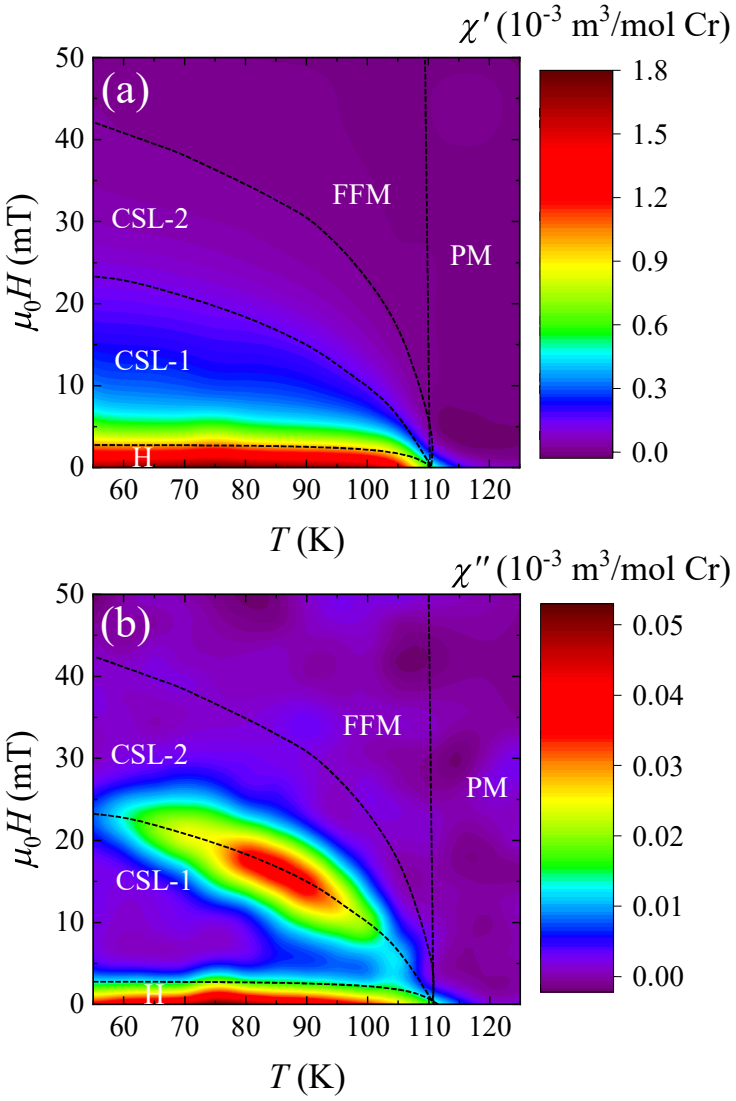

Figure 5.9: (a) In-phase χ' and (b) out-of-phase χ'' components of the *ac* susceptibility of $Cr_{1/3}NbS_2$ as a function of temperature and *dc* applied field. For both measurements, the *ac* and *dc* magnetic fields were applied perpendicular to the *c* axis. Guides to the eye have been added to the phase diagrams based on features present in the data to distinguish separate phases: the helimagnetic (H), high-helicity CSL-1, highly ferromagnetic CSL-2, forced ferromagnetic (FFM), and paramagnetic (PM) phases (as discussed in the text).

in $\chi''(T)$ in the H - T phase diagram and cross several potential phase boundaries (see Fig. 5.9). There was no frequency dependence in $\chi'(T)$ at the transition from the paramagnetic to the FFM state and the losses in the out-of-phase channel $\chi''(T)$ at this transition are small. For $Cr_{1/3}NbS_2$ there is a rapid upturn in $\chi'(T)$ and a

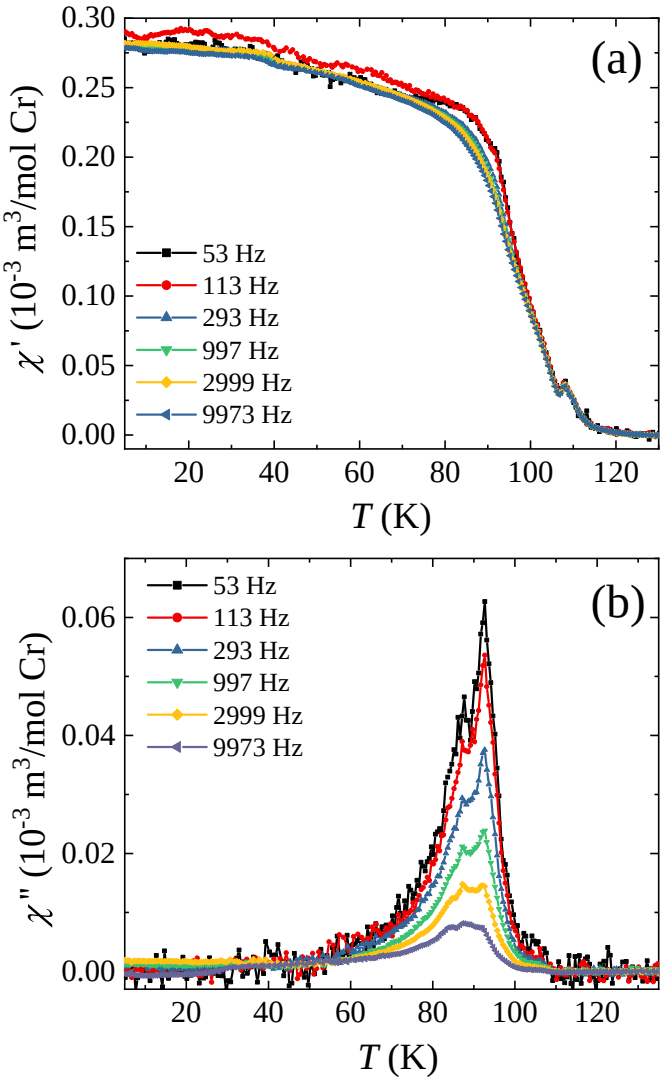

Figure 5.10: Temperature dependence of the *ac* susceptibility $\chi(T)$ at various *ac* frequencies for $Cr_{1/3}NbS_2$ in a *dc* field of 13 mT. The in-phase susceptibility $\chi'(T)$ is displayed in (a) and the out-of-phase susceptibility $\chi''(T)$ is displayed in (b).

clear shoulder that is suppressed with increasing frequency on entering the CSL-2 and CSL-1 phases. The temperature of the shoulder coincides with a peak in $\chi''(T)$.

For $Cr_{1/3}NbS_2$, the losses reflected in $\chi''(T)$ are located around the CSL-I and CSL-II phases boundaries [See Fig. 5.9(b)]. There are two peaks in $\chi''(T)$ that are suppressed with increasing frequency but remain at fixed temperatures. Below 60 K, $\chi''(T)$ is small and independent of temperature and frequency.

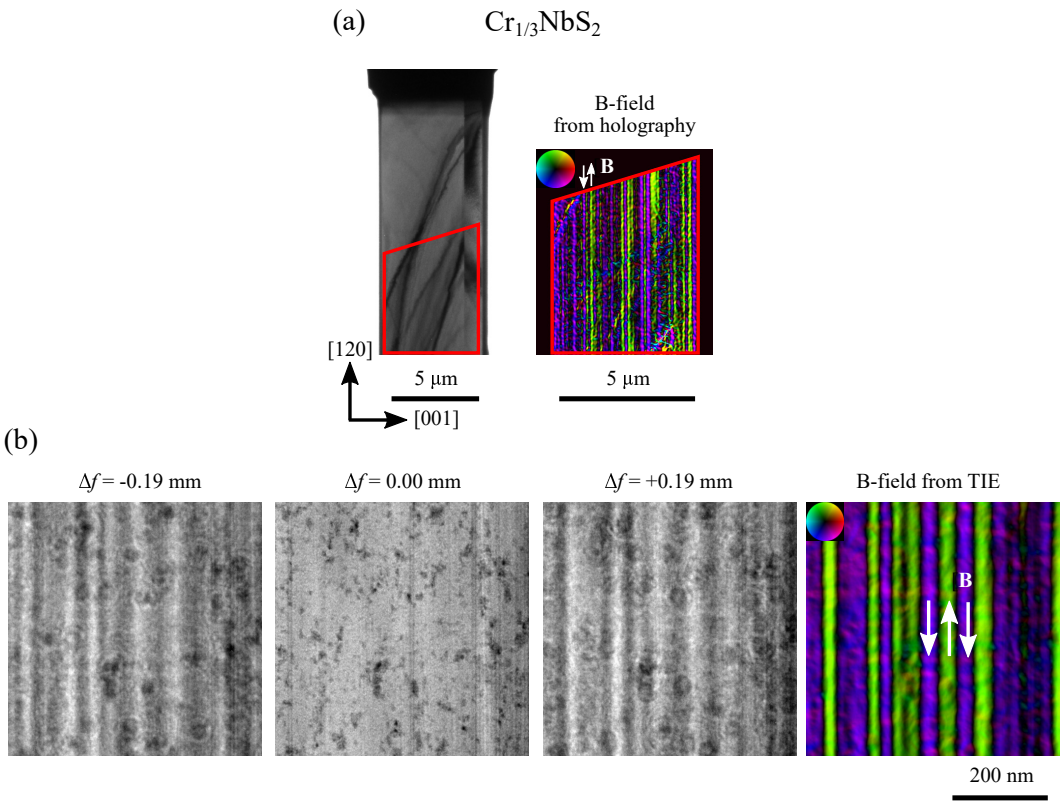

Figure 5.11: (a) An in-focus image from $Cr_{1/3}NbS_2$ together with the projected B field at 92 K in zero applied field obtained using off-axis holography from the area outlined in red. Holography was used as the closely-spaced magnetic features were difficult to discern with defocused imaging at this magnification. (b) Higher magnification images from $Cr_{1/3}NbS_2$ obtained at 91 K in zero applied field showing the specimen under-focus, in-focus and over-focus as well as the projected B field reconstructed from these images using the transport of intensity equation.

5.2.6 LTEM

Images acquired using transmission electron microscopy allow the 'projected B-field' to be calculated. This is the component of the magnetic flux density normal to the electron beam, averaged through the thickness of the sample.

Figure 5.11 shows the magnetic features observed in $Cr_{1/3}NbS_2$ by transmission electron microscopy. Instead of conventional magnetic domains, $Cr_{1/3}NbS_2$ [Figs. 5.11(a) and 5.11(b)] shows thin magnetic strips. Unlike the soliton lattice reported by Togawa *et al.* [3], the strips do not show a constant periodicity and their width varies between 25 and 65 nm. The magnetisation within these strips points mainly perpendicular to the c axis but some of the strips appear dark, indicating

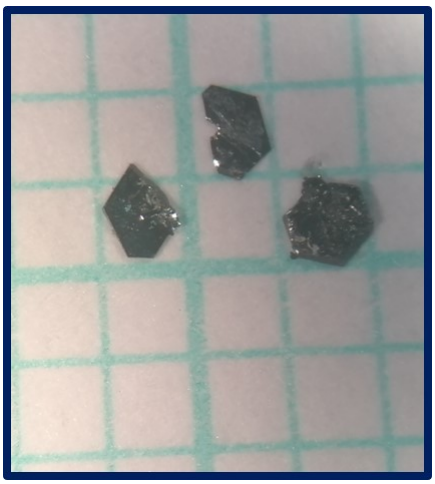

Figure 5.12: Single crystals of $Cr_{1/3}TaS_2$ on mm paper.

the magnetization is oriented out of the plane of the sample. The fact that the periodicity is not constant is likely to be a consequence of disorder in the crystal structure, which also results in the decrease in the field value at which magnetic phase transitions occur, as well as the transition temperature.

5.3 $Cr_{1/3}TaS_2$

5.3.1 Sample preparation

Polycrystalline and single crystal samples of $Cr_{1/3}TaS_2$ were prepared using the processes detailed in Section 3.1, i.e. with a solid state reaction within a box furnace and then cooled slowly to room temperature from 950 °C, and with chemical vapour transport (CVT) using the polycrystalline powder as a seed and iodine as a transport agent, respectively. 5 g of polycrystalline powder was synthesised, and 2.5 g was used during the CVT crystal growth process. Some of the crystals synthesised in this process are displayed on mm paper in Fig. 5.1. The size of the crystals varied from sub-mm in length and thickness, to approximately $1.0 \times 1.0 \times 0.2$ mm^3.

5.3.2 X-ray diffraction

As with $Cr_{1/3}NbS_2$, single crystal and Laue x-ray diffraction techniques were used to probe the structure of $Cr_{1/3}TaS_2$.

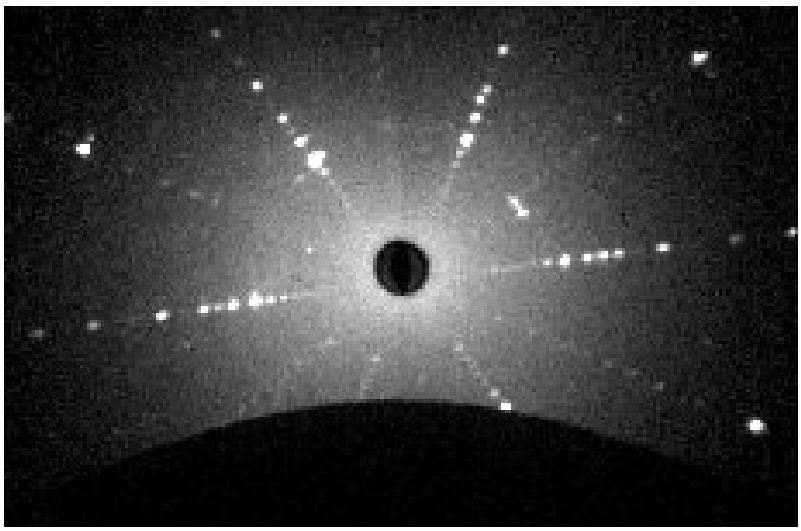

Figure 5.13: Laue backscattered reflection pattern along the [001] orientation of a $Cr_{1/3}TaS_2$ crystal.

Laue diffraction

A laue diffraction patterns was obtained along the c axis of a $Cr_{1/3}TaS_2$ crystal [See Fig. 5.13]. Several spots were not well-defined, indicating a small misalignment between crystal layers.

Single crystal x-ray diffraction

Single crystal x-ray diffraction data taken at room temperature were used to build a model of the nuclear structure of $Cr_{1/3}TaS_2$, shown in Fig. 5.14. The values extracted from the single crystal x-ray diffraction measurements, meanwhile, are displayed in Table 5.2. The Flack parameter was not well-defined, but the structure was well-modelled in the non-centrosymmetric space group. The calculated and observed structure factors were in excellent agreement while refinement in the centrosymmetric space group $P6_3/mmc$ provided a significantly worse fit as well as a less simple structural model. An inversion twin law was employed in the refinement for completeness for which the twin component scale factor refined with high ambiguity to effectively zero [0.4(6)]. A small proportion of disorder over the main site (occupancy 0.73(3)), site "i" (occupancy 0.05(3)), and site "ii" (occupancy 0.12(3)) was found.

Table 5.2: Atomic positions and occupancies for $Cr_{1/3}TaS_2$.

$Cr_{1/3}TaS_2$ ($P6_322$)					
$a = 5.7298(2)$ Å	$c = 12.1150(5)$ Å	$R_1 = 2.54\%$	$wR_2 = 9.68\%$	BASF = 0.4(5)	
Atom	Wyckoff	x	y	z	Occ.
Cr1	$2c$	$\frac{1}{3}$	$\frac{2}{3}$	$\frac{1}{4}$	0.73(3)
Ta1	$2a$	0	0	0.00000	1.000
Ta2	$4f$	$\frac{1}{3}$	$\frac{2}{3}$	0.99953(2)	1.000
S1	$12i$	0.33207(12)	0.00028(13)	0.13030(7)	1.000
Cr2	$2b$	0	0	$\frac{1}{4}$	0.05(3)
Cr3	$2d$	$\frac{2}{3}$	$\frac{1}{3}$	$\frac{1}{4}$	0.12(3)

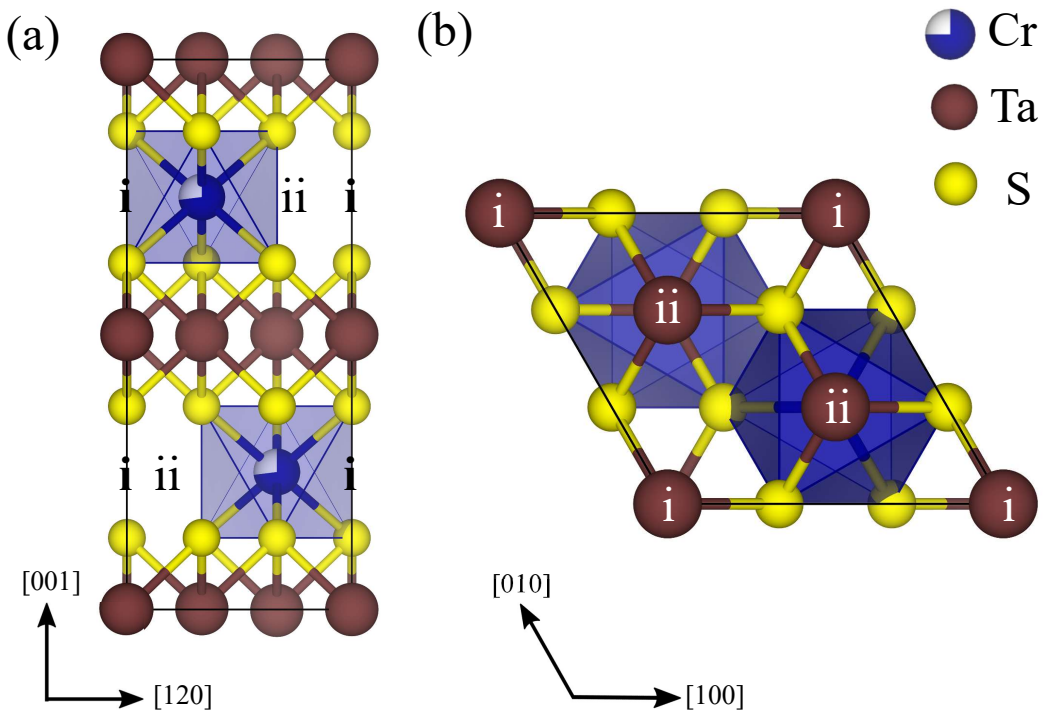

Figure 5.14: Crystal structure of $Cr_{1/3}TaS_2$ viewed along (a) the a axis and (b) the c axis, with S atoms shown in yellow, Ta atoms shown in brown, and Cr atoms shown in blue. The occupancy of the intercalated sites is reflected by the proportion of the site shown in blue. The octahedral sites of the 2c Wyckoff position are shown by blue polyhedra. The projection of the 2b and 2d sites as seen from each direction are indicated using i and ii, respectively.

5.3.3 *dc* susceptibility and magnetisation

The *dc* susceptibility of single crystal $Cr_{1/3}TaS_2$ was measured between 5 and 300 K in an applied field of 0.01 T, directed either parallel or perpendicular to the c axis, as displayed in Fig. 5.15. Due to the small sizes of the crystals measured, it was difficult to use the Curie-Weiss law to fit the high temperature data. Therefore, the isotropic paramagnetic state data for a polycrystalline powder sample was fit using the Curie-Weiss law to extract a Weiss temperature of +150(1) K for *dc* field $H \perp c$. This indicated that the interactions between the magnetic ions are ferromagnetic. The material was found to be highly anisotropic, with the signal of the *dc* susceptibility being considerably larger for $H \perp c$, indicating a strong preference for the moments to lie in the ab plane. The effective magnetic moment calculated from the Curie-Weiss law $\mu_{\text{eff}} = 2.78(3)\ \mu_{\text{B}}$/Cr for powder *dc* susceptibility measurements is close

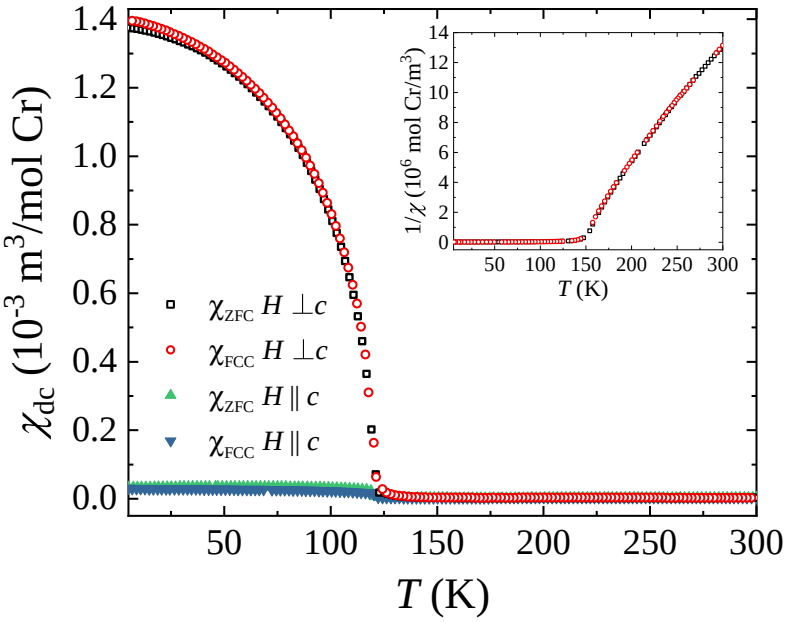

Figure 5.15: Temperature dependence of the *dc* susceptibility $\chi_{dc}(T)$, collected in zero-field-cooled (ZFC) warming and field-cooled cooling (FCC) modes, for $Cr_{1/3}TaS_2$ in an applied field of 10 mT. It is clear from the large difference between the susceptibility for each field direction that this is a highly anisotropic material, with the *ab* plane as the easy plane. Insets show the inverse ZFC and FCC susceptibility for a polycrystalline sample with an applied field of 33 mT.

to the quenched spin-only Cr^{4+} (2.83 μ_B/Cr^{4+}).

The single crystal of $Cr_{1/3}TaS_2$ ordered magnetically at 120 K, which is lower than the reported 150 K [26, 138], while the transition temperature of the polycrystalline material synthesised was in-line with the literature value. The lower transition temperature of the single crystal sample can be attributed to a degree of substitutional disorder [132] that increases during the single crystal growth process. This disordered state is a possible interpretation of the single crystal diffraction data taken for $Cr_{1/3}TaS_2$.

Fig. 5.16(a) shows the decrease in magnetisation with increasing temperature for a $Cr_{1/3}TaS_2$ single crystal, while Fig. 5.16(b) displays six-quadrant hysteresis curves at 10, 60, and 90 K. No hysteresis was visible at these temperatures.

5.3.4 *ac* susceptibility

Unless otherwise stated, an *ac* field of 113 Hz with an amplitude of 0.3 mT was applied perpendicular to the *c* axis of the crystals for all *ac* susceptibility measurements, which were used to build up a phase diagram for $Cr_{1/3}TaS_2$. The magnetic

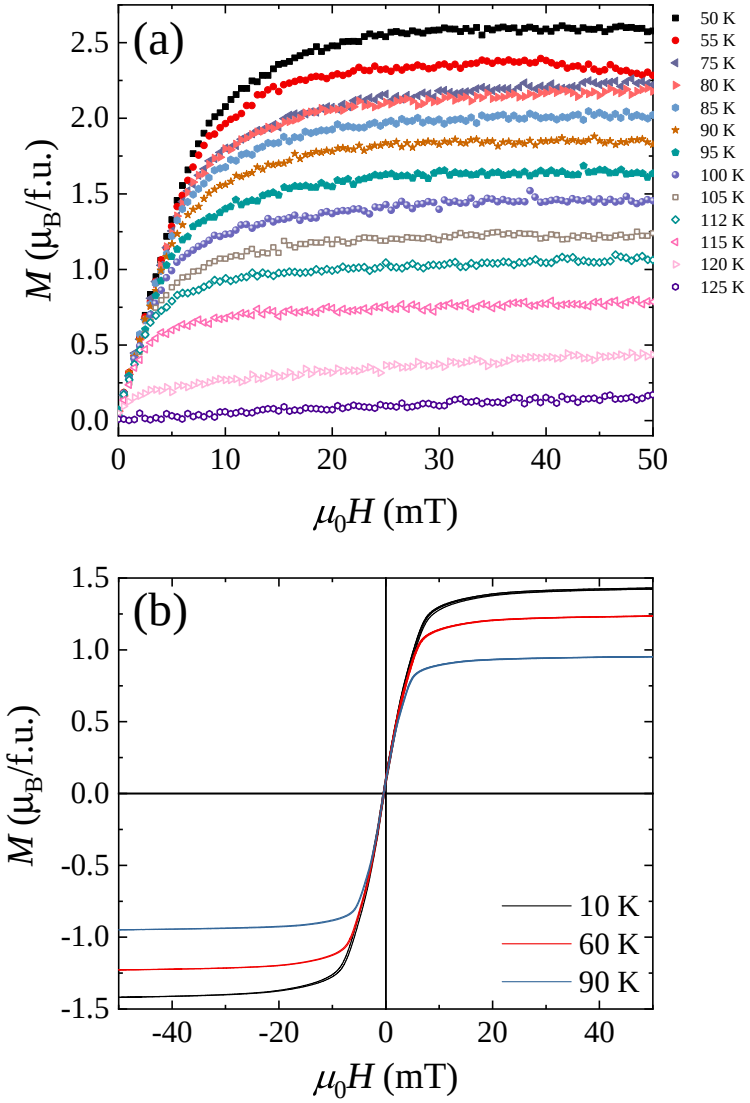

Figure 5.16: Magnetization M as a function of applied magnetic field H directed perpendicular to the c axis for single crystal $Cr_{1/3}TaS_2$ in (a) partial and (b) six-quadrant hysteresis loops at several temperatures.

phase boundaries were decided by noting changes in the gradient of *ac* susceptibility $\chi'(H)$, which are displayed in Fig. 5.17(a) along with the first derivative of the *ac* susceptibility with respect to the *dc* magnetic field $d\chi'(H)/dH$ in Fig. 5.17(b). Data taken at both 50 and 100 K is displayed. The obvious minimum visible in Fig. 5.17(b) denotes the H-CSL phase transition. The CSL-FFM phase boundary was chosen at the point where the susceptibility ceases to change significantly with

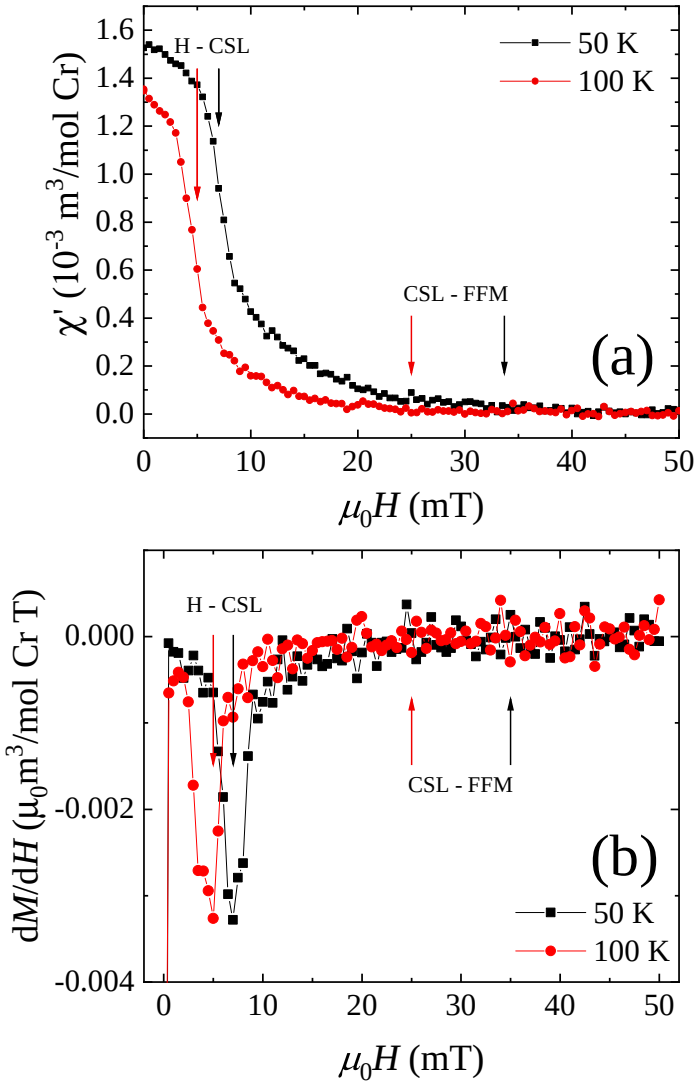

Figure 5.17: (a) In-phase component of the *ac* susceptibility χ' as a function of *dc* field H directed perpendicular to the c axis and (b) $d\chi'/dH$ versus *dc* field H at 50 and 100 K for $Cr_{1/3}TaS_2$. The features used to define magnetic phase boundaries are marked by the arrows. All the measurements were performed in an *ac* field of 0.3 mT at a frequency of 113 Hz.

field ($d\chi'/dH = 0$).

The magnetic field - temperature phase diagrams for $Cr_{1/3}TaS_2$ constructed using *ac* susceptibility versus field measurements at fixed temperatures, similar to those shown in Fig. 5.7, are displayed in Fig. 5.18. The temperatures of the transitions from the paramagnetic to a magnetically ordered state are in good agreement

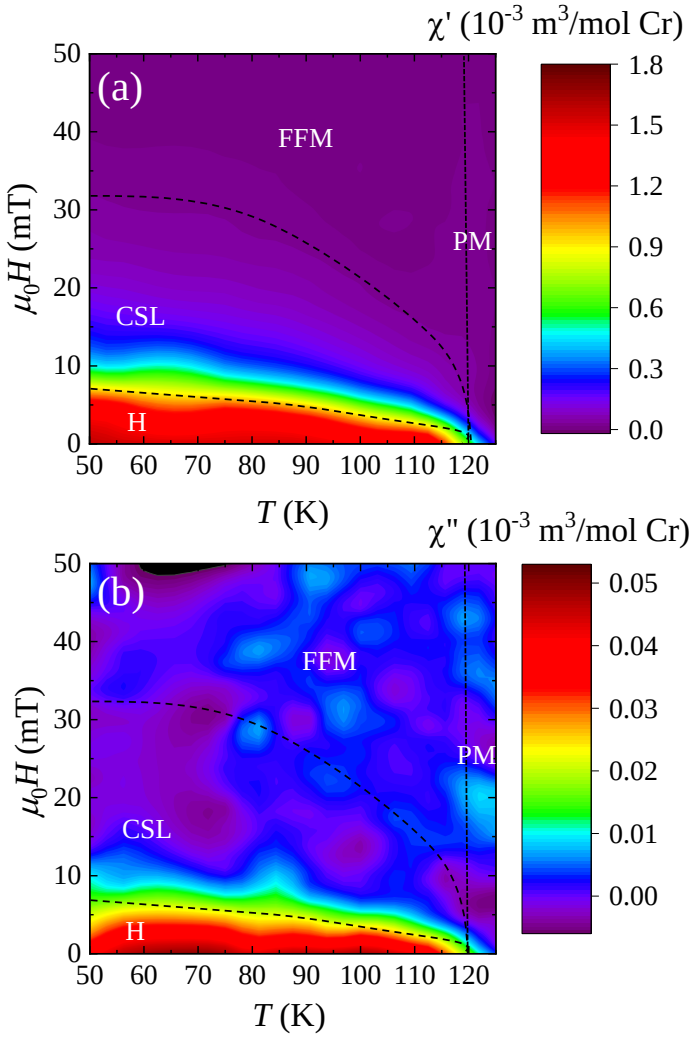

Figure 5.18: (a) In-phase χ' and (b) out-of-phase χ'' components of the *ac* susceptibility of $Cr_{1/3}TaS_2$ as a function of temperature and *dc* applied field. For both measurements, the *ac* and *dc* magnetic fields were applied perpendicular to the *c* axis.

with those obtained from *dc* susceptibility.

The H - T phase diagram for $Cr_{1/3}TaS_2$ can be divided into four regions. In addition to the paramagnetic and FFM regions, there is evidence in the *ac* (and *dc*) susceptibility for two phases labeled as helical (H) and chiral soliton lattice (CSL) appearing in the ordered state [see Figs. 5.18(a) and 5.18(b)]. As with $Cr_{1/3}NbS_2$, the imaginary component of the susceptibility χ'', shows a large increase in intensity for all temperatures at low magnetic fields below 10 mT that seems to coincide with the helimagnetic phase.

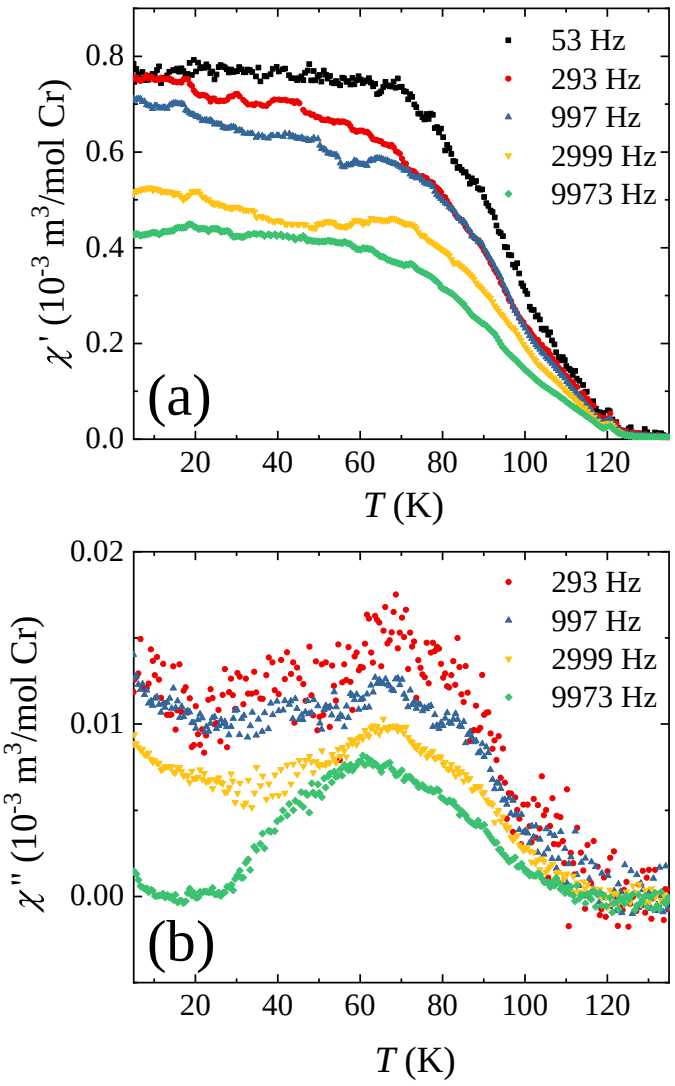

Figure 5.19: Temperature dependence of the *ac* susceptibility $\chi(T)$ at various *ac* frequencies for $Cr_{1/3}TaS_2$ in a *dc* field of 5.5 mT. The in-phase susceptibility $\chi'(T)$ is displayed in (a) and the out-of-phase susceptibility $\chi''(T)$ is displayed in (b).

A *dc* magnetic field of 5.5 mT was applied to the $Cr_{1/3}TaS_2$, and $\chi(T)$ at different applied frequencies was investigated. 5.5 mT was chosen to cut the H-T phase boundary at high temperatures. There was no frequency dependence in $\chi'(T)$ at the transition from the paramagnetic to the FFM state and the losses in the out-of-phase channel $\chi''(T)$ at this transition were small. $\chi''(T)$ was suppressed at low temperatures under 30 K for high frequencies above 2999 Hz. The peak that this

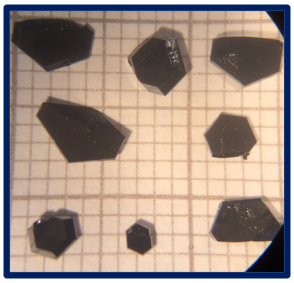

Figure 5.20: Single crystals of $Mn_{1/3}NbS_2$ on mm paper.

suppression creates in $\chi''(T)$ is suppressed as the frequency increases and is shifted to slightly lower temperatures.

5.4 $Mn_{1/3}NbS_2$

5.4.1 Sample preparation

Polycrystalline and single crystal samples of $Mn_{1/3}NbS_2$ were prepared using the processes detailed in Section 3.1, i.e. with a solid state reaction within a box furnace quenched in cold water from 950 °C, and with chemical vapour transport (CVT) using the polycrystalline powder as a seed and iodine as a transport agent, respectively. 5 g of polycrystalline powder was synthesised, and 2.5 g was used during the CVT crystal growth process. Some of the crystals synthesised in this process are displayed on mm paper in Fig. 5.20. The size of the crystals varied from sub-mm in length and thickness, to approximately 3.0 × 2.5 × 0.2 mm^3.

5.4.2 X-ray diffraction

Single crystal and Laue x-ray diffraction techniques were used to probe the structure of synthesised $Mn_{1/3}NbS_2$ single crystals.

Laue diffraction

Laue diffraction was used to check the crystallinity and orientation of single crystals of $Mn_{1/3}NbS_2$ [See Fig. 5.21]. Due to the relative thickness of the crystal and the x-ray beam, the pattern along [100] [Fig. 5.21(a)] was cut off on one side. Enough diffraction spots were visible to indicate that the crystal was high quality and to confirm that the [100] direction was being measured. The vast majority of the diffraction spots visible were well-defined, indicating few stacking faults present in the area measured, especially along [001] [Fig. 5.21(b)].

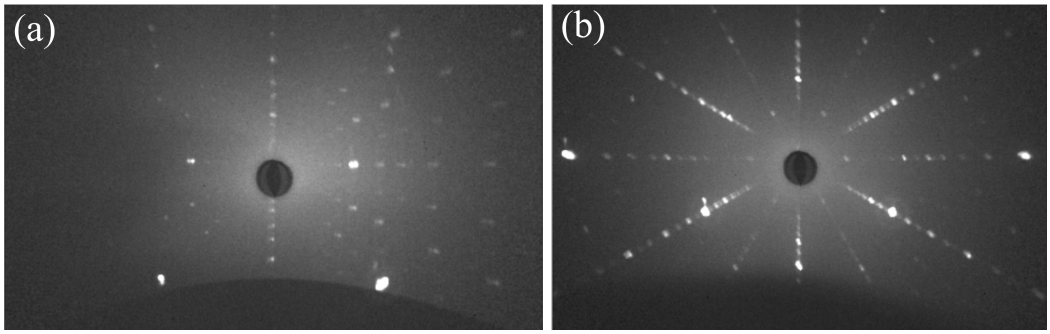

Figure 5.21: Laue diffraction patterns taken along the (a) [100] and (b) [001] directions of a single crystal of $Mn_{1/3}NbS_2$.

Single crystal x-ray diffraction

Single crystal x-ray diffraction measurements were used to probe the structure of $Mn_{1/3}NbS_2$. While the same refinement that was completed in Section 5.2.2 for the Cr phase is possible for the Mn phase, the true diffraction pattern exhibits a complex array of superstructure peaks along all axes. Efforts to resolve this remain ongoing but, for the purpose of this discussion, it is clear that the true structure likely forms a highly twinned approximation of that shown for $Cr_{1/3}NbS_2$ in Fig. 5.22 with significant breaking of the translational symmetry therein. A reconstruction of the Ewald sphere for this data set can be seen. Refinement of the known model to the aristotype peak set, i.e., the idealized high symmetry version of the low symmetry structure, yields a phase with disorder over the main site (occupancy 0.851(15)), site "i" (occupancy 0.079(15)), and site "ii" (occupancy 0.020(15)), and potentially greater inversion twinning than $Cr_{1/3}NbS_2$ with a Flack parameter of 0.57(10). Despite this inaccuracy, Table 5.3 reports the statistical fits of the aristotypical model to both data sets, along with the lattice and Flack parameters, atomic positions, and site occupancies for the purpose of discussion.

Select views of an Ewald sphere reconstruction of the single crystal x-ray diffraction data for $Mn_{1/3}NbS_2$ is displayed in Fig. 5.23. Additional reflections are visible according to rational vectors of the aristotypical cell in addition to those of the known $P6_322$ unit cell. This supercell is expected to correspond to a complex twin system present in the sample due to the weak van der Waals bonding between its layers.

Given the remaining ambiguity in the $Mn_{1/3}NbS_2$ structure further evidence to support non-centrosymmetry in these phases is desired. A complementary method

Table 5.3: Atomic positions and occupancies for $Mn_{1/3}NbS_2$.

$Mn_{1/3}NbS_2$ ($P6_322$)					
$a = 5.7933(4)$ Å	$c = 12.6451(7)$ Å	$R_1 = 3.49\%$	$wR_2 = 11.16\%$	Flack = 0.57(10)	
Atom	Wyckoff	x	y	z	Occ.
Mn1	$2c$	$\frac{1}{3}$	$\frac{2}{3}$	$\frac{1}{4}$	0.851(15)
Nb1	$2a$	0	0	0.00000	1.000
Nb2	$4f$	$\frac{1}{3}$	$\frac{2}{3}$	0.50054(2)	1.000
S1	$12i$	0.33342(12)	0.00360(2)	0.12401(8)	1.000
Mn2	$2b$	0	0	$\frac{1}{4}$	0.079(15)
Mn3	$2d$	$\frac{2}{3}$	$\frac{1}{3}$	$\frac{1}{4}$	0.020(15)

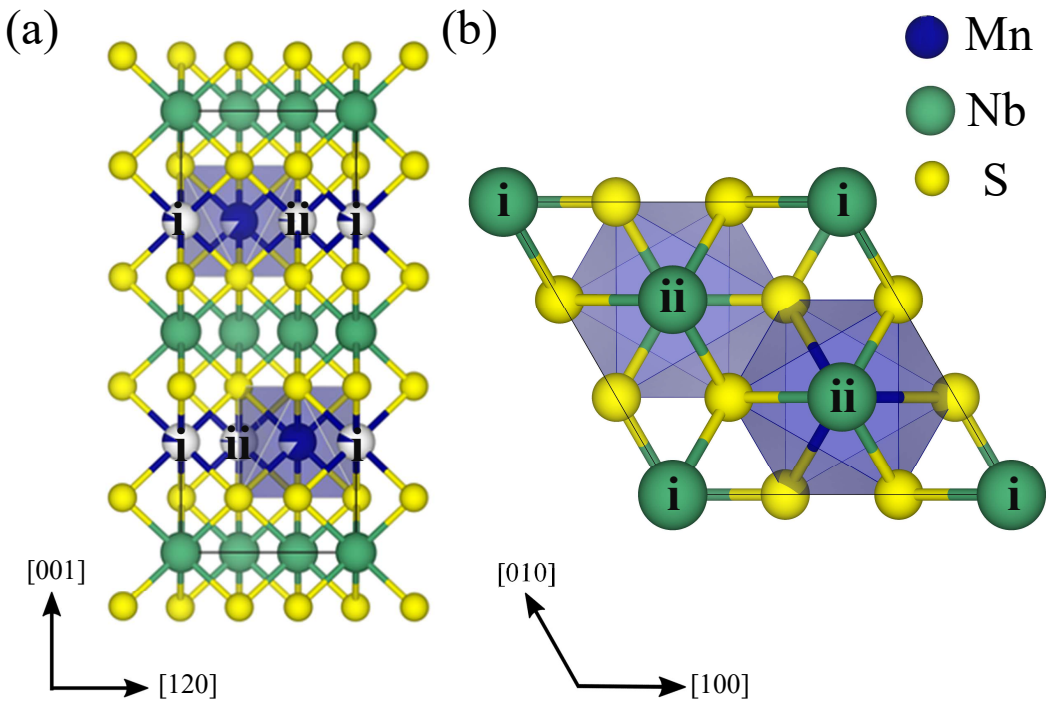

Figure 5.22: Crystal structure of $Mn_{1/3}NbS_2$ viewed along (a) the a axis and (b) the c axis, with S atoms shown in yellow, Nb atoms shown in green, and Mn atoms shown in blue. The occupancy of the intercalated sites is reflected by the proportion of the site shown in blue. The octahedral sites of the 2c Wyckoff position are shown by blue polyhedra. The projection of the 2b and 2d sites as seen from each direction are indicated using i and ii, respectively.

that can be used is transmission electron microscopy.

5.4.3 Electron diffraction

Using electron diffraction along the [001] direction [see Fig. 5.24(a) and (b)] of these materials, it is possible to compare simulated kinematic diffraction patterns (i.e., assuming single scattering) of $M_{1/3}NbS_2$ to $M_{1/4}NbS_2$. The difference between the relative intensities makes it obvious whether or not the desired concentration of M (i.e., 1/3) is present. Figure 5.24(c) displays an example of an electron diffraction pattern takesn at room temperature, measured for a $Mn_{1/3}NbS_2$ crystal, and is consistent with the simulation of the non-centrosymmetric structure.

Figure 5.24 also shows bright-field images and electron diffraction patterns acquired from $Mn_{1/3}NbS_2$ at room temperature and viewed in the [100] direction.

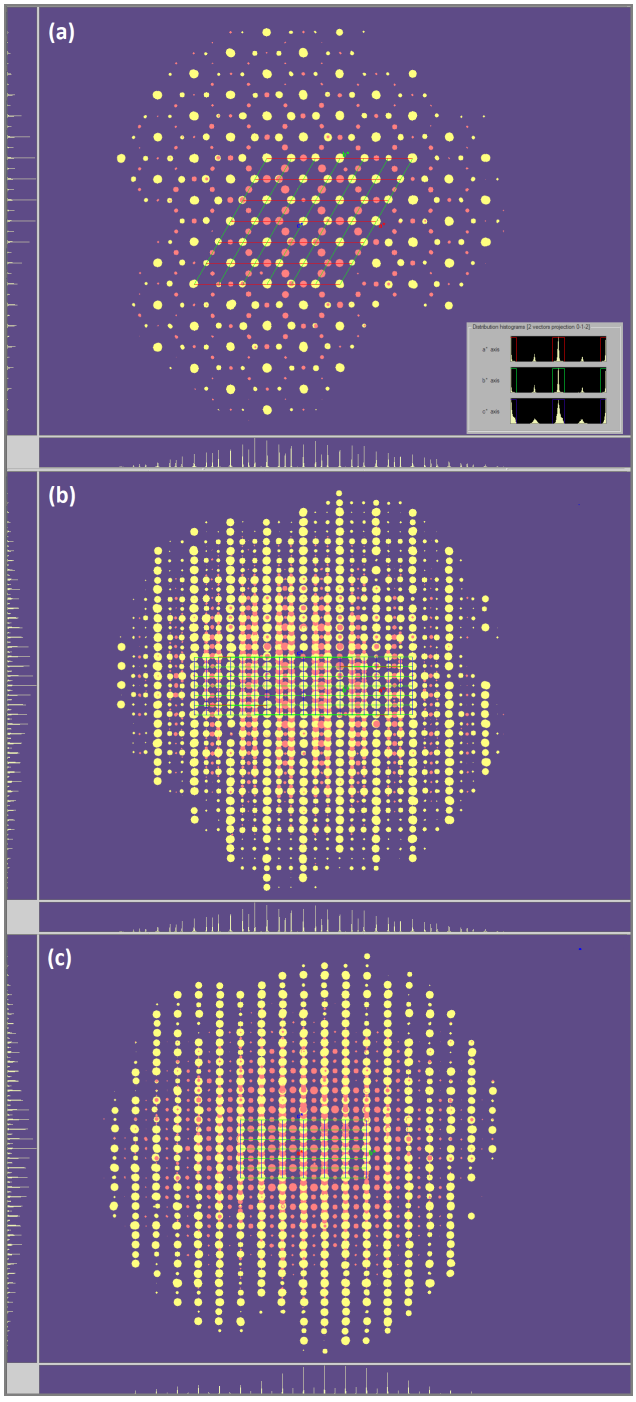

Figure 5.23: Single-crystal x-ray diffraction data for $Mn_{1/3}NbS_2$ plotted in an Ewald sphere construction, viewed (a) along c*, (b) perpendicular to the a*c* plane, and (c) along a*, showing peaks indexed to the aristotypical cell in yellow and those of the supercell in pink. Inset to (a) shows distribution histograms for the three aristotypical reciprocal vectors, and histograms for the pixel rows and columns are shown to the left and bottom of each image, respectively.

Figure 5.24(d) shows the arrangement of atoms expected in this orientation and Fig. 5.24(e) shows a simulated kinematic diffraction pattern. The experimental diffraction patterns were taken from regions 670 nm in diameter. The diffraction pattern for $Mn_{1/3}NbS_2$ [Fig. 5.24(f)] displays superlattice reflections in addition to the expected reflections. These reflections correspond to a superlattice with a period of $3c$ in the **c** direction and $7d_{010}$ in the $\mathbf{b}^*$ direction where d_{010} is the spacing of the (010) planes. This may indicate the presence of ordered Mn vacancies. The absence of a Mn atom would then allow the nearest-neighbor atoms to relax, forming a structure with a pattern similar to that shown in Fig. 5.24(f). To confirm that this is the cause of these superlattice reflections, further work to find a full structure solution for this $Mn_{1/3}NbS_2$ sample is needed.

The supercell seen in the electron diffraction is in disagreement with that found for the single-crystal x-ray diffraction, for which the pattern superficially corresponds to a doubling of all axes. This would then lead to a different ordering of the Mn vacancies. This difference could potentially be explained by the fact that the single-crystal x-ray diffraction data averages over a macroscopic sample, whereas the transmission electron diffraction data necessarily samples a small and very thin volume. This would then suggest that the period of the superlattice varies across the sample so that different results are observed in localised regions when compared with an average across the whole sample. Some evidence that this is a local effect can be seen by comparing the pristine (030) peak seen in Fig. 5.24(c) along the [001] direction to the (030) peak surrounded by superlattice reflections seen along [100] in Fig. 5.24(f).

5.4.4 *dc* susceptibility and magnetisation

The *dc* magnetization of $Mn_{1/3}NbS_2$ was measured at temperatures between 5 and 300 K with a field of 0.01 T applied either parallel or perpendicular to the c axis, (see Fig. 5.25) in order to better compare with the Cr intercalated crystals. In the paramagnetic state, the data were isotropic and could be fitted using the Curie-Weiss law. For *dc* field $H \perp c$ the Weiss temperature of +62(1) K for $Mn_{1/3}NbS_2$ indicated that the interactions between the magnetic ions are ferromagnetic. In the ordered state, the large difference between the magnitude of the susceptibility when the field is applied parallel or perpendicular to the c axis shows that the ordered moments strongly prefer to lie in the ab plane and that these materials are both highly anisotropic.

For $Mn_{1/3}NbS_2$, $\mu_{\text{eff}} = 5.43(1)\ \mu_B$/Mn, for $H \perp c$ as calculated with the Curie-Weiss law. This is consistent with previous reports on this material [144] that

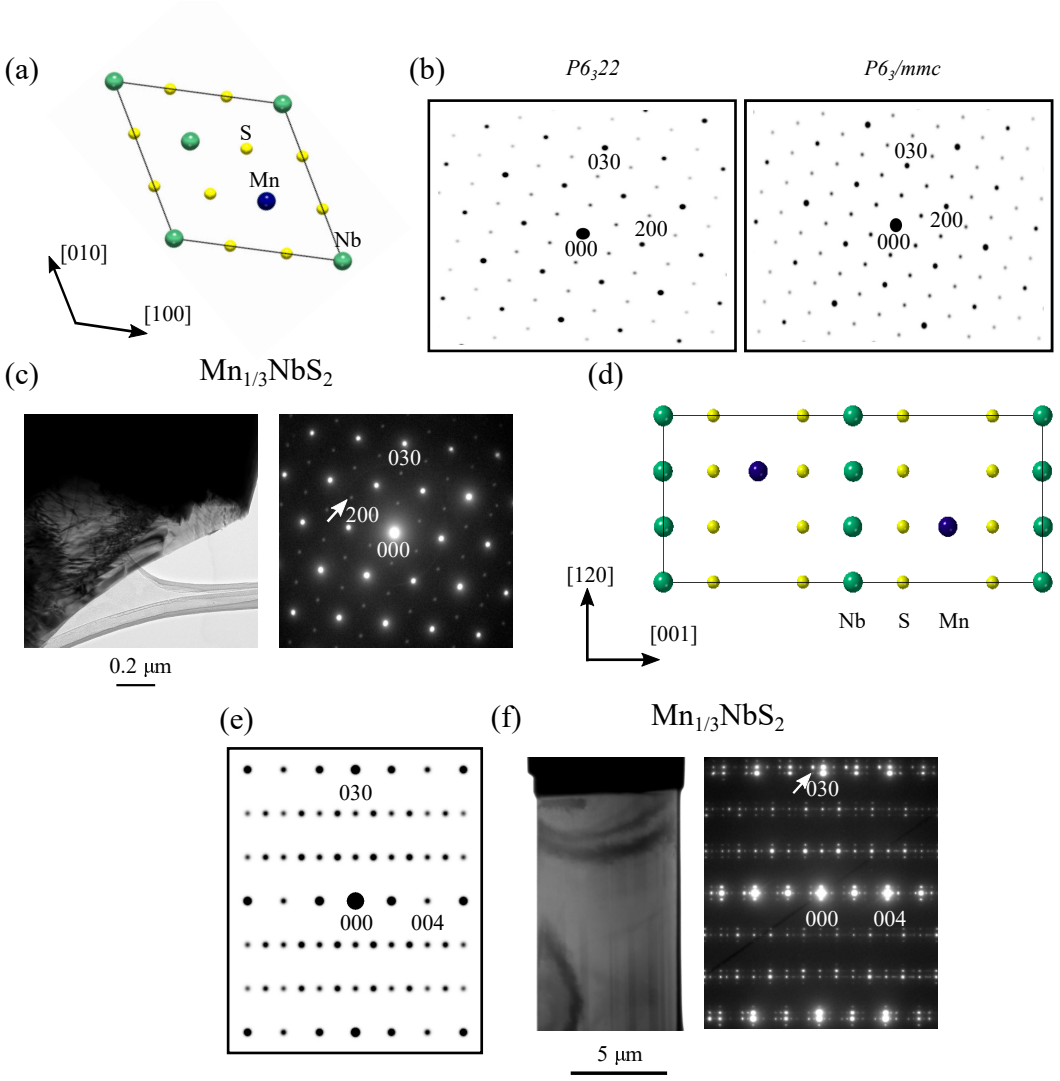

Figure 5.24: (a) Unit cell of $Mn_{1/3}NbS_2$ viewed down the [001] direction. (b) Simulated electron diffraction patterns along the [001] direction for both the non-centrosymmetric $P6_322$ structure and the centrosymmetric $P6_3/mmc$ structure, which differ from each other in the relative intensities of key spots (200) and (030), assuming kinematic scattering. An electron micrograph (c) of a crystal of $Mn_{1/3}NbS_2$ and an electron diffraction pattern from the same area are shown and match well with the simulation for the $P6_322$ space group, with the especially faint (200) spot marked with an arrow. (d) The unit cell viewed along [100] direction. (e) A simulation of the corresponding electron diffraction pattern. (f) Bright-field images and electron diffraction patterns from $Mn_{1/3}NbS_2$. Extra reflections are present indicating a superlattice with a period of $3c$ in the **c** direction and $7d_{010}$ in the $\mathbf{b}^*$ direction.

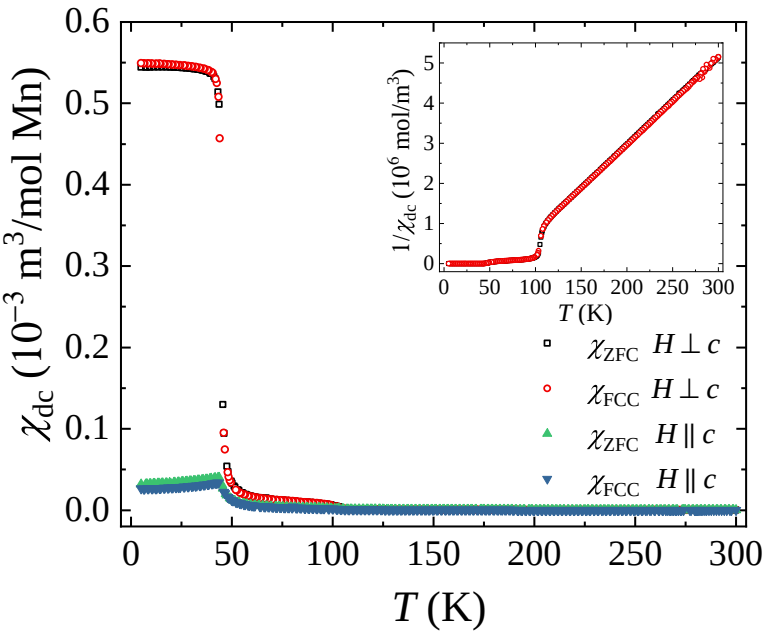

Figure 5.25: Temperature dependence of the *dc* susceptibility $\chi_{dc}(T)$, collected in zero-field-cooled (ZFC) warming and field-cooled cooling (FCC) modes, for $Mn_{1/3}NbS_2$ in an applied field of 10 mT. It is clear from the large difference between the susceptibility for each field direction that these are highly anisotropic materials, with the *ab* plane as the easy plane. Insets show the inverse ZFC and FCC susceptibility with $H \perp c$.

give values for the effective moment between the spin-only moments of 4.90 μ_B/Mn^{3+} and 5.92 μ_B/Mn^{2+}. The value may be modified by the presence of a small quantity of $Mn_{1/4}NbS_2$ within the samples [145].

A step at 100 K in the temperature dependence of the *dc* magnetization of the Mn-intercalated crystals is due to a small quantity of $Mn_{1/4}NbS_2$ [145, 22], which orders below this temperature. The bulk of the sample ($Mn_{1/3}NbS_2$) undergoes magnetic order at 45 K.

Four-quadrant *dc* magnetisation versus field measurements for $Mn_{1/3}NbS_2$ at different temperatures are displayed in Fig. 5.26. The $M(H)$ curves shown here differ in several important respects from those reported earlier [146, 147, 148]. No hysteresis is visible in the $M(H)$ measurements at any temperature while Refs. [146, 147, 148] report the presence of hysteresis at lower temperatures, $T < 20$ K. In contrast to the initial magnetization curves reported previously [146], there is no upward curvature in the magnetization with respect to the applied magnetic field at any temperature. The fields required to saturate the magnetization of the samples studied here are also higher than those reported earlier [146, 147, 148]. The reasons

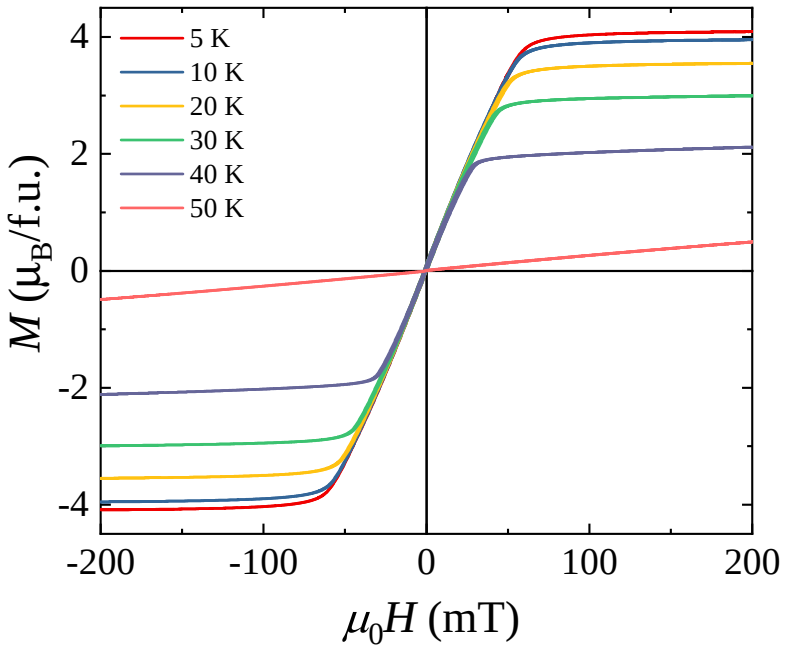

Figure 5.26: Magnetization M as a function of applied field H directed perpendicular to the c axis for single crystal $Mn_{1/3}NbS_2$ at several temperatures.

for these differences are not clear, although they suggest that structural factors such as subtle changes in the level of disorder may have a significant effect on the magnetic response of $Mn_{1/3}NbS_2$ in a magnetic field.

The *dc* magnetization measurements as a function of field for $Mn_{1/3}NbS_2$ are shown in Figs. 5.27(a) and 5.27(b). These data correspond well with the *ac* susceptibility measurements, with clear features in dM/dH marking potential phase boundaries. The $M\,(H)$ curves shown here differ in several important respects from those reported earlier [140, 22, 23].

5.4.5 *ac* susceptibility

As before, unless otherwise stated, all *ac* susceptibility measurements were taken in an *ac* field of 0.3 mT at a frequency of 113 Hz. Figure 5.28 shows the in-phase component of the *ac* susceptibility χ' and its first derivative with respect to the *dc* magnetic field $d\chi'/dH$, as a function of magnetic field H for for $Mn_{1/3}NbS_2$ at 10 and 36 K. For $Mn_{1/3}NbS_2$, all the magnetic phase boundaries are denoted by changes in gradient of $\chi'(H)$ [see Figs. 5.28(a) and 5.28(b)]. The obvious minimum visible in Fig. 5.28(b) denotes the I-II phase transition. The II-FFM phase boundary was chosen at the point where the susceptibility ceases to change significantly with

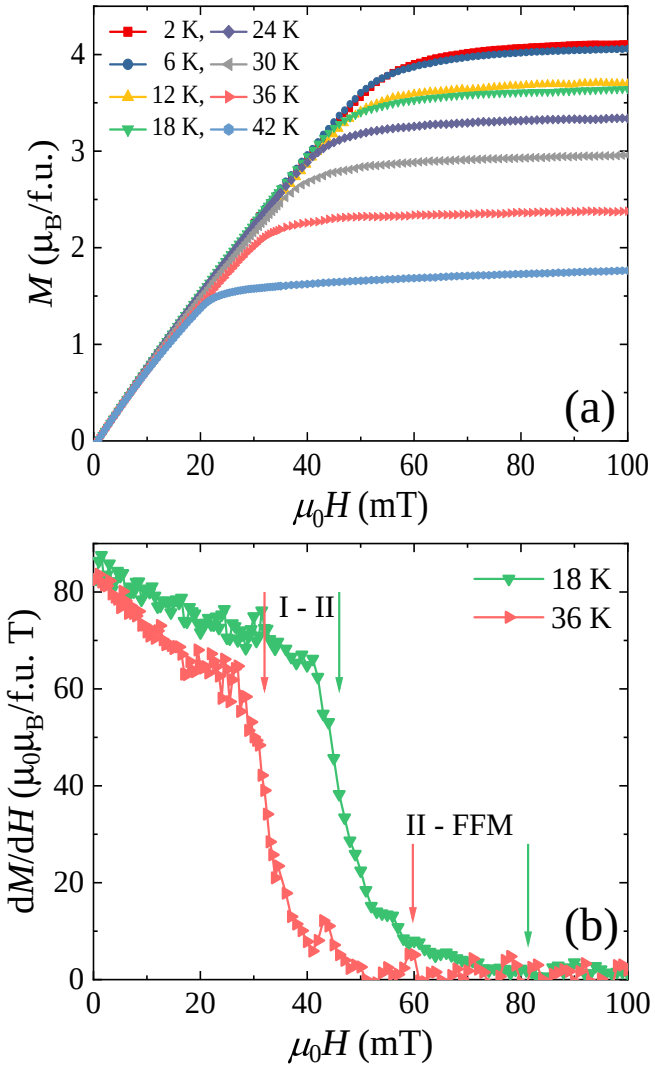

Figure 5.27: (a) Magnetization M as a function of magnetic field H directed perpendicular to the c axis for several temperatures and (b) dM/dH versus magnetic field at 18 and 36 K, for $Mn_{1/3}NbS_2$. The magnetic phase boundaries are marked by the arrows.

field ($d\chi'/dH = 0$).

The magnetic field - temperature phase diagrams for $Mn_{1/3}NbS_2$ constructed using *ac* susceptibility versus field measurements at fixed temperatures, similar to those shown in Fig. 5.28, are displayed in Fig. 5.29. Note, measurements of *ac* susceptibility versus temperature in fixed applied magnetic field are shown and are consistent with the phase diagrams presented here. The temperatures of the tran-

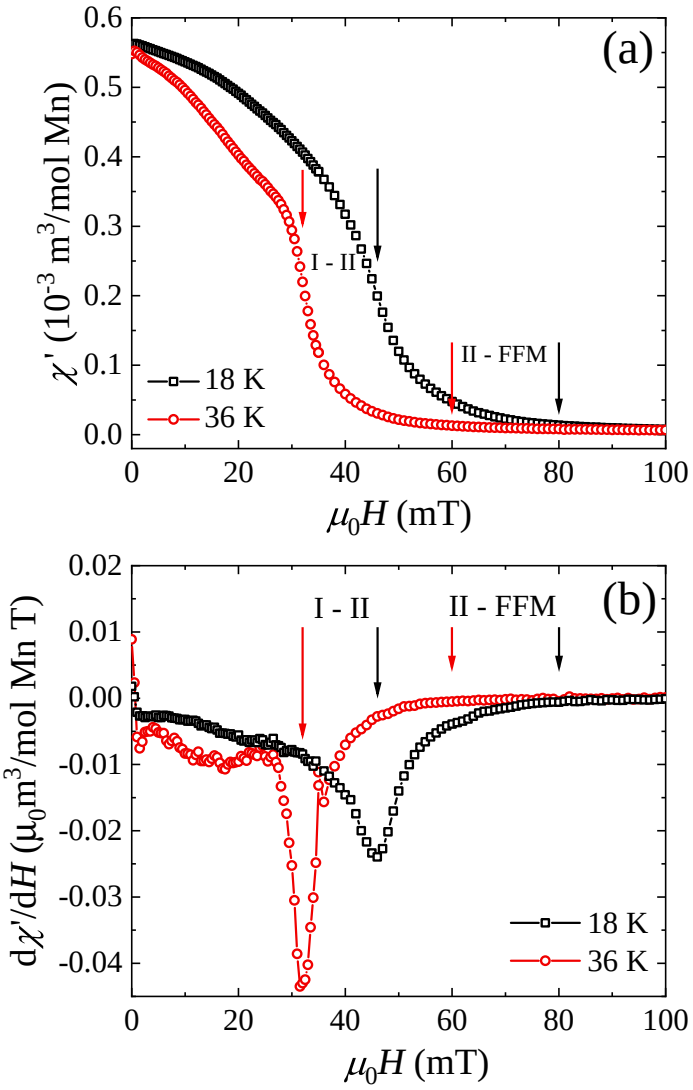

Figure 5.28: (a) In-phase component of the *ac* susceptibility χ' as a function of *dc* field H directed perpendicular to the c axis and (b) $d\chi'/dH$ versus *dc* field H at 18 and 36 K for $Mn_{1/3}NbS_2$. The features used to define the magnetic phase boundaries are marked by the arrows. All the measurements were performed in an *ac* field of 0.3 mT at a frequency of 113 Hz.

sitions from a paramagnetic to a magnetically ordered state are in good agreement with those obtained from *dc* susceptibility. The boundary in the phase diagram for $Mn_{1/3}NbS_2$ marking the entry to a FFM phase is shifted to higher fields [140]. This highlights the sensitivity of the magnetic response of these materials to disorder [132].

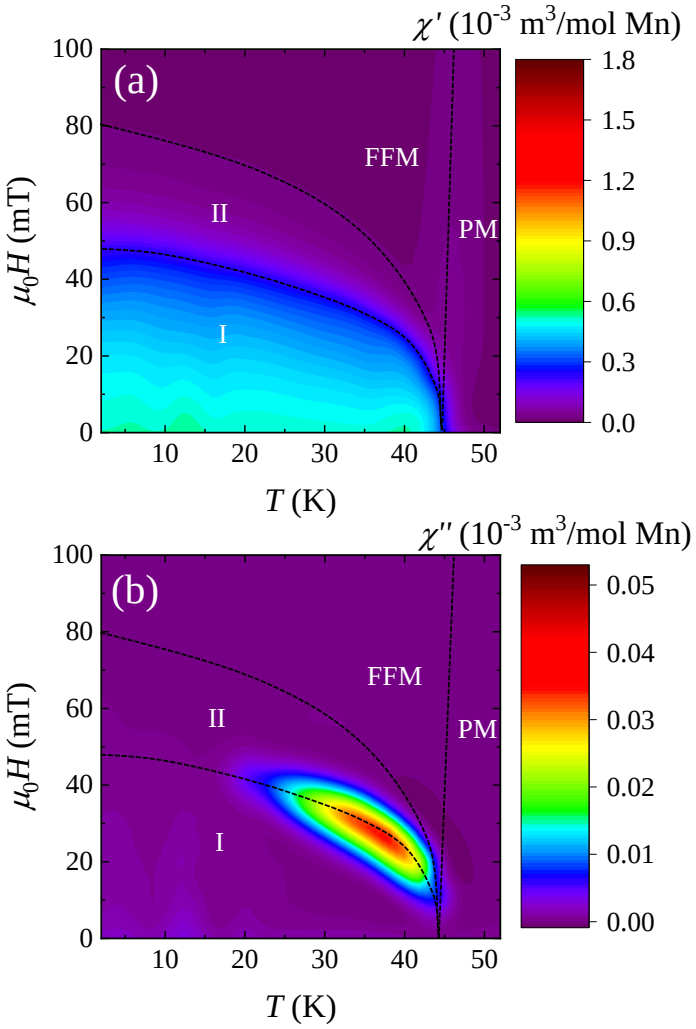

Figure 5.29: (a) In-phase and (b) out-of-phase components of the *ac* susceptibility of $Mn_{1/3}NbS_2$ as a function of temperature and *dc* applied field. For both measurements, the *ac* and *dc* magnetic fields were applied perpendicular to the *c* axis. Guides to the eye have been added to the phase diagrams based on features present in the data to distinguish the separate phases: the I, II, FFM, and PM phases (as discussed in the text).

The H-T phase diagram for $Mn_{1/3}NbS_2$ can be divided into four regions. In addition to the paramagnetic and FFM regions, there is evidence in the *ac* (and *dc*) susceptibility for two phases labeled as I and II appearing in the ordered state [see Figs. 5.29(a) and 5.29(b)]. χ' and χ'' are both significantly reduced in low *dc* fields compared to $Cr_{1/3}NbS_2$ and $Cr_{1/3}TaS_2$, indicating a difference between the ground states present in $Mn_{1/3}NbS_2$ and the Cr compounds. Once again, the

imaginary component of the susceptibility χ'', shows a large pocket of intensity just below the ordering temperature in low magnetic fields that cuts through the center of the phase boundary separating regions I and II. χ'' is reduced in intensity as the measuring frequency increases but is still clearly present at 10 kHz. This signal is most likely due to domain wall motion and pinning by defects.

The exact nature of phases I and II are unknown. It is possible that the features seen that mark these "phase boundaries" are due to the motion of magnetic domains, though it is also possible that the material experiences two non-collinear magnetic phases before the moments become field-polarized, neither of which were visible in the LTEM measurements. An alternative phase diagram for $Mn_{1/3}NbS_2$ with helimagnetic and CSL phases [140] was based on initial-magnetization versus field curves that contain a point of inflection and hysteresis. These features are not seen in similar data collected for the crystals studied in this thesis. Reference [23] proposed a helical phase at low-field and low-temperature, separated from a nearly ferromagnetic phase at higher temperatures by an almost vertical phase boundary at ~ 20 K, that coincides with the disappearance of hysteresis in the $M(H)$ curves. The measurements undertaken in this chapter provide no evidence for such a phase boundary below 20 K in these crystals of $Mn_{1/3}NbS_2$, although there is a significant increase in the losses in phase I, reflected by an increase in $\chi''(T)$, as the *ac* measuring frequency increases. The form of the boundary between phase II and the FFM phase matches qualitatively with the boundary shown in [23], albeit, as noted above, at lower fields.

Fig. 5.30 shows *ac* susceptibility versus temperature scans in different *dc* fields for $Mn_{1/3}NbS_2$. These data are consistent with those shown in Fig. 5.29. In both materials, the transition from the paramagnetic to an ordered state is marked by an increase in $\chi'(T)$ that occurs at an almost fixed temperature with increasing *dc* magnetic field. This increase in $\chi'(T)$ evolves into a peak, that is clearest in the $Mn_{1/3}NbS_2$ $\chi'(T)$ data at 28 mT, followed by a shoulder that shifts to lower temperatures as the applied *dc* magnetic field is increased.

For $Mn_{1/3}NbS_2$, there is an asymmetric peak in $\chi''(T)$ that is present at the boundary between phases I and II and disappears above 38 mT. The features in $\chi''(T)$ match well with the temperature at which the shoulder is visible in $\chi'(T)$. The temperature and field dependence of $\chi(T)$ observed here for $Mn_{1/3}NbS_2$ are similar to the results reported in Ref. [148].

The changes in $\chi(T)$ with frequency for $Mn_{1/3}NbS_2$ are investigated in Fig. 5.31. The data were collected in a *dc* field of 28 mT for $Mn_{1/3}NbS_2$, in order to cut through the maximum in $\chi''(T)$ in the H-T phase diagram and cross

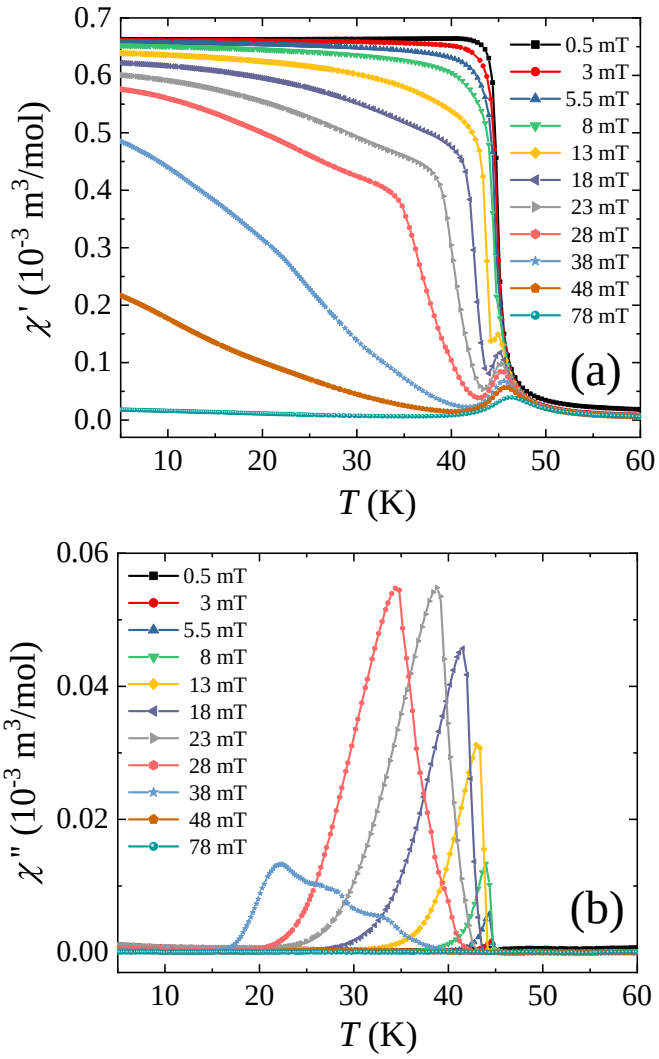

Figure 5.30: Temperature dependence of the *ac* susceptibility $\chi(T)$ in different *dc* magnetic fields applied perpendicular to the *c* axis of single crystals of $Mn_{1/3}NbS_2$. (a) In-phase component of the *ac* susceptibility $\chi'(T)$ and (b) out-of-phase component of the *ac* susceptibility $\chi''(T)$ for $Mn_{1/3}NbS_2$. All the measurements were performed using an *ac* field of 0.3 mT at 113 Hz.

several potential phase boundaries (see Fig. 5.29). There was no frequency dependence in $\chi'(T)$ at the transition from the paramagnetic to the FFM state and the losses in the out-of-phase channel $\chi''(T)$ at this transition are small. For $Mn_{1/3}NbS_2$ there is a rapid upturn in $\chi'(T)$ and a clear shoulder that is suppressed with increasing frequency on crossing into phases II and I. The temperature of the shoulder

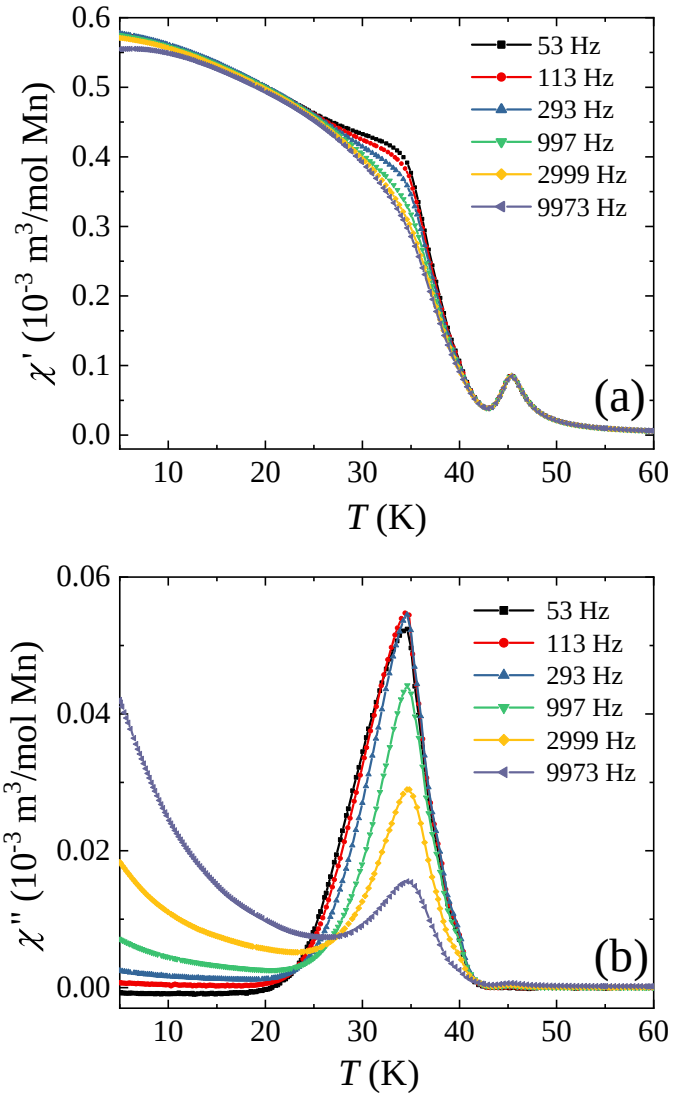

Figure 5.31: Temperature dependence of the *ac* susceptibility $\chi(T)$ at various *ac* frequencies for $Mn_{1/3}NbS_2$ in a *dc* field of 28 mT. The in-phase susceptibility $\chi'(T)$ is displayed in (a) and the out-of-phase susceptibility $\chi''(T)$ is displayed in (b).

coincides with a peak in $\chi''(T)$.

For $Mn_{1/3}NbS_2$ there is a single, broad, asymmetric anomaly in $\chi''(T)$ that extends down to 20 K, well into phase I [See Fig. 5.29(b)]. This peak in $\chi''(T)$ is suppressed as the frequency increases and is shifted to slightly higher temperature. The shifting of the peak in $\chi''(T)$ to higher temperatures with increasing frequency is reminiscent of spin glass effects [79, 80, 81] and requires further investigation. Below

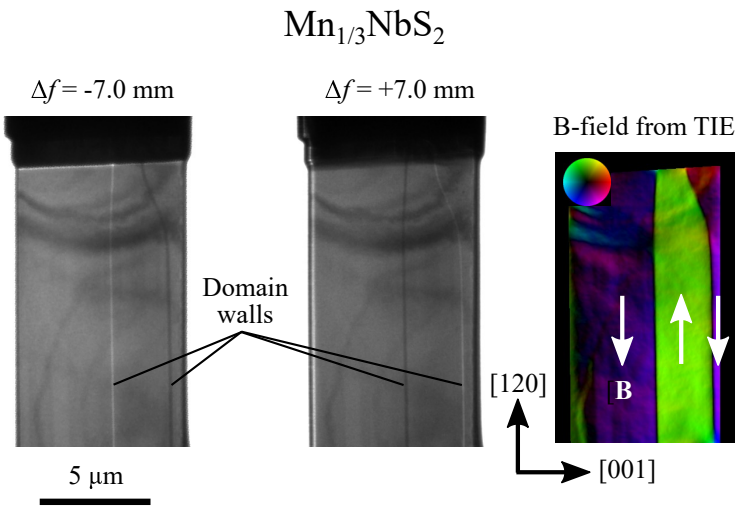

Figure 5.32: Transmission electron micrographs acquired from $Mn_{1/3}NbS_2$ at 35 K in a field of 63 mT, applied normal to the plane of the specimen. Images acquired under and over-focus are shown together with the projected B field reconstructed from these using the transport of intensity equation (TIE). White arrows and colors indicate the direction of the B field according to the inset color wheel.

25 K there is rapid increase in $\chi''(T)$ at higher frequencies indicating a different loss mechanism is present in the $Mn_{1/3}NbS_2$ sample in this field and temperature range.

5.4.6 LTEM

As with $Cr_{1/3}NbS_2$, the 'projected B-field' was calculated from images acquired with transmission electron microscopy. Figure 5.32 shows the magnetic features observed in $Mn_{1/3}NbS_2$ by transmission electron microscopy. Fig. 5.32(a) shows conventional magnetic domains separated by 180° domain walls with the magnetization lying in the (100) plane and oriented in the [120] ($\mathbf{b}^*$) direction. Images were acquired to search for chiral solitons throughout the range of field and temperature identified in Fig. 5.29(b), but nothing other than conventional magnetism was observed.

These LTEM observations are consistent with those reported in reference [23]. However, whilst this reference interprets these images as showing helimagnetism and magnetic solitons, the images obtained can also be interpreted as simply magnetic domains separated by 180° domain walls. The domains observed in Fig. 5.32 vary between $\sim$ 250 nm along the c axis, as previously observed in other work [22], and several micrometers in length. Due to the multiple phases seen in the *ac* susceptibility phase diagram for $Mn_{1/3}NbS_2$ [Fig. 5.29(a)] and the pockets of high χ'' seen in Figs. 5.9(b) and 5.29(b) for $Cr_{1/3}NbS_2$ and $Mn_{1/3}NbS_2$, respectively, it is

possible that $Mn_{1/3}NbS_2$ has a non-collinear aspect to its magnetism in phases I and II that is not visible in these LTEM measurements, but the features that have been used to mark these phase boundaries can also be attributed to the rearrangement of magnetic domains.

5.5 Summary

Single crystals of $Mn_{1/3}NbS_2$, $Cr_{1/3}TaS_2$ and $Cr_{1/3}NbS_2$ have been produced and established as crystallizing in the $P6_322$ space group. Table 5.4 summarises some of the properites of these materials. It is possible to use single crystal x-ray diffraction measurements to solve the aristotype structures for these materials in either the centrosymmetric or non-centrosymmetric form. While the non-centrosymmetric space group, $P6_322$, provides a discernibly better fit to the data, further evidence in support of this is provided using electron diffraction for $Mn_{1/3}NbS_2$ and $Cr_{1/3}NbS_2$. These electron diffraction measurements show additional superlattice reflections in $Mn_{1/3}NbS_2$ when compared to the simulated pattern, while for $Cr_{1/3}NbS_2$ the diffraction data match well with the simulated pattern. A similar yet distinctly different phenomenon is observed in the single crystal x-ray diffraction data and efforts to properly resolve the true nature of this superstructure are ongoing. The *dc* susceptibility measurements show that $Cr_{1/3}NbS_2$, $Cr_{1/3}TaS_2$, and $Mn_{1/3}NbS_2$ order magnetically below $T_C = 111$ K, $T_C = 120$ K, and $T_C = 45$ K respectively. The small step observed at 100 K in the *dc* susceptibility in $Mn_{1/3}NbS_2$, which coincides with the T_C expected for the $Mn_{1/4}NbS_2$ composition, supports the interpretation that these materials are prone to regions of Mn-deficiency.

The magnetic field – temperature phase diagrams for $Cr_{1/3}NbS_2$, $Cr_{1/3}TaS_2$, and $Mn_{1/3}NbS_2$ are mapped with *ac* susceptibility, with five phases identified in $Cr_{1/3}NbS_2$ and four phases in $Mn_{1/3}NbS_2$ and $Cr_{1/3}TaS_2$. One key difference between the three materials is that in $Cr_{1/3}NbS_2$ and $Cr_{1/3}TaS_2$ a region of high intensity χ' and χ'' is observed at low magnetic fields for all temperatures below the transition temperature, which corresponds to the continuous transformation of the helimagnetic ground state to the chiral soliton lattice phase. This feature is notably absent for $Mn_{1/3}NbS_2$.

Lorentz transmission electron microscopy measurements reveal that while $Cr_{1/3}NbS_2$ and $Cr_{1/3}TaS_2$ shows the expected chiral helimagnetism, in $Mn_{1/3}NbS_2$ there is only conventional ferromagnetic behavior with visible domain walls that are consistent with those reported previously [23]. It is therefore possible that the features seen in the *ac* susceptibility measurements of $Mn_{1/3}NbS_2$ are due to the

Table 5.4: Summary of properties of the transiton metal dichalcogenides $Mn_{1/3}NbS_2$, $Cr_{1/3}NbS_2$, and $Cr_{1/3}TaS_2$.

Formula	Space Group	T_C (K)	Magnetic Ordering	References
$Mn_{1/3}NbS_2$	$P6_322$	45	Either ferromagnetic or two phases of some incommensurate magnetic ordering not consistent with helimagnetism. No CSL exhibited.	[21, 22, 23]
$Cr_{1/3}NbS_2$	$P6_322$	111	Disordered helimagnet. Exhibits CSL	[21, 3, 86]
$Cr_{1/3}TaS_2$	$P6_322$	120	Disordered helimagnet. Exhibits CSL	[21, 26, 138]

motion of magnetic domains. Alternatively, the helimagnetic ground state could be of a modulation length longer than the thickness of the LTEM sample, resulting in changed behaviour when compared to the bulk. Further careful investigations at the various magnetic features identified in $Mn_{1/3}NbS_2$ phase diagram may be necessary in order to understand fully why in $Mn_{1/3}NbS_2$ we do not see clear evidence of helimagnetism or a CSL.

Chapter 6

Magnetisation studies of Mn_3IrSi, Mn_3RhGe, and Mn_3RhSi

6.1 Introduction

Materials such as Co-Zn-Mn alloys have been found capable of displaying skyrmions at temperatures up to, and even higher than, room temperature [18]. These materials adopt the $\beta-$Mn type structure, which crystallises in the $P4_132$ space group with a unit cell containing 20 atoms [51], with the Mn atoms occupying two different sites, the 8*c* and 12*d* Wyckoff positions, and the atoms filling the latter sites forming a sublattice of corner-sharing triangles. This form of structure type is therefore of considerable interest for topological magnetic phenomena.

The Mn_3XY family of materials adopt an ordered form of the $\beta-$Mn-type structure and form in the $P2_13$ space group, where the 12*b* site in $P2_13$ is in fact very similar to the 12*d* position in the $P4_132$ space group. Studies into this family of materials [52, 53, 47, 48] have found that Mn_3IrSi and several other members of this family adopt a frustrated antiferromagnetic configuration with 120° between the magnetic moments on the trillium lattice of Mn atoms. Mn_3CoSi, meanwhile, instead adopts a more complex magnetic ordering that is harder to identify, perhaps due to competition between the non-collinear antiferromagnetic phase and a ferrimagnetic ordering [47].

This chapter compares the structural and magnetic behaviour of three members of this family: the previously studied Mn_3IrSi, and the newly synthesised Mn_3RhGe, and Mn_3RhSi. All three of these materials show behaviour in line with

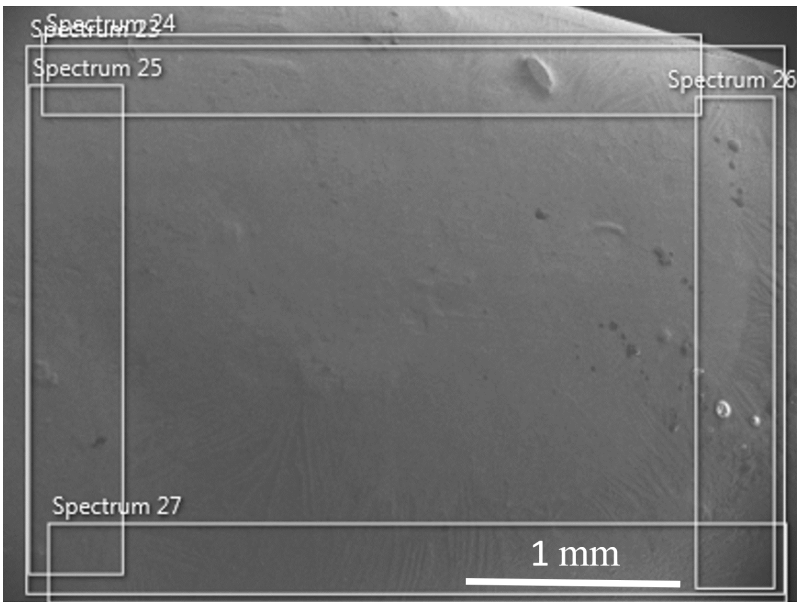

Figure 6.1: Example SEM image of Mn_3IrSi with spectra 23 - 27 marked.

frustrated antiferromagnetism, with evidence of an incommensurate magnetic phase shown at 200 K for Mn_3RhGe.

6.2 Mn_3IrSi

6.2.1 Sample preparation

A polycrystalline button of Mn_3IrSi was prepared by collaborators at the National Cheng Kung University by arc melting a stoichiometric ratio of Mn, Ir, and Si. While the button itself was used for most measurements, part of this button was ground into a powder and used for the powder x-ray diffraction, powder neutron diffraction, and heat capacity measurements.

6.2.2 Energy Dispersive X-ray Analysis

Energy dispersive x-ray analysis was used to analyse the stoichiometry of the Mn_3IrSi button, see Fig. 6.1. An average over eighteen spectra, which are tabulated in Table 6.1, gave a stoichiometry of $Mn_{2.5(4)}Ir_{1.1(2)}Si_{1.4(2)}$. The material appears to be deficient in manganese and to vary in manganese amounts significantly throughout the button. This is reflected by the signficant error value for the amount of Mn present.

Table 6.1: Energy dispersive x-ray analysis spectra measured from Mn_3IrSi with associated errors of ±1 %.

Spectrum Number	Mn (%)	Ir (%)	Si (%)
19	58	16	26
20	57	16	26
21	56	18	26
22	67	12	20
23	46	23	30
24	42	25	32
25	45	24	30
26	51	20	30
27	64	14	22
28	41	27	32
29	38	29	33
30	45	25	31
31	41	26	32
32	48	24	28
33	44	25	31
34	41	26	33
35	46	24	30
36	59	18	22
37	44	26	30

Table 6.2: Atomic coordinates used for powder x-ray diffraction Rietveld refinement for Mn_3IrSi for the cubic space group $P2_13$. A refined lattice parameter of 6.50226(8) Å is extracted from the data.

Atom	x	y	z	Occ.	B_{iso} (Å^2)
Mn1	0.1225(8)	0.2182(8)	0.4575(6)	1	0.1
Ir1	0.6832(2)	0.6832(2)	0.6832(2)	1	0.1
Si1	0.0738(6)	0.0738(6)	0.0738(6)	1	0.1

6.2.3 Powder x-ray diffraction

Powder x-ray diffraction measurements were used to check the phase purity of the sample. Several very small peaks were present that could not be indexed, indicating only a small amount of impurities present in this material. The R-factors extracted from the fit were $R_{wp} = 10.69\%$, $R_{exp} = 4.52\%$ and $R_p = 7.29\%$, indicating good agreement between the calculated and observed data. Atomic parameters extracted from this model are displayed in Table 6.2, with the lattice parameter refined as 6.50226(8) Å. The thermal parameters were set to 0.1 for the fitting as they could not be accurately refined from this data set.

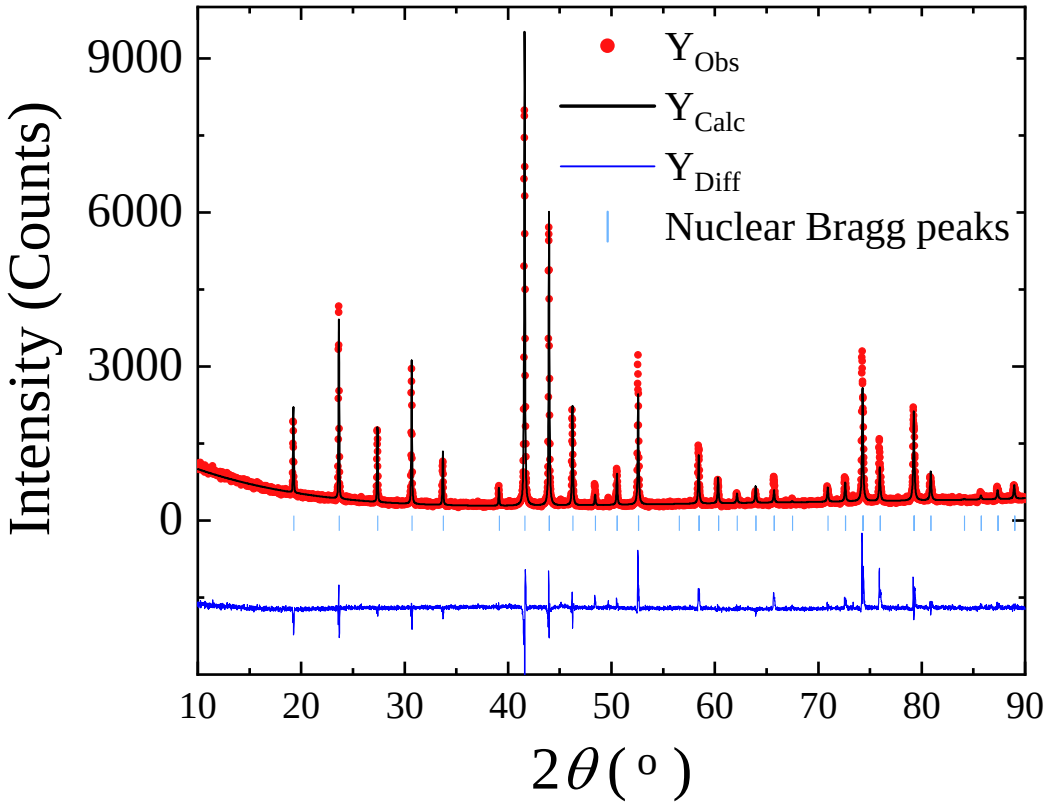

Figure 6.2: Powder x-ray diffraction profile of Mn_3IrSi, taken at room temperature.

6.2.4 Heat capacity

Heat capacity measurements for Mn_3IrSi are shown in Fig. 6.3. A transition is observable at $T = 225$ K in agreement with the transition observed for this material in the literature [47]. However, an additional shoulder is present at $T = 208$ K. The transitions here indicate the onset of long-range magnetic ordering.

At low temperatures, the Debye temperature can be calculated using the approximation $C(T)/T = \gamma + \beta T^2 + \delta T^4$, where γ is the electronic contribution to the heat capacity, the Debye temperature $\Theta_D = \sqrt[3]{\frac{12}{5}\frac{nR\pi^4}{\beta}}$, $n = 5$ is the number of atoms in the formula, and R is the molar gas constant. By fitting the low temperature data, between 1 and 100 K^2 to this function, values of $\gamma = 2.916(4) \times 10^{-4}$ J/mol K and $\Theta_D = 450(4)$ K can be extracted. The γ value here is in the range expected for a metallic material. It is worth noting that for a 3D antiferromagnetic material, it might be expected that at low temperatures the magnetic contribution to the specific heat, as well as the phonon contribution, would be linear. It is clear from the data that a quadratic relationship between specific heat and temperature

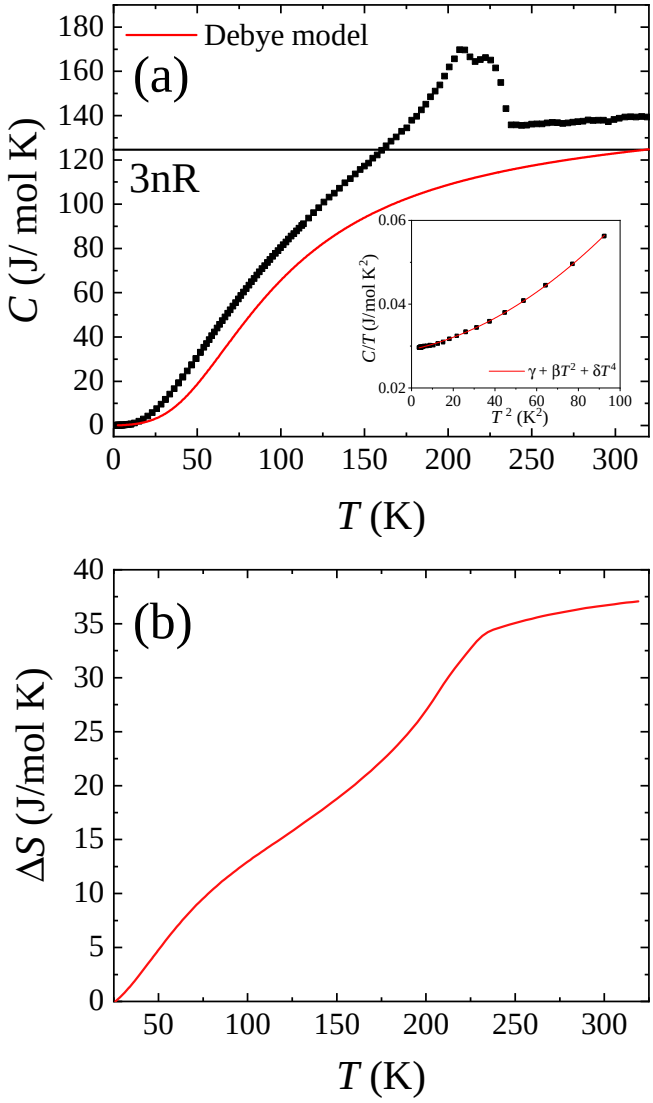

Figure 6.3: (a) Heat capacity versus temperature collected in zero field for Mn_3IrSi. (b) The change in the magnetic entropy as a function of temperature.

is observed, indicating a more complex relationship.

The lattice contribution to the heat capacity can be estimated using the Debye model:

$$C_{\mathrm{D}}(T) = \gamma T + nC_{\mathrm{D}}\left(\frac{T}{\Theta_{\mathrm{D}}}\right), \tag{6.1}$$

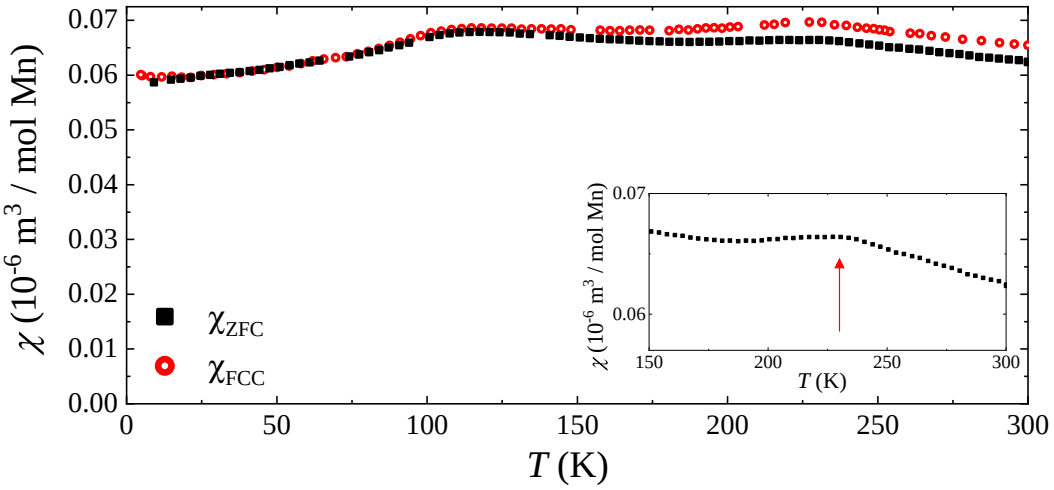

Figure 6.4: Temperature dependence of the dc susceptibility, $\chi_{\mathrm{dc}}(T)$, for Mn_3IrSi collected in zero-field-cooled warming and field-cooled cooling modes in an applied field of 25 mT. The inset shows the ZFC warming data around the transition temperature of the main phase, which is marked with an arrow.

where C_{D} is the Debye contribution. The Dulong-Petit value, $15R$, was exceeded at high temperatures for both materials, due to high γ contribution as well as possible anharmonic contributions to the lattice.

The phonon contribution was then subtracted in order to allow the calculation of the change in magnetic entropy over the magnetic transition, by integrating over $\Delta C/T$, where $\Delta C(T) = C(T) - C_{\mathrm{D}}(T)$ and gave $\Delta S = 37(5)$ J/mol K, for Mn_3IrSi, which is close to the expected value for Mn^{4+}, $\Delta S = 34.8$ J/mol K. The Debye temperature obtained from the model was $\Theta_{\mathrm{D}} = 400(30)$ K. This value falls well below the calculated value from the low temperature fit. This poor agreement is attributed to the high transition temperature limiting the amount of data able to be taken in the paramagnetic state.

6.2.5 *dc* magnetisation

The *dc* susceptibility measurements for Mn_3IrSi are displayed in Fig. 6.4. The Nèel temperature $T_N = 215$ K was extracted from maxima in $d(\chi T)/dT$. This value is very close to the average of the two transitions seen in the heat capacity data.

Another transition is present at $T = 97$ K, which has not previously been discussed in the literature, and was not visible in the heat capacity data. This additional transition is therefore likely due to a small magnetic impurity within the sample measured. The *dc* susceptibility profile is sitting on a high magnetic

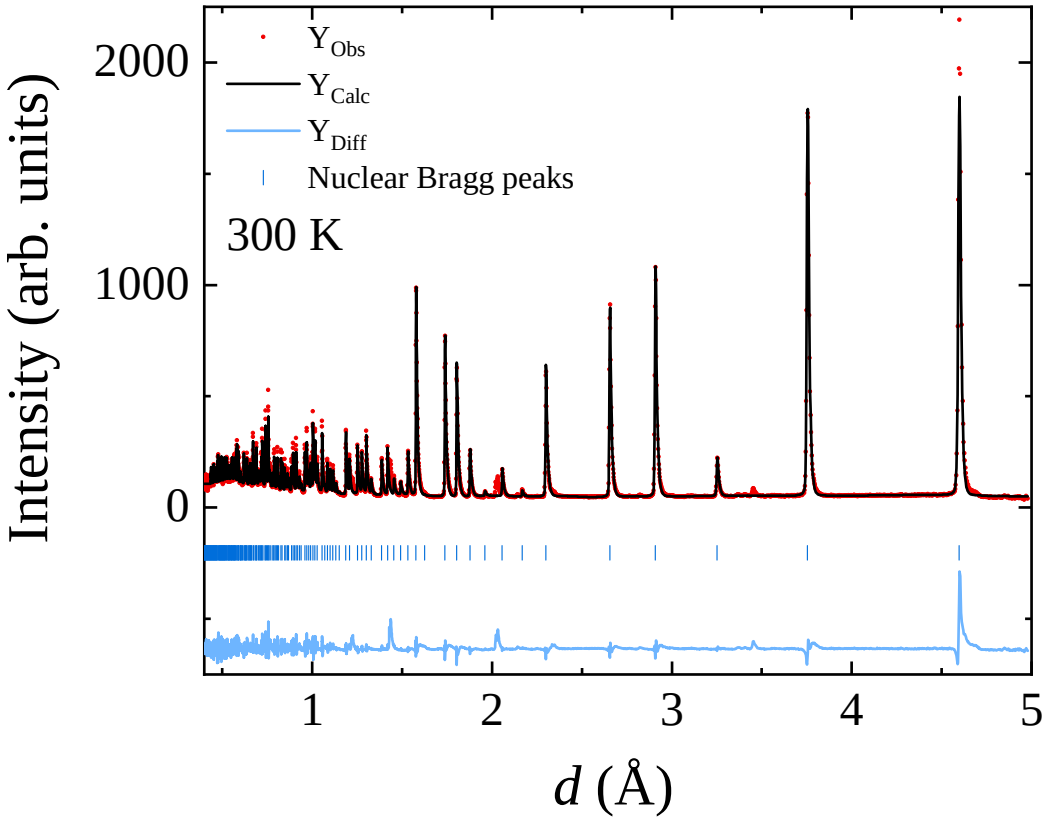

Figure 6.5: Neutron powder diffraction profiles at 300 K for Mn_3IrSi, with a calculated fit.

background at 300 K, which is consistent with observations of other materials with a trillium lattice [82], and additionally no hysteresis is observed between the ZFC and FCC measurements within error.

6.2.6 Powder neutron diffraction

Time-of-flight powder neutron diffraction data was taken for several temperatures between 1.5 and 300 K. First, the nuclear structure was calculated using the 300 K dataset, as illustrated in Fig. 6.5. The fit was calculated for Mn_3IrSi in the space group $P2_13$ with a lattice parameter of $a = 6.50407(7)$ Å. A small amount of impurity peaks are visible that were not considered when fitting the data.

The calculated Bragg R-factor for this fit was $R_{\text{Bragg}} = 6.459\%$. The atomic positions for this fit are tabulated in Table 6.3, where it can be seen that they are similar to the values in Table 6.2, as expected. The atomic positions found at 1.5 K are displayed in the same table.

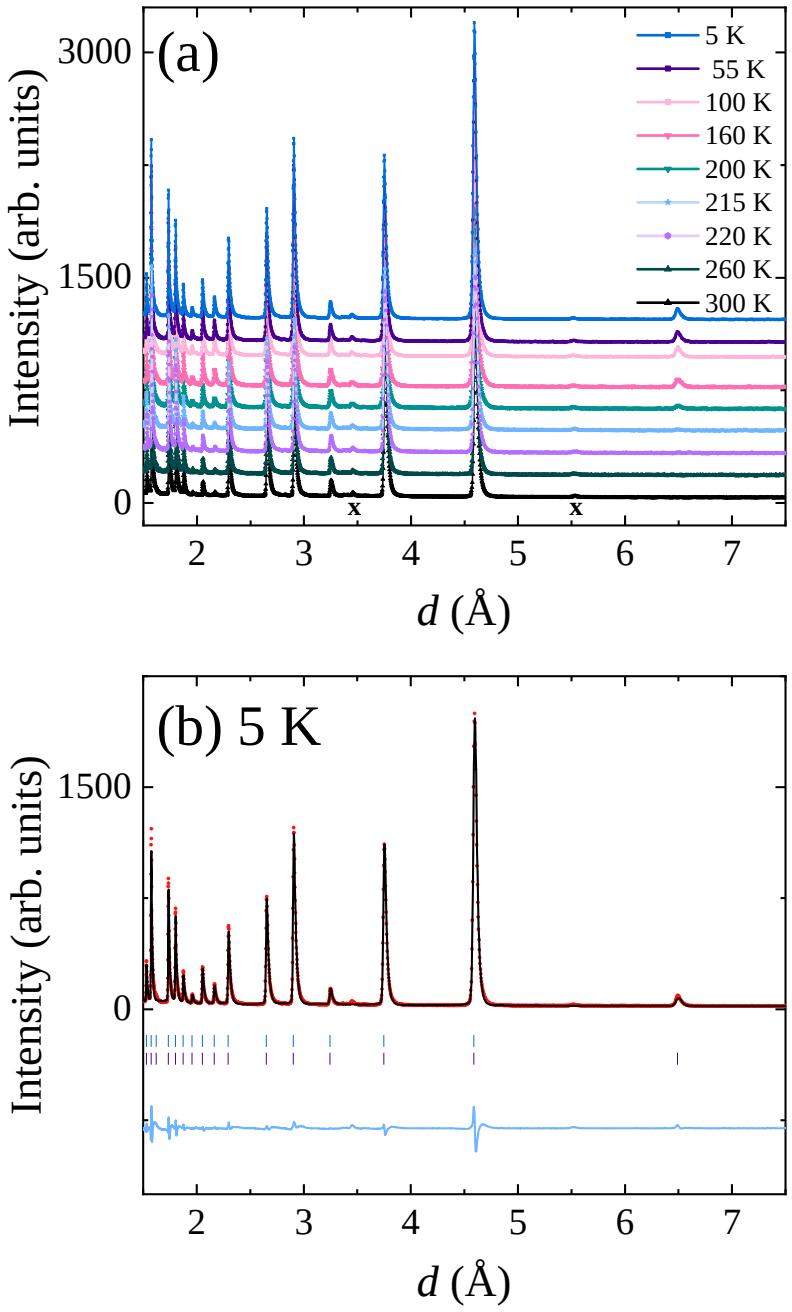

Figure 6.6: (a) Neutron powder diffraction profiles at temperatures ranging from base to 300 K for Mn_3IrSi, offset by 150 counts each for clarity, with impurity peaks marked with an x. (b) The nuclear and magnetic fit to the data at 5 K, with each phase refined separately.

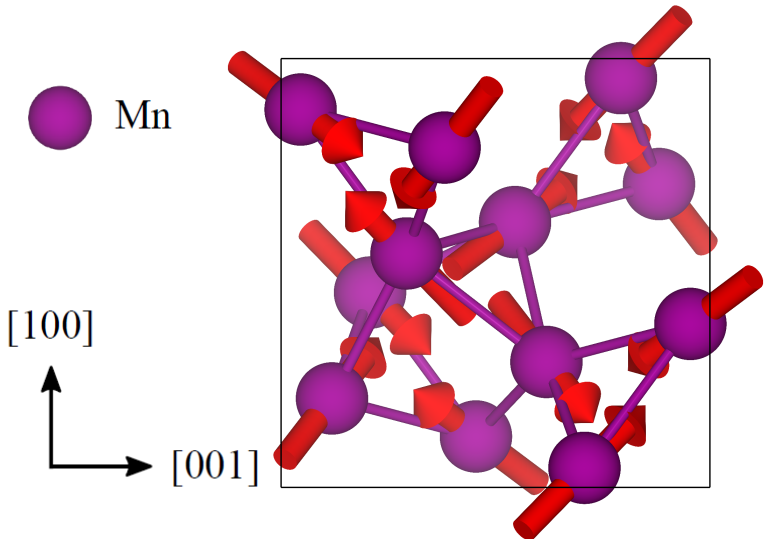

Figure 6.7: The twelve Mn atoms of Mn_3IrSi are displayed with magnetic moments (red arrows) to illustrate the ground state magnetic structure.

Table 6.3: Atomic coordinates for Mn_3IrSi extracted from the powder neutron diffraction refinement at 300 K and 1.5 K in the cubic space group $P2_13$. The lattice parameter $a = 6.50407(7)$ Å and the Bragg R-factor $R_{\text{Bragg}} = 6.459\%$.

300 K					
$R_{\text{Bragg}} = 6.459\%$				$a = 6.50407(7)$ Å	
Atom	x	y	z	Occ.	B_{iso} (Å^2)
Mn1	0.1179(13)	0.2073(8)	0.4549(7)	1	1.02(9)
Ir1	0.6831(3)	0.6831(3)	0.6831(3)	1	0.55(6)
Si1	0.0662(8)	0.0662(8)	0.0662(8)	1	0.3(2)
1.5 K					
$R_{\text{Bragg}} = 4.86\%$		$R_{\text{Mag}} = 2.35\%$		$a = 6.49081(7)$ Å	
Atom	x	y	z	Occ.	B_{iso} (Å^2)
Mn1	0.1187(14)	0.2074(10)	0.4544(8)	1	0.55(10)
Ir1	0.6829(4)	0.6829(4)	0.6829(4)	1	0.18(6)
Si1	0.066(1)	0.066(1)	0.0661(1)	1	0.4(2)

The evolution of the neutron powder diffraction profiles for Mn_3IrSi with temperature between d-values of 2.0 and 7.5 Å are displayed in Fig. 6.6(a). This region of interest was chosen to better show the evolution of the magnetic peaks with temperature. The data bank with an average 2θ value of 54° was chosen for the same reason. Magnetic peaks begin to appear between 215 and 220 K, which is in line with the transition temperature extracted from the *dc* susceptibility data. There is no evidence that the impurity peaks have a magnetic component, indicating

Table 6.4: Atomic components of the basis functions localised in the $P2_13$ paramagnetic space group and transformed by the irreducible representations associated with the $\mathbf{k_0} = (0,0,0)$ [mΓ_1 (η_1, η_2, η_3)] propagation vector.

Irrep	Mn_1	Mn_2	Mn_3	Mn_4	Mn_5	Mn_6	Mn_7	Mn_8	Mn_9	Mn_{10}	Mn_{11}	Mn_{12}
mΓ_1												
η_1	$(1,0,0)$	$(-1,0,0)$	$(-1,0,0)$	$(1,0,0)$	$(0,1,0)$	$(0,-1,0)$	$(0,-1,0)$	$(0,1,0)$	$(0,0,1)$	$(0,0,-1)$	$(0,0,-1)$	$(0,0,1)$
η_2	$(0,1,0)$	$(0,-1,0)$	$(0,1,0)$	$(0,-1,0)$	$(0,0,1)$	$(0,0,-1)$	$(0,0,1)$	$(0,0,1)$	$(1,0,0)$	$(-1,0,0)$	$(1,0,0)$	$(-1,0,0)$
η_3	$(0,0,1)$	$(0,0,1)$	$(0,0,-1)$	$(0,0,-1)$	$(1,0,0)$	$(1,0,0)$	$(-1,0,0)$	$(-1,0,0)$	$(0,1,0)$	$(0,1,0)$	$(-0,-1,0)$	$(0,-1,0)$

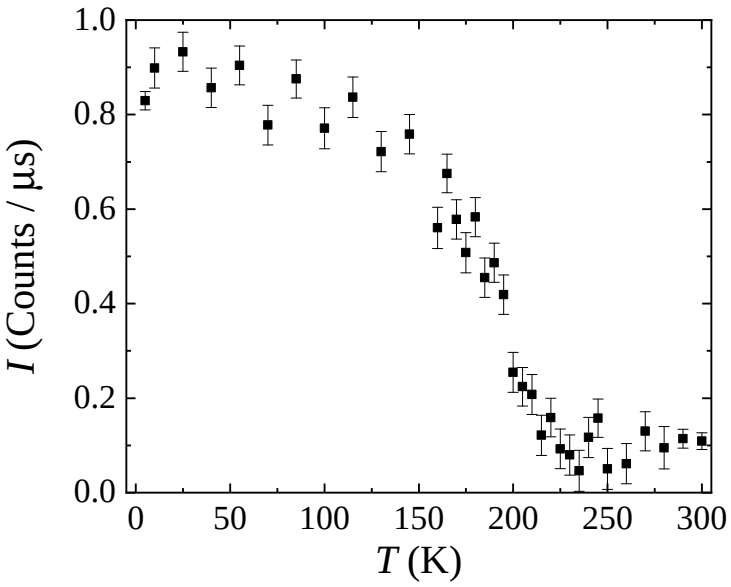

Figure 6.8: The integrated intensity of the Bragg reflection (001) as it varies with temperature.

that the visible impurities are non-magnetic.

The main magnetic phase fit at a base temperature of 5 K is displayed in Fig. 6.6(b) using the same average 2θ value as the other measurements. A $\mathbf{k_0} = (0, 0, 0)$ propagation vector was used to model the magnetic behaviour of the material. For this propagation vector, four possible irreducible representation vectors are available for this material: $\mathrm{m}\Gamma_1$, $\mathrm{m}\Gamma_2$, $\mathrm{m}\Gamma_3$, and $\mathrm{m}\Gamma_4$, all of which are indicative of frustrated antiferromagnetic structures. Each possible irreducible representation was trialed to the data.

The data were best modelled using the irreducible representation $\mathrm{m}\Gamma_1(\eta_1, \eta_2, \eta_3)$, the three orthogonal basis vectors of which are shown in Table 6.4. The magnetic structure consists of a frustrated antiferromagnetic lattice of corner-sharing triangles of Mn atoms as displayed in Fig. 6.7, with a refined moment size of 2.92(1) μ_B. This is consistent with the magnetic structure found in the literature [52].

The (001) Bragg reflection is then analysed by measuring how the integrated intensity of this reflection varies with temperature to visualise the order parameter for this reflection, as displayed in Fig. 6.8. A broad decrease in intensity was visible that reaches a minimum value by around 225 K, which agrees with the transition temperature extracted from heat capacity measurements. There are no obvious transitions at lower temperatures (i.e. at 208 K as seen in the heat capacity data) visible from the integrated intensity of this peak.

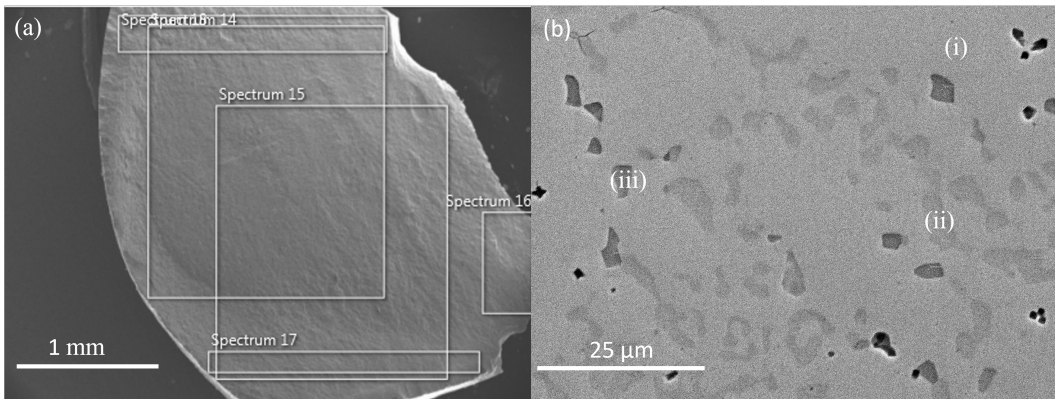

Figure 6.9: Example SEM image of (a) Mn_3RhGe polycrystalline button with spectra 14 - 18 marked and (b) Mn_3RhGe polycrystalline button polished atomically flat on a far smaller scale. Different contrast is indicative of different stoichiometry present. Three phases are identified and marked as (i), (ii), and (iii).

Due to the transition visible at 97 K in the *dc* magnetisation data [See Fig. 6.4], it can be assumed that magnetic impurities are present in the data but make up a very small percentage of the sample and thus are not detected with measurements like heat capacity and neutron diffraction.

6.3 Mn_3RhGe

6.3.1 Sample preparation

As in the previous section, a polycrystalline button of Mn_3RhGe was prepared by collaborators at the National Cheng Kung University by arc melting a stoichiometrically correct ratio of Mn, Rh, and Ge. Part of this button was ground into a powder and used for the powder x-ray diffraction, powder neutron diffraction, *dc* susceptibility, and heat capacity measurements, while the rest of the button was used for the *dc* susceptibility measurements.

6.3.2 Enery dispersive x-ray analysis

The stoichiometry of the Mn_3RhGe button was analysed using energy dispersive x-ray measurements. An average over seventeen spectra gave a stoichiometry of $Mn_{2.99(10)}Rh_{0.827(2)}Ge_{1.18(10)}$. This is very close to the desired stoichiometry, especially for the Mn content, which is critical. A deficiency in Rh exists throughout the material, however, which seems relatively constant throughout the material.An

Table 6.5: Energy dispersive x-ray analysis spectra measured from Mn_3RhGe with associated errors of ±1 %. The first table corresponds to the macroscopic surface of unpolished Mn_3RhGe, while the second displays spectra taken on a microscopic scale - see Fig. 6.9(a) and (b), respectively.

.

Polycrystalline button			
Spectrum Number	Mn (%)	Rh (%)	Ge (%)
2	64	17	20
3	64	16	20
4	64	17	20
5	58	17	25
6	61	17	23
7	60	17	23
8	60	17	24
9	58	17	25
10	58	17	26
11	60	16	24
12	59	16	25
13	60	15	24
14	60	17	24
15	58	17	25
16	59	17	24
17	57	17	27
18	59	17	25

Metallographic slide				
Spectrum Number	Area surveyed	Mn (%)	Rh (%)	Ge (%)
18	(i)	62	17	21
19	(i)	62	17	21
20	(i)	62	17	21
21	(i)	62	17	21
22	(i)	62	17	21
23	(i)	62	19	19
24	(i)	62	19	19
25	(i)	62	19	19
26	(ii)	61	11	28
27	(ii)	60	13	27
28	(ii)	60	11	28
29	(iii)	73	3	25
30	(iii)	72	3	24
31	(iii)	73	3	24

example of an SEM image is displayed in Fig. 6.9(a).

In order to examine the deficiency in Rh more closely, a metallographic slide

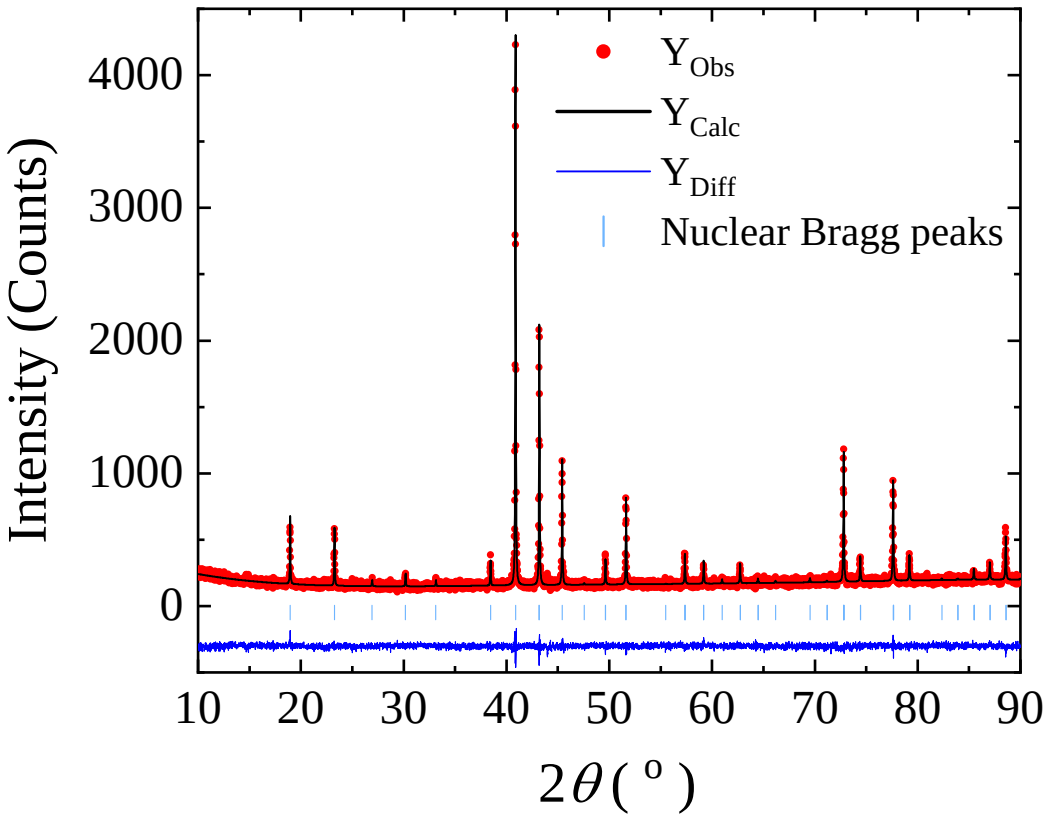

Figure 6.10: Powder x-ray diffraction profile of Mn_3RhGe, taken at room temperature.

was prepared by polishing a polycrystalline shard of Mn_3RhGe until it was appropriately flat, and this was examined in order to check for phase boundaries within this material [See Fig. 6.9(b)]. Three separate phases are observed with average stoichiometry of: (i) $Mn_{3.105(10)}Rh_{0.89(3)}Si_{1.00(4)}$, (ii) $Mn_{3.019(8)}Rh_{0.58(3)}Si_{1.39(2)}$, and (iii) $Mn_{2.902(12)}Rh_{0.122(13)}Si_{0.975(10)}$. The first phase, which is the desired phase, is the most prominent. The least prominent phase is likely Mn_3Ge, with the small amount of Rh seen in the EDX measurements due to the sampling of the surroundings because of the small size of the pockets of this phase. The values for both EDX measurements are displayed in Table 6.5.

6.3.3 Powder x-ray diffraction

Powder x-ray diffraction measurements were used to confirm the phase purity of Mn_3RhGe. The data was found to form in cubic space group $P2_13$ with a lattice parameter of a = 6.61727(12) Å. The R-factors extracted from the fit were

Table 6.6: Atomic coordinates used for powder x-ray diffraction Rietveld refinement for Mn_3RhGe for the cubic space group $P2_13$ and a refined lattice parameter of a = 6.61727(12) Å.

Atom	x	y	z	Occ.	B_{iso} (Å^2)
Mn1	0.1283(18)	0.2147(15)	0.4479(13)	1	0.1
Rh1	0.6866(6)	0.6866(6)	0.6866(6)	1	0.1
Ge1	0.0620(9)	0.0620(9)	0.0620(9)	1	0.1

$R_{wp} = 9.69\%$, $R_{exp} = 7.25\%$ and $R_p = 7.24\%$, which indicate excellent agreement between the calculated fit and the observed data. The atomic parameters extracted from the model are displayed in Table 6.6, with the thermal parameters set to 0.1. This was chosen as a reasonable estimate as the thermal parameters could not be refined accurately within this fit. The peaks that could not be indexed using this fit were both few in number and very low intensity, indicating that the impurity phases were small. These peaks did not match Mn_3Ge and thus may be associated with the unstudied Rh-deficient $Mn_{3.019(8)}Rh_{0.58(3)}Si_{1.39(2)}$ phase observed in the EDX measurements.

6.3.4 Heat capacity

Heat capacity measurements for Mn_3RhGe are shown in Fig. 6.11. Mn_3RhGe shows a transition at $T = 216$ K, which is strong evidence of long-range magnetic ordering in this material. No additional transitions are observed in this dataset.

The behaviour seen is qualitatively similar to the heat capacity results for Mn_3IrSi. At low temperatures, as before, $C(T)/T = \gamma + \beta T^2 + \delta T^4$. Fitting this function resulted in values of $\gamma = 2.636(7) \times 10^{-4}$ J/mol K and $\Theta_D = 398(4)$ K.

The lattice contribution to the heat capacity was estimated using the Debye model, as before (see Equartion 6.1), and the Dulong-Petit value, $15R$, was exceeded at high temperatures, due to high γ contribution as well as possible anharmonic contributions to the lattice. The Debye temperature obtained from the model was $\Theta_D = 340(30)$ K. This is considerably below the value calculated from the low temperature fit, indicating that these values are only an approximation due to the flexibility of the fit. The phonon contribution was then subtracted in order to allow the calculation of the change in magnetic entropy over the magnetic transition, giving $\Delta S = 36(5)$ J/mol K for Mn_3RhGe, which is close to the value expected for Mn^{4+}, $\Delta S = 34.8$ J/mol K.

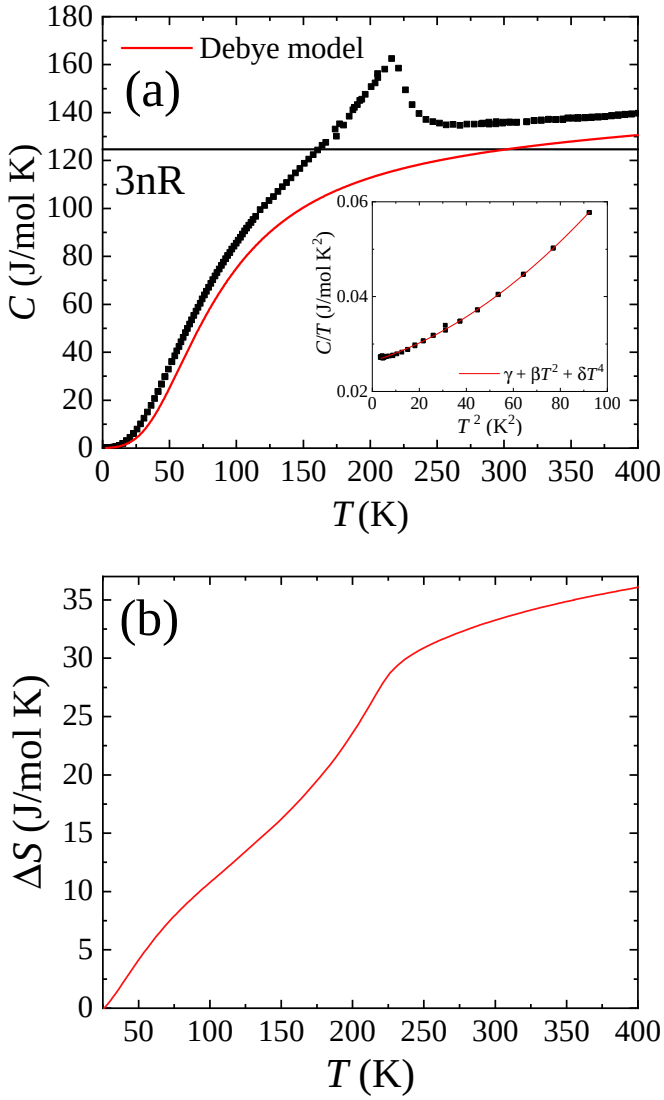

Figure 6.11: (a) Heat capacity versus temperature collected in zero field for Mn_3RhGe. (b) The change in the magnetic entropy as a function of temperature.

6.3.5 *dc* magnetisation

The *dc* susceptibility measurements for and Mn_3RhGe are shown in Fig. 6.12. The Nèel temperature T_N =225 K was extracted from maxima in $d(\chi T)/dT$. Another transition is present at 120 K that is attributed to an impurity phase of MnO in the material, and around this transition and at lower temperatures hysteresis is observed between the ZFC and FCC measurements.

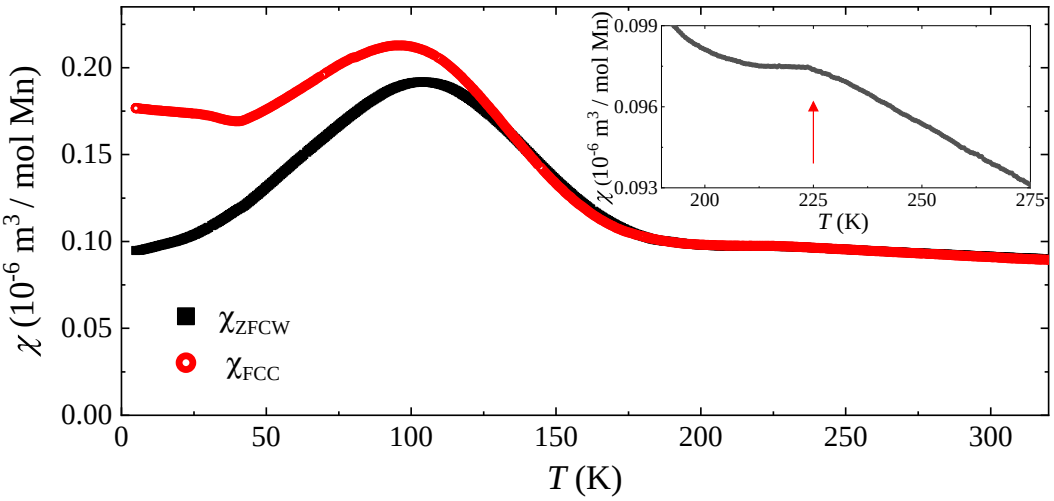

Figure 6.12: Temperature dependence of the dc susceptibility, $\chi_{\mathrm{dc}}(T)$, for Mn_3RhGe collected in zero-field-cooled warming (ZFC) and field-cooled cooling (FCC) modes in an applied field of 25 mT. The inset shows the ZFC warming data around the transition temperature of the main phase, which is marked with an arrow.

Mn_3XY family of materials are extremely sensitive to the exact stoichiometry of manganese in the material, with even very small variations in the amount present having visible effects on the magnetisation profiles [48]. Different shards of material from the same batch had small differences in magnetisation because of this, and the presence of MnO and other magnetic impurities seems to dominate the *dc* susceptibility measurements. The height of the Curie tail is one aspect that is very sample dependent.

In some measurements a further apparently ferromagnetic transition is present at 368 K that can be associated with Mn_3Ge, which is antiferromagnetic with a small ferromagnetic component. This can be confirmed by eye, as the Mn_3RhGe button was able to be manipulated with a magnet at room temperature. Despite this, no transition was present in the heat capacity at 368 K, which indicates that this impurity phase is very small.

6.3.6 Powder neutron diffraction

The nuclear structure of Mn_3RhGe was calculated using a powder neutron diffraction measurement at 300 K, see Fig. 6.13. It was found to form in the cubic $P2_13$ space group with a lattice parameter of $a = 6.62104(9)$ Å. This is close to the value found for the lattice parameter of this material in PXRD measurements, as illustrated in

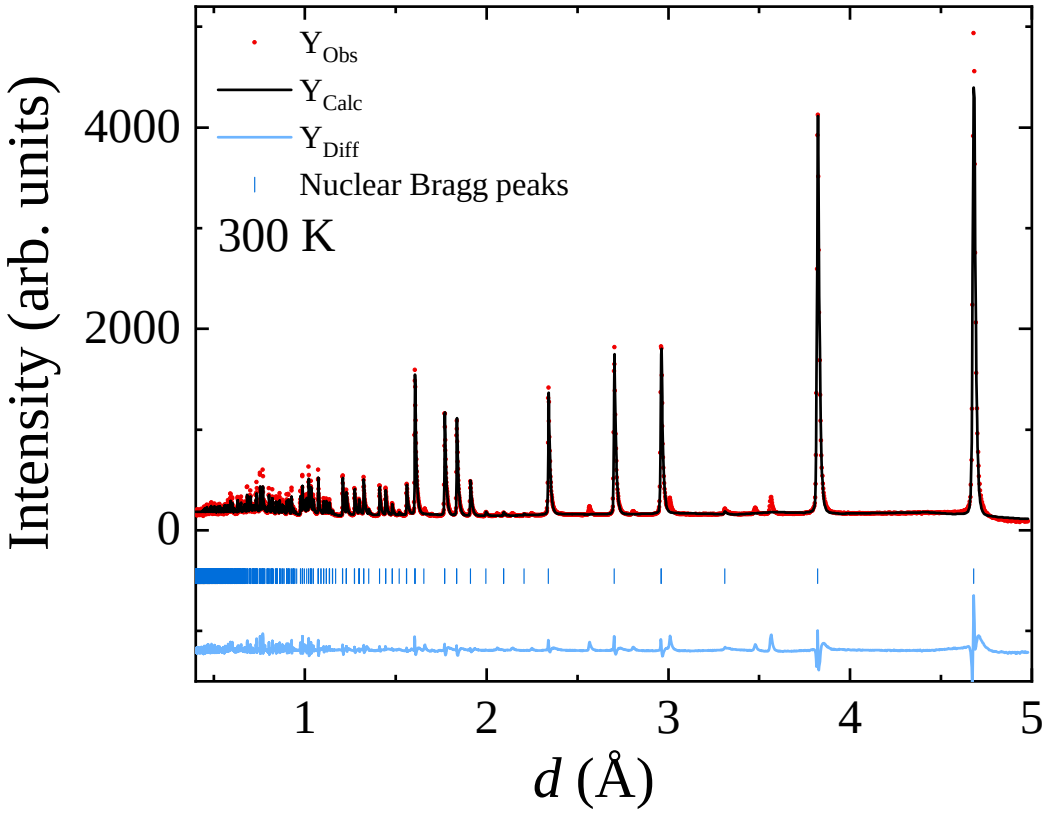

Figure 6.13: Neutron powder diffraction profiles at 300 K for Mn_3RhGe, with a calculated nuclear fit.

Fig. 6.10. Several impurity peaks were observed in the data, some of which were indexed as MnO, which was also visible in the *dc* susceptibility measurements (see Fig. 6.12) as part of the broad peak at 120 K. These impurities were excluded from the range of data for the calculated fit.

The calculated Bragg R-factor for this fit was $R_{\mathrm{Bragg}} = 4.612$ %. The atomic positions for this fit at several temperatures are tabulated in Table 6.7, where it can be seen that at room temperature they are similar to the values in Table 6.10, as expected.

The diffraction patterns for Mn_3RhGe for several different temperatures are displayed in Fig. 6.14(a). As with Mn_3IrSi, the data range has been restricted to be between 2.0 and 7.5 Å to focus on the region of interest and the data displayed is for an average 2θ value of 54°. Magnetic peaks begin to appear between 200 and 260 K, which is in line with the transition temperature of $T_{\mathrm{N}} =$ 216 K extracted from the heat capacity data. No obvious hallmarks of short range ordering, i.e.

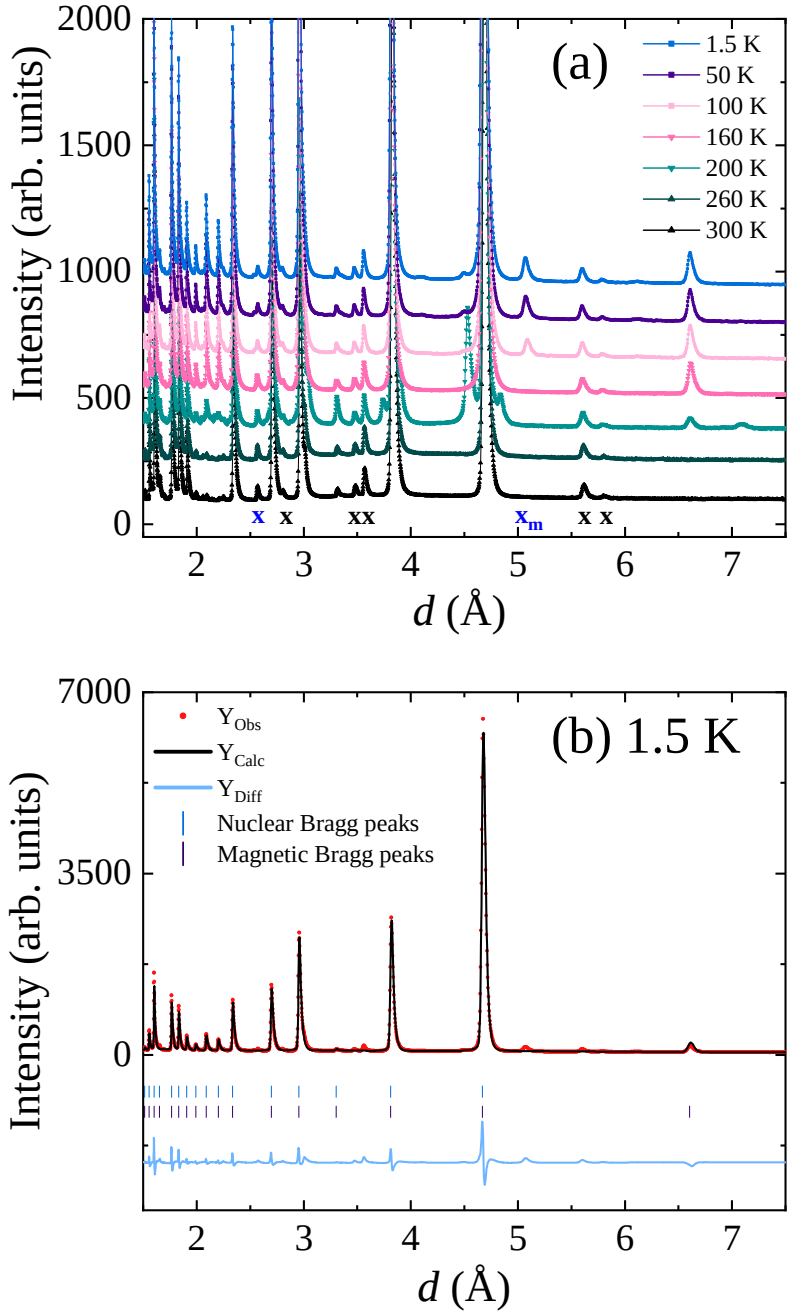

Figure 6.14: (a) Neutron powder diffraction profiles at temperatures ranging from base to 300 K for Mn_3RhGe, offset by 150 counts each for clarity. Impurity peaks are marked with an x, with magnetic impurity peaks marked with x_m. MnO impurity peaks are marked in blue whereas unindexed impurities are marked in black. (b) The nuclear and magnetic fit to the data at 1.5 K, with each phase refined separately.

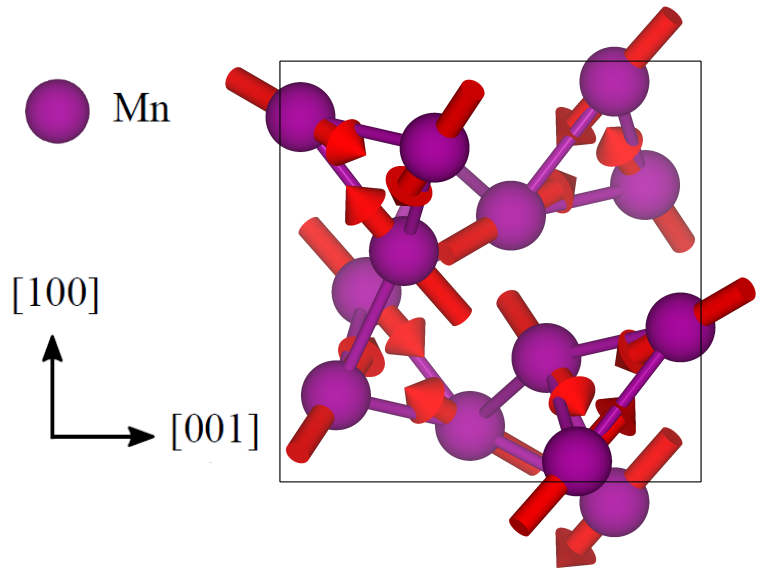

Figure 6.15: The twelve Mn atoms of Mn_3RhGe are displayed with magnetic moments (red arrows) to illustrate the ground state magnetic structure.

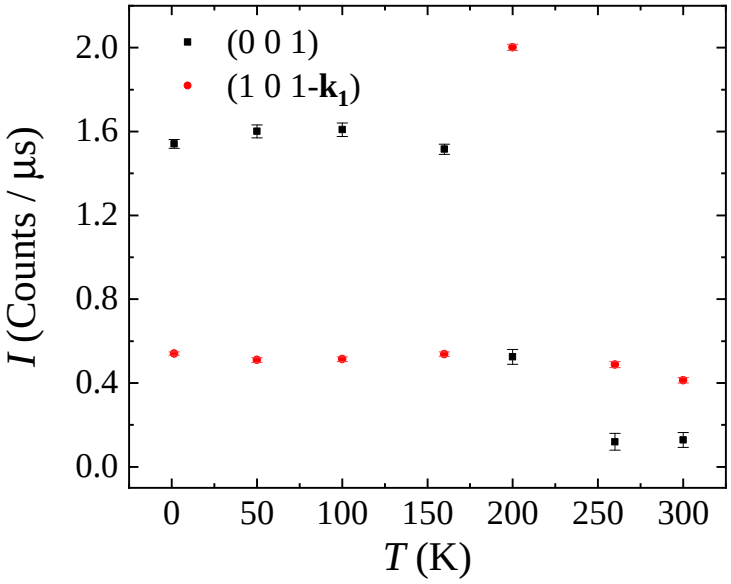

Figure 6.16: Integrated intensities of Bragg reflections (001) and $(101 - \mathbf{k_1})$ as a function of temperature.

broad magnetic peaks, are present at any temperatures for either material.

The main magnetic phase was fit at base temperature 1.5 K and is displayed

Table 6.7: Atomic coordinates for Mn_3RhGe extracted from a powder neutron diffraction refinement at 300 K in the cubic space group $P2_13$ with lattice parameter $a = 6.62104(9)$ Å and Bragg R-factor $R_{\text{Bragg}} = 4.612\%$.

300 K					
$R_{\text{Bragg}} = 4.612\%$				$a = 6.62104(9)$ Å	
Atom	x	y	z	Occ.	B_{iso} (Å^2)
Mn1	0.117(2)	0.2017(10)	0.4572(11)	1	1.37(10)
Rh1	0.6861(9)	0.6861(9)	0.6861(9)	1	1.5(3)
Ge1	0.0636(6)	0.0636(6)	0.0636(6)	1	0.91(12)
200 K					
$R_{\text{Bragg}} = 11.83\%$		$R_{\text{Mag}} = 14.83\%$		$a = 6.6105(1)$ Å	
Atom	x	y	z	Occ.	B_{iso} (Å^2)
Mn1	0.144(2)	0.2098(15)	0.454(2)	1	0.12(2)
Rh1	0.6888(11)	0.6888(11)	0.6888(11)	1	0.000(3)
Ge1	0.0671(9)	0.0671(9)	0.0671(9)	1	0.053(6)
1.5 K					
$R_{\text{Bragg}} = 4.21\%$		$R_{\text{Mag}} = 5.93\%$		$a = 6.60100(5)$ Å	
Atom	x	y	z	Occ.	B_{iso} (Å^2)
Mn1	0.120(2)	0.2060(14)	0.452(2)	1	1.05(9)
Rh1	0.6862(11)	0.6862(11)	0.6862(11)	1	1.4(3)
Ge1	0.0640(8)	0.0640(8)	0.0640(8)	1	0.36(14)

in Fig. 6.14(b) using the bank with an average 2θ of 54°. It was found that these data were best modelled using a $\mathbf{k_0} = (0, 0, 0)$ propagation vector with the same four possible irreducible representations available as for Mn_3IrSi, and the irreducible representation that best models this data is the same vector as found for Mn_3IrSi, $\text{m}\Gamma_1(\eta_1, \eta_2, \eta_3)$ and magnetic space group $P2_13.1$. The refined moment size was 3.07(1) μ_{B}. The magnetic structure for this material is displayed in Fig. 6.15, and more details regarding the irreducible representation are displayed in Table 6.4.

The (001) and $(101 - \mathbf{k_1})$, where $\mathbf{k_1} = (0.066, 0, 0)$, Bragg reflections were then analysed by measuring how the integrated intensity varied with temperature, as displayed in Fig. 6.16. A decrease in intensity is visible that reaches a minimum value between around 200 and 260 K, which agrees with the transition temperature extracted from heat capacity and dc susceptibility measurements. The $(101 - \mathbf{k_1})$ Bragg reflection was fully suppressed at temperatures below 160 K and above 260 K.

Additional magnetic phases are present in the measured sample of Mn_3RhGe. A small impurity phase of MnO becomes magnetic at temperatures below 120 K, and these magnetic peaks were excluded from the fit. This impurity is visible in the *dc* susceptibility data as part of the broad peak at 120 K. Furthermore, at 200 K,the

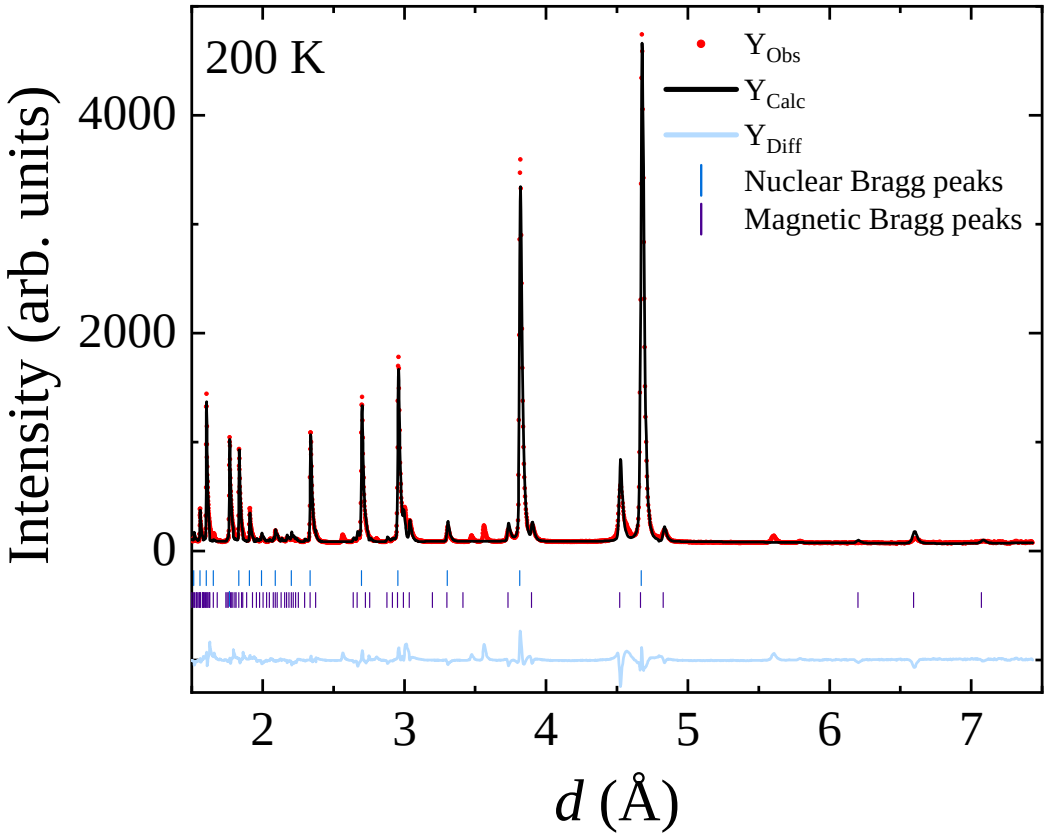

Figure 6.17: Neutron powder diffraction profile at 200 K for Mn_3RhGe.

magnetism is clearly incommensurate, with multiple large magnetic satellite peaks observable. These incommensurate peaks cannot be accounted for using the $\mathbf{k_0} = (0, 0, 0)$ propagation vector, and required the use of an incommensurate propagation vector of $\mathbf{k_1} = (0.066, 0, 0)$ instead to index them.

The fit to the incommensurate magnetic structure is displayed in Fig. 6.17, for which the best fit was found to be for magnetic space group $P2_12_12_1.1'(0, 0, g)000s$ and irreducible representation $\mathrm{m}\Delta_1(\xi_1, \xi_2, \xi_3)$, with a refined moment size of 3.10(4) μ_B. The other available irreducible representation, $\mathrm{m}\Delta_2$, was trialled and found a worse fit for the data. Fitting to the $P2_12_12_1.1'(0, 0, g)000s$ magnetic space group resulted in a helical magnetic winding along the direction indicated by the propagation vector $\mathbf{k_1}$. This winding is long, and is illustrated in Fig. 6.18. This pocket of incommensurate magnetism is a desirable area for future study due to the potential of stabilising some topological phenomenon such as skyrmions with the application of a magnetic field in this temperature region.

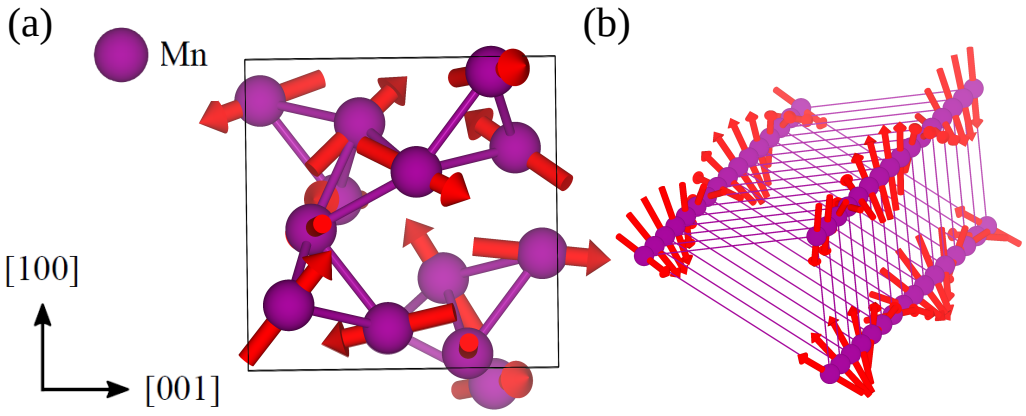

Figure 6.18: Structure of the incommensurate magnetic phase found in Mn_3RhGe at 200 K shown (a) in its nuclear unit cell and (b) extended along the c direction for a single triangular array of Mn atoms to better show the evolution of its helical winding. The refined moment size of the Mn atoms is found to be 3.10(4) μ_B.

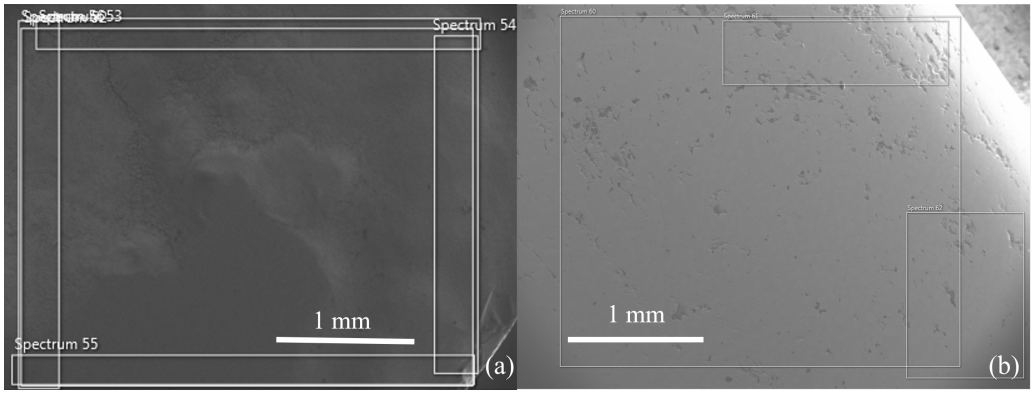

Figure 6.19: Example SEM images of Mn_3RhSi (a) polycrystalline button with spectra 52 - 55 marked and (b) single crystal with spectra 60 - 62 marked.

6.4 Mn_3RhSi

6.4.1 Sample preparation

A polycrystalline button of Mn_3RhSi was synthesised in-house at the University of Warwick by arc melting a stoichiometric ratio of Mn, Rh, and Si into three separate buttons before combining them. While the final button itself was used for most measurements, part of this button was ground into a powder and used for the

Table 6.8: Energy dispersive x-ray analysis spectra measured from polycrystalline and single crystal Mn_3RhSi with associated errors of ±1 %.

Polycrystalline button			
Spectrum Number	Mn (%)	Rh (%)	Si (%)
38	53	18	29
39	57	17	26
40	56	18	26
41	53	17	30
42	55	18	27
43	53	18	29
44	57	17	27
45	51	19	30
46	51	19	31
47	62	17	21
48	58	19	23
49	59	18	23
50	62	17	21
51	62	17	21
52	59	18	23
53	60	17	22
54	59	18	23
55	60	18	22
56	60	17	23
Single crystal			
Spectrum Number	Mn (%)	Rh (%)	Si (%)
57	50	23	28
58	48	21	31
59	46	25	29
60	49	24	28
61	45	25	30
62	47	24	29
63	52	23	25
64	49	24	27
65	48	24	29
66	51	23	26
67	55	22	23

powder x-ray diffraction measurements.

A single crystal of Mn_3RhSi was then grown from the final button using a modified version of Bridgman technique as discussed in Chapter 3: Experimental Details, by sealing the polycrystalline sample inside a conical alumina crucible inside a quartz ampoule. The ampoule was evacuated and then filled with 1/3 atm of argon

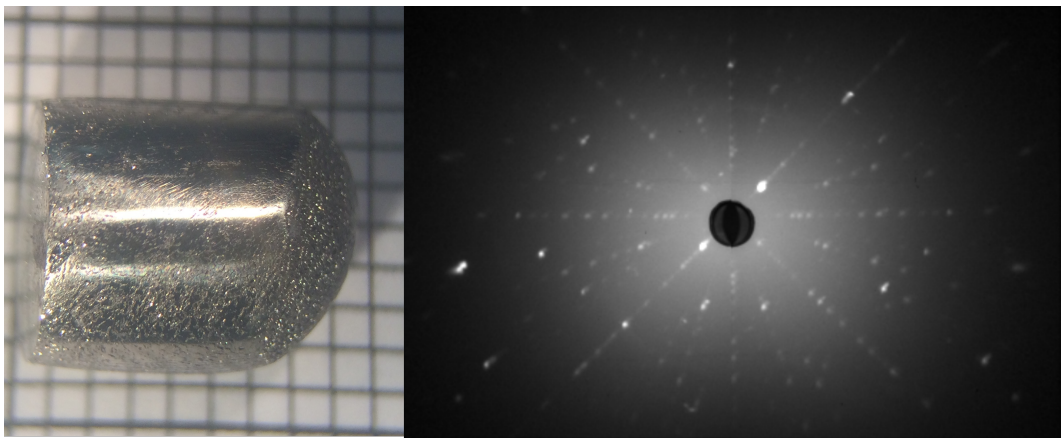

Figure 6.20: Single crystal of Mn_3RhSi and a Laue diffraction pattern of the [001] direction, taken from the cross-section of this crystal.

gas, before being heated in a box furnace to 950 °C and held at this temperature for 72 hours. The material was then cooled to 750 °C at a rate of 3°C/hr, held at this temperature for 24 hours, and quenched in cold water.

6.4.2 Energy dispersive x-ray analysis

Energy dispersive x-ray analysis was used to analyse the stoichiometry of the Mn_3RhSi button used in the *dc* susceptibility measurements. An average over nineteen spectra gave a stoichiometry of $Mn_{2.9(2)}Rh_{0.89(3)}Si_{1.3(2)}$. An example of an SEM image with some of the spectra marked is shown in Fig. 6.19(a). As with Mn_3RhGe, the material appears to be slightly deficient in rhodium, though in this case it is to a lesser degree.

The single crystal sample was analysed in the same manner, see Fig. 6.19(b). The stoichiometry was analysed over eleven spectra and found to be $Mn_{2.44(8)}Rh_{1.17(4)}Si_{1.38(7)}$, indicating that a significant amount of Mn was lost from the surface of the crystal during the process of crystal growth. This is likely to have happened due in part to a reaction of the Mn and the quartz, as some of the melt was found to have moved outside of the alumina crucible during the crystal growth process. The results for all spectra measured for both the polycrystalline and single crystal samples are tabulated in Table 6.8.

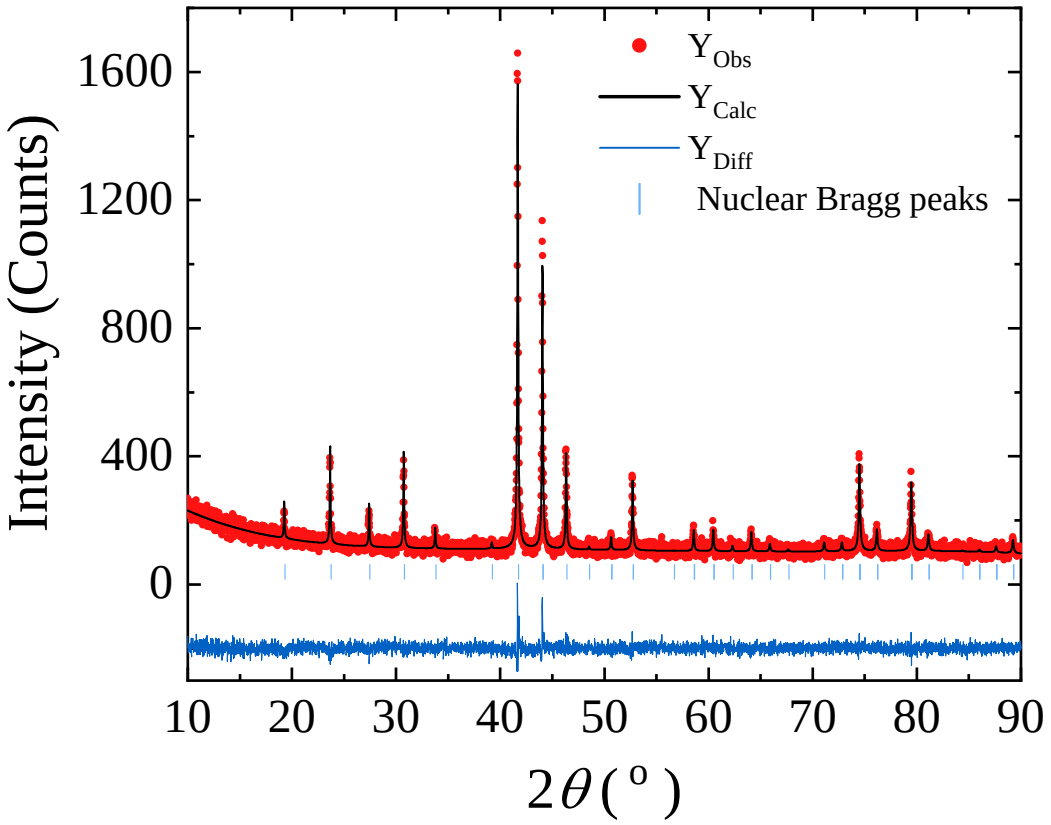

Figure 6.21: Powder x-ray diffraction profile of Mn_3RhSi, taken at room temperature.

Table 6.9: Atomic coordinates used for powder x-ray diffraction Rietveld refinement for Mn_3RhSi for the cubic space group $P2_13$.

Atom	x	y	z	Occ.	B_{iso} (Å^2)
Mn1	0.1216(8)	0.2087(9)	0.4562(7)	1	0.52(9)
Rh1	0.6828(4)	0.6828(4)	0.6828(4)	1	0.52(9)
Si1	0.0606(15)	0.0606(15)	0.0606(15)	1	0.52(9)

6.4.3 Laue diffraction

Laue diffraction was used to check the quality of the single crystal after polishing, as displayed in Fig. 6.20. The crystal was found to be single grain and highly crystalline through most areas of the crystal.

6.4.4 Powder x-ray diffraction

Powder x-ray diffraction measurements were used to check the phase purity of the sample, see Fig. 6.21. Most peaks were able to be indexed using the $P2_13$ space group with a lattice parameter of $a = 6.48491(15)$ Å, though several very small peaks associated with impurities were visible. The R-factors extracted from the fit were $R_{wp} = 9.26\%$, $R_{exp} = 8.75\%$ and $R_p = 7.37\%$, indicating good agreement between the calculated and observed data. The atomic parameters extracted from the model are displayed in Table 6.2. The thermal parameters were allowed to vary for this refinement but were constrained to the same value to limit the amount of free parameters that were refined.

6.4.5 *dc* magnetisation

An example of a *dc* susceptibility measurement on a polycrystalline Mn_3RhSi button is shown in Fig. 6.22. The Nèel temperatures are again extracted from maxima in $d(\chi T)/dT$. For Mn_3RhSi, we see three transitions at approximately $T_N =$ 181 K, 236 K, and 276 K. As in the case with Mn_3RhGe, these *dc* susceptibility measurements were dominated by impurities and thus were somewhat sample dependent. The transition at approximately 236 K was present in all samples and thus can be associated with the main phase.

A large amount of hysteresis occurs between the ZFC and FCC data below approximately 200 K, and a sharp downturn in the moment is present in the ZFC data at temperatures below 20 K that is not visible in the FCC data. Similar hysteresis is seen in the *dc* suscpetibility measurements for Mn_3RhGe.

6.5 Summary

In conclusion, in the investigation into the Mn_3XY family a single crystal of Mn_3RhSi has been successfully synthesised and then oriented with laue diffraction. Polycrystalline samples of Mn_3IrSi and Mn_3RhGe have been investigated using *dc* susceptbility and powder neutron diffraction measurements.

Mn_3IrSi, Mn_3RhGe, and Mn_3RhSi all undergo magnetic transitions, which are tabulated in Table 6.10. These transitions are antiferromagnetic in nature and determined using the $d(\chi T)/d(T)$ method. However, *dc* susceptibility measurements for these samples are dominated by magnetic impurities and show a degree of sample dependence.

The heat capacity measurements show no additional transitions present in

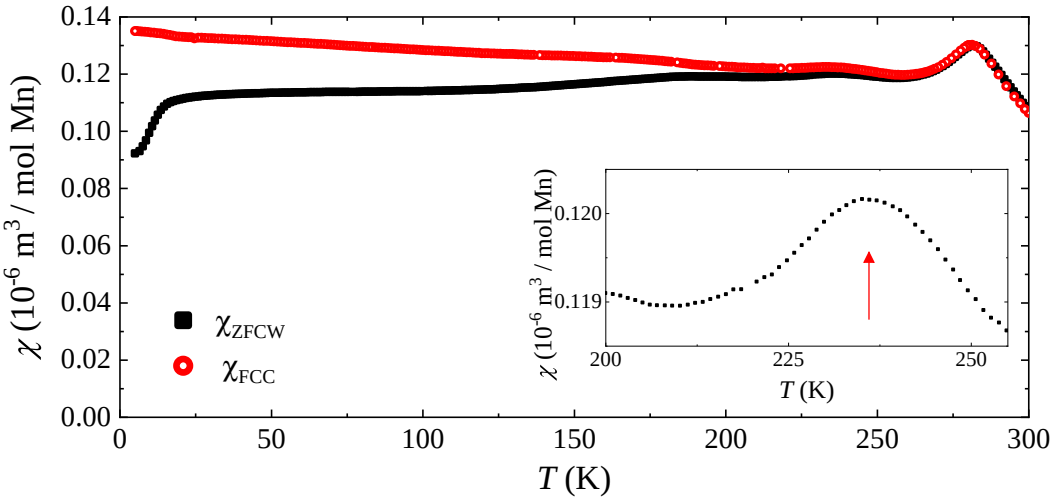

Figure 6.22: Temperature dependence of the dc susceptibility, $\chi_{\mathrm{dc}}(T)$, for Mn_3RhSi collected in zero-field-cooled warming (ZFC) and field-cooled cooling (FCC) modes in an applied field of 25 mT. The inset shows the ZFC warming data around the transition temperature of the main phase, which is marked with an arrow.

Mn_3RhGe, indicating that only small amounts of magnetic impurities are present, which is corroborated by the powder neutron and x-ray diffraction measurements. Two magnetic transitions are visible at 208 and 225 K in the heat capacity data for Mn_3IrSi. Only one transition temperature can be extracted from the *dc* susceptibility near these temperatures, which occurs at the average of them, 215 K. Likewise, in the neutron powder diffraction, only one transition is observed. The heat capacity data saturates at levels higher than $3nR$ in both materials due to a considerable contribution from the electronic heat capacity γ. The magnetic entropy indicates that the most likely valence state for these materials in Mn^{4+}.

The neutron powder difffraction measurements reveal that both Mn_3IrSi and Mn_3RhGe share a frustrated antiferromagnetic ground state that is consistent with the literature for Mn_3IrSi. A further incommensurate magnetic phase in Mn_3RhGe is stabilised before it relaxes into its ground state at a temperature between 200 and 160 K. This helical magnetic phase in Mn_3RhGe is interesting with regards to its potential for hosting novel magnetic phenomena. The Mn_3XY family and β-Mn structure-type materials are interesting candidates for further study with this in mind.

Table 6.10: Magnetic ordering and transition temperatures T_O obtained for Mn_3IrSi, Mn_3RhGe, and Mn_3RhSi from *dc* susceptibility and heat capacity (HC) measurements.

Formula	$T_{N,dc}$ (K)	$T_{N,HC}$ (K)	Ground state magnetic ordering	Additional Information
Mn_3IrSi	215	208, 225	Frustrated antiferromagnet	
Mn_3RhGe	225	216	Frustrated antiferromagnet	Helical state at 200 K seen with neutron powder diffraction.
Mn_3RhSi	236	N/A	Frustrated antiferromagnet	

Chapter 7

Conclusions and further work

In conclusion, detailed investigations have been carried out on several different chiral magnetic materials. In this chapter, the work will be summarised, and any potential avenues for future inquiry will be remarked upon.

A detailed investigation into the magnetic structure of intercalated transition metal dichalcogenide $V_{1/3}NbS_2$ was described in Chapter 4, using *ac* and *dc* susceptibility measurements, and powder and single crystal neutron diffraction. This material was found to display behaviour consistent with canted antiferromagnetism at temperatures below 50 K. For example, magnetic fields of up to 10 T were not sufficient to saturate $V_{1/3}NbS_2$, and the maximum moment reached was $\approx 0.2\ \mu_B$, which is expected for antiferromagnets. The *dc* susceptibility measurements indicated the presence of a small ferromagnetic component to $V_{1/3}NbS_2$.

Neutron measurements indicated that to fully describe the magnetism inherent to $V_{1/3}NbS_2$, two magnetic propagation vectors were required. A $\mathbf{k_0}$ = (0,0,0) propagation vector described an A-type antiferromagnetic ordering, while a $\mathbf{k_{1/3}}$ = (0,0,1/3) propagation vector described the evolution of an up-down-down configuration of moments along the *c* axis throughout the magnetic unit cell. Due to the small size of the ferromagnetic component, these measurements were unable to resolve which component of the magnetism it was associated with. Additionally, diffuse magnetic scattering was found between the (010) and $(01 \pm 1/3)$ Bragg peaks in single crystal neutron diffraction measurements.

In order to resolve the unanswered questions about the magnetic structure of $V_{1/3}NbS_2$, complementary techniques such as muon spin relaxation are needed. Beamtime has been awarded to members of the UK Skyrmion Project for this investigation. Additionally, high-field measurements are required to find the saturation magnetisation and field for this material.

In Chapter 5, three intercalated transition metal dichalcogenides - $Cr_{1/3}NbS_2$, $Cr_{1/3}TaS_2$, and $Mn_{1/3}NbS_2$ - were compared and contrasted. Phase diagrams were constructed for each material using *ac* susceptibility measurements that revealed the real susceptibility, χ', for the ground state magnetic orderings of $Cr_{1/3}NbS_2$ and $Cr_{1/3}TaS_2$ were considerably higher than that of the ground state ordering of $Mn_{1/3}NbS_2$. Additionally, a magnetic transition was found to vary in temperature with frequency in $Mn_{1/3}NbS_2$, which is reminiscent of spin glass behaviour. Furthermore, additional reflections in single crystal x-ray and electron diffraction measurements on single crystals of $Mn_{1/3}NbS_2$ indicate the presence of a complex twin system.

Using LTEM measurements, a helimagnetic ground state was observed in a single crystal of $Cr_{1/3}NbS_2$ with a suppressed transition temperature of 111 K. The suppression of this transition temperature was attributed to disorder effects, which were also used to explain the areas in the LTEM images where the helical order appeared to break. Additionally, the LTEM measurements for $Mn_{1/3}NbS_2$ below $T_C = 45$ K were consistent with what would be expected for a ferromagnet with domains.

Further work is required to understand both the nuclear and magnetic structure of $Mn_{1/3}NbS_2$. Neutron studies have been undertaken on this material and are currently being analysed in order to uncover its true magnetic ground state. Lorentz transmission electron microscopy on synthesised $Cr_{1/3}TaS_2$, the suppressed transition temperature of which would suggest that it is disordered, would also allow a comparison to see whether the periods of broken helicity seen for $Cr_{1/3}NbS_2$ are also present for this material.

Finally, this thesis described the investigation into the frustrated antiferromagnets Mn_3RhSi, Mn_3RhGe, and Mn_3IrSi in Chapter 6, which adopt an ordered form of the β-Mn structure. Powder neutron diffraction measurements on polycrystalline Mn_3IrSi and Mn_3RhGe revealed a frustrated antiferromagnetic ground state for both materials, with the angles of 120° between the magnetic moments. An additional incommensurate helical magnetic phase at 200 K was also measured for Mn_3RhGe. A single crystal of Mn_3RhSi was successfully synthesised and characterised using powder and Laue x-ray diffraction measurements, as well as *dc* susceptibility measurements.

To conclude the work on these materials, neutron diffraction measurements on Mn_3RhSi would be useful in determining its ground state magnetic ordering and magnetic phase diagram. Additional investigations into the helical phase of Mn_3RhGe and the synthesis of a single crystal of this material are required to fully

understand its magnetic behaviour.

The results in this thesis help to elucidate the differences between the magnetic structures of several intercalated transition metal dichalcogenides, and to indicate which members of the Mn_3XY family are interesting as potential skyrmion hosts.

Bibliography

[1] B. D. Cullity and C. D. Graham, *Introduction to Magnetic Materials*. John Wiley and Sons, 2 ed., 2008.

[2] A. Bauer and C. Pfleiderer *Springer Series in Materials Science*, vol. 228, pp. 1–28, 2016.

[3] Y. Togawa, T. Koyama, K. Takayanagi, S. Mori, Y. Kousaka, J. Akimitsu, S. Nishihara, K. Inoue, A. S. Ovchinnikov, and J. Kishine *Phys. Rev. Lett.*, vol. 108, p. 107202, 2012.

[4] Y. Cao, Z. Huang, Y. Yin, H. Xie, B. Liu, W. Wang, C. Zhu, D. Mandrus, L. Wang, and W. Huang *Materials Today Advances*, vol. 7, p. 100080, 2020.

[5] D. A. Mayoh, J. Bouaziz, A. E. Hall, J. B. Staunton, M. R. Lees, and G. Balakrishnan *Submitted*, 2021.

[6] T. Skyrme *Nuclear Physics*, vol. 31, pp. 556–569, 1962.

[7] S. Mühlbauer, B. Binz, F. Jonietz, C. Pfleiderer, A. Rosch, N. A., R. Georgii, and P. Böni

[8] S. Seki and M. Mochizuki, *Skyrmions in Magnetic Materials*. New York: Springer International Publishing, 2016.

[9] S. Heinze, K. von Bergmann, M. Menzel, J. Brede, A. Kubetzka, R. Wiesendanger, G. Bihlmayer, and S. Blügel

[10] N. Romming, C. Hannekan, M. Menzel, J. E. Bickel, B. Wolter, K. von Bergmann, A. Kubetzka, and R. Wiesendanger

[11] S. A. Meynell, M. N. Wilson, K. L. Krycka, B. J. Kirby, H. Fritzche, and T. L. Monchesky

[12] C. S. Spencer, J. Gayles, N. A. Porter, S. Sugimoto, Z. Aslam, C. J. Kinane, T. R. Charlton, F. Freimuth, S. Chadov, S. Langridge, J. Sinova, C. Felser, S. Blügel, Y. Mokrousov, and C. H. Marrows

[13] S. A. Meynell, M. N. Wilson, H. Frietzsche, A. N. Bogdanov, and T. L. Monchesky

[14] Y. Wu, S. Zhang, J. Zhang, W. Wang, Y. L. Zhu, J. Hu, G. Yin, K. Wong, C. Fang, and C. Wan

[15] W. Sun, W. Wang, H. Li, G. Zhang, D. Chen, J. Wang, and Z. Cheng

[16] C.-K. Li, X.-P. Yao, and G. Chen

[17] W. Sun, W. Wang, J. Zang, H. Li, G. Zhang, J. Wang, and Z. Cheng

[18] Y. Tokunaga, X. Z. Yu, J. S. White, H. M. Rønnow, D. Morikawa, Y. Taguchi, and Y. Tokura *Nat. Comm.*, vol. 6, p. 7638, 2015.

[19] V. Sliwko, P. Mohn, and K. Schwarz *J. Phys.: Condens. Matter*, vol. 6, p. 6557, 1994.

[20] H. Nakamura, K. Yoshimoto, M. Shiga, M. Nishi, and K. Kakurai *J. Phys.: Condens. Matter*, vol. 9, pp. 4701–4728, 1997.

[21] S. S. P. Parkin and R. H. Friend *Phil. Mag. B*, vol. 41:1, pp. 65–93, 1980.

[22] S. K. Karna, F. N. Womack, R. Chapai, D. P. Young, M. Marshall, W. Xie, D. Graf, Y. Wu, H. Cao, L. DeBeer-Schmitt, P. W. Adams, R. Jin, and J. F. DiTusa *Phys. Rev. B*, vol. 100, p. 184413, 2019.

[23] S. K. Karna, M. Marshall, W. Xie, L. DeBeer-Schmitt, D. P. Young, I. Vekhter, W. A. Shelton, A. Kovács, M. Charilaou, and J. F. DiTusa *Nano Lett.*, vol. 21, pp. 1205–1212, 2021.

[24] K. Lu, D. Sapkota, L. DeBeer-Schmitt, Y. Wu, H. B. Cao, N. Mannella, D. Mandrus, A. A. Aczel, and G. J. MacDougall *Phys. Rev. Materials*, vol. 4, p. 054416, 2020.

[25] F. Hulliger and E. Pobitschka *J. Solid State Chem.*, vol. 1, pp. 117–119, 1970.

[26] D. Obeysekera, K. Gamage, Y. Gao, S.-W. Cheong, and J. Yang *Adv. Electron. Mater.*, vol. 2021, p. 2100424, 2021.

[27]

[28] R. Yan, G. Khalsa, B. T. Schaefer, A. Jarjour, S. Rouvimov, K. C. Nowack, H. G. Xing, and D. Jenal *Appl. Phys. Express*, vol. 12, p. 023008, 2019.

[29] A. H. Castro Neto *Phys. Rev. Lett.*, vol. 86, p. 4382, 2001.

[30] R. L. Withers and J. A. Wilson *J. Phys. C.: Solid State Phys.*, vol. 19, p. 4809, 1986.

[31] J. A. Wilson, F. J. Di Salvo, and S. Mahajan *Adv. in Phys.*, vol. 24:2, pp. 117–201, 1975.

[32] K. Rossnagel *J. Phys.: Condens. Matter*, vol. 23, p. 213001, 2011.

[33] Z. Zhang, X. Zou, V. H. Crespi, and B. I. Yakobson *ACS Nano*, vol. 7, pp. 10475–10481, 2013.

[34] Z. Guguchia, A. Kerelsky, D. Edelberg, S. Banerjee, F. von Rohr, D. Scullion, M. Augustin, M. Scully, D. A. Rhodes, Z. Shermadini, H. Luetkens, A. Shengelaya, C. Baines, E. Morenzoni, A. Amato, J. C. Hone, R. Khasanov, S. J. L. Billinge, E. Santos, A. N. Pasupathy, and Y. J. Uemura *Sci. Adv.*, vol. 4, p. eaat3672, 2018.

[35] S. Tang, R. S. Fishman, S. Okamoto, J. Yi, Q. Zou, M. Fu, A.-P. Li, D. Mandrus, and Z. Gai *Nano. Lett.*, vol. 18, pp. 4023–4028, 2018.

[36] J. Lee, S. Pak, Y.-W. Lee, Y. Park, A.-R. Jang, J. Hong, Y. Cho, B. Hou, S. Lee, H. Y. Jeong, H. S. Shin, S. M. Morris, S. Cha, J. I. Sohn, and J. M. Kim *ACS Nano*, vol. 13, pp. 13047–13055, 2019.

[37] J. M. van den Berg and P. Cossee *Inorg. Chim. Acta*, vol. 2, p. 143, 1968.

[38] S. S. P. Parkin and R. H. Friend *Phil. Mag. B*, vol. 41:1, pp. 95–112, 1980.

[39] S. S. P. Parkin and A. R. Beal *Phil. Mag. B*, vol. 42:5, pp. 627–642, 1980.

[40] B. Van Laar, H. M. Rietveld, and D. J. W. Ijido *J. Solid State Chem.*, vol. 3, pp. 154–160, 1971.

[41] N. L. Nair, E. Maniv, C. John, S. Doyle, J. Orenstein, and J. G. Analytis *Nat. Mater.*, vol. 19, pp. 153–157, 2020.

[42] A. Little, C. Lee, C. John, S. Doyle, E. Maniv, N. L. Nair, W. Chen, D. Rees, S. Lee, H. Y. Jeong, H. S. Shin, S. M. Morris, J. W. F. Venderbos, R. M. Fernandes, J. G. Analytis, and J. Orenstein *Nat. Mater.*, vol. 19, pp. 1062–1067, 2020.

[43] N. J. Ghimire, A. S. Botana, J. S. Jiang, J. Zhang, Y. S. Chen, and J. F. Mitchell *Nat. Comm.*, vol. 9, p. 3280, 2018.

[44] Y. Kousaka, Y. Nakao, J. Kishine, M. Akita, K. Inoue, and J. Akimitsu *Nucl. Inst. Meth. Phys. Res. A*, vol. 600, pp. 250–253, 2009.

[45] Y. Kousaka, Y. Nakao, H. Furukawa, and J. Akimitsu *Activity Report on Neutron Scatt. Res.: Exp. Reports*, vol. 16, p. 814, 2009.

[46] G. W. Paterson, T. Koyama, M. Shinozaki, Y. Masaki, F. J. T. Goncalves, Y. Shimamoto, T. Sogo, M. Nord, Y. Kousaka, Y. Kato, S. McVitie, and Y. Togawa *Phys. Rev. B*, vol. 99, p. 224429, 2019.

[47] T. Eriksson, L. Berbqvist, O. Nordblad, O. Eriksson, and Y. Andersson *J. Solid State Chem.*, vol. 177, pp. 4058–4066, 2004.

[48] T. Eriksson, L. Bergqvist, Y. Andersson, P. Nordblad, and O. Eriksson *Phys. Rev. B*, vol. 72, p. 144427, 2005.

[49] D. Hobbs, J. Hafner, and D. Spišák *Phys. Rev. B*, vol. 68, p. 014407, 2003.

[50] Y. Kohori, Y. Noguchi, and T. Kohara *J. Phys. Soc. Jpn*, vol. 62, pp. 447–450, 1993.

[51] M. O'Keeffe and S. Andersson *Acta Crystallogr. A*, vol. 33, p. 914, 1977.

[52] T. Eriksson, R. Lizárraga, S. Felton, L. Bergqvist, Y. Andersson, P. Nordblad, and O. Eriksson *Phys. Rev. B*, vol. 69, p. 054422, 2004.

[53] T. Eriksson, S. Felton, R. Lizárraga, O. Eriksson, P. Nordblad, and Y. Andersson *Journal of Magnetism and Magnetic Materials*, vol. 272-276, pp. 823–825, 2004.

[54] T. Kurumaji, T. Nakajima, M. Hirschberger, A. Kikkawa, Y. Yamasaki, H. Sagayama, H. Nakao, Y. Taguchi, T.-H. Arima, and Y. Tokura *Science*, vol. 365, pp. 914–918, 2019.

[55] M. Hirschberger, T. Nakajima, S. Gao, L. Peng, A. Kikkawa, T. Kurumaji, M. Kriener, Y. Yamasaki, H. Sagayama, H. Nakao, K. Ohishi, K. Kakurai, Y. Taguchi, X. Yu, T.-H. Arima, and Y. Tokura *Nat. Commun.*, vol. 10, p. 5831, 2019.

[56] J. Kübler, *Theory of Itinerant Electron Magnetism*. Oxford Science Publications, 2000.

[57] R. Lizárraga, L. Nordström, L. Bergqvist, A. Bergman, E. Sjöstedt, P. Mohn, and O. Eriksson *Phys. Rev. Lett.*, vol. 93, p. 107205, 2004.

[58] C. Kittel, *Introduction to Solid State Physics*. New California: John Wiley and Sons.

[59] G. Bertotti, *Hysteresis in Magnetism: For Physicists, Materials Scientists, and Engineers*. San Diego: Academic Press, 1998.

[60] B. D. Cullity and S. R. Stock, *Elements of X-Ray Diffraction*. New Jersey: Prentice Hall, 3 ed., 2001.

[61] D. S. Sivia, *Elementary Scattering Theory: For X-ray and Neutron Users*. Oxford, UK: Oxford University Press, 2011.

[62] D. B. Williams and C. B. Carter, *Transmission Electron Microscopy*. New York, USA: Springer, 2nd ed., 2009.

[63] S. Blundell, *Magnetism in Condensed Matter*. Oxford University Press, 2001.

[64] J. B. Goodenough *Phys. Rev.*, vol. 100, p. 2, 1955.

[65] J. B. Goodenough *J. Phys. Chem. Solids*, vol. 6, pp. 2–3, 1958.

[66] J. Kanamori *J. Phys. Chem. Solids*, vol. 10, pp. 87–98, 1958.

[67] J. N. Lalena, D. A. Cleary, and O. B. M. H. Duparc, *Principles of Inorganic Materials Design*. Hoboken: John Wiley and Sons, 3 ed., 2020.

[68] M. A. Ruderman and C. Kittel *Phys. Rev.*, vol. 96, p. 99, 1954.

[69] T. Kasuya *Prog. Theor. Phys.*, vol. 16, pp. 45–47, 1956.

[70] K. Yosida *Phys. Rev.*, vol. 106, p. 893, 1957.

[71] Y. Yafet *Phys. Rev. B*, vol. 36, p. 3948, 1987.

[72] I. Dzyaloshinsky *Journal of Physics and Chemistry of Solids*, vol. 4, p. 241, 1958.

[73] T. Moriya *Phys. Rev.*, vol. 120, p. 91, 1960.

[74] P. Bak and M. H. Jensen *J. Phys. C.*, vol. 13, p. L881, 1980.

[75] L. D. Landau and E. M. Lifshitz, *Statistical Physics. Course of Theoretical Physics.* Oxford: Pergamon, 1997.

[76] Y. Tokura and N. Kanazawa *Chem. Rev.*, vol. 121, pp. 2857–2897, 2021.

[77] A. N. Bogdanov, U. K. Rößler, M. Wolf, and K.-H. Müller *Phys. Rev. B.*, vol. 66, p. 214410, 2002.

[78] M. E. Fisher *Phil. Mag.*, vol. 7:82, pp. 1731–1743, 1962.

[79] P. Bag, P. R. Baral, and R. Nath *Phys. Rev. B*, vol. 98, p. 144436, 2018.

[80] M. Perovic, V. Kusigerski, V. Spasojevic, A. Mrakovic, J. Blanusa, M. Zentkova, and M. Mihalik *J. Phys. D.: Appl. Phys.*, vol. 46, p. 165001, 2013.

[81] J. A. Ramos-Guivar, F. J. Litterst, and E. C. Passamani *Magnetochemistry*, vol. 7, p. 52, 2021.

[82] J. Hopkins and H. Kim *Phys. Rev. B*, vol. 74, p. 224441, 2006.

[83] A. Solontsov *J. Mag. Mag. Mater.*, vol. 383, pp. 19–22, 2015.

[84] M. Toda and K. Sogo *J. Phys. A. Math. Theor.*, vol. 51, p. 060201, 2018.

[85] A. Chacon, L. Heinen, M. Halder, A. Bauer, W. Simeth, S. Mühlbauer, H. Berger, M. Garst, A. Rosch, and C. Pfleiderer *Nat. Phys.*, vol. 14, pp. 936–941, 2018.

[86] Y. Togawa, T. Koyama, Y. Nishimori, Y. Matsumoto, S. McVitie, D. McGrouther, R. L. Stamps, Y. Kousaka, J. Akimitsu, S. Nishihara, K. Inoue, I. G. Bostrem, V. E. Sinitsyn, A. S. Ovchinnikov, and J. Kishine *Phys. Rev. B*, vol. 92, p. 220412(R), 2015.

[87] S. S. P. Parkin, M. Hayashi, and M. Thomas *Science*, vol. 320, pp. 190–194, 2008.

[88] N. Kanazawa, S. Seki, and Y. Tokura *Adv. Mater.*, vol. 29, p. 1603227, 2017.

[89] I. Kézsmárki, S. Bordács, P. Milde, E. Neuber, L. M. Eng, J. S. White, H. M. Rønnow, C. D. Dewhurst, M. Mochizuki, K. Yanai, H. Nakamura, D. Ehlers, V. Tsurkan, and A. Loidl *Nat. Mater.*, vol. 14, pp. 1116–1122, 2015.

[90] A. Štefančič, S. H. Moody, T. J. Hicken, M. T. Birch, G. Balakrishnan, S. A. Barnett, N. Crisanti, J. S. O. Evans, S. J. R. Holt, J. A. Franke, P. D. Hatton, B. M. Huddart, M. R. Lees, F. L. Pratt, C. C. Tang, M. N. Wilson, F. Xiao, and T. Lancaster *Phys. Rev. Mat*, vol. 2, p. 111402(R), 2018.

[91] T. Okubo, S. Chung, and H. Kawamura *Phys. Rev. Lett.*, vol. 108, p. 017206, 2012.

[92] F. R. Gamble, J. Disalvor, A. Klemmand, and T. H. Geballe, "Superconductivity in layered structure organometallic crystals," *Science*, vol. 168, no. 3931, pp. 568–570, 1970.

[93] J. C. Lund, F. Olschner, and A. Burger, *Semiconductors and Semimetals*, vol. 43. Elsevier Ltd., 1995.

[94] R. Bachmann, F. J. DiSalvo Jr., T. H. Geballe, R. L. Greene, R. E. Howard, C. N. King, H. C. Kirsch, K. N. Lee, R. E. Schwall, H. U. Thomas, and R. B. Zubeck *Rev. Sci. Instrum.*, vol. 43, p. 205, 1972.

[95] R. J. Schutz *Rev. Sci. Instrum.*, vol. 45, p. 548, 1974.

[96] S. Banerjee, M. W. J. Prins, K. P. Rajeev, and A. K. Raychaud-huri *Pramana––J. Phys.*, vol. 39, p. 391, 1992.

[97] K. Ema, T. Uematsu, A. Sugata, and H. Yao *Jpn. J. Appl. Phys.*, vol. 32, p. 1846, 1993.

[98] H. Yao, K. Ema, and C. W. Garland *Rev. Sci. Instrum.*, vol. 69, p. 172, 1998.

[99] I. Hatta *Rev. Sci. Instrum.*, vol. 50, p. 292, 1979.

[100] L. S. Azechi, R. F. da Costa, A. N. Medina, and F. C. G. Gandra *Rev. Fís. Apl. Instrum.*, vol. 10, p. 70, 1995.

[101] E. S. R. Gopal, *Specific Heats at Low Temperatures.* New York: Springer, 1966.

[102] JEOL, "Jem 2100 electron microscope," *Instruction Manual*, no. IEM210-1, 2004.

[103] A. A. Coelho, "Topas and topas-academic: an optimization program integrating computer algebra and crystallographic objects written in c++," *J. Appl. Crystallogr.*, vol. 51, pp. 210–218, 2018.

[104] H. Rietveld *Acta Crystallographica*, vol. 22, pp. 151–152, 1967.

[105] H. M. Rietveld *J. Appl. Crystallogr.*, vol. 2, pp. 65–71, 1969.

[106] R. E. Dinnebier, A. Leineweber, and J. S. Evans, *Rietveld refinement: practical powder diffraction analysis using TOPAS.*

[107] J. Cosier and A. M. Glazer *J. Appl. Cryst.*, vol. 19, pp. 105–107, 1986.

[108] R. O. Diffraction, *CrysAlis PRO.* Yarnton, UK: Oxford Diffraction Ltd., 2019.

[109] G. M. Sheldrick *Acta. Crystallogr. Sect. A*, vol. 71, pp. 3–8, 2015.

[110] G. M. Sheldrick *Acta. Crystallogr. Sect. C*, vol. 71, pp. 3–8, 2015.

[111] O. V. Dolomanov, L. J. Bourhis, R. J. Gildea, J. A. K. Howard, and H. Puschmann *J. Appl. Crystallogr.*, vol. 42, pp. 339–341, 2009.

[112] L. C. Chapon, P. Manuel, P. G. Radaelli, C. Benson, L. Perrott, S. Ansell, N. J. Rhodes, D. Raspino, D. Duxbury, E. Spill, and J. Norris *Neutron News*, vol. 22, p. 22, 2011.

[113] O. Arnold, J. Bilheux, J. Borregeuro, A. Buts, S. Campbell, L. Chapon, M. Doucet, N. Draper, R. Ferraz Leal, M. Gigg, V. Lynch, A. Markvardsen, D. Mikkelson, R. Mikkelson, R. Miller, K. Palmen, P. Parker, G. Passos, T. Perring, P. Peterson, S. Ren, M. Reuter, A. Savici, J. Taylor, R. Taylor, R. Tolchenov, W. Zhou, and J. Zikovsky *Nucl. Instrum. Meth. A*, vol. 764, p. 156, 2014.

[114] J. Rodríguez-Carvajal *IUCr Commission on Powder Diffraction Newsletter*, vol. 26, pp. 12–19, 2001.

[115] V. Petříček, M. Henriques, and M. Dušek *Acta Cryst.*, vol. A77, p. C175, 2021.

[116] J. Clarke and A. Braginski, *The SQUID Handbook: Vol. I Fundamentals and Technology of SQUIDS and SQUID Systems.* Weinheim: Wiley-VCH.

[117] Q. Design, *Coupling Magnetic Signals to a SQUID Amplifier.* 2001.

[118] C. Zuo, J. Li, J. Sun, Y. Fan, J. Zhang, L. Lu, R. Zhang, B. Wang, L. Huang, and Q. Chen *Opt. Las. Eng.*, vol. 135, p. 106187, 2020.

[119] A. Kohn, A. Habibi, and M. Mayo *Ultramicroscopy*, vol. 160, pp. 44–56, 2016.

[120] L. M. Volkova and D. V. Marinin *J. Appl. Phys.*, vol. 116, p. 133901, 2014.

[121] P. M. Ostrovsky, V. Gornyi, and A. D. Mirlin *Phys. Rev. B*, vol. 74, p. 235443, 206.

[122] I. Grosu and T.-L. Biter *Phys. Lett. A*, vol. 382, pp. 3042–3045, 2018.

[123] H. T. Stokes, D. M. Hatch, and B. J. Campbell, "Isotropy software suite." iso.byu.edu.

[124] B. J. Campbell, H. T. Stokes, D. E. Tanner, and D. M. Hatch *J. Appl. Crystallogr.*, vol. 39, p. 607, 2006.

[125] D. G. Porter, M. S. Senn, D. D. Khalyavin, A. Cortese, N. Waterfield-Price, P. G. Radaelli, P. Manuel, H. C. zur Loye, C. Mazzoli, and A. Bombardi *Phys. Rev. B*, vol. 94, p. 134404, 2016.

[126] T. Moriya and T. Miyadai *Solid State Commun.*, vol. 42, p. 209, 1982.

[127] Y. Togawa, Y. Kousaka, K. Inoue, and J.-I. Kishine *J. Phys. Soc. Jpn.*, vol. 85, p. 112001, 2016.

[128] C. D. Dashwood, L. S. I. Veiga, Q. Faure, J. G. Vale, D. G. Porter, S. P. Collins, P. Manuel, D. D. Khalyavin, F. Orlandi, R. S. Perry, R. D. Johnson, and D. F. McMorrow *Phys. Rev. B*, vol. 102, p. 180410(R), 2020.

[129] A. Kadomtseva, A. Zvezdin, Y. Popov, A. Pyatakov, and G. Vorobev *JETP Lett.*, vol. 79, p. 571, 2004.

[130] K. Tsuruta, M. Mito, H. Deguchi, J. Kishine, Y. Kousaka, J. Akimitsu, and K. Inoue *Phys. Rev. B*, vol. 93, p. 104402, 2016.

[131] Y. Kousaka, T. Ogura, J. Zhang, P. Miao, S. Lee, S. Torii, T. Kamiyama, J. Campo, K. Inoue, and J. Akimitsu *J. Phys.: Conf. Series*, vol. 746, p. 012061, 2016.

[132] V. Dyadkin, F. Mushenok, A. Bosak, D. Menzel, S. Grigoriev, P. Pattison, and D. Chernyshov *Phys. Rev. B*, vol. 91, p. 184205, 2015.

[133] T. Ma, A. K. Sharma, R. Saha, A. K. Srivastava, P. Werner, P. Vir, V. Kumar, C. Felser, and S. S. P. Parkin *Adv. Mater.*, vol. 32, p. 2002043, 2020.

[134] K. Chai, Z.-A. Li, R. Liu, B. Zou, M. Farled, and J. Libef *Nanoscale*, vol. 12, pp. 14919–14925, 2020.

[135] S. McVitie, S. Hughes, K. Fallon, S. McFadzean, D. McGrouther, M. Krajnak, W. Legrand, D. Maccariello, S. Collin, K. Garcia, N. Reyren, V. Cros, A. Fert, K. Zeissler, and H. C. Marrows *Sci. Rep.*, vol. 8, p. 5703, 2018.

[136] J. J. Chess, S. A. Montoya, E. E. Fullerton, and B. J. McMorran *AIP Advances*, vol. 7, p. 056807, 2017.

[137] J. I. Yonemura, Y. Shimamoto, T. Kida, D. Yoshizawa, Y. Kousaka, S. Nishihara, F. J. T. Goncalves, J. Akimitsu, K. Inoue, M. Hagiwara, and Y. Togawa *Phys. Rev. B*, vol. 96, p. 184423, 2017.

[138] K. Du, F.-T. Huang, J. Kim, S. J. Lim, K. Gamage, J. Yang, M. Mostovoy, J. Garlow, M.-G. Han, Y. Zhu, and S.-W. Cheong *PNAS*, vol. 118 (40), p. e2023337118, 2021.

[139] Y. Kousaka, Y. Nakao, J. Kishine, M. Akita, K. Inoue, and J. Akimitsu *Nucl. Inst. Meth. Phys. Res. A*, vol. 600, pp. 250–253, 2009.

[140] Y. Dai, W. Liu, Y. Wang, J. Fan, L. Pil, L. Zhang, and Y. Zhang *J. Phys.: Condens. Matter*, vol. 31, p. 195803, 2019.

[141] V. V. Ogoblichev, Y. V. Piskunov, and F. B. Mushenok *J. Exp. Theor. Phys.*, vol. 2, pp. 317–322, 2017.

[142] J. Kishine, K. Inoue, and Y. Yoshida *Prog. Theor. Phys. Suppl.*, vol. 159, p. 82, 2005.

[143] Y. Kousaka, S. Yano, J. Kishine, Y. Yoshida, K. Inoue, K. Kikuchi, and J. Akimitsu *J. Phys. Soc. Jpn.*, vol. 76, p. 123709, 2007.

[144] S. S. P. Parkin and R. H. Friend *Phil. Mag. B*, vol. 41, pp. 65–93, 1980.

[145] Y. Ōnuki, K. Ina, T. Hirai, and T. Komatsubara *J. Phys. Soc. Jpn.*, vol. 55, pp. 347–356, 1986.

[146] Y. Dai, W. Liu, Y. Wang, J. Fan, L. Pil, L. Zhang, and Y. Zhang *J. Phys.: Condens. Matter*, vol. 31, p. 195803, 2019.

[147] S. K. Karna, F. N. Womack, R. Chapai, D. P. Young, M. Marshall, W. Xie, D. Graf, Y. Wu, H. Cao, L. DeBeer-Schmitt, P. W. Adams, R. Jin, and J. F. DiTusa *Phys. Rev. B*, vol. 100, p. 184413, 2019.

[148] S. K. Karna, M. Marshall, W. Xie, L. DeBeer-Schmitt, D. P. Young, I. Vekhter, W. A. Shelton, A. Kovács, M. Charilaou, and J. F. DiTusa *Nano Lett.*, vol. 21, pp. 1205–1212, 2021.